

Non-Neutral Sheath Region Around Surfaces In  
Low Temperature Plasma Containing Negative Ions

*By*  
AVNISH KUMAR PANDEY  
PHYS06201404002

Institute for Plasma Research, Gandhinagar

*A thesis submitted to the*  
*Board of Studies in Physical Sciences*  
*In partial fulfillment of requirements*  
*For the Degree of*  
DOCTOR OF PHILOSOPHY  
*of*  
HOMI BHABHA NATIONAL INSTITUTE



July, 2020



# Homi Bhabha National Institute

## Recommendations of the Viva Voce Board

As members of the Viva Voce Board, we certify that we have read the dissertation prepared by AVNISH KUMAR PANDEY entitled "Non-Neutral Sheath Region Around Surfaces In Low Temperature Plasma Containing Negative Ions" and recommend that it maybe accepted as fulfilling the dissertation requirement for the Degree of Doctor of Philosophy.



SUDIP SENGUPTA

Date: 21/12/2021

Chair -

Shantamu Karikan



Date: 21/12/2021

Guide/Convener -

Date:

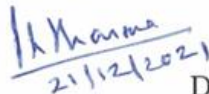
Examiner -



HK Malik 20/12/2021

Date:

Member 1 - Dr. Promod Kumar Sharma



Date: 21/12/2021

Member 2 -

Dr. Mainak Bandyopadhyay



Date: 21.12.2021

Member 3 -

Final approval and acceptance of this dissertation is contingent upon the candidate's submission of the final copies of the dissertation to HBNI.

I hereby certify that I have read this dissertation prepared under my direction and recommend that it may be accepted as fulfilling the dissertation requirement.

Date: 21/12/2021

Place: Chandigarh



Guide



## STATEMENT BY AUTHOR

This dissertation has been submitted in partial fulfillment of requirements for an advanced degree at Homi Bhabha National Institute (HBNI) and is deposited in the Library to be made available to borrowers under rules of the HBNI.

Brief quotations from this dissertation are allowable without special permission, provided that accurate acknowledgment of source is made. Requests for permission for extended quotation from or reproduction of this manuscript in whole or in part may be granted by the Competent Authority of HBNI when in his or her judgement the proposed use of the material is in the interests of scholarship. In all other instances, however, permission must be obtained from the author.

*Avnish Kumar Pandey*  
21/12/21

Avnish Kumar Pandey



## **Declaration**

I, hereby declare that the investigation presented in the thesis has been carried out by me. The work is original and has not been submitted earlier as a whole or in part for a degree / diploma at this or any other institution / university.

*Avnish Kumar Pandey*

Avnish Kumar Pandey





## CERTIFICATION ON ACADEMIC INTEGRITY

1. I Avnish Kumar Pandey HBNI Enrolment No. PHYS06201404002 hereby undertake that, the Thesis titled "*Non-Neutral Sheath Region Around Surfaces In Low Temperature Plasma Containing Negative Ions*" is prepared by me and is the original work undertaken by me and free of any plagiarism. That the document has been duly checked through a plagiarism detection tool and the document is plagiarism free.
2. I am aware and undertake that if plagiarism is detected in my thesis at any stage in future, suitable penalty will be imposed as per the applicable guidelines of the Institute/UGC.

*Avnish Km. Pandey*  
21/12/21

Signature of Student

Endorsed by the thesis Supervisor:

(I certify that the work done by the Researcher is plagiarism free)

Signature



Name: Dr. S.K. Karkari

Designation: Asso. Professor - F

Department/Centre:

Name of CI/OCC: Institute for Plasma Research, Gandhinagar



## List of Publications from this thesis

### a) Journal Publications

1. **Pandey, A. K.**, & Karkari, S. K. (2017). Characteristics of floating potential of a probe in electronegative plasma. *Physics of Plasmas*, 24(1), 013507.
2. **Pandey, A. K.**, Joshi, J. K., & Karkari, S. K. (2020). Inferring plasma parameters from the sheath characteristics of a dc biased hairpin probe. *Plasma Sources Science and Technology*, 29(1), 015009.
3. **Pandey, A. K.**, & Karkari, S. K. (2020). Positive ion speed at the plasma–sheath boundary of a negative ion-emitting electrode. *Contributions to Plasma Physics*, 60(3), e201900116.

### b) Other Publications : Conferences/Symposium

1. **Pandey, A. K.**, & S K Karkari, Poster presentation on “*Using biased hairpin probe for determining oxygen negative Ions in a double plasma device*”. 45th EPS-2018 conference on plasma physics, Prague, Czech Republic.
2. **Pandey, A. K.**, Jay K Joshi & S K Karkari, Oral presentation on “*Determining electron temperature & negative ion concentration in argon/oxygen discharge using a biased hairpin probe*” 33rd National Symposium on Plasma Science & Technology (PLASMA-2018) Department of Physics and Astrophysics, University of Delhi, Delhi
3. **Pandey, A. K.** , & S K Karkari, Poster presentation on “*Floating sheath characteristic of a negative ion emitting electrode in electronegative plasma*”, 3rd Asia Pacific conference on Plasma physics (AAPPS-DPP 2019), Hefei, China.



*Dedicated  
to my  
Parents*



## ACKNOWLEDGEMENTS

First and foremost, I would like to offer a deep sense of gratitude to my thesis mentor Dr. Shantanu Kumar Karkari for his continued support and insightful supervision since the day I joined under him as a research scholar. I honestly feel very grateful to have opportunity to work under his guidance. His exceptional attitude towards elucidating the research problems motivated me to overcome many challenging situation related to my research work and finally I could finish my thesis. It would have been unimaginable for me to complete this thesis work without his support & encouragement. Thank you sir!

I am also very much grateful to the chairman of my doctoral committee, Prof. Sudip Sengupta and the committee members Dr. M Bandyopadhyay, Dr. P. K. Sharma and Late Dr. R. Srinivasan for their insightful comments and important suggestion given during my doctoral reviews which has helped me to improve this work. I am grateful to the other faculty members Prof. S. Mukherjee, Prof. R. Ganesh, Prof. A. Das, Dr. M. Kundu, Dr. Ramasubramanian, Dr. V. P. Anitha, Dr. R. Goswami, Dr. Maya, Dr. Ravi and others who have taught me the basic/experimental plasma physics, computational techniques and the other fundamental courses in physics during the 1st year course work. A shout out to all my teachers including in school-time and university professors during graduate and post-graduate who have great contribution to make me the person, I am today. A special thanks to Prof. Rajaram Yadav of Allahabad University, who has always motivated me whenever I get a chance to meet him.

This acknowledge would not be complete without mentioning my father for his unconditional support in every aspect of my life. I truly cannot shape my feelings of gratitude into words for the sacrifices that you have made over the past 28 years. An equal contribution to this work also comes from my mother, whose prayers to

almighty God would always include a dozen of blessing for me. I am indebted to my late grandfather for his wholehearted support during my early education. I would also like to show my love & affection to my younger brother Rupesh, elder brother Avanindra, his wife Pooja and their children Pari and Mangalam for their appreciation & unconditional love. A special mention to a beautiful lady Ms. Ruchi pandey, who is going to be in wedding-knot with me. I am deeply touched by her supporting nature and for believing in me as a true friend.

The IPR library, Computer section, Drafting section, Mr. Vijay Patel from Workshop, IPR stores; all have their contribution in this work and deserves a worthy mention in this acknowledgement. I would also like to thank my fellow researchers and labmates Shivam, Rupak, Jay, Montu, Shikha, Swati, Pawandeep and Satadal for having mind storming discussion with them on various physics problems. It helped me to understand my research area better. I thank to all my hostel mates, Jagannath, Prince, Piyush, Vijay Shankar, Shirish, Sanjeev and Pawandeep Kaur who have always wished me well. I also warmly thanks to my seniors Neeraj Chaubey, Rupendra, Mangilal, Vidhi, Ratan, Atul, Alamgir, Pallavi, Debraj, Umesh, Narayan, Bibhu, Sagar, Prabhakar and other scholars for giving important advices regarding research and for creating scientific atmosphere around me. I ask for compassion if I forgot to mention anyone who have contributed in this work by any means.

Finally, I take this opportunity to show my gratitude towards my institute which has given me so much support & appreciation that I will always be remain indebted.



# Abstract

Sheath is a non-neutral region which is ubiquitously formed at the surfaces of macroscopic bodies in contact with a plasma. Charged particles from the plasma then interacts with the surfaces due to the electric field present inside this non-neutral region. The physical phenomena associated with the sheaths is of interest primarily due to its immense applications in plasma assisted technologies, plasma-wall interaction in tokomaks, plasma based ion sources and in electrostatic probe diagnostics. Sheaths in low temperature plasmas containing negative ions is one of the fundamental areas of research which has relevance in production and extraction of negative ions from a plasma source.

In this study, sheaths in the presence of negative ions has been investigated with primary motivations to study the effect of surface produced negative ion emission on the sheath/ bulk plasma properties and application of sheaths in negative ion diagnostics. A simple one-dimensional model has been developed to study the nature of a collision-less, non-neutral sheath region at a planar electrode and its adjacent quasi-neutral pre-sheath region for the case of a negative ion emitting electrode. The analytical model is found to reproduce popular results and it also shows qualitative agreement with more rigorous particle-in-cell simulation by other authors. Some of the key highlights obtained from the analytical model suggests that counter-flowing negative ions injected from the quasi-neutral plasma boundary increases the potential drop inside the pre-sheath. Increase in negative ion emission leads to the thickening

of positive ion rich sheath, while maximum amount of negative ions flux emitted from the surface is actually governed by the positive ion flux that enters the sheath boundary from the bulk plasma. The analytical model also reveals the space charge effects and its dependence over the ion mass.

Negative ion density and temperature are the two most crucial parameters which are required in the modelling of a negative ion source. The well-known methods to determine these parameters are based on pulsed laser photo-detachment and cavity-ring-down spectrometry. These are largely sophisticated and expensive techniques. The electric probes are relatively simple and easily adaptable to any plasma systems. However, interpretation of negative ion parameters based on electrical probes are subjected to various errors associated with measurements and the various sheath theories related to it.

In the thesis, two important diagnostic techniques based on conventional Langmuir probe and a DC biased resonance hairpin probe to determine negative ion parameters in an oxygen discharge has been demonstrated. The Langmuir probe method based on the saturation current ratio has been combined with the floating potential information to estimate both electronegativity parameter  $\alpha$  (density ratio of negative ions to electron) and negative ion temperature  $T_v$  simultaneously. The DC biased resonance hairpin probe has been developed to measure the sheath width around the cylindrical probe along with the electron density, negative ion density and the electron temperature in an argon and/or oxygen discharge. To apply these diagnostics, a DC discharge device has been developed using a constricted anode and parallel plate cathode.

# Contents

<b>1</b>	<b>Introduction</b>	<b>1</b>
1.1	Plasma state . . . . .	4
1.1.1	Some basic properties . . . . .	5
1.2	The Sheath . . . . .	7
1.3	The Bohm speed: Requirement of pre-sheath . . . . .	11
1.4	Fluid description of plasma and sheath . . . . .	14
1.5	Dielectric description of plasma . . . . .	16
1.6	Brief overview of various Sheath theories and its application to Langmuir probe . . . . .	18
1.6.1	Ion collection by Langmuir probe for Collision-less sheath . . . . .	18
1.6.2	Ion collection by Langmuir probe for Collisional sheath . . . . .	21
1.7	Plasma containing negative Ions . . . . .	25
1.7.1	Volume production . . . . .	25
1.7.2	Surface production of negative ions . . . . .	27
1.8	Boltzmann distribution of negative ions . . . . .	30

1.9	Electric probes for determining negative ion parameters . . . . .	32
1.9.1	Measurement based on electrostatic probes . . . . .	33
1.9.2	Application of hairpin resonator probe . . . . .	36
1.10	Outline of the thesis . . . . .	37
<b>2</b>	<b>Experimental set-up and diagnostics</b>	<b>41</b>
2.1	Plasma sources for Negative Ion production . . . . .	41
2.2	The experimental setup . . . . .	42
2.2.1	The Plasma Source . . . . .	43
2.2.2	Experimental Vacuum chamber . . . . .	45
2.2.3	The Discharge Circuit . . . . .	46
2.2.4	DC plasma Characteristics . . . . .	48
2.3	Electric Probe Diagnostic . . . . .	49
2.3.1	Langmuir probes . . . . .	49
2.4	Hairpin resonance probe . . . . .	59
2.4.1	Resonance signal determination . . . . .	62
2.4.2	Limitation of hairpin probe diagnostic . . . . .	64
<b>3</b>	<b>Sheaths associated with Negative ion emitting Electrode</b>	<b>67</b>
3.1	Space charge region near a negative ion emitting electrode . . . . .	68
3.2	Analytical Model: Sheath with Negative Ion Emitting electrode . . . . .	73

3.2.1	Potential distribution inside sheath below space charge limited emission . . . . .	73
3.2.2	The positive ion Bohm speed . . . . .	76
3.2.3	Space Charge Limited Current . . . . .	78
3.2.4	Transported negative ion flux above the space charge limiting current . . . . .	79
3.2.5	Potential distribution due to virtual cathode . . . . .	82
3.3	Bohm speed during Negative Ion Emission from the electrode . . . . .	85
3.4	Sheath width characteristics . . . . .	88
3.5	Discussion . . . . .	90
3.6	Summary & Conclusion . . . . .	94
<b>4</b>	<b>The Pre-Sheath region of a negative ion emitting electrode</b>	<b>97</b>
4.1	Pre-sheath in negative ion plasma . . . . .	98
4.2	1-D model of pre-sheath . . . . .	99
4.3	Results and discussion . . . . .	103
4.3.1	Pre-sheath dependence on volume negative ions . . . . .	103
4.3.2	Pre-sheath dependence on injected negative ions . . . . .	106
4.3.3	Characteristic Pre-sheath Length . . . . .	108
4.4	Interpretation of Bohm speed . . . . .	109
4.5	Summary & conclusion . . . . .	111
<b>5</b>	<b>Floating Potential and its application in negative ion plasma</b>	<b>113</b>

5.1	Floating potential of a negative ion emitting electrode . . . . .	114
5.1.1	Analytical Model . . . . .	115
5.1.2	Analytical results and Comparison with PIC simulation . . . . .	120
5.2	Sheath potential of a floating non-emitting electrode . . . . .	126
5.2.1	Floating potential dependence over bulk plasma parameters . . . . .	127
5.3	Application of cold probe floating potential for determining negative ion parameters . . . . .	130
5.3.1	Finding the electronegativity parameter $\alpha$ and $\gamma_v$ . . . . .	130
5.3.2	Experimental Results and discussion . . . . .	133
5.4	Summary & Conclusion . . . . .	144
<b>6</b>	<b>Cylindrical DC sheath and its application to hairpin probe</b>	<b>147</b>
6.1	Introduction . . . . .	147
6.2	The radial flow model for cylindrical sheath . . . . .	148
6.3	DC biased hairpin probe: Underlying concept . . . . .	152
6.4	DC Biased hairpin Probe: The experimental process . . . . .	156
6.5	Experimental results . . . . .	160
6.5.1	Determining the Sheath Width . . . . .	160
6.5.2	Finding Electron temperature . . . . .	161
6.5.3	Finding $\alpha_0$ and $T_e$ in an electro-negative plasma . . . . .	165
6.6	Summary and Conclusion . . . . .	167

**7 Summary, Conclusions and Future scope of work** **169**

7.1 Summary & Conclusion . . . . . 169

7.2 Future Scope of the Work . . . . . 172





# List of Figures

1.1	Formation of sheath around spherical object biased at a negative potential with respect to a reference electrode; $r_{max}$ is maximum distance over which the quasi-neutrality is violated . . . . .	9
1.2	One dimensional representation of sheath, pre-sheath and bulk plasma. The potential on the electrode $\phi_{wall}$ is with respect to the sheath edge defined at a distance $x = s$ from the electrode ( $x = 0$ ). The electrons and ions have almost equal density in pre-sheath i.e. $n_e \approx n_p$ , but smaller than the common density $n_0$ in bulk plasma. . . . .	12
1.3	Different sheath models namely (a) continuous plasma-wall model, (b) diffuse electron boundary model, (c) step-front sheath model and (d) matrix sheath model depending on the density distribution of electrons (red) & positive ions (black); $n_0$ is bulk plasma density, $n_{es}$ and $n_{ps}$ are density of electrons and positive ions at the sheath edge respectively. . . . .	16
1.4	Bryant's plot representing the scaling of various probe theories based on parameters $D_\lambda = r_p/\lambda_D$ , $K_{e,i} = \lambda_{i,e}/r_p$ and $\tau = T_e/T_p$ . . . . .	24

1.5	Total $H^-$ ion yield, $Y(T_g)$ as a function of neutral temperature. Courtesy: <i>Brian S Lee and M Seidl. "Surface production of <math>H^-</math> ions by hyper-thermal hydrogen atoms". In: Applied physics letters 61.24 (1992), pp. 2857-2859.</i> . . . . .	29
1.6	One dimensional density profiles for chlorine discharge of discharge length $l_p = 0.45$ cm, electron density $n_{e0} = 10^{16} m^{-3}$ at pressure (a) 30 mTorr and (b) 300 mTorr. The density gradient $\frac{dn_v}{dx}$ for low pressure case (30 mTorr) is slowly varying function of $x$ ; while for high pressure case $\frac{dn_v}{dx} \approx 0$ in the center of the discharge. Courtesy: <i>A J Lichtenberg et al 1997 Plasma Sources Sci. Technol. 6 437</i> . . . . .	32
1.7	The second derivative of probe current (curve A) with respect to probe bias showing two distinct peak (solid curves) corresponding to electron and negative ions. Courtesy: <i>Amemiya, H, Journal of the Physical Society of Japan, 57(3), 887-902 (1988).</i> . . . . .	34
2.1	Schematic of discharge setup showing the constricted anode and pair of annular cathode plates. Axial magnetic field is generated by two external electromagnet coils EM1 and EM2 arranged in Helmholtz configuration. . . . .	44
2.2	Experimental setup with circular electromagnetic coils in Helmholtz configuration. . . . .	45
2.3	Schematic of unregulated power supply. In the figure $D_1, D_2, D_3$ and $D_4$ are diodes, $C$ is capacitor and $V_{dc}$ is output DC voltage. . . . .	47
2.4	Schematic of discharge circuits: In setup-I, the anode is grounded through a high resistance value $1k\Omega$ , while in setup-II, the voltage is divided between cathode and anode with respect to the grounded chamber. . . . .	47

2.5	Plot of discharge current verses discharge voltage for setup-1 and setup-II. . . . .	48
2.6	The anodic glow or fireball structure around the anode in oxygen plasma. . . . .	49
2.7	A schematic of Probe current $I$ verses applied bias $V_B$ applied on the cylindrical Langmuir probe, shown in solid black line. The red dotted line corresponds to the current due to electron, while the positive ion current is shown by the black dotted line. . . . .	50
2.8	A typical $I(V_B)$ characteristic (black curve) using a cylindrical probe of length 6 mm and diameter 0.2 mm in experimental setup-I. The maxima observed in first derivative of the probe current (red curve) corresponds to plasma potential $V_p = 4.2$ V. The typical discharge parameters are $P = 5$ Pa and $P_w = 86$ watts. . . . .	52
2.9	The ionic part of $I(V_B)$ characteristic curve. The straight line fit of the ion current and extrapolating up to floating potential $V_f = 1.6$ V gives the ion saturation current $I_{ps} = 54 \mu\text{A}$ . . . . .	53
2.10	The semi-log plot for electron saturation current with respect to the probe bias $V_B$ . The straight line fit namely AB and CD indicates the presence of bi-Maxwellian electrons having temperature $T_{eh}$ and $T_{eb}$ respectively. . . . .	54
2.11	The plot for percentage fraction of hot population electrons with respect to pressure and discharge power. . . . .	55

2.12 (a) A typical Langmuir probe circuit showing a cylindrical probe inside a plasma biased at a positive potential with respect to the (Grounded) reference electrode. (b) Equivalent circuit is shown in which $R_m$ , $R_p$ and $R_G$ are respectively the current measuring resistance, resistance of the probe sheath and the resistance between the plasma and the Grounded reference electrode. . . . .	56
2.13 Schematic of Langmuir probe circuit. DAQ represents data acquisition, OP-AMP denotes operational amplifier. . . . .	58
2.14 (a) Open circuit signal with (Red) and without (black) subtraction of the background. (b) Plot of $I(V_B)$ trace with and without calibration. . . . .	58
2.15 Comparison of plasma potential by different method. Here $V_{p1}$ is obtained by 1st derivative of probe current, $V_{p2}$ is obtained by locating the inflection point in semi-log plot of electron current, $V_{p3}$ is obtained from floating condition of the probe and $V_{p4}$ is obtained from OML theory. . . . .	60
2.16 (a) The schematic of floating hairpin resonator probe and (b) The organ pipe experiment showing the standing wave pattern due to resonance . . . . .	61
2.17 Schematic of the floating hairpin measurement circuit . . . . .	62
2.18 (a) The reflected signal by hairpin probe when the probe is in vacuum (red) and in plasma medium (black). (b) the reflected signal subtracted from the vacuum resonance signal. The typical discharge parameters are $P = 1.4$ Pa & $P_w = 17.2$ W. . . . .	63
2.19 The electron density measurement with the help of a floating hairpin probe in argon plasma with regards to discharge power for a range of gas pressure. . . . .	64

3.1	A schematic of sheath in front of an electrode emitting negative ions. The arrows indicate the flow of surface produced negative ions and other plasma species such as electrons, volume negative ions and positive ions. . . . .	69
3.2	Schematic representation of potential distribution in front of a negative ion emitting electrode for the cases when (a) the emission is below the space charge limit and (b) above space charge limit. In the case (b) a virtual cathode of depth $\eta_k$ is created, which separate the entire sheath into two region namely A & B. The potentials are normalized with electron temperature, i.e. $\eta = e\phi/K_B T_e$ . . . . .	70
3.3	Spatial distribution of potential inside the negative ion emitting sheath for three distinct values of $J_n = 0, 0.7$ and $0.95$ . The parameter used here are $\eta_c = -10, \varepsilon_b = 0.2$ and $\alpha_s = 0$ . . . . .	79
3.4	Plot of (a) negative ion flux $J_{nvc}$ transported at the sheath edge and (b) depth of the potential minima as a function of $J_n$ . The parameters used are $\varepsilon_b = 0.2, \alpha_s = 0$ and $\eta_c = -10$ . . . . .	81
3.5	The plots showing (a) density $\beta_s$ and (b) speed $V_{ns}$ of transported negative ions at the sheath edge. The typical parameters are $\varepsilon_b = 0.2, \alpha_s = 0$ and $\eta_c = -10$ . . . . .	82
3.6	The plot of potential distribution inside the sheath for $J_n = 2, 6$ and $12$ . The parameter used here are $\eta_c = -10, \varepsilon_b = 0.2$ and $\alpha_s = 0$ . The electrode position is defined at $X = 30$ . . . . .	85
3.7	The variation of Bohm speed $U_B$ of positive ions as a function of emitted flux $J_n$ . The typical parameters are $\varepsilon_b = 0.2$ and $\alpha_s = 0$ . The electrode is at constant potential $\eta_c = -10$ . . . . .	86

3.8	The variation of (a) the negative ion density $\beta_s$ (b) the speed $V_{ns}$ and (c) $U_B$ as a function of electrode potential $\eta_c$ for constant initial energy $\varepsilon_b = 0.2$ and flux $J_n = 12$ . . . . .	88
3.9	Variation of sheath thickness with respect to (a) electrode potential $\eta_c$ for constant $J_n = 4$ and $\varepsilon_b = 0.2$ and (b) emitted negative ion flux $J_n$ for a constant electrode bias $\eta_c = -10$ . A comparison with Child-Langmuir (CL) sheath-width is shown; the dotted and the dashed curve correspond to the approximate CL solution ( $U_B = 0$ ) and exact CL solution ( $U_B \neq 0$ ) respectively. The typical parameters $\alpha_s = 0$ is assumed. . . . .	89
3.10	(a) The cross sectional view of a penning type negative ions source with an independent biased emitter placed at a variable spacing $\delta$ from the plasma edge. (b) The extracted $H^-$ current as a function of emitter bias $U_c$ for two different spacing $\delta = 0.1$ mm and 0.7 mm from the plasma column edge. <i>Courtesy: Belchenko, Y. I. et al (2018)</i>	91
3.11	The variation of transported flux $J_{nvc}$ of negative ions at the sheath edge as a function of electrode potential $\eta_c$ . The injected flux $J_n = 12$ , $\alpha_s = 0$ and initial kinetic energy $\varepsilon_b = 0.2$ are assumed as parameter.	91
3.12	The plot of potential distribution inside the sheath for $J_n = 6.86$ . The parameter used here are $\eta_c = -2, \varepsilon_b = 0.6, \alpha_s = 0.27$ and $\gamma_v = 1$ . The electrode position is defined at $X = 31$ . . . . .	93
4.1	A schematic showing the charged particle transport inside the pre-sheath region, represented by arrow. A finite flux of negative ion beam is assumed to enter at the plasma-sheath boundary ( $x = x_l$ ). The center of the bulk plasma is represented at $x = 0$ ; where the electric field and potential are assumed to be zero. . . . .	100

4.2	Plots showing spatial profile of (a) the charge particle density of individual species and (b) the positive ion speed. The vertical dashed line shows the pre-sheath end. The parameter considered at $X = 0$ are $\alpha_0 = 0.2$ and $\gamma_v = 10$ . . . . .	104
4.3	Plots showing spatial variation of pre-sheath potential $\eta$ for $J_n = 0$ and different values of bulk electro-negativity parameter $\alpha_0 = 0, 1.5, 2$ & $\gamma_v = 10$ . The origin inside the bulk plasma is defined at $X = 0$ where potential and electric field is zero. Symbols ‘ $\times$ ’ denotes the end of the pre-sheath regio. . . . .	105
4.4	The spatial distribution of pre-sheath potential $\eta(X)$ for a range of injected flux $J_n = 0$ to 20. The position $X = 0$ is the center of discharge and the symbol ‘ $\times$ ’ denotes the end of the pre-sheath at $X = X_l$ . The typical parameters are $\alpha_0 = 0, A'_e = 0.1, A'_i = 0, \mu_{np} = 1, \delta_{n,p} \approx 0$ . . . . .	107
4.5	Plot for pre-sheath length with respect to emission flux $J_n$ , where $J_{nmax} \approx 0.95$ . The parameters are same as considered in fig-4.4 . . . . .	109
5.1	The spatial distribution of potential inside the floating sheath in H-plasma for the cases when (a) the emitted flux $J_n < J_{nmax}$ and (b) $J_n > J_{nmax}$ . Here $J_{nmax} = 0.69$ is space charge limited value of emission. The parameters are $\alpha_s = 0$ and $\varepsilon_b = 0.35$ . . . . .	121
5.2	The plot for transported flux $J_{nvc}$ at the sheath edge as a function of injected flux $J_n$ of $H^-$ ion from the electrode. Here $J_{nmax} = 0.69$ is space charge limited value corresponding to the parameters $\alpha_s = 0$ and $\varepsilon_b = 0.35$ . The slope= 1 signifies the fact that the emitted flux $J_n$ gets totally transported at the sheath edge for $J_n < J_{nmax}$ . . . . .	122

5.3	(a) The variation in magnitude of floating potential $\eta_f$ and (b) positive ion Bohm speed $U_B$ as a function of injected flux $J_n$ for H-plasma ( $\mu_{pn} = 1$ ). The region-I & II corresponding to $J_n < J_{nmax}$ and $J_n > J_{nmax}$ denotes the emission below and above the space charge limited value $J_{nmax}$ respectively. . . . .	123
5.4	The spatial distribution of (a) potential and (b) charged particle density inside the floating sheath for $J_n = 0.77$ . The floating potential at the electrode is found to be $\eta_f = -1.91$ ; whereas the virtual cathode depth is $\eta_k = -0.10$ . The density ratio $N_n/N_e = 1$ is found at normalized distance $X \approx 5.0$ from the floating electrode ( $X = 0$ ). The parameters $\alpha_s = 0$ and $\varepsilon_b = 0.35$ are used. . . . .	125
5.5	The density distribution (left y-axis) and potential distribution (right y-axis) inside the sheath of a floating negative ion emitting electrode placed at origin $X = 0$ . <i>Courtesy: D. Wunderlich, Plasma Sources Science and Technology, 18.4 (2009): 045031.</i> . . . . .	126
5.6	Plots of absolute value of normalized floating potential $ \eta_f $ as a function of $\alpha_s$ for $\gamma_v = 1, 10, 60$ . . . . .	128
5.7	Plot of (a) $\alpha_{sc}$ and (b) $ \eta_{fc} $ as a function of $\gamma_v$ . . . . .	129
5.8	Variation of normalized Bohm velocity $U_B \equiv V_{ps} = v_{ps}/c_s$ with electro-negativity parameter $\alpha_s$ for $\gamma_v = 1, 10$ & $60$ . . . . .	130



5.9	Plot of (a) a typical $I(V_B)$ characteristics in an oxygen discharge, (b) ion saturation current $I_{ps} = 45 \mu\text{A}$ obtained by extrapolating up to floating potential $V_f = 1.3 \text{ V}$ and (c) the first derivative ( $dI/dV_B$ ) curve giving the plasma potential $V_p = 3.8\text{V}$ . The current corresponding to $V_p$ gives the net saturation current $(I_{es} + I_{vs}) = 0.7\text{mA}$ . The discharge power is $P_w = 143 \text{ watts}$ & operating pressure is $P = 4 \text{ Pa}$ . . . . .	134
5.10	The plot for electron current $I_e$ (left y-axis) and natural log of $I_e$ (right y-axis) with respect to the probe bias $V_B$ . Two slopes in $\ln(I_e)$ plot corresponds to the two electron temperature $T_{eb} = 0.6\text{eV}$ and $T_{eh} = 4.6\text{eV}$ . The discharge power is $P_w = 143 \text{ watts}$ & operating pressure is $P = 4 \text{ Pa}$ . . . . .	135
5.11	The plot for electron temperature $T_{eb}$ and $T_{eh}$ with respect to discharge power in oxygen plasma for pressure range $P = 4 \text{ Pa}$ to $7 \text{ Pa}$ . . . . .	136
5.12	The plot for saturation current ratio with respect to discharge power in argon and oxygen discharge. The operating pressure is kept fixed at $P = 4 \text{ Pa}$ . . . . .	137
5.13	The plot for saturation current ratio with respect to discharge power and for various pressure in oxygen discharge. . . . .	138
5.14	The plot for normalized value of floating potential $(V_p - V_f)/T_e$ with respect to discharge power and for various pressure in oxygen discharge. . . . .	139
5.15	The plot for (a) the electro-negativity parameter $\alpha_0$ and (b) the temperature ratio $\gamma_v$ with respect to discharge power and for various pressure in oxygen discharge. . . . .	140

5.16	The electro-negativity parameter $\alpha_0 = n_-/n_e$ with respect to pressure for three distinct discharge power 100, 500 and 1500 W. Courtesy: <i>J. T. Gudmundsson et al, J. Phys. D: Phys. 34, 1100–1109 (2001).</i> . . .	141
5.17	The theoretical plots of normalized value of floating potential $\eta_f$ a function of $\alpha_s$ for different $\gamma_v$ . The scattered data points are obtained in the experiment for which the polynomial fit of $2^{nd}$ order is observed to be the best fit coinciding with the theoretical curves for (a) $\gamma_v \approx 12.5$ at pressure $P = 4$ Pa, (b) $\gamma_v \approx 11$ at pressure $P = 5$ Pa (c) $\gamma_v \approx 9$ at $P = 6$ Pa and (d) $\gamma_v \approx 7.5$ at $P = 7$ Pa. . . . .	144
6.1	Schematic of sheath formation around the cross-section of a cylindrical probe with radius $a$ . The sheath radius is $b$ . The potential on the probe and at the sheath edge are respectively $\phi_a$ and $\phi_b$ . . . . .	149
6.2	The schematic of the sheath formed around the hairpin tips. The sheath radius is $b$ , and probe radius is $a$ (front view). The separation between the hairpin is $2h$ . . . . .	152
6.3	The schematic of DC biased hairpin probe. The total length of hairpin is $L + h$ . . . . .	157
6.4	The reflected microwave signal (subtracted by the vacuum value) with respect to the frequency sweep $f_r$ (GHz) for various bias applied to the probe. The operating pressure is $P = 1.8$ Pa and discharge power is $P_w = 49.5$ W. . . . .	157
6.5	Schematic of the biased hairpin measurement circuit. The resonance detection circuit and the biasing circuit to the hairpin are individually shown in black and red color respectively. . . . .	158

6.6	The variation in (a) resonance frequency $f_r$ and (b) current collected by the hairpin with respect to the probe bias voltage $V_B$ at a typical discharge power $P_w = 49.5$ W and operating pressure $P = 1.8$ Pa. The peaks observed in frequency curve and the (c) first derivative curve coincide at the same bias, providing the plasma potential $V_p = 11.5$ V, whereas the floating potential $V_f = 7.5$ V is obtained directly by measuring the potential on the floating probe inside the discharge.	159
6.7	The variation in sheath thickness, $s = (b - a)$ with probe bias $V_B$ for a typical operating pressure 1.8 Pa is shown. The probe radius is $a = 0.075$ mm; whereas the sheath radius $b$ is calculated by solving (6.11) & (6.12).	161
6.8	The variation in electron temperature, $T_e$ with regards to the power & pressure in argon plasma.	162
6.9	$T_e$ obtained in fig-6.8 along with the $n_{e0}$ found from measured resonance frequency at the $V_p$ are used in equation-6.8 to obtain the sheath thickness with respect probe bias (solid curve). The typical discharge power considered are (a) $P_w = 49.5$ W (b) $P_w = 82.8$ W at pressure 1.8 Pa. The solid curve obtained from the analytical model shows a good match with the sheath thickness found from the experiment (bubbled curve).	163
6.10	The variation in (a) ion saturation current $I_{ps}$ , (b) the sheath radius $b$ and (c) the absolute electron density $n_{e0}$ as a function of discharge power in argon plasma. Figure-(d) compares $T_e$ obtained from ion saturation current (#1) and floating potential condition (#2) respectively. The operating pressure is 1.8 Pa	164

6.11 Plot of electro-negativity parameter $\alpha_0$ as a function of discharge power & pressure in oxygen plasma; $\alpha_0$ and $T_e$ are found out by solving equation (6.16), (6.17) and (6.18) simultaneously, assuming the negative ion temperature to be $T_v \approx 0.05$ eV. . . . .	166
6.12 Variation in electron temperature $T_e$ with discharge power & pressure in oxygen plasma. . . . .	167

# List of Tables

5.1	Comparison of un-normalized floating potential $\phi_f$ and virtual cathode depth $\phi_k$ obtained from fluid model with the PIC simulation using the same plasma parameters. . . . .	125
6.1	The various measured parameters from the experiment for 1.8 Pa pressure in argon plasma . . . . .	161
6.2	The various measured parameters from the experiment for 1.8 Pa pressure in oxygen plasma. . . . .	162



# Chapter 1

## Introduction

In recent decades, industrialization of low temperature plasmas has rapidly happened due to its vast applications in semiconductor industries for etching of silicon wafer [1] and depositing anti-reflection coating on glass substrates [2]. These plasmas are created using electronegative gases which have a very high probability to form negative ions. The Negative hydrogen ions produced using low temperature plasmas are also required to generate MeV range neutral beams by charge exchange collision between the extracted negative ion beams from the plasma with the background gas neutrals [3]. Neutral beam injection (NBI) is one of the primary heating source in ITER fusion device [4, 5]. Plasmas containing negative ions have unique properties. Since the negative ions are colder and are quite massive than the electrons, it has a direct impact on the screening electric field inside the Debye sheaths and the ambipolar electric field inside the plasma. In addition to this, the ion acoustic speed, which is largely governed by electron temperature in an electron-positive ion plasma system, is determined by the temperature of negative ions assuming the role of electron in ion-ion plasma [6].

The presence of negative ions reduces the ambipolar electric field inside the bulk plasma. This property enables to achieve a flatter density and potential profile [7, 8].

Besides, the negative ions impact the behavior of the non-neutral region that occurs between the plasma and the substrate [9]. This non-neutral region, also regarded as ‘Sheath’, is of phenomenal importance in plasma processing applications. The positive ions in the sheath region are accelerated towards the substrate with a kinetic energy proportionate to the potential drop in this non-neutral region [10].

Negative ions inside the discharge are produced by two primary mechanisms. The first mechanism involves production of negative ions in the bulk due to electron attaching process. This involves either direct attachment of electrons to an electronegative atom/molecule or by a two-step dissociative attachment (DA) process [11]. In the DA process, gas molecules are excited by the energetic electrons inside the discharge, which are then dissociated by capture of a low energy electrons to form negative ions.

The negative ions are also produced from low work function, oxide or caesium coated surfaces [12]. In this process electrons from the Fermi-level of a low work function surfaces transfer an electron to the incoming positive ions or neutrals bombarding the material surfaces. This mechanism is predominantly found in hydrogen negative ions sources [13]. In magnetron discharges, surface produced negative ions of oxygen can be extremely energetic as they carry the energy corresponding to the potential drop in the cathode sheath [14]. These energetic negative ions is generally a point of concern because it can sputter the depositing films grown on the substrate placed in line of sight along the target. The negative ions originated from a high voltage electrode can modify not only the non-neutral region around the surface, but it can also affect the pre-sheath potential inside the bulk plasma. The pre-sheath is the region which provides acceleration to the positive ions towards the sheath boundary. Therefore the negative ions in the discharge has a tremendous influence on the equilibrium properties of bulk plasma. So far the effect of surface emitted negative ions on the pre-sheath potential; and its connection with the positive ion



speed entering the non-neutral region has not been established. The emission of negative ions is relevant for both the floating [15, 16] and an electrically biased electrode [17] in negative ion sources. In the present study, the effect of negative ion emission on the equilibrium properties of sheath and pre-sheath due to negative ion emission from an electrode surface has been investigated theoretically.

Sheath due to negative ion emission from an electrode has been researched by a few authors based on analytical models [18–20] and numerical simulation [21, 22]. One of the crucial results addresses negative space charge creation near an ion emitting electrode. The space charge region inhibits the further emission of negative ions from the electrode surface. Although sheaths in presence of volume negative ions has been extensively researched in context of electronegative discharges [11]; however, the role of negative ions emission on sheath width, the pre-sheath potential drop and its consequence on positive ion speed at the sheath boundary has not been adequately addressed. The sheath properties fundamentally depends on the positive ion speed and ion density at the sheath edge. The positive ion density at the sheath edge is again related to the potential fall across the pre-sheath region inside the bulk plasma. The sheath width is also an important parameter required in the analytical modelling of plasma devices like in ion extraction grids [23]. There exists no direct means to quantify the sheath width experimentally.

One of the fundamental application of sheaths in presence of negative ion arises in the diagnostic of negative ions based on electrostatic probe techniques [24–28]. The electrical probes provide a cost-effective solution for determining plasma parameters. In this study, two promising electric probe techniques based on a Langmuir probe [29] and resonance hairpin probe [30, 31], has been developed and characterized to determine negative ion parameters and sheath width experimentally in an electronegative oxygen discharges.

Before we proceed to the subsequent chapters, here we present a brief overview

of the basic properties of plasma & the non-neutral sheath region in presence of negative ions.

## 1.1 Plasma state

Plasma is a quasi-neutral collection of freely moving charged particles, yet they are bound together by long range coulomb forces. Plasma can be naturally occurring like in stellar matters [32], the stars [33], gaseous nebulae [34], exosphere of earth's atmosphere [35] etc. or it can be created artificially in the laboratory by electric discharge. Florescent lamps and electric arc used for welding of metal joints are some commonly used plasmas in our daily life. It is estimated that 99% of the matter in the universe exist in plasma state. Plasma technologies have tremendous applications that spans from processing of thin film in semiconductor industries [1] to space, military and in auxiliary plasma heating systems in fusion devices [36].

The charged particles inside plasma have a very high temperatures in the range of 10's of thousands of degree kelvin. As a result, the kinetic energy associated with the plasma particles enable them to exist freely against the attractive coulomb forces. This unique property of plasma allows a considerable number of charged particles to organize themselves collectively to shield any electric field created due to charge imbalance inside plasma. The motion of charged particles can also generate currents and magnetic fields associated with them and intern can influence the dynamics of the neighboring charges. The collective behavior is one of the fundamental properties, which is responsible for a wealth of physical phenomena occurring inside the plasma. This property ensures that the motion of charged particles is not only governed by the local conditions but also depends on the state of the plasma that is far away from the point of interest.

The naturally occurring plasma that are found in earth's exosphere are created by

photo-ionization by the cosmic rays from space [37]. In contrast, laboratory plasmas are created in an evacuated discharge chamber by electron impact ionization of background gas neutrals, by providing electrical energy from a radio-frequency (RF) or direct-current (DC) sources [38]. Due to lighter mass, the electrons efficiently absorb energy from the applied electric field. The fractional energy transferred from electrons to gas neutrals is very small ( $\approx 2m_e/m_p \sim 10^{-3}$ ), as a result the electrons remain at an elevated temperature  $T_e$  than the positive ions ( $T_p$ ) which usually tend to remain in thermal equilibrium with the background neutrals ( $T_g$ ). Such types of plasmas in which  $T_e \gg T_g$ , are commonly regarded as non-equilibrium plasmas. Typically, all the industrial plasmas and low temperature plasma created in laboratories falls under this category; whereas fusion plasmas are close to thermal equilibrium since  $T_e \approx T_p$ .

The degree of ionization,  $n_p/n_g$  is given by Saha's equation which states that the fractional ionization of the gas atoms increases with the rise in the gas temperature. Here  $n_p$  and  $n_g$  are number density of ionized atoms and gas neutrals respectively. Based on the degree of ionization, plasmas can be classified in to weakly and strongly ionized. The DC discharges created at low pressures have fractional ionization  $< 1\%$ ; whereas wave heated plasmas like helicon [39] and ECR plasmas [40] can achieve ionization efficiency close to 90%.

### 1.1.1 Some basic properties

#### (a) Debye shielding

Plasma is considered to be macroscopically neutral. However, there exist enough free energy in the system which can spontaneously create a local charge imbalance. Hence the perfect shielding gets locally violated and an intrinsic electric field exists locally inside the plasma. The charged particles then quickly reorganize to screen this electric field with in a characteristic length defined as Debye length  $\lambda_D$ .

This screening effect is known as Debye shielding. The Debye shielding is one of the fundamental collective property of plasma which is responsible to assure charge neutrality inside plasma. In the case of a non-equilibrium plasma, the positive ions are assumed to be cold, therefore the shielding process is mainly carried out by the randomly moving electrons. The Debye length is given by  $\lambda_D = \sqrt{\frac{\epsilon_0 K_B T_e}{e^2 n_e}}$ ; where  $n_e$  &  $T_e$  are density and temperature of electrons. For a spherically symmetric distribution of shielding charged particles around a test charge, the Debye length  $\lambda_D$  is typically the radius of sphere over which the potential due to test charge falls exponentially and almost vanishes at a radius  $r > \lambda_D$ .

### (b) Plasma frequency

If the plasma is instantaneously disturbed against a uniform background of ions, an electric field will be set up due to charge separation. The electric field will exert a restoring force to re-establish the neutrality of the plasma by pulling the electrons back to their initial equilibrium position. However in this process, the electrons will results in an inertial overshoot and begins to perform a periodic oscillation about their equilibrium position. The frequency of such oscillations is characteristic of a plasma and is known as plasma frequency  $\omega_{pe}$ . For electrons, it is given by  $\omega_{pe} = \sqrt{\frac{n_e e^2}{\epsilon_0 m_e}}$ ; where  $n_e$  and  $m_e$  are density and mass of electrons. A similar characteristic frequency can be defined for the case of positive ions of mass  $m_p$  and density  $n_p$  as  $\omega_{pi} = \sqrt{\frac{n_p e^2}{\epsilon_0 m_p}}$ .

### (c) Plasma criteria

Plasma is an ionized gas, however not all the ionized gases can be called as plasma. To qualify for a plasma, certain criterion needs to be satisfied. The first criteria states that the characteristic length  $L$  of a plasma column has to be much larger than the Debye length  $\lambda_D$ , i.e.  $\lambda_D \ll L$ ; otherwise the quasi-neutrality property of plasma

cannot exist. In the region outside of Debye sphere, the plasma is generally neutral having almost equal numbers of positive and negative charges per unit volume. The quasi-neutral condition is mathematically expressed as;

$$n_e + \sum_i n_{ni} = \sum_j Z_j n_{pj} \quad (1.1)$$

Where  $n_{ni}$  represents the densities of negatively charged species,  $n_{n1}$ ,  $n_{n2}$ ,  $n_{n3}$  etc. And  $Z_j n_{pj}$  denotes the densities of positively charged species,  $n_{p1}$ ,  $n_{p2}$ ,  $n_{p3}$  etc. having corresponding charged state  $Z_1$ ,  $Z_2$ ,  $Z_3$ ...on them.

The second criteria states that the number of charge particles inside the Debye sphere given by  $N_D = \frac{4}{3}\pi\lambda_D^3 n$  should be sufficiently large ( $N_D \gg 1$ ) to provide effective shielding of the test charge. The electron plasma frequency should be high compared to frequency of electron-neutral collision. If  $\tau$  be the mean time between the electrons collision with the neutrals, then the third condition for an ionized gas to be qualified as plasma is given by  $\omega_{pe}\tau > 1$ .

## 1.2 The Sheath

Sheath is a thin, non-neutral region of strong electric field that exist between the plasma and a material object in contact with it. Sheath is ubiquitously formed over all the material bodies that are exposed to plasma. The common examples are the vacuum chamber walls, discharge electrodes, probes introduced for plasma diagnostics and spacecraft body in ionospheric plasma. In outer space, the sheath formed around cosmic dust particles is responsible for dust coagulation process resulting the proto-planetary disc formation [41, 42]. Moreover, exposure of planetary bodies and space ships to the solar wind plasma and ultraviolet radiation leads to the surface charging and formation of sheath above the surface [43].

Since the electrons have a lighter mass, their mobility and thermal speed are relatively very high as compared to positive ions. Therefore, some plasma electrons immediately escape to the walls and leaves an excess of positive ions inside the plasma. This phenomena gives rise to an outwardly directed electric field, which acts to counter the further escape of electrons towards the boundaries, whereas it speeds the ion to match the electron flux leaving the plasma boundary. In equilibrium, both electrons and ions fluxes diffuses towards the walls at the same rate. This mechanism is called *ambipolar diffusion*. The ambipolar electric field inside plasma volume over the length scale  $l$  is typically of the order of  $\sim (K_B T_e / el)$ . However, it increases in magnitude towards the walls. Therefore plasma always remain at a relatively higher potential with respect to the walls of the container which is commonly regarded as *plasma potential*.

A similar charging mechanism also appears when a conducting or a non-conducting electrode is introduced inside the plasma. Due to high mobility of electrons, the electrode gets quickly charged to a negative potential relative to the plasma. As the electrode reach an equilibrium potential, the net current collected by the electrode is zero. This potential is commonly referred as *floating potential*.

In fig-1.1, a spherical metallic ball biased at a negative potential with respect to a reference electrode, which is also in contact with the plasma, is schematically presented. The reference electrode can be the grounded wall of the vacuum chamber or the plasma itself far from the spherical object. The spherical ball is assumed to be much smaller than the plasma volume so that perturbation/disturbance caused by the object at a distance far away can be ignored.

Due to negative potential on the object, the electrons are repelled away, while it creates a non-neutral space charge region consisting of positive ions around the spherical ball. Let us assume that  $r_{max}$  is the largest radius of sphere which could spontaneously become depleted of electrons due to the applied negative potential to

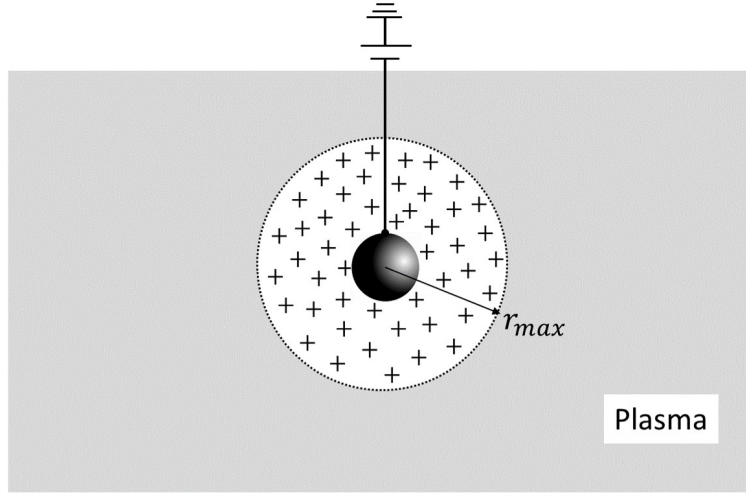


Figure 1.1: Formation of sheath around spherical object biased at a negative potential with respect to a reference electrode;  $r_{max}$  is maximum distance over which the quasi-neutrality is violated

the ball. However, complete depletion of electrons inside the sphere can occur if all the electrons originally in the presumed sphere vacate the sphere and move out to its surface. In this situation the electrons at the surface of sphere would have to come to rest because if it is not, they would still have available thermal kinetic energy which could then be used to move them outward to even at larger radius, and this would violate our assumption that  $r_{max}$  is the radius of maximum non-neutrality.

The electric field due to uniform distribution of ions inside the sphere at radius  $r < r_{max}$  is  $E_r = ner/3\epsilon_0$ ; where  $n$  is the number density of ions in the spherical volume. Therefore, the electrostatic energy  $W_r$  stored in the sphere due to the electric field  $E_r$  will be equal to the work done  $W_{kin}$  by the equal number of electrons on leaving the sphere. These are given respectively as;

$$W_r = \int_0^{r_{max}} \frac{\epsilon_0 E_r^2}{2} (4\pi r^2) dr = \frac{2\pi e^2 n^2}{45\epsilon_0} \quad (1.2)$$

$$W_{kin} = \frac{3}{2} n K_B T \left( \frac{4}{3} \pi r_{max}^3 \right) \quad (1.3)$$

From (1.2) & (1.3), equating the electrostatic energy  $W_r$  stored in the sphere to the

initial thermal energy  $W_{kin}$  of electrons, we get;

$$r_{max}^2 = 45 \frac{\varepsilon_0 K_B T}{n e^2} \quad (1.4)$$

This gives  $r_{max} \approx 7\lambda_D$ . Thus the maximum radius of sphere that could spontaneously becomes depleted of electrons is of few Debye length.

The above situation of charging of sphere and forming the sheath around it is extremely artificial. It is because of the reason that the electrons possess thermal energy and therefore there would always be an availability of electrons inside the spherical volume due to their thermal agitation. The distribution of electrons would then have an explicit dependence on spatially varying potential  $\phi(r)$  inside the spherical volume and therefore  $r_{max}$  is expected to have a functional dependence on  $\phi(r)$ . In equilibrium, the distribution of electrons inside the presumed sphere is Maxwellian [11]. Therefore, the extent up to which the spherical volume remains non-neutral is basically obtained by finding the potential distribution  $\phi(r)$  using Poisson's equation;

$$\nabla^2 \phi(r) = \frac{e}{\varepsilon_0} (n_e - n_p) \quad (1.5)$$

Above equation can be solved by using appropriate boundary condition. For approximation let us assume that the scale length over which  $\phi(r)$  varies is  $R$ . Then on substituting  $\nabla^2 \sim 1/R^2$  in Poisson's equation, we get;

$$\left| \frac{e\phi}{K_B T_e} \right| \approx \frac{R^2}{\lambda_D^2} \left( \frac{n_p}{n_e} - 1 \right) \quad (1.6)$$

From (1-6), it can be observed that the ratio  $\left| \frac{e\phi}{K_B T_e} \right|$  cannot be much greater than 1. It is because when a large potential is applied to the spherical object, a cloud of charge having opposite polarity will immediately buildup around the object to



shield out the potential disturbance. In the main body of plasma,  $\phi$  would vary over the distance depending on the plasma size. For a typical laboratory plasma considering  $T_e \sim 5$  eV and  $n_e \sim 10^{17}m^{-3}$  the Debye length can be calculated as  $\lambda_D \approx 50\mu m$ . If the average size of plasma is taken to be order of  $\sim 100$  cm, the ratio  $(R/\lambda_D)^2 \sim 10^8$  is so large that the density  $n_p$  should be approximately equal to electron density  $n_e$  in the bulk of the plasma in order to make the LHS of (1.6) reasonably small.

Inside the sheath region where the length scale  $R \sim \lambda_D$ , the density ratio  $n_p/n_e$  need not be near to unity and therefore quasi-neutrality is primarily violated inside the sheath. We also observe from (1.6) that  $n_p > n_e$  inside the sheath even for a small value of  $\phi$ . This is the primary condition for a positive ion sheath to exist.

### 1.3 The Bohm speed: Requirement of pre-sheath

In between the region of sheath and the bulk plasma, there exists a transition region of weak electric field, called the pre-sheath. The pre-sheath is created due to the influence of ionizing collisions leading to production/loss of particles or due to momentum transfer collisions between ions and neutrals. In low pressure, the pre-sheath region can become comparable to plasma dimension. However the electric field inside the pre-sheath is weak enough so that the quasi-neutrality is not quite violated. Therefore the electron density must be approximately equal to ion density. But the ambient electric field inside the pre-sheath allows the positive ions to get accelerated from the bulk plasma while it retards the flow of electrons. The scale length of sheath is few Debye length  $s \sim \lambda_D$ , whereas the scale length of pre-sheath is of the order of ion-neutral mean free path  $l \sim \lambda_{in}$ . In equilibrium, the common plasma density at any location inside the pre-sheath is always lower than the bulk plasma density  $n_0$ .

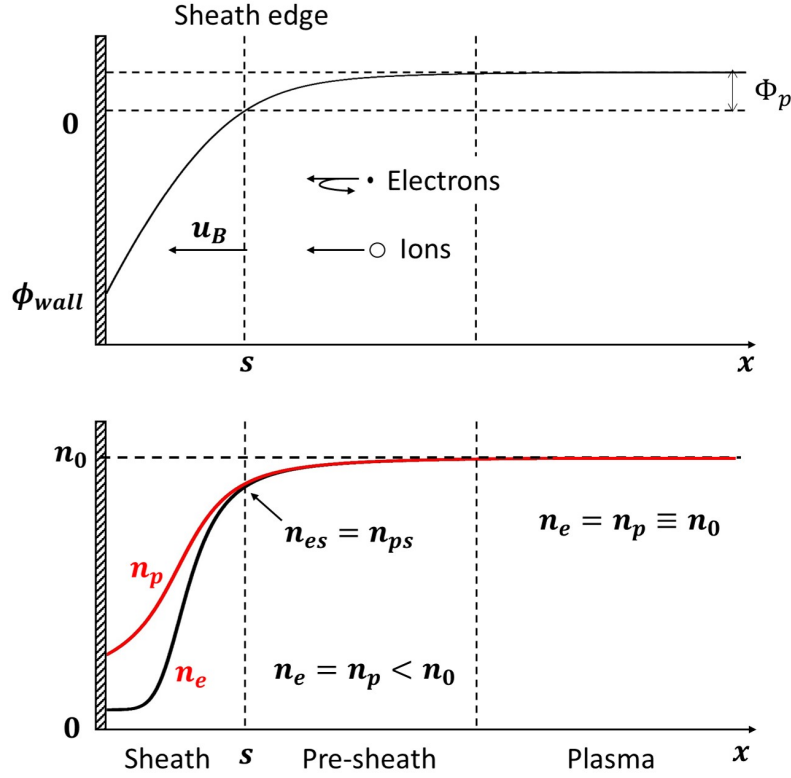


Figure 1.2: One dimensional representation of sheath, pre-sheath and bulk plasma. The potential on the electrode  $\phi_{wall}$  is with respect to the sheath edge defined at a distance  $x = s$  from the electrode ( $x = 0$ ). The electrons and ions have almost equal density in pre-sheath i.e.  $n_e \approx n_p$ , but smaller than the common density  $n_0$  in bulk plasma.

In order to get an insight in to the pre-sheath region, we consider a planar electrode immersed inside the plasma as shown in fig-1.2. The positive ion rich sheath is formed extending up to distance  $s$  from the electrode. The artificial vertical dashed line designated as the sheath edge separates the sheath region from the quasi-neutral plasma. For the sake of convenience, the potential at the sheath edge is usually assigned to be 0. The spatial potential  $\phi(x)$  inside the sheath is negative with respect to the sheath edge. The electrons are assumed to have a Maxwellian distribution, hence their density decays exponentially inside the sheath as follows;

$$\frac{n_e}{n_{es}} = \exp\left(\frac{e\phi}{K_B T_e}\right) \quad (1.7)$$

Where,  $n_{es}$  is electron density at the sheath edge. The positive ions inside the sheath

are continuously accelerated towards the electrode. In absence of collision, the ion flux remain conserved throughout the sheath. Therefore according to the equation of continuity;

$$n_p v_p = n_{ps} u_B \quad (1.8)$$

In (1.8),  $n_{ps}$  and  $u_B$  are density and speed of positive ions at the sheath edge.

On the other hand, conservation of energy for ions gives;

$$\frac{1}{2} m_p v_p^2 = \frac{1}{2} m_p u_B^2 - e\phi \quad (1.9)$$

Equation (1.8) & (1.9) can be solved to obtain an expression of positive ion density inside the sheath as a function of  $\phi$ ;

$$\frac{n_p}{n_{ps}} = \left( 1 - \frac{2e\phi}{m_p u_B^2} \right)^{-1/2} \quad (1.10)$$

Since inside the sheath,  $n_p > n_e$  should be satisfied for even a small value of  $\phi$ , therefore the Taylor expansion of (1.7) & (1.10) gives;

$$\frac{n_e}{n_{es}} = 1 + \frac{e\phi}{K_B T_e} + \dots \quad \& \quad \frac{n_p}{n_{ps}} = 1 + \frac{e\phi}{m_p u_B^2} + \dots \quad (1.11)$$

For  $\phi$  to be negative inside the sheath, the condition  $n_p > n_e$  immediately gives;

$$u_B > \left( \frac{K_B T_e}{m_p} \right)^{1/2} \quad (1.12)$$

This gives a necessary condition for the existence of sheath and popularly known as Bohm criteria [44]. It implies that the positive ion should enter into the sheath with a speed which should be greater or equal to the positive ion sound speed. The requirement to have Bohm speed for positive ions at the sheath edge clearly indicates that there must be a potential drop of the order of  $e\Phi_p \equiv \frac{1}{2} m_p u_B^2 = \frac{1}{2} K_B T_e$  between the sheath edge and main body of the plasma [see fig-1.2].

In conclusion, a plasma can coexist with a material boundary if a thin sheath is created between them. The sheath isolates the bulk plasma from the material surface. Inside the sheath, there is a coulomb barrier of magnitude several time  $K_B T_e$  which repel the electron and accelerates the positive ions to the material surface.

## 1.4 Fluid description of plasma and sheath

In fluid description [44], the individual species (electrons and ions) are considered to be separate fluid, described by a specific energy distribution. Then the ensemble average of these particles over their thermal motion results in fluid like equation for the density, temperature, flux etc. The fluid description of plasma is generally suitable for discharges operated at high pressure where collisions are more frequent such that the collision mean free path is small compared to the length scale of the system. As a result of this, individual species is able to sustain a local equilibrium distribution function, so that each species behave as a fluid described by a local density, macroscopic velocity and local temperature. The plasma is then considered as a mixture of two or more inter-penetrable fluid, depending on the number of different species considered. In addition to the usual electrodynamic equations, there is a hierarchy of hydrodynamic equations expressing conservation of mass, conservation of momentum and energy to describe the dynamics of each species fluid inside the plasma.

In contrast, kinetic model is applied when the inter-particle collisions are relatively infrequent so that the deviation from local thermodynamic equilibrium is maintained for longer times [45]. The description based on kinetic model requires the knowledge of distribution function for the system of particles and then solving the appropriate kinetic equations that govern the evolution of the distribution func-

tion in the phase space. The kinetic simulation is relatively more exact as it rely on the position and the momentum of individual charged particle inside plasma and track their path in a given electric and magnetic field. However, tracking a huge number of particles via computer is often cumbersome.

In the fluid model, there are two important assumptions to describe the sheath at low pressure. First, the electrons are in equilibrium with the sheath electric field and secondly, the ionization inside the sheath can be neglected. The first condition gives the Boltzmann relation for electrons in a repelling potential inside the sheath; whereas in the second assumption is necessary to apply the flux conservation of positive ions inside the sheath. There are various kinds of sheath models [46–49] available in the literature such as **(a)** continuous plasma-wall model **(b)** diffuse electron boundary model **(c)** step-front sheath models and **(d)** matrix sheath models.

In continuous plasma-wall model, the fluid equations are solved with definite production/loss balance in the plasma. The boundary conditions are usually defined at the center of the discharge and at the wall considering the whole plasma volume as a single entity. This is shown in fig-1.3(a) in which the charge imbalance increases towards the electrode defined at origin.

In diffused electron boundary model, the transition of quasi-neutral plasma to the sheath region is clearly identified by locating the plasma-sheath boundary at a location where the positive ions acquire the characteristic sound speed  $c_s = \sqrt{K_B T_e / m_p}$  (Bohm criteria) [44]. This is shown in fig-1.3(b). In step front sheath model, the electron density inside the sheath is totally neglected [see fig-1.3(c)]. This is applied when the potential across sheath is much larger than electron temperature  $T_e$ . Finally, in the matrix sheath model, the sheath is assumed to be completely electron free and the positive ion density are uniformly distributed inside so that a matrix of positive ions is created inside the sheath as shown in fig-1.3(d).

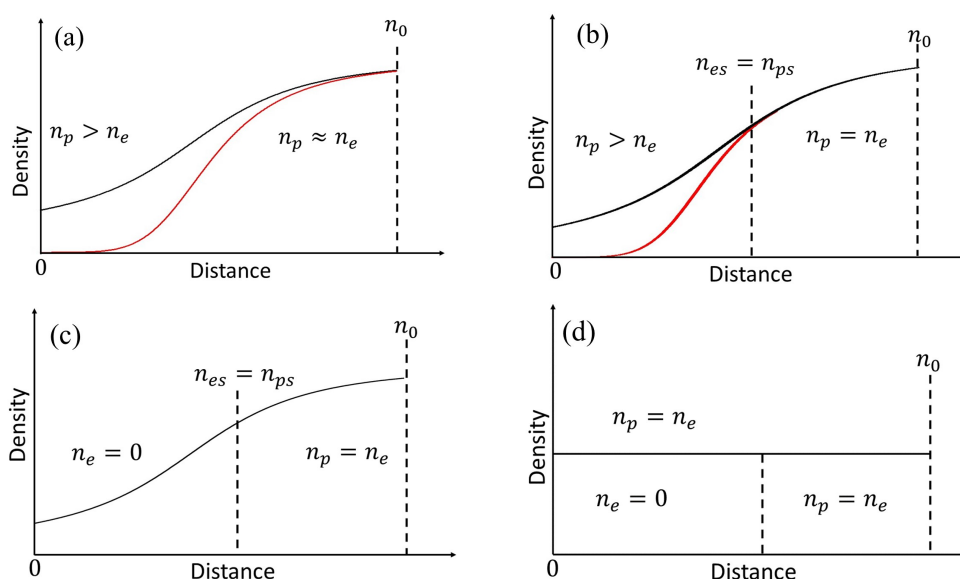


Figure 1.3: Different sheath models namely (a) continuous plasma-wall model, (b) diffuse electron boundary model, (c) step-front sheath model and (d) matrix sheath model depending on the density distribution of electrons (red) & positive ions (black);  $n_0$  is bulk plasma density,  $n_{es}$  and  $n_{ps}$  are density of electrons and positive ions at the sheath edge respectively.

## 1.5 Dielectric description of plasma

Plasma being a dispersive medium, its constituent particle's (electrons & ions) response to an externally applied time varying electric field varies as a function of frequency. Since the electrons and ions react at different time scales to the applied field, they can get polarized and behave as a dielectric. The polarization produces an intrinsic electric field which counters the applied field. The dynamic of charged particles inside the plasma is dependent on the frequency of applied field.

Consider a uniform plasma in one dimension, excited by a low amplitude time varying electric field  $E_x(t) = \tilde{E}_x \cos \omega t = \text{Re}(\tilde{E}_x e^{j\omega t})$ . Due to lighter mass, the electric field induced oscillation of electrons is of much higher amplitude than the ions. To a first approximation, the electrons oscillation can be assumed with respect to stationary ions in the background, provided  $\omega > \omega_{pi}$ .

The electrons equation of motion in time varying electric field  $E_x(t)$  can be written

as;

$$m_e \frac{\partial u_x(t)}{\partial t} = -eE_x(t) - m_e \nu_e u_x(t) \quad (1.13)$$

Where  $\nu_e$  is electron-neutral collision frequency.

Substituting  $E_x(t) = \tilde{E}_x \cos \omega t$  in equation (1-13) and solving for the velocity  $u_x(t)$ , we get;

$$\tilde{u}_x = -\frac{e}{m_e} \frac{1}{(j\omega + \nu_e)} \tilde{E}_x(t) \quad (1.14)$$

The total current  $J_{tx}$  flowing through the plasma dielectric is given by the sum of conduction current  $J_x$  due to electron's motion and the displacement current  $\varepsilon_0 \frac{\partial E_x}{\partial t}$ ;

$$J_{tx} = \varepsilon_0 \frac{\partial E_x}{\partial t} + J_x \quad (1.15)$$

For cold plasma approximation ( $T_e \gg T_p$ ), we have;

$$J_x = -en_0 \tilde{u}_x \quad (1.16)$$

Substituting  $\frac{\partial E_x}{\partial t} = \text{Re}(j\omega \tilde{E}_x e^{j\omega t})$  and  $J_x$  from (1-16) into (1-15), we get;

$$\tilde{J}_{tx} = j\omega \varepsilon_0 \left[ 1 - \frac{\omega_{pe}^2}{\omega(\omega - j\nu_e)} \right] \tilde{E}_x \equiv j\omega \varepsilon_p \tilde{E}_x \quad (1.17)$$

In (1-17),  $\varepsilon_p$  is the complex plasma dielectric given by;

$$\varepsilon_p = \varepsilon_0 \left[ 1 - \frac{\omega_{pe}^2}{\omega(\omega - j\nu_e)} \right] \quad (1.18)$$

The ratio  $\epsilon = \varepsilon_p/\varepsilon_0$  is termed as dielectric constant of plasma. It has practical importance while launching electromagnetic wave inside the plasma. Considering collision-less case ( $\nu_e < \omega$ ), it can be seen from (1.18) that the dielectric constant is positive for  $\omega > \omega_{pe}$  ( $\omega$  typically in GHz). Therefore, an electromagnetic wave can propagate into plasma. However for  $\omega < \omega_{pe}$ , the electromagnetic wave launched inside the plasma gets reflected, as the dielectric constant becomes negative.

## 1.6 Brief overview of various Sheath theories and its application to Langmuir probe

One of the most prominent applications of sheath physics applies to electric probes used in plasma diagnostics. Electric probes comes in a wide variety of forms like single [29], double [50] or triple [51] Langmuir probe, emissive probe [52], pin-plane probe [53], directional probe [54] etc. The most commonly used Langmuir probe is a piece of cylindrical metallic wire made from a high refractory materials like tungsten.

Various sheath theories developed for a cylindrical/spherical Langmuir probe can be broadly classified into collision-less and collisional regimes, depending on whether the ion/electron collision mean free paths are respectively greater or less than the sheath dimension. The collision-less and collisional regime are further distinguished on the basis of relative dimension of sheath with the characteristic Debye length.

The impact on ion current due to relative size of the probe with respect to sheath dimension and ion-neutral collisions can be described by two dimensionless parameters namely the Debye number  $D_\lambda = r_p/\lambda_D$  and Knudsen number  $K_{e,i} = \lambda_{i,e}/r_p$ ; where  $r_p$  is probe radius and  $\lambda_{i,e}$  are ion-neutral/electron-neutral collision mean free path. Another factor that influence the ion collection to a probe surface is the ratio  $\tau = T_e/T_p$  of electron temperature ( $T_e$ ) to the ion temperature ( $T_p$ ). Depending on the above three parameters, there are various probe theories that describes the motion of ions approaching towards the probe.

### 1.6.1 Ion collection by Langmuir probe for Collision-less sheath

Mott Smith & Langmuir (1926) [55] developed a theory to describe the ion/electron motion inside the sheath and their collection to the probe surface. The theory was



initially developed for collision-less case by considering the orbital motion of ions around the axis of a cylindrical/spherical probe. The ions were assumed to have a finite angular momentum when they enter into the sheath region of a biased cylindrical/spherical probe. Due to this, the grazing incidence of ions on the probe surface limits the ion current collected by the probe. Therefore popularly known as Orbital Motion Limited (OML) theory.

Assuming the conservation of angular momentum and energy, the ion current collected by the probe as per OML theory is given by [56];

$$i_p = A_p n_0 e \frac{2}{\sqrt{\pi}} \left( \frac{K_B T_p}{2\pi m_p} \right)^{1/2} (1 + \eta)^{1/2} \quad (1.19)$$

Where,  $\eta = -\frac{e(V_B - V_p)}{K_B T_p}$ ;  $V_B$  &  $V_p$  are respectively the probe bias and plasma potential with respect to a reference electrode and  $T_p$  is ion temperature. In the limit  $T_p \rightarrow 0$ , the current  $i_p$  becomes [57];

$$i_p = A_p n_0 e \frac{2}{\sqrt{\pi}} \left( \frac{e|V_B - V_p|}{m_p} \right)^{1/2} \quad (1.20)$$

From (1.20), it is seen that  $i_p^2$  vs  $V_B$  is a straight line whose slope is  $\frac{2e^3 A_p^2 n_0^2}{\pi^2 m_p}$ . Therefore, by measuring the slope from  $i_p^2$  vs  $V_B$  plot of probe characteristic, the plasma density can be easily found.

Although OML theory provides a straight forward measurement of plasma density, however the assumption of orbital motion in most of the plasma, particularly at high pressure are not always satisfied [58, 59]. The ions entering the sheath region of cylindrical/spherical probe can have radial component of velocity greater than that in the azimuthal direction, so that the impact of angular momentum on the ion motion becomes insignificant. Moreover, there may exist an ‘absorption radius’ greater than the probe dimension, so that the only charged particles (ions & electrons) which are inside the absorption radius are destined to hit the probe surface

and get collected [56, 60].

In another approach proposed by Allen et al (1957) [60], also known as ABR model, the ions were assumed to be cold ( $T_p = 0$ ) and therefore their motion inside the sheath were assumed to have strict radial motion while moving towards the probe surface. The radial variation of potential inside the sheath was obtained by solving Poisson's equation. The ABR model was originally derived for a spherical probe. But later on, the model was extended for cylindrical geometry by Chen (1965b) [61], and popularly recognized afterwards as ABR-Chen model.

Bernstein and Rabinowitz (1959) [62] incorporated both the radial and orbital motion of ions by considering the isotropic distribution of mono-energetic ions. Their theory was further refined by Laframboise (1966) by including a Maxwellian ion distribution at temperature  $T_p$  and recognized as BRL (Bernstein, Rabinowitz & Laframboise) theory after their name [63]. The generalized form of dimensionless ion current according to Laframboise theory is expressed as;

$$i_L = eA_p n_0 \left( \frac{K_B T_e}{2\pi m_p} \right)^{1/2} I_L(\eta, D_\lambda, \tau) \quad (1.21)$$

Where  $I_L(\eta, D_\lambda, \tau)$  is dimensionless current as a function of  $\eta$ ,  $D_\lambda$  and  $\tau$ . The details of form of  $I_L$  can be found in the original article [63].

The Laframboise theory accounted for all the factors affecting the ion motion, and therefore applicable to a wide range of Debye number  $D_\lambda$  and  $\tau = T_e/T_p$ . The theory has been experimentally verified in a variety of conditions by numerous authors [64, 65]. However, the Laframboise theory is difficult to apply directly in experiments as it involves a lot of computations. Several approximate fits to the Laframboise theory have been made by different researchers to determine the plasma density from the experimentally measured ion current for a wide range of operating gas pressure [58, 66–69]. By using these approximate fits, the plasma density from the experimentally

measured ion current can be determined for a wide range of operating range of gas pressure.

D Bohm (1949) [10] proposed that the ions enters the sheath boundary with characteristic sound speed  $c_s = \sqrt{K_B T_e / m_p}$ ; which depends on the electron temperature ( $T_e$ ) and positive ion mass ( $m_p$ ). This is popularly recognized as Bohm criteria. It is satisfied for moderately dense plasma, in which the thin sheath approximation ( $D_\lambda \gg 1$ ) usually holds. The ion current collected by probe is known as Bohm current and is given by;

$$i_{Bohm} = 0.61en_0A_s\sqrt{K_B T_e / m_p} \quad (1.22)$$

Where,  $A_s$  is sheath area and the numerical factor 0.6 appears due to pre-sheath correction [44]. The above formula is often applied due to its simplicity, however its application in low density plasma ( $D_\lambda \ll 1$ ) may result severe overestimation of plasma density. Narasimhan et al. (2001) [69] compared the Bohm current with that given by Laframboise theory and recommended that the ion density should be found using Laframboise theory for  $D_\lambda \leq 35$ ; whereas for  $D_\lambda > 35$ , the Bohm description of ion current (equation-1.22) is more appropriate.

## 1.6.2 Ion collection by Langmuir probe for Collisional sheath

As the neutral density increases due to rise in gas pressure, the ion-neutral collision mean free path is considerably reduced compared to the sheath dimension. This can affect the ion collection to the probe surface in two different ways: (a) The frequent collisions of ions with the neutrals can destroy the ion orbits leading to increase in ion current [70, 71] and (b) The momentum loss collision between ions and neutrals can leads to the elastic scattering of ions from their original direction of motion, leading to reduction in ion current [72].

One of the earliest theory to address the elastic scattering of ions during collision with neutrals was proposed by Chou & Talbot et al [73, 74]. Their result predicts the reduction in ion current and was found to be valid for a wide range of Knudsen number. The ion current in presence of scattering collision was obtained as a correction to the normalized Laframboise current  $I_L$  for collision-less case [equation-1.21]. This is expressed as;

$$I_p = \bar{\gamma} I_L \quad (1.23)$$

The correction factor  $\bar{\gamma}$  is given by [74];

$$\bar{\gamma} = \left( 1 + \frac{J_i I_L \tau^{1/2}}{K_i} \right)^{-1} \quad (1.24)$$

Where  $J_i$  is integral over reduced potential between the unperturbed plasma and the probe surface.

Zakrzewski & Kopiczynski (1974) [71] considered both the opposing mechanism of ion-neutral collision i.e. the increase in the collected ion current due to destruction of ion orbit and reduction due to scattering. They proposed that in collision-less limit, the current collected at the probe is given by Laframboise theory ( $I_L$ ); whereas at the sheath edge, it should be obtained from ABR theory ( $I_A$ ). Therefore, the residual ion current associated with destruction of ion orbit inside the sheath is given by ( $I_A - I_L$ ). The general expression for ion current according to Zakrzewski & Kopiczynski is obtained as;

$$I_p = \gamma_1 \gamma_2 I_L \quad (1.25)$$

Where,  $\gamma_1$  is the rate with which the ion current collected by the probe increases due to destruction of ion orbit and  $\gamma_2$  is the decreasing rate due to scattering. They obtained both in terms of  $X_i$ , the number of ion-neutral collisions inside the sheath as follows;

$$\gamma_1 = \begin{cases} 1 + X_i \left( \frac{I_A}{I_L} - 1 \right) & \text{for } X_i \leq 1 \\ \frac{I_A}{I_L} & \text{for } X_i > 1 \end{cases} \quad (1.26)$$

$$\gamma_2 = \begin{cases} \frac{3-2\exp(-X_i)}{1+2X_i} & \text{for } X_i < 1 \\ \frac{3-\exp(-X_i)}{2(1+X_i)} & \text{for } X_i \geq 1 \end{cases} \quad (1.27)$$

In the above equations, the number  $X_i$  of ion-neutral collisions occurring inside the sheath can be calculated by dividing the sheath thickness ( $s$ ) by ion neutral mean free path  $\lambda_i = 1/n_g\sigma_i$ ;  $n_g$  is neutral gas density and  $\sigma_i$  is ion-neutral collision cross section.

The correction factor  $\gamma_2$  derived by Zakrzewski & Kopiczynski [71] was limited for few collision inside the sheath i.e. for lower  $K_i$  values. Their results were experimentally tested by Rousseau & Teboul et. al. [75] with microwave interferometry measurement and was found in good agreement.

The theory given by Zakrzewski & Kopiczynski [71] was further extended for an arbitrary Knudsen number ( $0 \leq K_i < \infty$ ) by Tichý et al. [76]. It was done by replacing  $\gamma_2$  to  $\bar{\gamma}$  as proposed by Talbot & Chou [74] and therefore often known as ‘modified Talbot & Chou model’ [76]. It is given by;

$$I_p = \gamma_1 \bar{\gamma} I_L \quad (1.28)$$

The ion current determined from the above ‘modified Talbot & Chou model’ was tested with simulation [77] as well as in experiment [78]. The measured electron density was found to match with the ‘modified Talbot & Chou model’.

The ion current  $I_p$  collected to the probe according to various probe theories described above [see equation- 1.21, 1.23, 1.25 & 1.28] can be written in the generalized

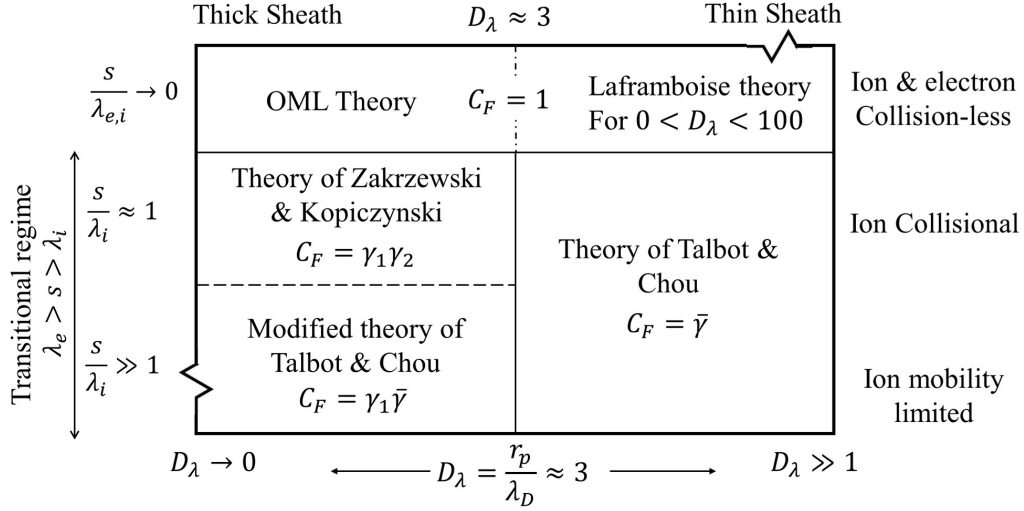


Figure 1.4: Bryant's plot representing the scaling of various probe theories based on parameters  $D_\lambda = r_p/\lambda_D$ ,  $K_{e,i} = \lambda_{i,e}/r_p$  and  $\tau = T_e/T_p$ .

form as;

$$I_p = C_F I_L \quad (1.29)$$

Where  $C_F = 1$  for collision-less Laframboise theory (equation-1.21),  $C_F = \bar{\gamma}$  for theory of Talbot & Chou (equation-1.23),  $C_F = \gamma_1 \gamma_2$  for theory of Zakrzewski & Kopiczynski (equation-1.25) and  $C_F = \gamma_1 \bar{\gamma}$  corresponds to modified Talbot & Chou model (equation-1.28).

Figure-1.4 graphically shows the scaling of various probe theories on the basis of three parameters ( $K_i, D_\lambda, \tau$ ) in collision-less and collisional regimes and known as modified Bryant's plot [79]. From Bryant's plot, the appropriate theory for using Langmuir probe in a given plasma can be decided to estimate plasma parameters.

In our case, the plasma density varies from  $10^{16}$  to  $10^{16} \text{ m}^{-3}$  and electron temperature in the range  $0.5 - 1.5 \text{ eV}$  with respect to the pressure range  $1.4 - 7.0 \text{ Pa}$ . Therefore, the corresponding Debye number  $D_\lambda$  and Knudsen number  $K_i$  are found to be in the range  $\sim 2$  to  $\sim 7$  and  $\sim 6$  to  $\sim 28$  respectively. Therefore, the sheath should be described collision-less under thin sheath limit; since  $D_\lambda > 1$  &  $K_i > 1$ .

## 1.7 Plasma containing negative Ions

There are situations when apart from electrons and positive ions contributing to the bulk plasma quasi-neutrality, presence of negative ions inside this system will dramatically change the equilibrium properties of the bulk plasma and the phenomenon leading to formation of the sheath. Such types of plasma, known as electro-negative plasma, can be easily seen in surface processing applications [1, 80, 81], where electron-attaching gases having very high electron affinity is used during etching and oxide coatings [2, 82]. There are two principle mechanisms by which negative ions can be created inside a discharge: **(a)** Volume process: for strongly electro-negative/ electron-attaching gases; **(b)** Surface process: common in weakly electro-negative gases.

### 1.7.1 Volume production

Electron attaching gases such as  $H_2$ ,  $O_2$ ,  $Cl_2$ ,  $CCl_4$ ,  $CF_4$  etc. have a very high affinity to form negative ions. The production of negative ions is a two-step process that involves dissociative attachment (DA) of the electrons to the neutrals. The first step is a resonant attachment in which the parent atom/molecule of the gas is attached with high energetic electrons and get converted into excited state atom/molecule. Further, the excited state of the parent atom/molecule stabilizes by colliding with low energy electrons and gives the final product as negative ions in the second step.



The energy  $\Delta E$  is the sum of internal energy and electron affinity of  $AB$ , and electron energy. Another low probability process is auto detachment in which the original parent atom/molecule is retained during de-excitation of resonant state.

The above dissociative-attachment is generally favored by lighter molecular species like  $H_2$  &  $O_2$ . However for heavier molecular species, the energy in the resonant state is internally redistributed into its vibrational & rotational modes via non-dissociative attachment [83]. Dissociative attachment generally occur at the ground vibrational state; however it may be from higher vibrational states like in  $H_2$  [84].

The negative ions produced in the volume process is generally lost by detachment of electron in course of collision with the electrons or excited neutrals and recombination with positive ions. These losses are basically dependent on the gas pressure as well as the relative density of negative ions to electrons in the discharge [11]. The recombination loss dominates the detachment loss at relatively low gas pressures and for high electro-negativity gases like  $Cl_2$  and  $I_2$  [85, 86]; whereas at high pressure and for low electro-negativity discharge, the detachment loss exceeds the recombination loss as in case of  $O_2$  gas [8].

The production & loss process involving negative ions in oxygen plasma can be mathematically expressed in particle balance equation as [11];

$$\nabla \cdot \Gamma_v = K_{att}n_gn_e - K_{rec}n_pn_v - K_{det}n_xn_v \quad (1.30)$$

Where  $n_g$  is neutral gas density,  $n_x$  is density of electron or excited species involved in detachment process of negative ions;  $K_{att}$ ,  $K_{rec}$  and  $K_{det}$  are respectively the rate constant for attachment, recombination and detachment.

In electro-negative discharges, electron-positive ion recombination loss is generally less probable than recombination loss due to positive and negative ions. It is because the threshold energy of the former is always higher than the later [11]. On the other hand, the relative importance of negative ion loss, whether by recombination or detachment, depends on the gas pressure as well as on the concentration of negative ions itself [8]. At low pressures or for high negative ion concentration,



the dominant loss mechanism is the recombination loss, whereas a relatively small loss can be attributed due to detachment with excited neutrals [7, 87]. With the increase in pressure or at relatively low negative ion concentration, the detachment loss supersedes the recombination loss at quite modest pressure, since the electron density in the discharge increases [8].

In this thesis, an oxygen dc discharge has been produced in the pressure range 10 – 50 mTorr and discharge power in range 20W to 200W. The dominant contribution of ions are assumed to be  $O^-$  and  $O_2^+$ . Using Langmuir probe and resonance hairpin probe in the discharge, the relative fraction of negative ion to the electron is measured and compared with the global electro-negative discharge model as well as with the experiments [88, 89].

### 1.7.2 Surface production of negative ions

Another important mechanism of negative ion formation is based on surface processes, in which positive ions/ neutral atoms during interaction with a low work function substrate captures an electron from the conduction band of the substrate through quantum tunneling (Augur process) and form a negative ions [90, 91]. Very close to the substrate, the electron affinity level of bombarding particles (positive ions and neutrals) moves towards lower value close to the work function and overlap with the Fermi level of substrate. Finally, the electron from the Fermi level of the substrate tunnel into affinity level to form negative ions. The negative ions formed at the substrate are attracted by the bulk plasma which is usually at a positive potential relative to the electrode surface.

Lowering down the work function by depositing a few monolayer alkali/alkaline metals like caesium & barium at the substrate can increase the probability of surface production of negative ions [92–94]. The dependency of work function ( $W$ ) on

surface production of negative ions was studied in the work by Verbeek et al. [95] in which three metallic surfaces namely Ta ( $W = 5.6\text{eV}$ ), Au ( $W = 4.8\text{eV}$ ) and  $\text{ThO}_2$  ( $W = 2.0\text{ eV}$ ) were considered. It was found that only those neutrals and positive ions can form negative ions upon reflection from the electrode, which have energy greater than the threshold value  $E_{th} = W - E_A$ ; where  $E_A$  is electron affinity of positive ions or neutrals. The bombarding particles having energy lower than  $E_{th}$  cannot form negative ions. It was also found that the relative density of  $H^-$  produced at these metallic surfaces due to bombarding protons increases when the surface was changed from Ta to  $\text{ThO}_2$ . This implies that lower the work function of the substrate, smaller will be the threshold energy and therefore greater would be probability of negative ion formation.

Since the emitting surface is usually negatively charged [96], hence the newly created negative ions are accelerated due to sheath electric field and enters in to bulk of the plasma. This technique is employed in plasma based negative ion sources to produce high energy/flux of negative ions. The surface production of oxygen negative ions is also found in magnetron sputtering discharges during the oxide coating of a substrate [97, 98]. Since these negative ions are produced inside the sheath, therefore they are ballistically accelerated due to sheath electric field and effectively alter the quality of growing thin films on a substrate.

It is experimentally verified that the negative ions are actually emitted with finite distribution in their energy, which is basically inherited from the energy distribution of impinging background neutrals and positive ions on the electrode [94]. According to the study by Lee & Seidl [12], the flux of emitted negative ions can be calculated as a function of impinging flux of neutral on the electrode. For a Maxwellian distributed neutrals having temperature  $T_g$ , the impinging flux  $\Gamma_g$  at the electrode is given by [12];

$$\Gamma_g = n_g \sqrt{\frac{K_B T_g}{2\pi m_g}} \quad (1.31)$$

This flux  $\Gamma_g$  is related to the initial flux  $j_n$  of negative ions emitted from the electrode as;

$$j_n = eY(T_g)\Gamma_g \quad (1.32)$$

Where,  $Y(T_g)$  is negative ion yield for a Maxwellian distributed neutrals having temperature  $T_g$ . The variation of  $Y(T_g)$  as a function of inverse of neutral temperature, borrowed from the work by Lee & Seidl [12], is presented in fig-1.5.

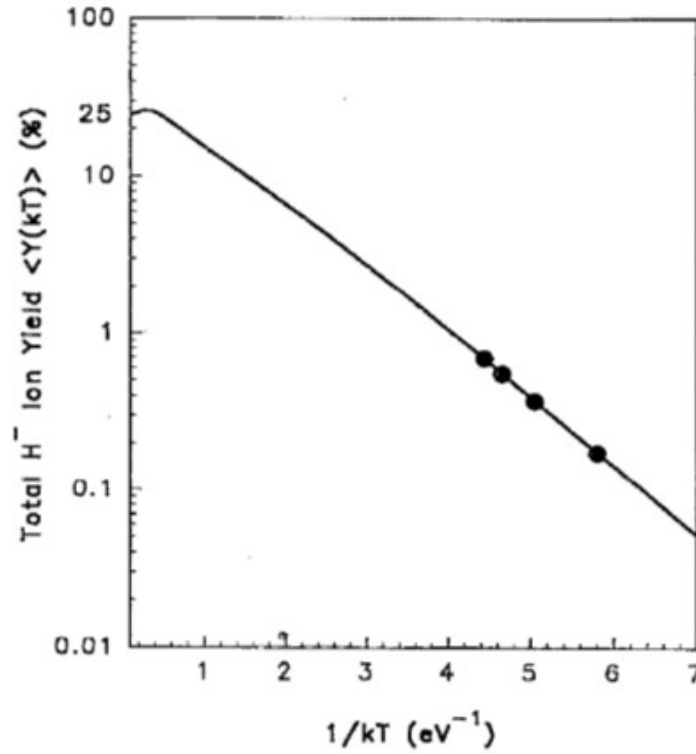


Figure 1.5: Total  $H^-$  ion yield,  $Y(T_g)$  as a function of neutral temperature. Courtesy: Brian S Lee and M Seidl. “Surface production of  $H^-$  ions by hyper-thermal hydrogen atoms”. In: *Applied physics letters* 61.24 (1992), pp. 2857-2859.

The survival of surface produced negative ions in the bulk plasma depends on their initial energy/flux as well as the plasma conditions. These negative ions are destroyed in the discharge through electron detachment and recombination with positive ions. It plays a very significant role in negative ion beam extraction from plasma based negative ion sources [99]. Thus the negative ions in the bulk plasma not only influence the sheath properties, but their production inside the sheath can

also implicitly affect the bulk plasma characteristics.

In Chapters-3 & 4 of the present thesis, an analytical study has been conducted on the sheath and pre-sheath associated with a planar electrode that emits negative ions. The analytical models provide insight in to the space charge effects due to negative ion emission, its influence on the characteristic length of the sheath and the pre-sheath and most importantly impact of negative ion emission on the characteristic speed of positive ions entering at the sheath edge. The analytical models have been compared with the particle-in-cell simulation works as well as experiments reported in the literature.

## 1.8 Boltzmann distribution of negative ions

At low pressures, the electro-negative discharges can be approximately described by using the Boltzmann distribution of negative ion similar to electrons. This can be qualitatively explained from one dimensional drift-diffusion equation for both electrons and negative ions as follows:

$$\Gamma_{e,v} = -D_{e,v} \frac{dn_{e,v}}{dx} - n_{e,v} \mu_{e,v} E \quad (1.33)$$

Here  $D_{e,v}$  are diffusion constants and  $n_{e,v}$  are the density of electrons and negative ions respectively;  $\mu_{e,v}$  are mobility for electrons and negative ions respectively such that  $\mu_e \gg \mu_v$ ;  $E$  is ambient electric field inside the plasma.

Since for electrons, the pressure gradient force  $\left(D_e \frac{dn_e}{dx}\right)$  exactly balances the electric force  $(n_e \mu_e E)$  so that the net electron flux  $\Gamma_e$  is zero. Therefore from (1-33);

$$D_e \frac{dn_e}{dx} = -n_e \mu_e E \quad (1.34)$$

Substituting  $D_e = (\mu_e K_B T_e)/e$  from Einstein relation &  $E = -\frac{d\phi}{dx}$  in (1-34), we get;

$$\frac{1}{n_e} \frac{dn_e}{dx} = \frac{d}{dx} \left( \frac{e\phi}{K_B T_e} \right) \quad (1.35)$$

With boundary condition  $\phi(0) = 0$  &  $n_e(0) = n_0$ , (1-35) gives;

$$n_e(x) = n_0 \exp \left( \frac{e\phi}{K_B T_e} \right) \quad (1.36)$$

Therefore, the electrons are described by Boltzmann distribution.

In case of negative ions, since  $T_v \ll T_e$ ; the flux due to pressure gradient force  $D_v \frac{dn_v}{dx} = \left( \frac{K_B T_v}{m_v \nu_m} \right) \frac{dn_v}{dx}$  is relatively small as compared to the electrons. Therefore Boltzmann description of negative ions is generally not valid.

In low pressure electronegative discharges, usually the negative ion loss due to local recombination with positive ions is relatively small as compared to the ambipolar diffusion loss of negative ions. This condition is satisfied when characteristic time of electron attachment (ionization process) is small compared to the ambipolar diffusion time of negative ions [100]. Therefore, the ambipolar diffusion of negative ions across the discharge gives rise to a non-zero flux arising from pressure gradient force  $D_v \frac{dn_v}{dx}$ .

At low pressures, (1) the density gradient term  $\frac{dn_v}{dx}$  can be sufficiently large; and also (2)  $D_v = \frac{K_B T_v}{m_v \nu_m}$  is large, owing to fall in the collision rate  $\nu_m$  with decrease in pressure. Hence similar to the electrons, an equilibrium can be established between negative ion fluxes due to pressure gradient force  $D_v \frac{dn_v}{dx}$  and the intrinsic electric field ( $n_v \mu_v E$ ) developed inside the discharge volume.

Fig-1.6(a)&(b) respectively shows the density profile for negative ions in a chlorine discharge for pressures (a) 30 mTorr and (b) 300 mTorr. The discharge length is  $l_p = 0.45$  cm and the central density is  $n_{e0} = 10^{16} \text{ m}^{-3}$  [87]. From fig-1.6(a), it can be seen that for low pressure case at 30 mTorr, the negative ion density profile can

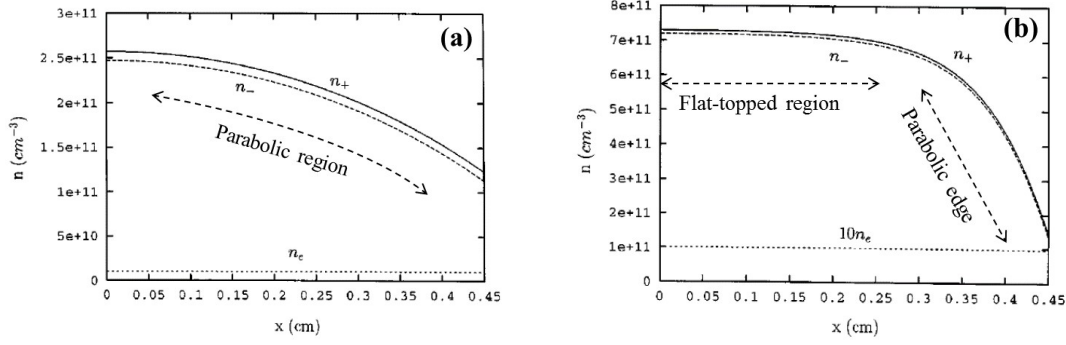


Figure 1.6: One dimensional density profiles for chlorine discharge of discharge length  $l_p = 0.45$  cm, electron density  $n_{e0} = 10^{16} \text{ m}^{-3}$  at pressure (a) 30 mTorr and (b) 300 mTorr. The density gradient  $\frac{dn_v}{dx}$  for low pressure case (30 mTorr) is slowly varying function of  $x$ ; while for high pressure case  $\frac{dn_v}{dx} \approx 0$  in the center of the discharge. Courtesy: *A J Lichtenberg et al 1997 Plasma Sources Sci. Technol. 6 437*

be approximated by a parabola (Ch-10 in [11]). Therefore, the density gradient  $\frac{dn_v}{dx}$  is a slowly varying function with  $x$ .

On the other hand at high pressure (300 mTorr), the diffusion constant  $D_v = \frac{K_B T_v}{m_v \nu_m}$  reduces due to increase in collision frequency  $\nu_m$ . Therefore  $D_v$  (At low pressure)  $> D_v$  (At high pressure). Moreover, the parabolic solution does not adequately describe the solution to the ambipolar diffusion equation but give rise to a central flattening of density profile with parabolic edge region such that  $\frac{dn_v}{dx} \approx 0$  in the center of discharge [see fig-1.6(b)]. This results  $D_v \frac{dn_v}{dx}$  negligible at higher pressure so that  $D_v \frac{dn_v}{dx}$  is not exactly balanced by the force term  $n_v \mu_v E$  in (1-33). Therefore it can be concluded that Boltzmann distribution is not valid for high pressure electronegative discharge.

## 1.9 Electric probes for determining negative ion parameters

From various application point of view, the physical nature of electronegative plasma is important to understand. This has been largely achieved by analytical

modeling [6, 101–103]. However this requires information of different plasma parameters inside the discharge including the negative ion density and the temperature. The density ratio of negative ions to electrons i.e.  $\alpha = n_v/n_e$ , and the temperature ratio of electrons to the negative ions, defined as  $\gamma_v = T_v/T_e$  are the two important parameters in electro-negative discharges. The popularly used method to determine them is based on laser assisted photo-detachment methods [104–106], however the associated diagnostics is generally restricted to line-of-sight region along the laser beam path. Beside, the laser system is a sophisticated instrument and it is inaccessible for general use.

On the other hand, the Langmuir probe is an adorable device for experimental plasma physicists and it has also been used to determine negative ion parameters [24–28, 107, 108]. The Langmuir probe allows to measure the local density and temperature from the current-voltage  $I - V_B$  characteristic of the probe using a relatively simple experimental setup. The underlying idea behind application of Langmuir probe to determine negative ion parameters and their limitations is presented below:

### 1.9.1 Measurement based on electrostatic probes

There are two methods for finding the relative concentration of negative ions to the electron in an electro-negative plasma; (a) The Druyvesteyn’s second derivative method and (b) the saturation current ratio method. These methods are briefly described below:

#### (a) The Druyvesteyn’s second derivative method

In Druyvesteyn’s method, the second derivative of the probe current  $I(V_B)$  can be used to determine negative ion density in a discharge. As shown in fig–1.7, the double derivative of probe current  $I''(V_B)$  shows two distinct peaks in curve

corresponding to electrons and negative ions respectively. The slope of  $\ln(I'')$  vs  $V_B$  curve gives the negative ion temperature  $T_v$ . The negative ion density, on the other hand, can be obtained in terms of ratio  $\alpha_0 = n_{v0}/n_{e0}$  by measuring the electron saturation current. The detailed description of this method can be found in [24].

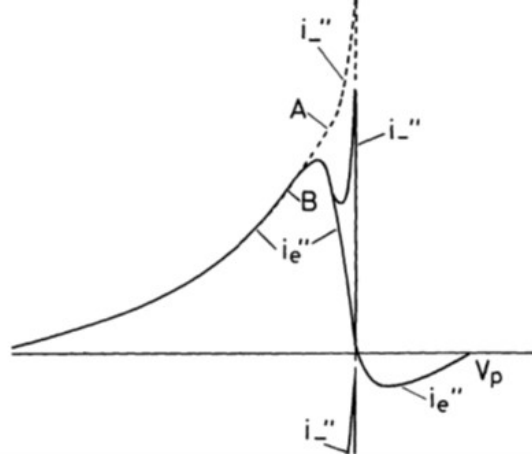


Figure 1.7: The second derivative of probe current (curve A) with respect to probe bias showing two distinct peak (solid curves) corresponding to electron and negative ions. Courtesy: Amemiya, H, *Journal of the Physical Society of Japan*, 57(3), 887-902 (1988).

However, this method has some limitation. The distinguishability in the peaks observed in  $I''(V_B)$  curve is highly sensitive on the density and temperature ratio of electrons and negative ions. In the limit  $T_v \ll T_e$  and  $n_v/n_e \gg 1$ , the negative ion distribution is masked with electron distribution so that identifying different slope of  $I''(V_B)$  curve is almost impossible.

### (b) The saturation current ratio method

To overcome the above limitations, the saturation current method is generally applied. In this method, the saturation current ratio  $R$  due to negative charges (electrons & negative ions) and positive ions is determined from the probe characteristics. In an electro-positive plasma, where the only negative charges are electrons, this ratio  $R$  is a constant value  $R \approx \sqrt{m_p/2\pi m_e}$ , which simply depends on the positive ion mass only [29]. However, in case of an electronegative plasma, the ratio  $R$



not only depends on  $m_p$  but also on the density and temperature ratio,  $n_v/n_e$  and  $T_v/T_e$  respectively. By measuring  $R$  experimentally, one can determine the density ratio  $n_v/n_e$  for a given  $T_v/T_e$ .

Amemiya (1987) [24] presented the comparative study about the applicability of the two method in  $Ar + I_2$  mixture and concluded that the Druyvesteyn's second derivative method loses its credibility for highly electro-negative plasma. Whereas the saturation current ratio method cannot be applied for weakly electro-negative plasma because of uncertainty involved in finding the correct electron saturation current.

The method of finding negative ion concentration  $\alpha_0$  from the measured saturation current ratio of a Langmuir probe had been adopted by various authors in the past. M Bowes and J W Bradley (2014) [107] investigated the negative ion formation in afterglow region of a pulsed oxygen plasma in a HiPIMS discharge and applied the saturation current method to find  $\alpha_0$  in the afterglow region with the help of a cylindrical Langmuir probe. M. Shindo (1999) [27] used the same technique to find the negative ion density for mixture of  $Ar/C_4F_8$  in ECR plasma, however, in their calculation of  $\alpha_0$ , the modification in ion saturation current due to presence of negative ions was not considered. S D You et al (2010) [108] compared the  $\alpha_0$  value obtained from the saturation ratio in a pulsed dc- magnetron with the more direct method of laser photo detachment and found that  $\alpha_0$  value obtained from two method agree with in a factor of 2 to 5 for varying oxygen partial pressure. The mismatch between the two methods was found to be manifested with the underestimated values of saturation current ratio. A similar comparative analysis of  $\alpha_0$  between the two method was done by A G Nikitin et al (1995) [25] using a planar and cylindrical probe in a hybrid multi-cusp plasma generator in which the negative ion concentration could be varied over a wide range.

Another study by P Chabert et al (1999) [28] involves the finding of  $\alpha_0$  in a

diffusion chamber of an  $SF_6$  helicon reactor using a planar probe assisted with a guarded ring configuration. The planar probe was used to measure the positive ion flux, while guarded ring measures the electron flux. The  $\alpha_0$  values was thus found from the saturation current ratio and compared with that obtained from the floating potential condition of the probe. However, in their study the electron to negative ion temperature ratio was assumed a priory and used to find the best fit between the two methods.

In all the above study, one point was common that the negative ion temperature was assumed a priory. In Chapter-5 of the present thesis, a floating potential method has been developed to determine the electro-negative parameter  $\alpha_0$  as well as negative ion temperature in electro-negative oxygen discharge.

## 1.9.2 Application of hairpin resonator probe

In addition to Langmuir probe, the resonance hairpin probe had been used for determining negative ion density in the discharge using following ways; (1) Pulse laser photo-detachment (2) pulse-biasing method. In pulse photo-detachment method, the hairpin probe is synchronized with pulsed laser beam to collect the time-resolved electron density data arising from photo-detached electrons from negative ions [105, 106]. The difference between the excess electron density created in the photo-detachment region and the background density provide a direct measure of negative ion density population in the volume. The main advantage of using hairpin probe is that the electron density measurement is repeatedly accurate and perturbation to the plasma is small as the probe is electrically floating.

In the pulse-biasing method, a train of negative voltage pulse is applied to the hairpin to create a rapid expansion and collapse of cylindrical sheath around the hairpin-tips [109]. The electron density characteristic shows a time-dependent be-

havior due to disparity in electron and negative ion response time towards the probe at the instance of withdrawal of negative voltage from the probe. As a result a peak in electron density is observed which corresponds to positive space charge around the probe. Though the concept is highly elegant but it requires the support of analytical model as well as benchmarking by other known methods.

In Chapter-6, an independent concept of using a dc biased hairpin probe for determining negative ion parameters in the discharge has been demonstrated. The method enables to find a range of plasma parameters inside the discharge; including electron temperature, density of negative ions, and plasma potential. In addition, the sheath width around the cylindrical wire can be found.

## 1.10 Outline of the thesis

The present thesis primarily focuses on two important aspects associated with non-equilibrium sheaths involving negative ions; (i) Sheath properties during negative ion emission from surfaces and (ii) development of probing techniques to determine negative ion parameters which are based on underlying probe theories.

The sheath due to negative ion emission from an electrode is an imminent problem in negative ion sources. Due to cesium deposition on the chamber walls and on ion-acceleration grids, the potential structure inside the sheaths can dramatically affect the emission and transport properties of negative ions from these surfaces. The surface produced negative ions can also affect the pre-sheath potential drop. Although some recent analytical works have been performed on sheaths with a negative ion emitting electrode, however the effect of negative ion emission on the pre-sheath properties has not been adequately discussed. The pre-sheath is the region where the positive ions are accelerated towards the sheath boundary. Furthermore the previous works did not account for the role of negative emission on the sheath

width.

Determining negative ion parameters in a discharge is one of the key issues in research of negative ions. The conventional electrical probes are based on sheath theories. In the present thesis, a brief account of various limitation associated with the conventional probe techniques has been provided and a comprehensive work has been dedicated to develop concepts how to utilize the conventional probes to determine negative ions parameters. Two major contributions in this area are the development of a floating potential method to determine negative ion parameter using a Langmuir probe and introduction of a DC-biased hairpin resonator probe that enable to find a wide range of plasma parameters such as electron density, electron temperature, plasma potential, negative ion density and the sheath width etc.

The thesis has been organized as follows:

Chapter-2 details specifically designed experimental setup and diagnostic technique for diagnosing the negative ion parameters in an argon/oxygen dc discharge. In Chapter-3, the fluid model for a planar sheath of a negative ion emitting electrode is presented. In particular, the chapter deals with the parametric study of Bohm speed for positive ions as a function of negative ions flux emitted from the electrode. In continuation with the result obtained in chapter-3, the impact on pre-sheath potential distribution and its characteristic length are discussed when a constant flux of negative ions is assumed to enter into pre-sheath, oppositely moving to the positive ions. The increase in positive ion Bohm speed due to emission from the electrode surface has been explained in conjunction with the increase in potential drop across the pre-sheath. The floating sheath characteristics for emitting/non-emitting electrode are presented in Chapter-5. Using the floating potential characteristics of a cylindrical Langmuir probe, the negative ion temperature is determined in an oxygen plasma. It is found that the temperature ratio of negative ions to the elec-

trons lies in the range  $\sim 8$  to  $\sim 12$  for the typical discharge parameters considered in the experiment. A qualitative discussion is given to explain the observation. In Chapter-6, the technique based on a dc biased hairpin probe is demonstrated. It is shown that using this technique not only the absolute electron density can be measured, which the resonance hairpin is popular for, but a range of other plasma parameters such as electron temperature and negative ion concentration can also be determined. Finally, Chapter-7 present a summary of important results along with conclusion and future scope of work.



# Chapter 2

## Experimental set-up and diagnostics

This chapter describes the experimental setup developed to investigate the application of electric probes for negative ion diagnostics in low pressure, non-equilibrium plasma, created using a DC discharge with a constricted anode and a pair of parallel plate cathode. The chapter provides a comprehensive description about the DC plasma source and the probe techniques based on Langmuir probe and resonance hairpin probe.

Section 2.1 provides a brief background of negative ion sources. The description of the experimental setup is given in section-2.2. The performance of the DC discharge is presented in section-2.3. A comprehensive description of Langmuir probe and hairpin probe is provided in sections 2.4 and 2.5 respectively.

### 2.1 Plasma sources for Negative Ion production

Electro-negative plasmas are mainly produced with highly electron attaching gases like oxygen and halogen, as a result these gases readily produce negative ions by attaching electrons from the ambient plasma [11, 110]. Therefore the reactive plasmas that are typically used in semiconductor industries for anisotropic

---

etching of silicon wafer [1, 80, 111], thin film deposition [2, 82, 112, 113], cleaning or activation of material substrate [114, 115] etc. have a large concentration of negative ions. The negative ions inside bulk plasma are produced by dissociative attachment, as the vibrationally excited molecules gets dissociated and captures an electron to form negative ions [81, 116]. In this process, the electron temperature has an important role in the excitation of the gas molecules. This will be briefly introduced in section-2.2.1. Another mechanism of negative ion production is based on interaction of positive ions and neutrals with a low work function surface. As these particles interact with the substrate surface, they bounce back as negative ions after capturing an electron from the Fermi-energy level of the metal. [117–119].

To create negative ions, the foremost requirement is to produce a plasma, which can be achieved by various mechanism. In laboratories, the non-equilibrium plasma ( $T_e \gg T_p$ ) at low pressures can be conveniently created by hot cathode filament [120]. The Kamaboko Ion Source is one such example, which provides primary source of  $H^-$  ions [121]. Bi-polar pulsed-DC magnetrons [14, 122] and HiPIMS discharges [97, 98] are examples of other types of negative ion sources which are widely used in industries for sputter deposition of oxide films on substrates. These sources use external permanent magnets to confine the plasma locally near the cathode surface which gives rise to high density plasma near the sputtering target. The magnetic field also helps to create a strong electron temperature gradient in the region adjacent to the cathode [123]; hence it is also favorable for the volume production of negative ions. Helicon plasma sources have also been used in negative ion production for thruster application [124].

## 2.2 The experimental setup

In the present experiment, we have chosen the oxygen as the primary gas. Oxygen



being an electronegative gas, it readily forms negative ions by dissociative electron attachment to the neutrals [...]. It is easily available, and relatively less corrosive than other halogen gases. In literature, widely found data is also available for oxygen [85, 89, 125, 126].

While considering the various possibilities to create oxygen plasma, the magnetron discharges was one of the viable mechanism to produce non-equilibrium DC discharges at low pressures [104, 127]; however plasmas created by DC magnetron are composed of metal ions inside bulk plasma; and therefore the life-time of diagnostics probe can be severely impaired due to deposition of insulating oxide films on the probe tips [128]. On the other hand, the discharges based on hot cathode filament have the limitation in oxygen environment due to maintenance issues, as the tungsten filaments are quickly oxidized and broken, therefore need frequent replacement. The RF discharges are much cleaner, but electric probe diagnostics can be very challenging due to large fluctuation in plasma potential. Hence looking at various limitations, a simple DC discharge based on a constricted anode and a pair of parallel plate cathode has been designed. This set-up is similar to the one reported in [129], however in our setup a weak axial magnetic field ( $B < 3\text{mT}$ ) has also been introduced between the cathode plates which consist of a pair of annulus plates. The schematic of the discharge setup is shown in fig-2.1.

### 2.2.1 The Plasma Source

The schematic of the plasma source is shown in figure-2.1. In this source, a high DC voltage up to 1.0 kV is applied between the cathode (C) and the constricted anode (A) [see fig-2.1]. The electrodes are made of stain-less steel (SS-304) and are electrically isolated from the grounded vacuum chamber. The cathode plates with circular cutout in the center have the outer diameter  $OD = 142\text{ mm}$  and inner diameter  $ID = 40.0\text{ mm}$ ; while they are separated by a gap of 27.0 cm. A weak magnetic

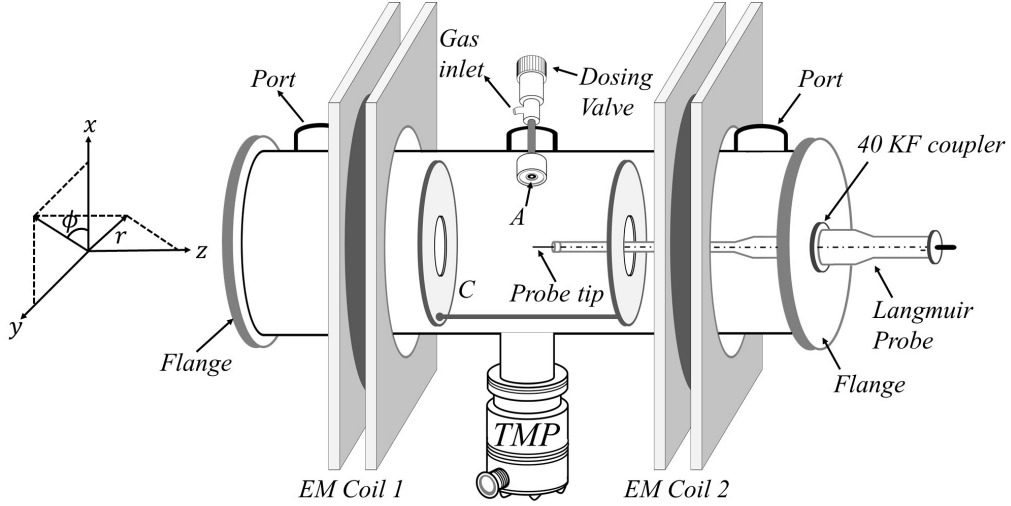


Figure 2.1: Schematic of discharge setup showing the constricted anode and pair of annular cathode plates. Axial magnetic field is generated by two external electromagnet coils EM1 and EM2 arranged in Helmholtz configuration.

field ( $B < 3.0$  mT) has been applied to partially magnetize the electrons (Larmor radius  $r_{Le} \approx 1$ mm), while positive/negative ions remain un-magnetized since their larmor radius  $\sim 27$ cm, which is comparable to chamber dimension. The working gas (argon and oxygen) is introduced through the anode tube. The constricted hollow anode is encapsulated inside a ceramic tube, except for the small tip through which the discharge current completes the circuit. Due to the constricted anode surface, an intense electric field is developed around the anode tip which facilitate a DC breakdown at low filling pressure (1.0 Pa - 7.0 Pa). As the DC discharge is sustained, a bright glow is seen around the anode region [see fig-2.6].

The mechanism of plasma formation in this set-up can be explained as follows. Generally in a DC discharge, the secondary electrons emitted from the cathode helps in self-sustainment of discharge at low pressures [130]. In the present configuration, a significant fraction of electrons that are emitted from the cathode surface gets trapped between the opposing high voltage cathode plates. The weak axial magnetic field between the plates helps to intensify the population of such electrons. However, the ionizing electrons can reach the central region by random walk process. Therefore the population of hot ionizing electrons is higher between the parallel plate cathodes,

whereas the central plasma region constitute of low temperature electrons which arrives from the outer region through cross-field diffusion across axial magnetic field line. In the experiment, typical electron temperature found in central region varies from 0.5 eV to 1.5 eV with gas pressure.

The characteristic feature of the source can be summarized as follows: **(1)** the energetic electrons are confined between the parallel plates, allowing the discharge to operate at low pressures; **(2)** The discharge constitute of two temperature electrons, which is favorable for the dissociative-attachment process [110], and **(3)** the plasma potential is relatively close to grounded electrode, hence electrical probe diagnostics can be conveniently applied to this system.

### 2.2.2 Experimental Vacuum chamber

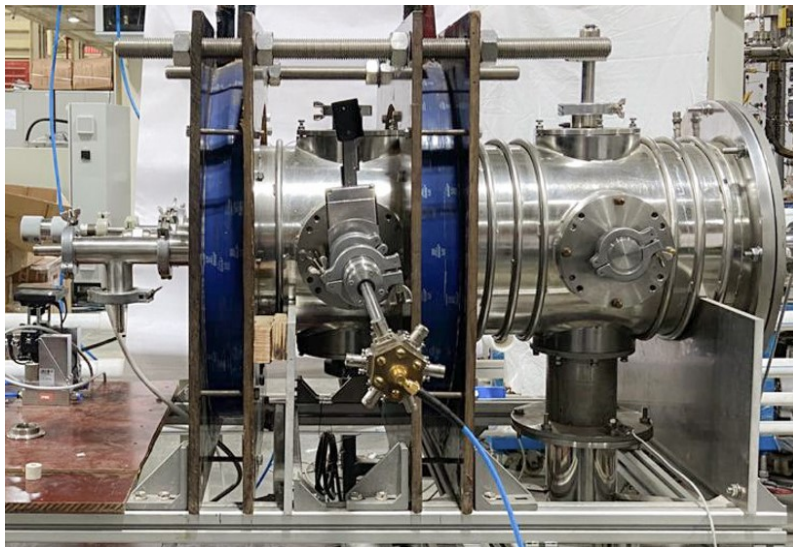


Figure 2.2: Experimental setup with circular electromagnetic coils in Helmholtz configuration.

The experimental system shown in figure-2.2 consists of a cylindrical vacuum chamber made of stainless steel (SS-304). The length is 70.0 cm and inner diameter is 26.6 cm. For inserting various probes inside the source, a number of 40 KF vacuum feed-thru ports are provided at specific position on the chamber surface. Base

pressure of  $3 \times 10^{-5}$  Pa is achieved inside the vacuum chamber with a combination of turbo molecular (Pfeiffer make HiPace-700) and a rotary pump. The base pressure inside the chamber is continuously monitored using a combination of hot cathode pirani/penning gauge (Pfeiffer: Model-No D-35614 Asslar). A precision gas dosing valve is used to regulate the pressure inside the discharge chamber. All the experiments are carried with 99.9% pure argon and oxygen gas. To maintain the working pressure, the rpm of TMP was reduced at 50% of its total capacity to reduce excess loading on the TMP vanes.

The pair of electro-magnets shown in Fig- 2.2 have a mean diameter of 37 cm. These magnets are placed outside the cylindrical vessel in Helmholtz configuration. In the operating pressure range of 1.4 Pa to 7.0 Pa, the plasma density range from  $\sim 10^{16} - 10^{17} m^{-3}$  and electron temperature  $T_e \sim 0.5 - 2$  eV respectively. The mean free path length for the ion-neutral momentum transfer in argon varies from  $\sim 2.8$  mm to  $\sim 0.57$  mm corresponding to the pressure variation from 1.4 Pa to 7.0 Pa. The electron-neutral collision frequency  $\nu_e$  is typically in the range of  $\nu_e = 3 - 30 \times 10^5$  Hz.

### 2.2.3 The Discharge Circuit

Figure-2-3 shows the schematic of the floating DC power supply used for producing the discharge. The circuit basically comprises a 1.0 kV step-up transformer, a bridge rectifier, a current limiting resistor and filter capacitors of 100's of microfarad at the output terminal. The output DC voltage is varied by controlling the 50 Hz current in the primary side of the transformer.

The positive output terminal of the DC source is connected to constricted anode and the negative terminal is connected to the cathode plates. Furthermore, two different circuit configuration has been applied in the experiment, which are

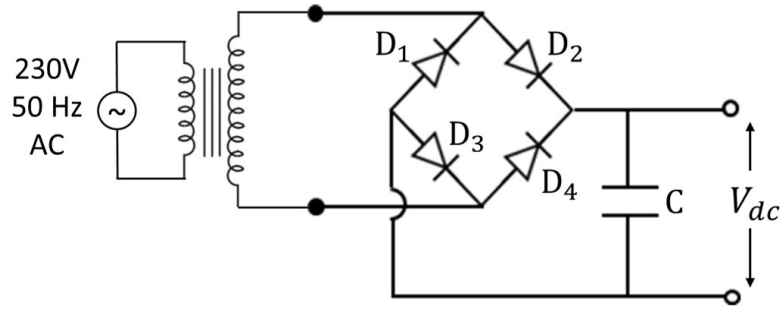


Figure 2.3: Schematic of unregulated power supply. In the figure  $D_1$ ,  $D_2$ ,  $D_3$  and  $D_4$  are diodes,  $C$  is capacitor and  $V_{dc}$  is output DC voltage.

schematically shown in fig-2.4. In setup-I, the constricted anode was grounded to the vacuum chamber via a high wattage  $1\text{k}\Omega$  resistor; whereas in Setup-II, a voltage divider circuit was introduced between the anode and the cathode. In this case external resistance across the anode to grounded chamber is  $0.5\text{ k}\Omega$ .

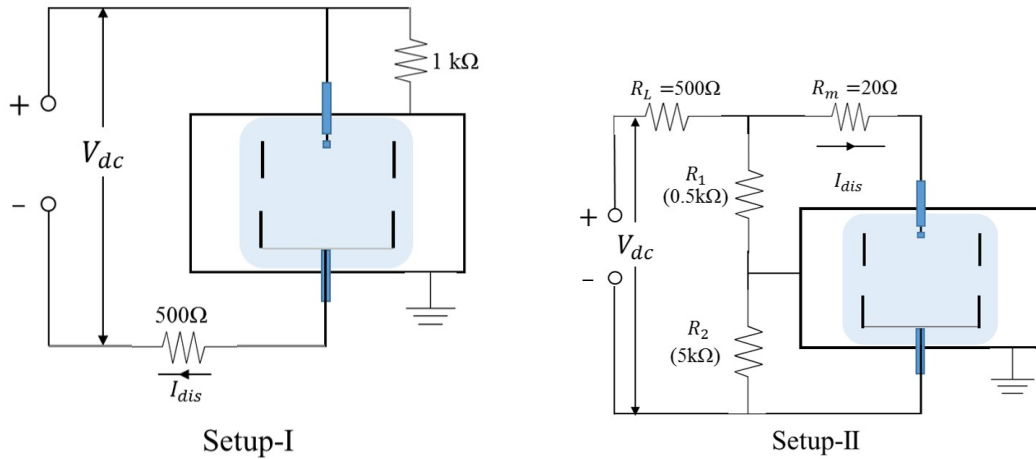


Figure 2.4: Schematic of discharge circuits: In setup-I, the anode is grounded through a high resistance value  $1\text{k}\Omega$ , while in setup-II, the voltage is divided between cathode and anode with respect to the grounded chamber.

The discharge current primarily flows between the cathode and the anode, but with above configuration, a small fraction of the discharge current also flows through the grounded chamber. This helps to shift the anode potential closer to the ground. In setup-I, due to the high resistance ( $1\text{k}\Omega$ ) connected between the anode and the grounded chamber, the maximum discharge current  $I_{dis}$  therefore flows through the

constricted anode. In setup-2, the resistors  $R_1$  and  $R_2$  can be varied to regulate the anode and cathode potential with respect to ground. In the entire experiment, the voltage drop measured across  $20\Omega$  resistance provides the discharge current  $I_{dis}$  which is observed in the range of 200 mA. The above current is mainly limited by the resistance  $R_L$  which restrict the discharge current from going in to arc mode [38]. The plasma potential was typically in the range of +3.0 to +15.0 V for a pressure range of 1.0 Pa to 7.0 Pa.

## 2.2.4 DC plasma Characteristics

Figure-2.5 (a) & (b) plots the variation in discharge current  $I_{dis}$  against discharge voltage  $V_{dis}$  for both setups-I & II respectively. The discharge voltage  $V_{dis}$  is measured between cathode and anode. The plasma impedance can be estimated in the range of a few  $k\Omega$ , and it decreases with the increase in gas pressure.

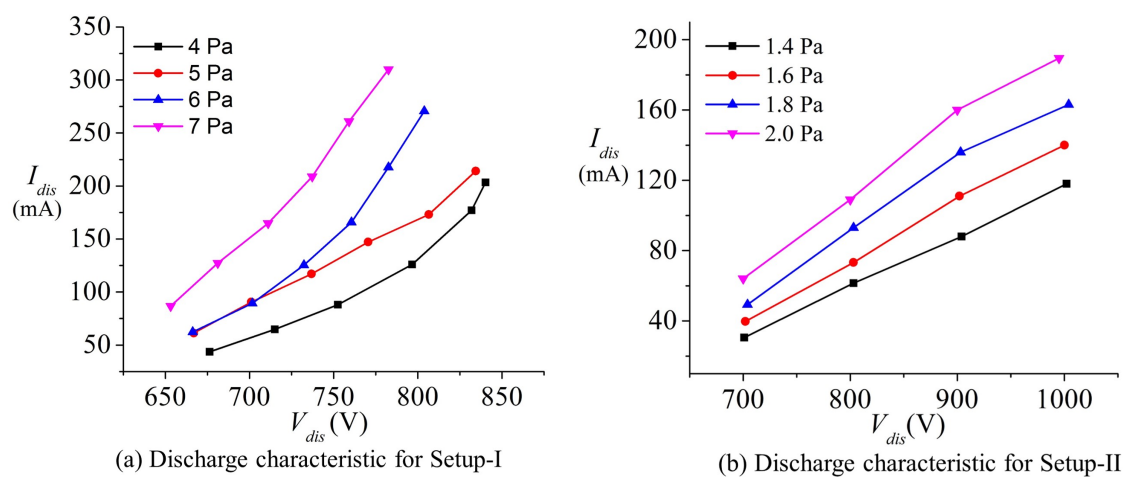


Figure 2.5: Plot of discharge current verses discharge voltage for setup-1 and setup-II.

In above figures, discharge current increases with the applied voltage, showing a positive plasma resistance, observed when DC discharge operates in abnormal glow region [38].

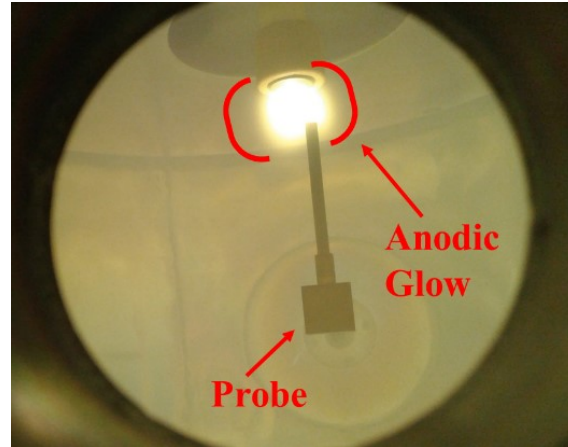


Figure 2.6: The anodic glow or fireball structure around the anode in oxygen plasma.

## 2.3 Electric Probe Diagnostic

For the experiments, two types of electric probes were developed; **(a)** Langmuir Probe and **(b)** Hairpin probe. The underlying principle behind these probe techniques are presented in the following sections. These probes have been used to obtain the plasma parameters and also applied to study the characteristics of DC sheath around the cylindrical wire. In chapter-5 & 6, the above probing techniques have been discussed exclusively for determining the negative ion parameters.

### 2.3.1 Langmuir probes

#### **(i) The underlying concept**

A Langmuir probe is simply a piece of tungsten wire which is inserted inside a plasma to determine various plasma parameters. The probe is essentially biased with respect to a reference electrode, usually the grounded vacuum chamber, which is assumed to be in contact with plasma. The total current drawn by the probe is basically the sum of individual currents contributed by electrons and positive ions. Depending on the polarity of the probe with regard to the plasma potential  $V_p$ , the electrons and positive ions are either collected or they are repelled from the probe

surface. Figure-2.7 shows a schematic, how the individual currents due to electrons

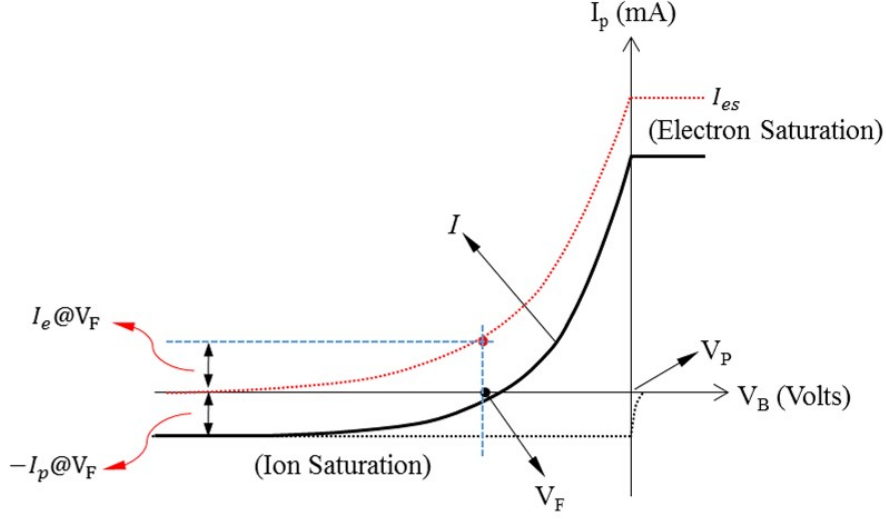


Figure 2.7: A schematic of Probe current  $I$  versus applied bias  $V_B$  applied on the cylindrical Langmuir probe, shown in solid black line. The red dotted line corresponds to the current due to electron, while the positive ion current is shown by the black dotted line.

and positive ions varies as the probe bias  $V_B$  changes. Conventionally, electron current is plotted along the +Y-axis, while the positive ion current is plotted in the negative -Y-axis. The total probe current,  $I$  is the summation of both components, i.e.  $I(V_B) = I_e + I_p$  which is shown by the solid black line.

Electrons are assumed to follow Maxwellian distribution; hence for  $V_B < V_p$ , the electron component of the current is given by;

$$I_e = I_{es} \exp\left(\frac{V_B - V_p}{T_e}\right) \quad (2.1)$$

In equation (2.1),  $I_{es}$  is saturation value of the electron current at the plasma potential i.e.  $V_B = V_p$ ; which is given by;

$$I_{es} = \frac{1}{4} e A_p n_{e0} \langle v_e \rangle \quad (2.2)$$

Here  $A_p$  is probe area,  $n_{e0}$  unperturbed density of electrons in the bulk;  $\langle v_e \rangle = \sqrt{\frac{8K_B T_e}{\pi m_e}}$  is the average thermal speed of electron having mass  $m_e$  and temperature



$T_e$ .

When  $V_B$  is sufficiently negative with respect to plasma potential  $V_p$ , then probe dominantly collects positive ions and quickly attains a saturation value  $I_{ps}$ , which is shown by black dotted line. The positive ions collected by the probe remains almost constant for all  $V_B$  values varying up to  $V_p$ . Above  $V_p$ , the probe begins to repel positive ions; however a negligibly small positive ion current due to their thermal motion characterized by ion temperature  $T_p$  is collected. For an electro-positive argon plasma, the ion saturation  $I_{ps}$  current is determined by the Bohm flux [11];

$$I_{ps} = eA_s n_{ps} u_B \quad (2.3)$$

Where,  $n_{ps}$  is the positive ion density at the probe sheath edge;  $A_s$  is the area of the probe sheath and Bohm speed  $u_B = \sqrt{\frac{K_B T_e}{m_p}}$ . The sheath edge density  $n_{ps}$  is always smaller than the bulk density  $n_{p0}$  due to presence of pre-sheath, over which the ions are accelerated to achieve Bohm speed  $u_B$ . They are related by;

$$n_{ps} = 0.61n_{p0} \quad (2.4)$$

It is important to note that while writing the positive ion current in (2.3), the collecting area of probe has been considered to be the sheath area  $A_s$ . This is because the positive ion flux remains conserved throughout the sheath region, therefore it is convenient to define it in terms of Bohm current at the sheath edge rather than at the actual probe surface [58]. However for electron saturation current, the collecting area of probe has been assumed to be the geometrical area  $A_p$  of the probe. This correction is only valid for a collision-less sheath around the cylindrical probe, as the sheath width increases due to the application of negative bias [131].

A typical  $I(V_B)$  characteristic of a cylindrical probe obtained from the present experiment is shown in figure-2.8. Using this plot a number of plasma parameters can be determined. This has been described below;

(a) **Plasma Potential ( $V_p$ )** : The plasma potential can be estimated from the inflexion point of first derivative of the probe current with respect to  $V_B$ . As shown in fig-2.8, the plasma potential corresponds to  $V_B = V_p = 4.2$ .

(b) **Floating potential ( $V_f$ )** : This is the potential at which the net current

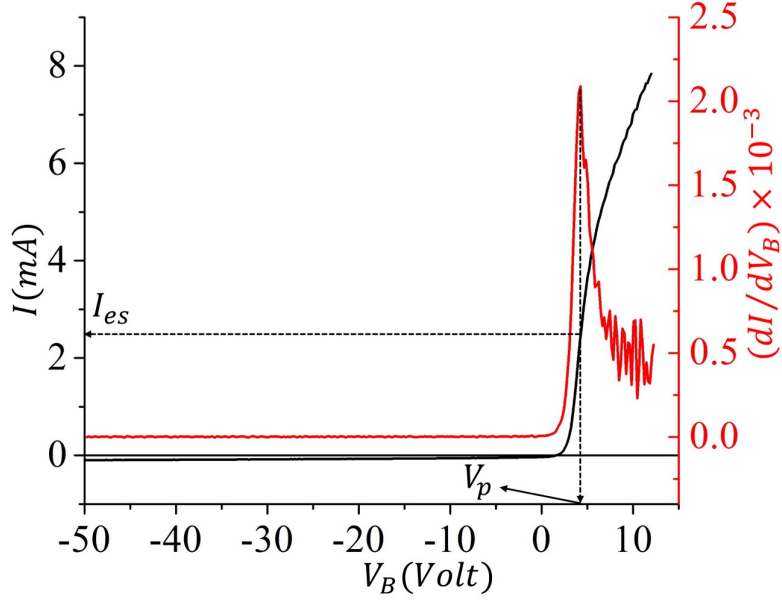


Figure 2.8: A typical  $I(V_B)$  characteristic (black curve) using a cylindrical probe of length 6 mm and diameter 0.2 mm in experimental setup-I. The maxima observed in first derivative of the probe current (red curve) corresponds to plasma potential  $V_p = 4.2$  V. The typical discharge parameters are  $P = 5$  Pa and  $P_w = 86$  watts.

drawn by the probe is zero, i.e.

$$I_e(V_f) = I_p(V_f) \quad (2.5)$$

On substituting  $V_B = V_f$  in (2.1) and using (2.2), (2.3) and (2.4) the floating potential can be obtained as;

$$V_f = V_p + T_e \ln \left[ 0.61 \left( \frac{A_s}{A_p} \right) \sqrt{\frac{2\pi m_e}{m_p}} \right] \quad (2.6)$$

In (2.6),  $A_s$  is the sheath area when the probe is at floating potential  $V_f$ . For planar probe  $A_s = A_p$ , however for cylindrical probe  $A_s > A_p$  always [131]. In spite of this

fact, the sheath area is generally considered to be equal to the probe area in thin sheath limit.

**(c) Ion and electron saturation currents :** The expansion of sheath around the cylindrical probe leads to error during estimation of ion saturation current. However, as suggested by Chen et al [131], this error can be minimized if it is measured at the floating potential. Therefore the technique to find  $I_{ps}$  involves fitting a straight line in ionic part of  $I(V_B)$  curve and extrapolating it to the floating potential  $V_B = V_f$ . This is shown in figure-(2.9) in which ion part of the  $I(V_B)$  curve in figure-(2.8) has been zoomed-in to clearly visualize the ion saturation current. Once  $I_{ps}$  is determined, then the electronic part of the probe current can be obtained

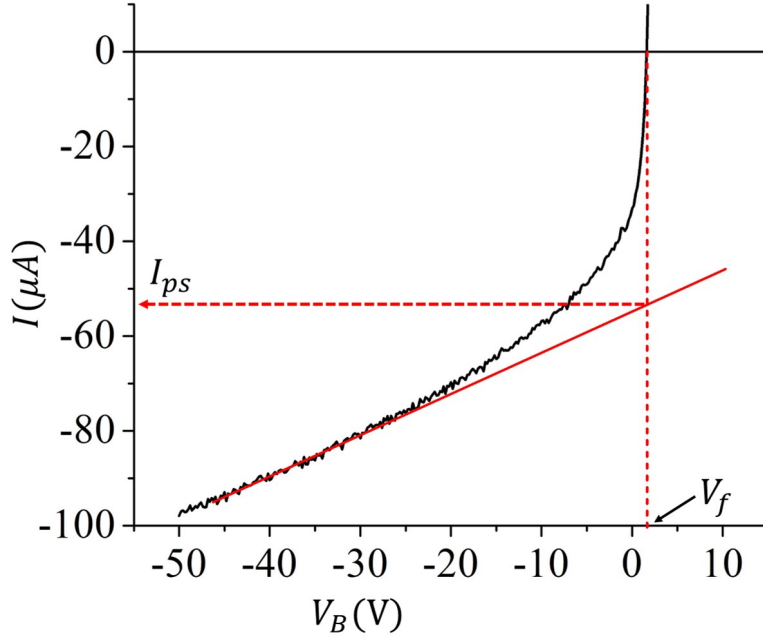


Figure 2.9: The ionic part of  $I(V_B)$  characteristic curve. The straight line fit of the ion current and extrapolating up to floating potential  $V_f = 1.6$  V gives the ion saturation current  $I_{ps} = 54 \mu\text{A}$ .

by subtracting  $I_{ps}$  from the total probe current, i.e.  $I_e = I - I_{ps}$ .

**(d) Electron Temperature:** On taking the natural logarithm of electronic part of the current equation-(2.1), we get;

$$\ln I_e = \ln I_{es} + \left( \frac{V_B - V_p}{T_e} \right) \quad (2.7)$$

Since plasma electrons are assumed to have a Maxwellian electron distribution, hence semi-log plot of  $I_e$  vs  $V_B$  is straight line. The inverse of the slope gives the electron temperature  $T_e$ . The semi-log plot of the data corresponding to figure-2.8 is plotted in figure-2.10. In the above figure, the two slopes namely AB and CD can be identi-

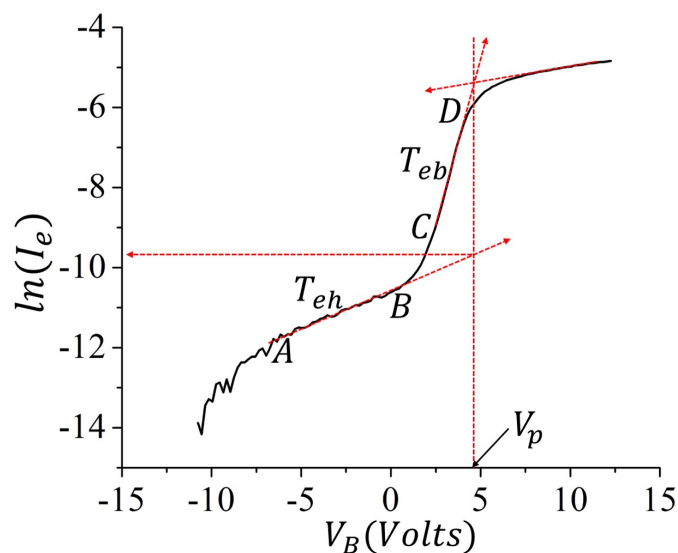


Figure 2.10: The semi-log plot for electron saturation current with respect to the probe bias  $V_B$ . The straight line fit namely AB and CD indicates the presence of bi-Maxwellian electrons having temperature  $T_{eh}$  and  $T_{eb}$  respectively.

fied. The inverse of these slopes provide the electron temperature corresponding to the hot and the cold electron population  $T_{eh}$  and  $T_{eb}$  respectively. Once  $T_{eh}$  and  $T_{eb}$  are known, then it is possible to determine the corresponding plasma densities belonging to hot and cold plasma electrons by extrapolating the straight lines AB and CD in the semi-log plot to the plasma potential  $V_p$ . The presence of hot electrons in the central region suggests that some of the hot electron population originated from the region between the parallel cathode plates crosses the magnetic field to reach the central region after undergoing collisions with the background atoms.

Figure-2.11 shows the relative fraction of the hot and the bulk electron population as a function of discharge power, for argon operated in pressure range of 4.0 pa to 7.0 Pa. It is found that the hot population of electrons maximally constitute only  $\sim 1\%$  of the total electron population. Furthermore, with increase in discharge

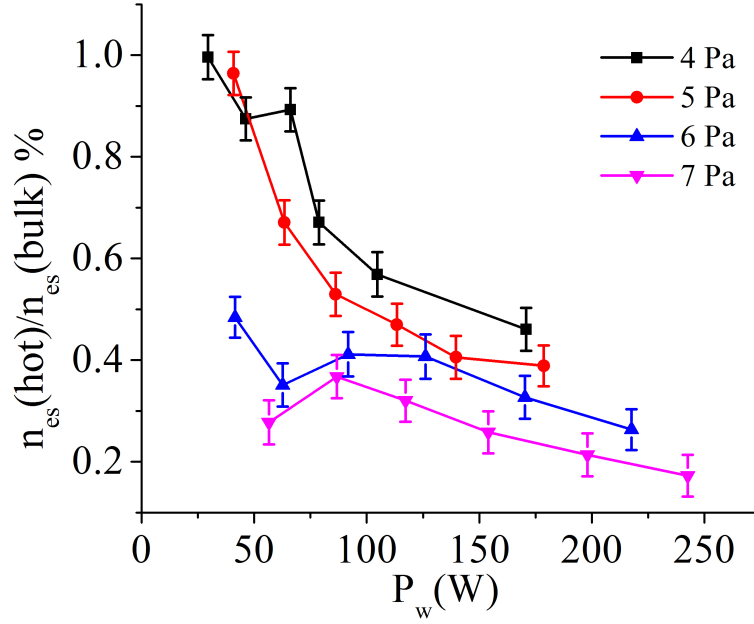


Figure 2.11: The plot for percentage fraction of hot population electrons with respect to pressure and discharge power.

power and pressure, these hot electron fraction decreases drastically due to increase in electron collision with background neutrals.

## ii. The Langmuir Probe Circuit

Figure-2.12 shows a typical electrical circuit for Langmuir probe. The plasma has been assumed to be in good electrical contact with the grounded vacuum chamber having area  $A_G$ . As the probe is biased above the ground potential, the probe draws an electron current whereas an electron repelling sheath gets created at the opposing grounded electrode. The ground sheath impedance  $R_G$  can be roughly estimated by  $R_G \approx \frac{V_p}{eA_G n_{ps} c_s}$ ; where,  $c_s$  is ion-sound speed and  $n_{ps}$  is positive ion density at the sheath edge of the grounded electrode.

Similarly, a sheath resistance  $R_p$  will also appear at the probe tip. The resistance  $R_p$  will vary according to the applied probe bias  $V_B$ . When  $V_B = V_p$ , the probe

sheath resistance should be ideally vanishing and the collected current at the probe surface is mainly contributed by the flux of thermal electrons. The current drawn by the probe for any other bias  $V_B < V_p$  is returned by the positive ions collected at the grounded electrode. If grounded electrode area is small, then the ground sheath

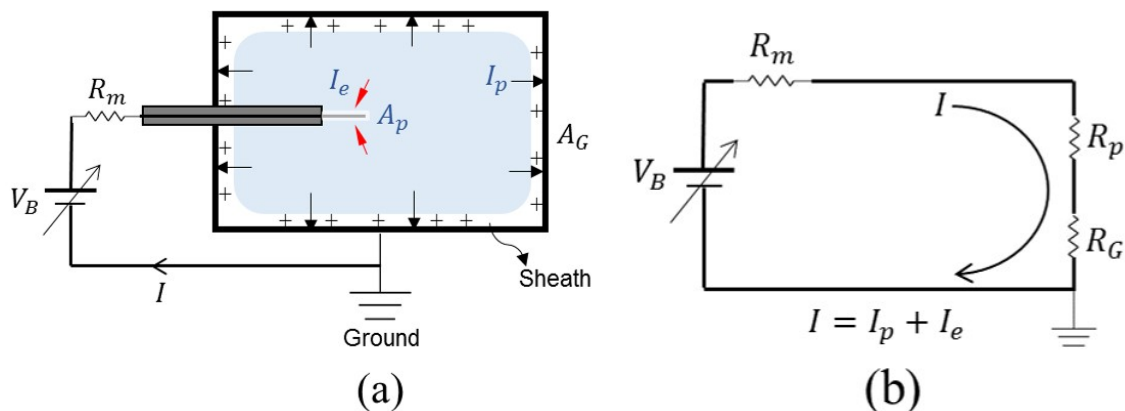


Figure 2.12: (a) A typical Langmuir probe circuit showing a cylindrical probe inside a plasma biased at a positive potential with respect to the (Grounded) reference electrode. (b) Equivalent circuit is shown in which  $R_m$ ,  $R_p$  and  $R_G$  are respectively the current measuring resistance, resistance of the probe sheath and the resistance between the plasma and the Grounded reference electrode.

resistance  $R_G$  limits the net current drawn by the probe. In addition, the current sensing resistor  $R_m$  also appears in series with the probe circuit; which limits the maximum electron current drawn by the probe. Ideally  $R_m + R_G \ll R_p$  so that the probe is able to draw maximum electron saturation current  $I_{es}$ . From the probe characteristic shown in figure-(2.8), assuming  $I_{es} \approx 3$  mA and  $V_p \approx +4.0$  V, the ground resistance  $R_G \approx 1.0$  k $\Omega$ . The current measuring resistance in the above experiment was  $R_m = 220\Omega$  which is smaller than the ground sheath resistance.

However, if the plasma is poorly in contact with the grounded reference electrode, for example- due to contamination on the chamber walls or when an external magnetic field is applied, then in such cases, electron saturation current can attain a lower value, which will directly underestimate the plasma potential.

Equating the thermal electron current collected to the probe (equation-2.2) with

positive ion current collected at the grounded reference electrode (equation-2.3), gives a relation that how much should be the collecting area of a reference electrode for collecting maximum probe current. For argon discharge, it is given by;

$$A_G \approx 180 (n_p/n_s) A_p \quad (2.8)$$

In above equation,  $A_G$  and  $A_p$  are respectively the surface area of the reference electrode and the probe surface in contact with the plasma. The densities  $n_p$  and  $n_s$  are plasma densities in the vicinity of probe surface and at the grounded sheath respectively. Equation-2.8 implies that the area of grounded electrode should be at least  $\sim 180(n_p/n_s)$  times the probe area.

To minimize the effect of measuring resistor  $R_m$  on the performance of  $I(V_B)$  characteristics, an  $I - V$  converter circuit has been used, as shown in figure-2.13. This circuit takes the advantage of high input impedance of the Op-Amp, which maintains a constant voltage irrespective of the current drawn by the probe as a function of probe bias  $V_B$ .

In the experiment, the probe bias  $V_B$  is provided using an operational amplifier (PA-85) and typically varied in the range of  $-80V$  to  $+20V$  in step of  $0.25V$ . The differential voltage across the input and the output of  $I - V$  convertor (PA-85) is measured using a differential amplifier (AD-629). The advantage of this circuit is that the loading effect due to the external circuit resistance can be avoided. The data acquisition is done using NI-DAQ controlled by a Lab-View program.

The above Langmuir probe circuit is calibrated by performing an open circuit test (i.e. in absence of plasma). It gives a small DC current ( $\sim \mu A$ ) which increases with biasing voltages as shown in figure-2.14(a) (black). These are the DC noise signals due to capacitive loading of the cables connected to the probe. The DC background signals are removed by subtracting it from the final  $I(V_B)$  traces obtained in the ex-

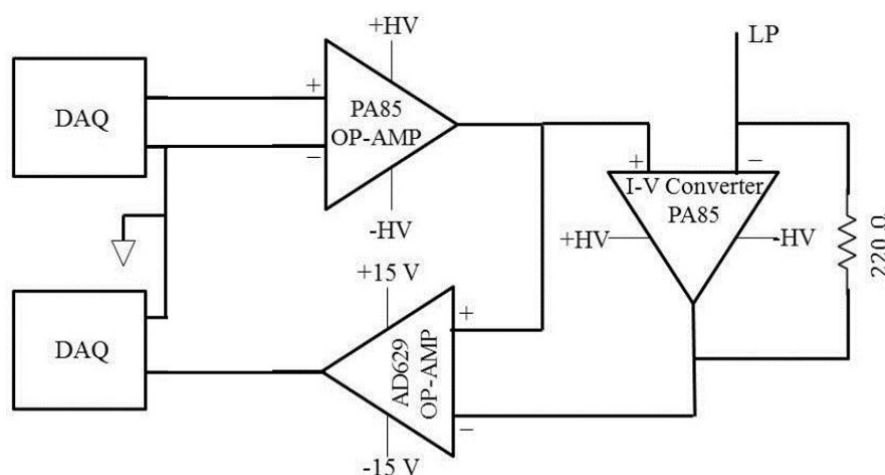


Figure 2.13: Schematic of Langmuir probe circuit. DAQ represents data acquisition, OP-AMP denotes operational amplifier.

periments. Therefore, as shown in figure 2.14(a), the current collected by the probe after calibration reduces to zero as expected for open circuit test in the absence of plasma. Figure 2.14(b) compares the measured  $I(V_B)$  traces with and without calibration. It can be seen that without calibration, the measured  $I(V_B)$  trace results in the overestimated values of the ion current with variation in ion saturation current by  $< 10\%$ .

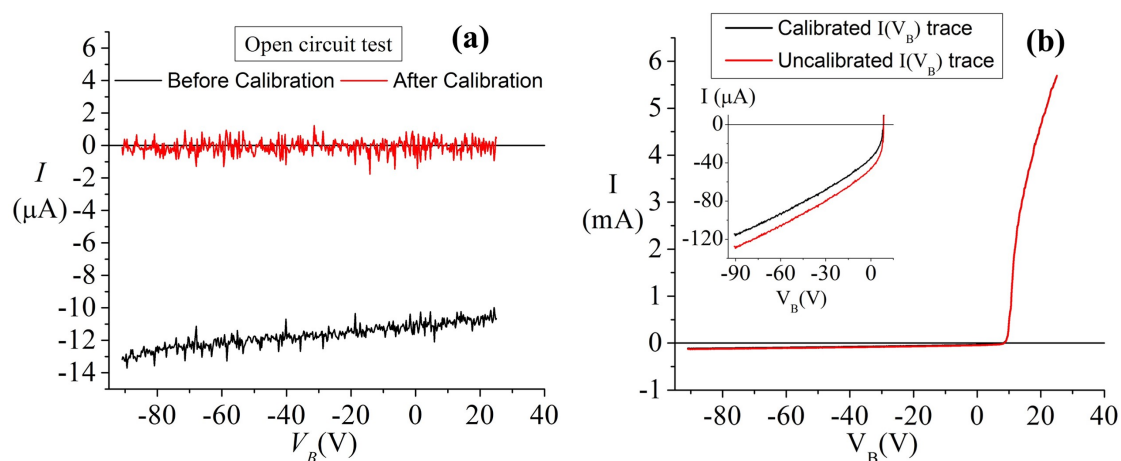


Figure 2.14: (a) Open circuit signal with (Red) and without (black) subtraction of the background. (b) Plot of  $I(V_B)$  trace with and without calibration.

### iii. Effect of electron temperature on $V_p$ measurement



For a single electron temperature plasma, the plasma potential  $V_p$  and the floating potential  $V_f$  are uniquely related to electron temperature  $T_e$  by the relation given in (2-6). In principle, if  $T_e$  and  $V_f$  are measured accurately, then  $V_p$  can be found from the relation (2-6).

For a thick cylindrical sheath, it is possible to find  $V_p$  using OML theory introduced in chapter-1. According to this, the probe current is related to the applied voltage  $V_B$  as follows [60];

$$I(V_B) = eA_p n \frac{\sqrt{2}}{\pi} \left( \frac{e|V_p - V_B|}{m_p} \right)^{1/2} \quad (2.9)$$

Hence  $I^2$  vs  $V_B$  plot gives a straight line, where the intercept at  $V_B$  axis corresponds to plasma potential  $V_p$ .

Fig-2.15 shows a comparison of plasma potential obtained by different techniques, i.e. namely (1) inflexion point on the first-derivative, (2) intersection of semi-log plot of probe current below and above  $V_p$ . (3) from floating potential and (4) from OML theory.

In the figure,  $V_{p1}$  has been obtained from the first derivative of the probe current;  $V_{p2}$  is obtained from the semi-log plot of the electron current;  $V_{p3}$  is obtained by measuring the floating potential and finally  $V_{p4}$  is found from OML theory. From above figure, the first three methods gives a reasonable measure of  $V_p$  and they are closely in agreement. However OML gives an excessively overestimated values of  $V_p$ . Hence it can be concluded that the OML theory is not applicable in the presence case.

## 2.4 Hairpin resonance probe

The hairpin resonance probe is an electromagnetic resonator, alike to a quarter-

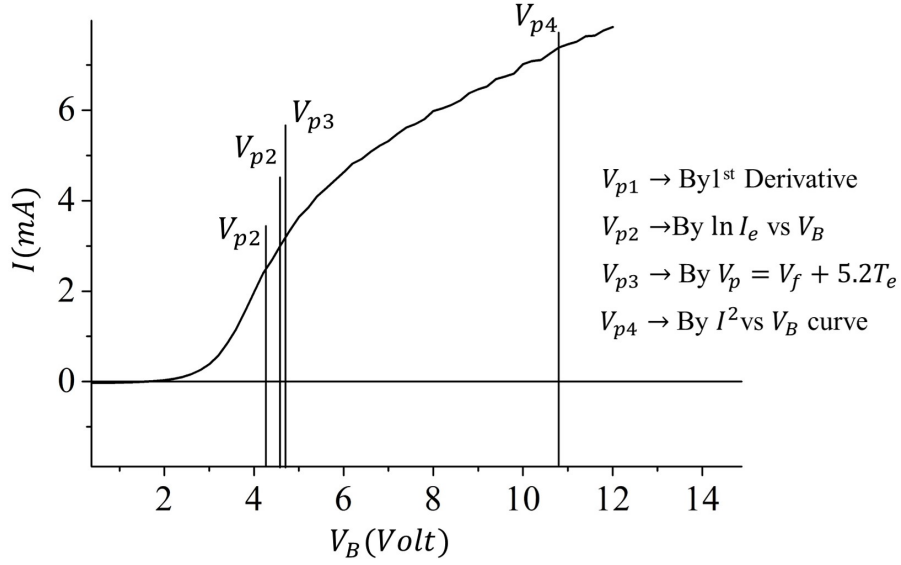


Figure 2.15: Comparison of plasma potential by different method. Here  $V_{p1}$  is obtained by 1st derivative of probe current,  $V_{p2}$  is obtained by locating the inflection point in semi-log plot of electron current,  $V_{p3}$  is obtained from floating condition of the probe and  $V_{p4}$  is obtained from OML theory.

wavelength parallel wire transmission line, whose one end is shorted and other end is open. Hence the structure resembles a hairpin as shown in fig-2.16(a). The probe is excited by coupling a small amplitude micro-wave signal to a loop antenna, placed adjacent to the short-circuited end of the hairpin. The probe exhibits resonance at a particular value of frequency, typically in GHz range, such that its quarter wavelength becomes equal to the physical length  $l$  of the hairpin and a standing wave is supported between its two ends. This can be understood from its mechanical analog- the tuning fork experiment. In this case a loud sound is produced when the length of the air column  $L_n$  becomes multiple of the quarter wavelength  $(2n + 1)\frac{\lambda}{4}$  of the sound wave.

The propagation constant  $k$  corresponding to the wavelength  $\lambda$  along the length  $l$  of the hairpin is given by;

$$k = \frac{\omega}{c} \sqrt{\epsilon_p} = \frac{2\pi}{\lambda} \quad (2.10)$$

Here  $c$  is speed of light,  $\omega = 2\pi f_r$  is angular frequency and  $\epsilon_p$  is the relative permittivity of the medium surrounding the hairpin.

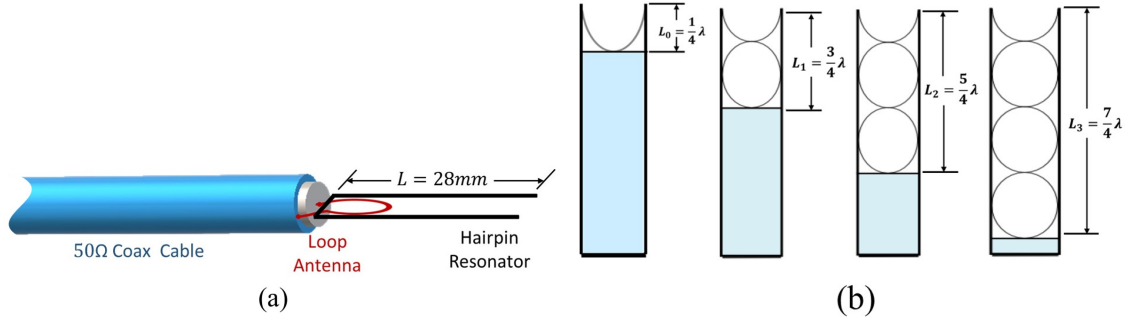


Figure 2.16: (a) The schematic of floating hairpin resonator probe and (b) The organ pipe experiment showing the standing wave pattern due to resonance

If the probe is immersed in a dispersive plasma medium, it gives rise to resonance at a frequency  $f_r$  such that the resonance condition  $\lambda = 4l$  is satisfied. Substituting the resonance condition  $\lambda = 4l$  in (2-10), we get;

$$f_r = \frac{c}{4l\sqrt{\epsilon_p}} = \frac{f_0}{\sqrt{\epsilon_p}} \quad (2.11)$$

Here  $f_0 = c/4l$  is resonance frequency in the vacuum ( $\epsilon_p = 1$ ).

Thus the resonance frequency  $f_r$  is inversely proportional to the square root of the relative permittivity of plasma medium  $\epsilon_p$ . It is also inversely proportional to the length of the hairpin. In the collision-less limit, the plasma permittivity  $\epsilon_p$  is related to electron plasma frequency  $f_p$  by  $\epsilon_p = 1 - (f_p^2/f_r^2)$ ; which on substituting in (2-11), we get;

$$f_p^2 = f_r^2 - f_0^2 \quad (2.12)$$

Here,  $f_p = (n_e e^2 / 4\pi^2 \epsilon_p m_e)^{1/2}$  is electron-plasma frequency.

From equation (2-12), it is straightforward to determine the electron density  $n_e$  by measuring  $f_r$  and  $f_0$  in the experiment and substituting in the formula:

$$n_e = \frac{f_r^2 - f_0^2}{0.81} \times 10^{16} m^{-3} \quad (2.13)$$

Here  $f_r$  and  $f_0$  are in GHz.

### 2.4.1 Resonance signal determination

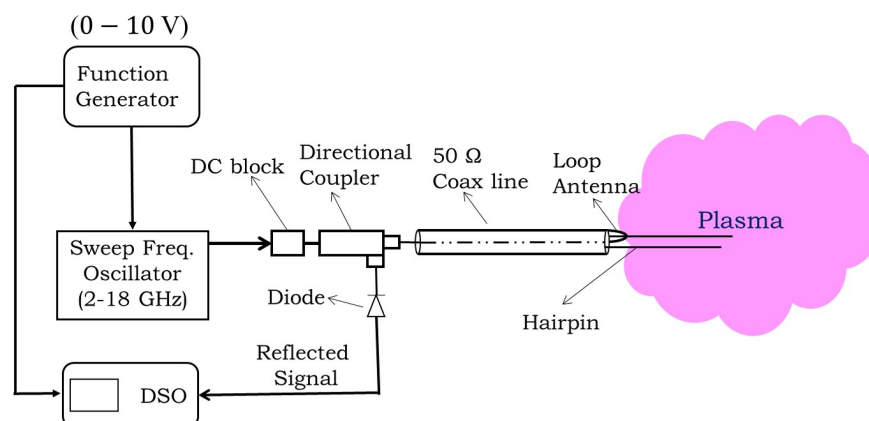


Figure 2.17: Schematic of the floating hairpin measurement circuit

Fig-(2-17) gives the schematic of resonance detection circuit for hairpin probe. The probe is excited by varying the microwave frequency in the loop antenna, typically in the range of 2.0 to 4.0 GHz. For this purpose, a voltage controlled YIG oscillator (VCO) is used, which provides a variable frequency from 2.0 GHz to 18.0 GHz by controlling the input voltage between 0 – 10 volt. A  $50\Omega$  coax line carries the microwave signal from the YIG oscillator to the loop antenna via a directional coupler. At the resonance frequency  $f_r$ , a strong coupling takes place between the loop antenna and the hairpin; and gives rise to maximum power transfer, hence the reflected rms signal undergoes a minimal. The corresponding resonance frequency is determined by observing the minima of the reflected signal using the directional coupler and a Schottky diode (PE 2210-10). The rms value of the reflected microwave signal is acquired in a digital storage oscilloscope (DSO Tektronix 3034C).

Fig-2-18(a) shows the rms value of reflected microwave signal (red) when the probe tip is in vacuum. The observed peak in the reflected signal corresponds to the vacuum resonance frequency  $f_0 = 2.46$  GHz on the X-axis. The length of the hairpin is  $l = 30.0$  mm, corresponding to which the vacuum resonance frequency can

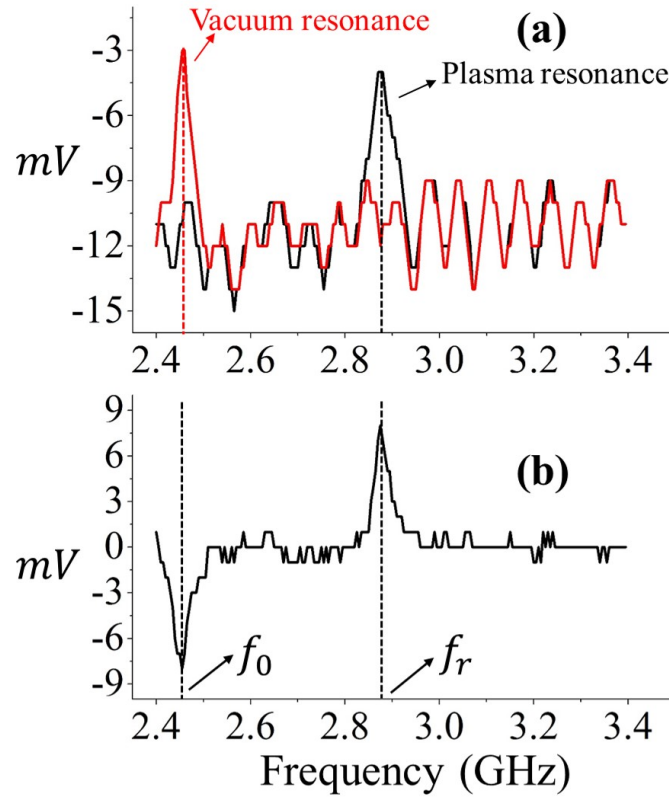


Figure 2.18: (a) The reflected signal by hairpin probe when the probe is in vacuum (red) and in plasma medium (black). (b) the reflected signal subtracted from the vacuum resonance signal. The typical discharge parameters are  $P = 1.4$  Pa &  $P_w = 17.2$  W.

be found from (2-11) as  $\sim 2.50$  GHz. This is close to the experimentally measured value. In presence of plasma, the resonance peak shifts to a higher frequency at  $f_r = 2.72$  GHz (black), since  $\epsilon_p < 1$ . In the fig-2.18(b), the resonance frequency signal corresponding to  $f_r$  has been subtracted from the signal acquired in the absence of plasma. Therefore the vacuum resonance frequency  $f_0 = 2.46$  GHz corresponds to downward peak in the above plot. Once  $f_0$  and  $f_r$  are measured, the electron density  $n_0$  can be determined from (2-13).

Figure-2.19 plots the electron density for a typical argon plasma discharge. The electron density is found to increase with power and pressure. The error in determining the resonance frequency is about 3MHz, corresponding to which the error in measured value of electron density is found to be around  $\sim 2$  to  $\sim 4$  %.

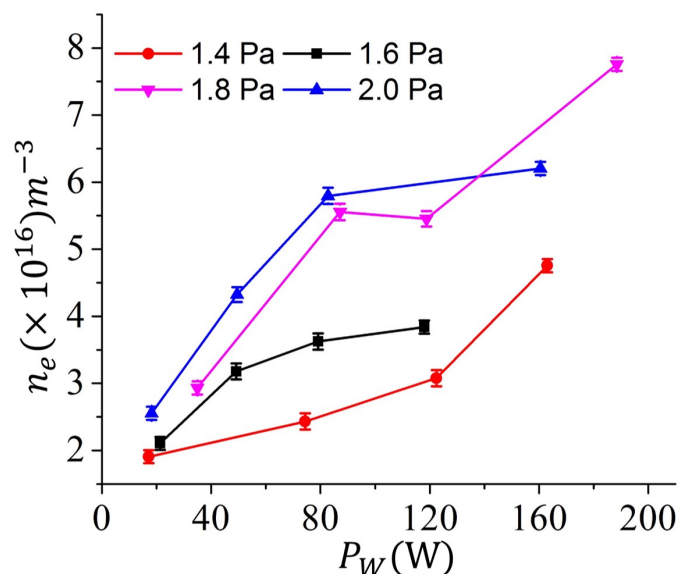


Figure 2.19: The electron density measurement with the help of a floating hairpin probe in argon plasma with regards to discharge power for a range of gas pressure.

## 2.4.2 Limitation of hairpin probe diagnostic

Though the hairpin probe is simple and straightforward technique to determine electron density, however it is unable to provide other plasma parameters in low pressure plasma. This limitation has therefore motivated researchers to broaden its scope by introducing additional refinements to the conventional hairpin [104, 105, 132–143]. For example Haas and Braitwaite et al [144], determined plasma potential by applying a DC potential to the hairpin. It was shown that the sheath around the hairpin gets reduced as it approaches towards the plasma potential. The authors also introduced a step-front-sheath model to calculate the sheath width [31]. Using this method the sheath capacitance around the cylindrical wire was determined and applied for the correction of electron density using hairpin probe. However, electron temperature required in the model as an input to the above method was separately measured by a Langmuir probe.

In-spite of above promising developments, application of hairpin probe to provide other plasma parameters in addition to electron density remains an outstanding problem. In chapter-6 a DC bias hairpin probe has been introduced to determine

electron temperature and negative ion concentration in oxygen discharge.





## Chapter 3

# Sheaths associated with Negative ion emitting Electrode

Negative ion emission from an electrode surface is a common phenomenon occurring in both laboratory as well as in industrial plasma devices. A few examples are oxides of metal ions generated from a sputtering target [98, 127, 145]; or the negative hydrogen ions emission from a substrate coated with low work-function element like cesium or barium in hydrogen negative ion source [90, 93, 118]. A major influence of negative ion emission is on the sheath potential structure; which can get modified due to a negative space charge created inside the sheath as similar to an electron emitting surface. Although electron emission from a hot cathode  $LaB_6$  plate of an ion source [146, 147] and electron emitting probes [52, 148, 149] have been widely reported, however negative ion emission from an electrode and its impact on positive ion flow towards the electrode surface has not been adequately addressed.

In this chapter, the space charge region in front of a planar, negative ion emitting electrode has been investigated theoretically by formulating a 1-dimensional fluid model, in which the emission flux and potential drop across the sheath have been varied independently. In particular, the effect of negative ion emission flux on the

potential distribution inside sheath and its impact on positive ion speed has been addressed.

In Section-3.1, a brief survey of various theoretical works pertaining to space charge region adjacent to a negative ion emitting electrode are presented. The analytical model and methodology to determine the potential structure inside the sheaths is then introduced in Section-3.2 for the case when; (i) emission is below the space charge limit and; (ii) when a virtual cathode is formed inside the sheath. The following sections-3.3 and 3.4 presents the impact of negative ion flux on the positive ion speed and sheath width respectively. A comprehensive discussion of results is given in section-3.5. Finally the major outcome of the chapter has been summarized in section-3.6.

### **3.1 Space charge region near a negative ion emitting electrode**

Sheath in front of a negative ion emitting surface has a major impact on the energy and flux of negative ions entering in to the bulk plasma region. In magnetron discharges, highly energetic metal oxygen ions have been detected by means of mass-energy analyzer system, positioned directly in front of the sputtering cathode target [150, 151]. These negative ions are the ones which are created at the target's sheath and travels towards the substrate. Likewise, in negative ion sources, cesium is deposited in the entire vacuum chamber walls and negative ion extracting grids; hence these surfaces become the local source of negative ion emitter in the discharge [90, 94]. These negative ions are transported towards the bulk plasma with a kinetic energy proportionate to the potential drop across the sheath [152]. Therefore the role of sheath in negative ion transport is a fundamental problem in context to the aforesaid applications.

One of the problem that directly affects the negative ion transport relates to

virtual cathode formation inside the sheath [18–22, 153]. The existence of virtual cathode is fundamentally similar to the negatively charged cloud inside the sheath as seen in the case of electron emitting surfaces and probes [17, 52, 149, 154]. However, the effect is expected to be much more pronounced in case of negative ion emission due to large mass ratio of negative ion to electron. Mc-Adams et al [18] addressed this problem by formulating a planar 1-dimensional model of sheath with negative ion emitting electrode as shown in figure-3.1.

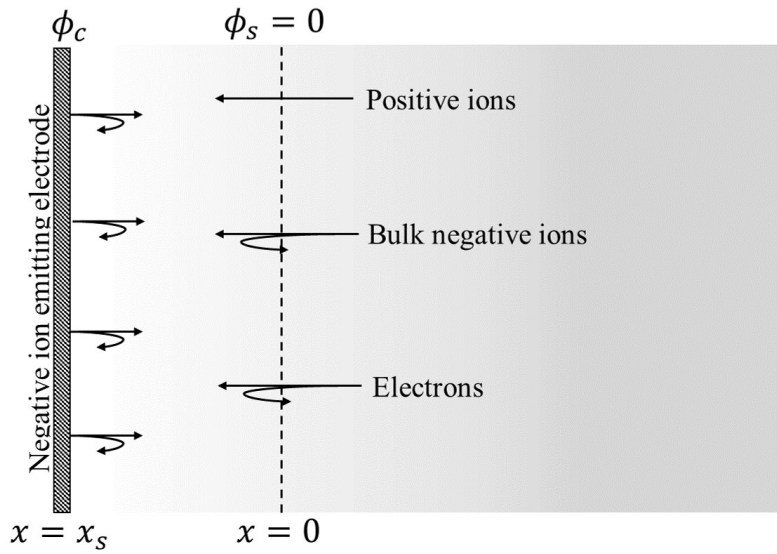


Figure 3.1: A schematic of sheath in front of an electrode emitting negative ions. The arrows indicate the flow of surface produced negative ions and other plasma species such as electrons, volume negative ions and positive ions.

The model was based on a similar treatment as done for the case of electron emitting sheath by Amemiya [149]. Since negative charge density inside the sheath is approximately  $\sqrt{m_n/m_e}$  times greater than its corresponding value for an equivalent electron emitting sheath. Therefore, comparatively a lower negative ion emission flux would greatly change the monotonic nature of potential fall inside the sheath. Moreover, there will be a greater density contribution of negative ions in deciding quasi-neutrality condition at the plasma-sheath boundary compared to the equal flux of electron emission. Therefore, the Bohm flux for positive ions entering the sheath edge from the bulk plasma will also get influenced.

Referring to figure-3-1, the sheath edge has been defined at  $x = 0$ ; whereas the electrode is situated at  $x = x_s$ . The potential on the electrode  $\phi_c < 0$  is defined relative to the sheath edge ( $\phi_s = 0$ ) and is considered to be sufficiently large compared to the electron temperature ( $\phi_c \gg T_e$ ), so that a positive-ion rich sheath is developed in the region  $x > 0$ , up to  $x = x_s$ . The arrows respectively shows the direction of electrons, positive ions, bulk negative ions and surface produced negative ions. The curved arrows indicates a fraction of charged particles that are reflected or returned towards its origin.

One of the major findings by Mc-Adams [18] was formation of virtual cathode during negative ion emission from the electrode surface. This is schematically shown in figure-3.2.

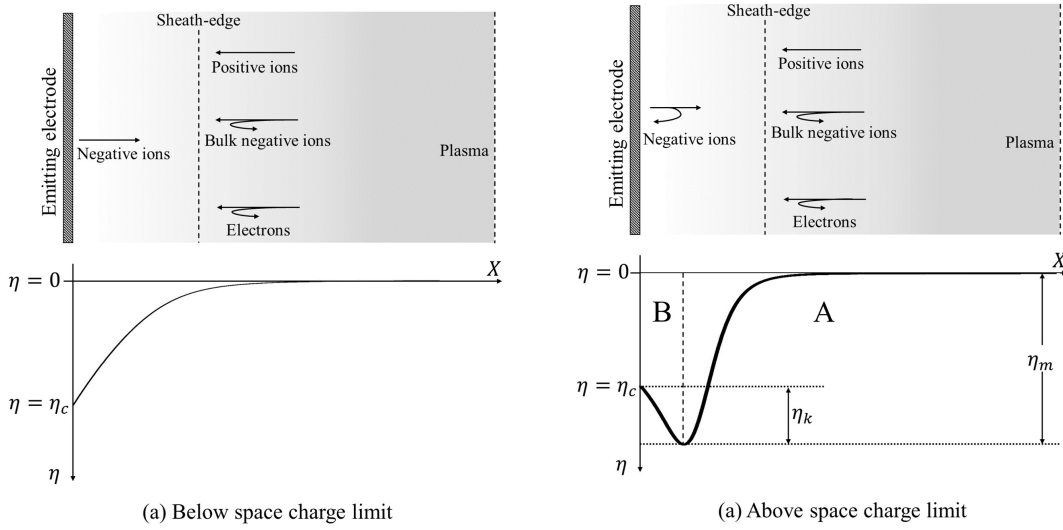


Figure 3.2: Schematic representation of potential distribution in front of a negative ion emitting electrode for the cases when (a) the emission is below the space charge limit and (b) above space charge limit. In the case (b) a virtual cathode of depth  $\eta_k$  is created, which separate the entire sheath into two region namely A & B. The potentials are normalized with electron temperature, i.e.  $\eta = e\phi/K_B T_e$

In the above figure, the potentials have been normalized with electron temperature. The electrode is at fixed potential  $\eta_c$ . The potential fall shown in fig-3.2(a) is initially monotonic but it modifies into a potential well or a virtual cathode having depth  $\eta_k = \eta_m - \eta_c$  with respect to the electrode as shown in fig-3.2(b) [region-B].

Outside this region, potential profile becomes monotonic again [region-A].

Potential distribution inside the sheath can be analytically found by solving the Poisson equation. The positive ion density inside the sheath can be expressed using flux and energy conservation across the sheath. On the other hand, electrons and volume negative ions are described by Boltzmann distribution [155]. When the potential fall is monotonic in nature as in fig-3.2(a), then negative ions emerging from the electrode surface will see an accelerating force towards the sheath boundary; whereas after the formation of virtual cathode as shown in fig-3.2(b), a fraction of the negative ions will get reflected towards the electrode surface from the potential minima  $\eta_k$  and eventually get absorbed at the electrode surface.

S Shah et al [19] demonstrated an analytical model of a negative ion emitting sheath by associating the negative ion production as a fraction of positive ions impinging the electrode surface; however, the scope of that study was limited for examining the behavior of multi-valued solution of sheath edge potential as a function of positive to negative ion conversion factor. Moreover, the model had a limitation as it did not account for negative ions production by energetic neutrals interacting with the electrode surface, which is usually a dominant mechanism in low pressure discharges [118]. The negative ions are actually emitted from low work function surfaces with finite spread in their energy, basically inherited from background neutrals and positive ions bombarding the surface [94]. Under normal conditions, the negative ion distribution at the surface can be considered to be Maxwellian [156] [see section-1.7.2 of Chapter-1].

In Mc Adams model, negative ion emission flux from the electrode surface was assumed to be an independent parameter [18]. While the model provided a limiting value of negative flux that could be transported across the sheath; however his simplistic model did not account for its impact on positive ion speed at the sheath edge.

The virtual cathode formation due to a negative ion emitting electrode had also been reported by D Wunderlich et al using particle-in-cell simulation of a plasma grid in  $H^-$  negative ion source [22]. The study mainly focused on space charge saturated emission of  $H^-$  &  $D^-$ , which was found to differ due to difference in their masses. PIC simulation study by S. Mochalskyy & A. F. Lifschitz [157] found that the virtual cathode limits the maximum extracted negative ion current from a plasma grid in the hydrogen negative ion source; whereas Osamu Fukumasa et al [158] showed that the extracted  $H^-$  current from a negative hydrogen ion source is also dictated by extraction potential on the grid and intrinsic parameters inside the bulk plasma.

For virtual cathode to exist, there are following three requirements;

- (1) The emerging flux of negative ions must exceed the space charge limited value. [18, 22].
- (2) The negative ions should be emitted with a finite energy from the electrode [94], and
- (3) The emitted flux of negative ions should have spread in their energy [156].

Because if the emitted negative ions are mono-energetic, then according to flux conservation equation, it may lead to an infinite density buildup in the virtual cathode not allowing the negative ions to reach at the sheath edge.

However the above studies did not reported: **(1)** how the entering speed of positive ions at the sheath boundary is affected due to negative ions emission from the electrode surface? **(2)** What is the effect of negative ion emission on the characteristic sheath width? **(3)** How the space charge limited current density will depend on the potential drop across the sheath?

To address the above mentioned points, this chapter briefly re-visits the underlying model by Mc Adams et al [18] for low pressure case, in which the sheath was assumed to be collision-less and the flux and energy of ions were assumed to be

conserved throughout the sheath region.

## 3.2 Analytical Model: Sheath with Negative Ion Emitting electrode

### 3.2.1 Potential distribution inside sheath below space charge limited emission

Referring to fig-3.1, density distribution of electrons and volume negative ions inside the sheath are described by Boltzmann distribution [100, 155]:

$$n_e = n_{es} \exp\left(\frac{e\phi}{K_B T_e}\right) \quad (3.1)$$

$$n_v = n_{vs} \exp\left(\frac{e\phi}{K_B T_v}\right) \quad (3.2)$$

where  $n_{es}$  and  $n_{vs}$  are density of electrons and volume negative ions respectively at the sheath edge;  $K_B$  is Boltzmann constant and  $T_{e,v}$  denotes respective temperatures of electrons and bulk/volume negative ions.

A constant flux  $j_n$  of negative ions having initial average kinetic energy  $E_b$  are assumed to be emitted from the electrode surface. These negative ions are accelerated towards the sheath boundary  $x = 0$  due to negative ion repelling potential  $\phi_c$  at the electrode. On the other hand, the cold positive ions ( $T_p \ll T_e$ ;  $T_p$  is positive ion temperature) with mass  $m_p$  enters the sheath edge at a finite speed  $v_{ps}$ , and are accelerated towards the electrode.

In the presence of potential field  $\phi(x) \equiv \phi$ , positive ion density density  $n_p(x) \equiv n_p$  and corresponding speed  $v_p(x) \equiv v_p$  can be derived from the following continuity and the momentum equations;

$$n_p \left(\frac{dv_p}{dx}\right) + v_p \left(\frac{dn_p}{dx}\right) = 0 \quad (3.3)$$

$$m_p n_p v_p \left( \frac{dv_p}{dx} \right) = -en_p \left( \frac{d\phi}{dx} \right) \quad (3.4)$$

Furthermore, if  $n_{nw}$  and  $n_{ns}$  are the respective densities of negative ions at the electrode surface (or wall) and at the sheath edge; then the flux  $j_n$  and energy  $E_b$  of these negative ions can be expressed accordingly as:

$$en_{nw}v_{nw} = en_{ns}v_{ns} = en_n(x)v_n(x) \equiv j_n \quad (3.5)$$

$$E_b - e\phi_c = \frac{1}{2}m_n v_n^2 - e\phi \quad (3.6)$$

In (3-5),  $v_{nw}$  and  $v_{ns}$  are respectively speed of negative ions at the electrode and the sheath edge.

From (3-6), negative ions speed  $v_n(x) \equiv v_n$  at any arbitrary location  $x$  and at the sheath boundary ( $v_{ns}$ ) can be obtained as:

$$v_n = \sqrt{\frac{2}{m_n} [E_b + e(\phi - \phi_c)]} \quad (3.7)$$

$$v_{ns} = \sqrt{\frac{2}{m_n} [E_b - e\phi_c]} \quad (3.8)$$

On substituting (3-7) and (3-8) in (3-5), the negative ion density  $n_n(x) \equiv n_n$  in the potential field  $\phi$  can be expressed in terms of  $\phi_c$  and  $E_b$  as;

$$n_n = n_{ns} \sqrt{(E_b - e\phi_c) / [E_b + e(\phi - \phi_c)]} \quad (3.9)$$

Furthermore, the quasi-neutrality condition is also satisfied at the sheath edge;

$$n_{ps} = n_{es} + n_{vs} + n_{ns} \quad (3.10)$$

Finally, the Poisson equation inside the sheath is given by;

$$\varepsilon_0 \frac{d^2\phi}{dx^2} = -e(n_p - n_n - n_v - n_e) \quad (3.11)$$



Introducing the following dimensionless quantities:

$$\begin{aligned}
N_{e,v,n,p} &= \frac{n_{e,v,n,p}}{n_{es}}, \alpha_s = \frac{n_{vs}}{n_{es}}, \beta_s = \frac{n_{ns}}{n_{es}}, \gamma_v = \frac{T_e}{T_v}, V_p = \frac{v_p}{c_s}, V_{ns} = \frac{v_{ns}}{c_s}, \\
c_s &= \sqrt{\frac{K_B T_e}{m_p}}, X = \frac{x}{\lambda_{Ds}}, X_s = \frac{x_s}{\lambda_{Ds}}, V_{ps} = \frac{v_{ps}}{c_s}, \eta = \frac{\phi}{T_e}, \eta_c = \frac{\phi_c}{T_e}, J_n = \frac{j_n}{en_{es}c_s}, \\
\varepsilon_b &= \frac{E_b}{T_e}, \mu_{pn} = \frac{m_p}{m_n} \quad (3.12)
\end{aligned}$$

In (3-12), densities are normalized by  $n_{es}$ , the speeds of ionic species are normalized with characteristic sound speed  $c_s$ , potentials  $\phi_c$  and  $\phi$  are normalized by electron temperature  $K_B T_e$  and the position coordinates  $x$  and  $x_s$  are normalized by Debye length  $\lambda_{Ds}$  defined at the sheath edge. Hence (3-1 to 3-11) reduces to dimensionless form as:

$$N_e = \exp(\eta) \quad (3.13)$$

$$N_v = \alpha_s \exp(\gamma_v \eta) \quad (3.14)$$

$$\frac{d}{dX} (N_p V_p) = 0 \quad (3.15)$$

$$V_p \frac{dV_p}{dX} = -\frac{d\eta}{dX} \quad (3.16)$$

$$N_n = \beta_s \left[ 1 + \frac{\eta}{(\varepsilon_b - \eta_c)} \right]^{-1/2} \quad (3.17)$$

$$\frac{d^2 \eta}{dX^2} = (N_n + N_v + N_e - N_p) \quad (3.18)$$

In (3-14) and (3-17),  $\alpha_s$  and  $\beta_s$  are the normalized densities of negative ions at the sheath edge, wherein  $\alpha_s$  corresponds to volume negative ions and  $\beta_s$  corresponds to surface produced negative ions. The parameter  $\gamma_v = T_e/T_v$  is the normalized electron temperature corresponding to volume negative ions.

The density  $\beta_s$  is related to the dimensionless negative ion flux  $J_n = j_n/en_{es}c_s$  as follows;

$$\beta_s = J_n (2\mu_{pn})^{-1/2} (\varepsilon_b - \eta_c)^{-1/2} \quad (3.19)$$

Where,  $\mu_{pn} = m_p/m_n$  is mass ratio of positive ion to the negative ion.

The positive ion density  $N_p$  in (3-18) can be obtained by integrating equation (3-15) and (3-16) with the boundary conditions;  $\eta(0) = 0, N_p(0) = N_{ps}$  and  $V_p(0) = V_{ps} \equiv U_B$ ; where  $U_B$  and  $N_{ps}$  is the dimensionless speed and density of positive ions at the sheath edge, respectively. Therefore, the Poisson's equation (3-18) can be rewritten in terms of the respective densities as follows:

$$\frac{d^2\eta}{dX^2} = e^\eta + \alpha_s e^{\gamma_v \eta} + J_n (2\mu_{pn})^{-1/2} [(\varepsilon_b - \eta_c) + \eta]^{-1/2} - \frac{N_{ps} U_B}{(U_B^2 - 2\eta)^{1/2}} \quad (3.20)$$

In (3-20), the positive ion density  $N_{ps}$  satisfies the quasi-neutrality condition at the sheath edge,

$$N_{ps} = 1 + \alpha_s + J_n (2\mu_{pn})^{-1/2} (\varepsilon_b - \eta_c)^{-1/2} \quad (3.21)$$

Integrating equation (3-20) with boundary condition  $\eta'(0) = 0$  gives the electric field inside the sheath as;

$$E(\eta) = \sqrt{2(e^\eta - 1) + 2\left(\frac{\alpha_s}{\gamma_v}\right)(e^{\gamma_v \eta} - 1) + B\left(\sqrt{1 + \frac{\eta}{(\varepsilon_b - \eta_c)}} - 1\right) + A\left(\sqrt{1 - \frac{2\eta}{U_B^2}} - 1\right)} \quad (3.22)$$

The parameters  $A$  and  $B$  are defined as;  $A = 2N_{ps}U_B^2$  and  $B = \frac{4J_n}{\sqrt{2\mu_{pn}}}\sqrt{\varepsilon_b - \eta_c}$ .

The Poisson's equation (3-20) can be solved to find the potential profile inside the sheath provided the appropriate boundary conditions are given. One of the important boundary condition is the entering speed for positive ions or Bohm speed  $U_B$  which is determined as follows.

### 3.2.2 The positive ion Bohm speed

The positive ion speed  $U_B$  corresponds to a minimal ion speed for which  $E(\eta) = 0$

at the sheath edge. Palacio et al [159] determined the Bohm speed by directly solving the matrix differential equation corresponding to (3-15) and (3-16) as;

$$\begin{bmatrix} N_p & V_p (dN_p/d\eta) \\ N_p V_p & N_p \end{bmatrix} \begin{bmatrix} dV_p/dX \\ d\eta/dX \end{bmatrix} = 0 \quad (3.23)$$

The above equation has a singularity at the plasma sheath boundary ( $\eta = 0$ ), which is determined by equating the determinant of the above matrix to zero, i.e.

$$N_p^2(\eta)|_{\eta=0} - \left[ N_p(\eta) V_p^2(\eta) \frac{dN_p(\eta)}{d\eta} \right] |_{\eta=0} = 0 \quad (3.24)$$

In the immediate vicinity of the sheath edge ( $\eta = 0$ ), it is possible to express  $N_p$  by assuming a quasi-neutral approximation:

$$N_p = \exp(\eta) + \alpha_s \exp(\gamma_v \eta) + \beta_s \left( 1 + \frac{\eta}{\varepsilon_b - \eta_c} \right)^{-1/2} \quad (3.25)$$

From (3-25),  $N_p(\eta)|_{\eta=0}$  and  $\frac{dN_p(\eta)}{d\eta}|_{\eta=0}$  are found in the limiting condition  $\eta \rightarrow 0$  and substituted in (3-24) to obtain the positive ion speed  $V_p(0) = U_B$  at the sheath edge as follows;

$$U_B = \sqrt{\frac{1 + \alpha_s + \beta_s}{1 + \alpha_s \gamma_v - \frac{\beta_s}{2} (\varepsilon_b - \eta_c)^{-1}}} \quad (3.26)$$

In (3-26),  $U_B$  is modified Bohm speed of positive ions due to a negative ion emitting electrode.

Furthermore, the parameter  $\beta_s$  expressed in terms of negative ion flux  $J_n = \beta_s V_{ns}$  [c.f. (3-19)]; will give

$$U_B = \sqrt{\frac{1 + \alpha_s + \frac{J_n}{\sqrt{2\mu_{pn}}} (\varepsilon_b - \eta_c)^{-1/2}}{1 + \alpha_s \gamma_v - \frac{J_n}{2\sqrt{2\mu_{pn}}} (\varepsilon_b - \eta_c)^{-3/2}}} \quad (3.27)$$

Where  $V_{ns} = \sqrt{2\mu_{pn}} (\varepsilon_b - \eta_c)^{1/2}$  [c.f. (3-8)] is negative ion speed at the sheath

edge. From (3-27), it can be seen that the Bohm speed  $U_B$  not only depends on the negative ion flux  $J_n$  and initial energy  $\varepsilon_b$  but it is also a function of the electrode potential  $\eta_c$ . On substituting  $J_n = 0$  (i.e. in absence of emission), equation (3-27) reduces to the Bohm speed  $U_B = \sqrt{\frac{1+\alpha_s}{1+\alpha_s\gamma_v}}$  in an electronegative plasma [11]. On further substituting  $\alpha_s = 0$ , one can obtain the original Bohm speed ( $U_B = 1$ ) for the case of a pure electro-positive plasma [10].

### 3.2.3 Space Charge Limited Current

The Poisson's equation (3-20), being a second order differential equation, requires two boundary conditions which are given as  $\eta(0) = 0$  and  $\eta(X_s) = \eta_c$ . Since  $X_s$  is unknown, therefore (3-20) can be iteratively solved with above boundary condition to find a value of  $X_s$  until it satisfies the condition  $\eta'(0) = 0$ , i.e the electric field at the sheath edge must vanish.

Fig-3.3 shows some typical plots of spatial potential distribution for  $J_n = 0, 0.7$  and  $0.95$ . The electrode potential in the model has been fixed at  $\eta_c = -10$ . From the plot, it can be seen that the potential falls monotonically towards the electrode. However at a particular value of  $J_n \equiv J_{nmax} = 0.95$ , the electric field  $E_c$  at the electrode surface becomes zero i.e. the derivative  $(-d\eta/dX)$  at  $\eta = \eta_c$  vanishes at the electrode surface. This is familiar Child-Langmuir limit for space charge limited condition [160]. The flux  $J_{nmax}$  is the maximum negative ion flux below which all negative ions emitted from the electrode can cross the sheath and eventually reach at the sheath boundary.

On substituting  $E_c = 0$  in equation (3-22), the corresponding value of  $J_{nmax}$  can be obtained as;

$$J_{nmax} = \frac{N_{ps}U_B^2 \left[ \left(1 - \frac{2\eta_c}{U_B^2}\right)^{1/2} - 1 \right] + (e^{\eta_c} - 1) + \left(\frac{\alpha_s}{\gamma_v}\right) (e^{\gamma_v\eta_c} - 1)}{2(2\mu_{pn})^{-1/2} (\varepsilon_b - \eta_c)^{1/2} \left[ 1 - \left(1 + \frac{\eta_c}{(\varepsilon_b - \eta_c)}\right)^{1/2} \right]} \quad (3.28)$$

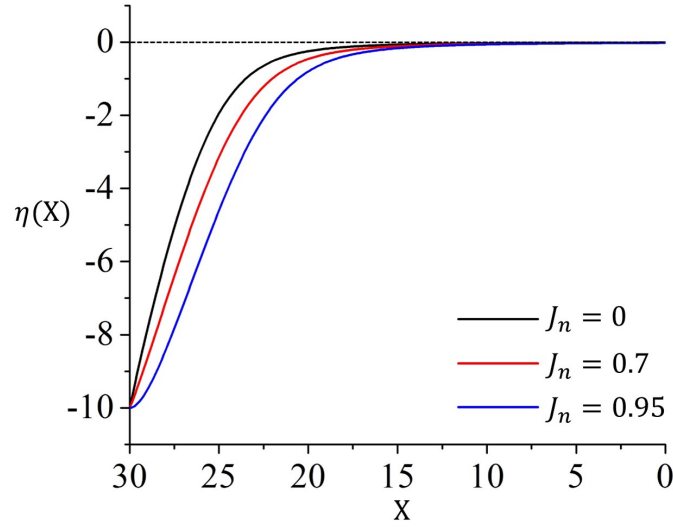


Figure 3.3: Spatial distribution of potential inside the negative ion emitting sheath for three distinct values of  $J_n = 0, 0.7$  and  $0.95$ . The parameter used here are  $\eta_c = -10, \varepsilon_b = 0.2$  and  $\alpha_s = 0$

It is seen that in (3-28), both  $N_{ps}$  and  $U_B$  are also a function of  $J_{nmax}$  [c.f. (3-21) & (3-27)]. Therefore for a given set of parameters ( $\varepsilon_b$  and  $\eta_c$ ), equation (3-28) can be numerically solved to obtain a unique value of  $J_{nmax}$ . Once  $J_{nmax}$  is known, then it is possible to find the density  $N_{ps}$  and the positive ion speed  $U_B$  corresponding to space charge limit by substituting  $J_n = J_{nmax}$  in (3-21) and (3-27) respectively.

### 3.2.4 Transported negative ion flux above the space charge limiting current

The case refers to the situation when  $J_n > J_{nmax}$ ; that is when the injected flux of negative ions from the electrode is greater than the space charge limiting value. In this situation, a virtual cathode of depth  $\eta_k$  near the electrode surface is formed, as is shown schematically in fig-3.2(b). Due to presence of virtual cathode, only a fraction of the emitted negative ion flux  $J_{nvc}$ , whose energy is greater than  $\eta_k$ , will be able to cross the potential minima to reach at the sheath edge.

In the region between the electrode surface and potential minima, since the neg-

ative ions experiences a repulsive potential. Therefore, the flux  $J_{nvc}$  reaching at the potential minima with average energy  $\varepsilon_b$  can be described by an exponentially falling function of  $\eta_k$  [18]. This is related to the injected negative ion flux  $J_n$  through the relation;

$$J_{nvc} = J_n e^{\eta_k} \quad (3.29)$$

In order to determine the transported negative ion flux  $J_{nvc}$  across the sheath, let us assume a hypothetical electrode [shown by the vertical dashed line in fig-3.2(b)], having a potential  $\eta_m$  defined with respect to the sheath edge such that  $\eta_m = \eta_c + \eta_k$ . The dashed line separates the sheath in to two distinct regions. On the right of virtual electrode (Region-A), a monotonic fall in potential is observed between potential minima and the sheath edge. On the left (Region-B), the potential rises towards the electrode.

Since the electric field at the minima of virtual electrode is zero, therefore this situation is similar to space charge limited value  $J_{nmax}$ , as if the electrode is virtually shifted at the potential minima  $\eta_m$  and it emits negative ions with flux  $J_{nvc}$ . The flux  $J_{nvc}$  shall remain conserved in the region-A. Therefore on replacing  $J_{nmax}$  and  $\eta_c$  in (3-28) by  $J_{nvc}$  and  $\eta_m$  respectively, the amount of transported negative ion flux  $J_{nvc}$  crossing the sheath for the case  $J_n > J_{nmax}$  can be obtained as;

$$J_{nvc} = \frac{N_{ps} U_B^2 \left[ \left( 1 - \frac{2\eta_m}{U_B^2} \right)^{1/2} - 1 \right] + (e^{\eta_m} - 1) + \left( \frac{\alpha_s}{\gamma_v} \right) (e^{\gamma_v \eta_m} - 1)}{2 (2\mu_{pn})^{-1/2} (\varepsilon_b - \eta_m)^{1/2} \left[ 1 - \left( 1 + \frac{\eta_m}{(\varepsilon_b - \eta_m)} \right)^{1/2} \right]} \quad (3.30)$$

It is to be noted that average energy of negative ions  $\varepsilon_b$  remain unchanged while moving from electrode surface to potential minima. This is because of the fact that the average energy corresponding to a Maxwellian distribution moving through a retarding potential remains constant [161]. Thus for a given values of  $J_n$  and  $\varepsilon_b$  at the electrode, equations (3-29) and (3-30) can be simultaneously solved to obtain

$J_{nvc}$  and  $\eta_k$ .

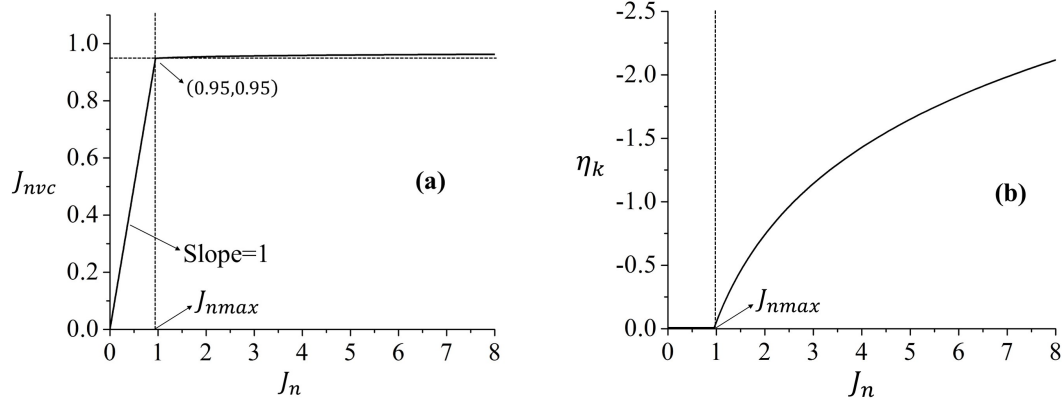


Figure 3.4: Plot of (a) negative ion flux  $J_{nvc}$  transported at the sheath edge and (b) depth of the potential minima as a function of  $J_n$ . The parameters used are  $\varepsilon_b = 0.2$ ,  $\alpha_s = 0$  and  $\eta_c = -10$ .

Fig-3.4 shows the plot for (a) transported flux  $J_{nvc}$  and (b) the virtual cathode depth  $\eta_k$  as a function of emitted flux  $J_n$  from the electrode. From fig-3.4(a), it is seen that on increasing the injected negative ion flux  $J_n$  from the electrode surface, the transported flux  $J_{nvc}$  increases linearly up to a critical value  $J_{nmax} = 0.95$ . This marks the origin of the virtual cathode inside the sheath. In this limit no potential well exist, as  $\eta_k = 0$  observed in fig-3.4(b). The slope = 1 observed in  $J_{nvc}$  vs  $J_n$  plot suggests that all the emitted flux is transported totally across the sheath when the emission is below the space limited value. However, as soon as the injected negative ions crosses the space charge limiting current value, i.e.  $J_n > J_{nmax}$ , there is a monotonic increase in  $\eta_k$  as  $J_n$  increases. On the other hand, there is only a marginal increase in transported flux of negative ion across the sheath. The reason is because the potential well only allows a fraction ( $J_{nvc}/J_n$ ) of energetic negative ions to cross the potential well, which is an exponentially falling function of depth  $\eta_k$  [c.f. (3-29)]. This phenomena is also commonly observed in the case of an electron emitting surfaces [149, 154].

Likewise, below space charge limited emission i.e.  $J_n < J_{nmax}$ , the density  $\beta_s$  transported to the sheath edge increases linearly with  $J_n$ ; as  $\beta_s = J_n \times \text{Const}$  [c.f.(3-

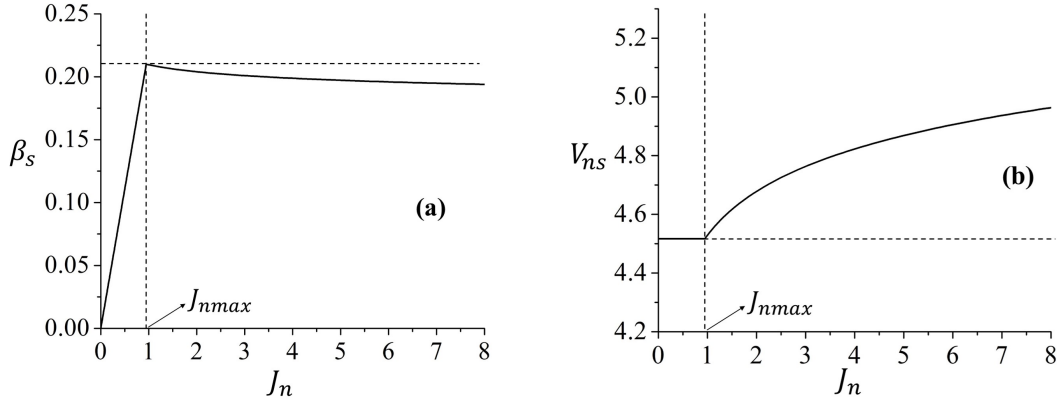


Figure 3.5: The plots showing (a) density  $\beta_s$  and (b) speed  $V_{ns}$  of transported negative ions at the sheath edge. The typical parameters are  $\varepsilon_b = 0.2$ ,  $\alpha_s = 0$  and  $\eta_c = -10$ .

19)]. However, it continues to decrease when  $J_n > J_{nmax}$ . In this case negative charged density  $\beta_s$  depends on  $J_{nvc}$  by the relation  $\beta_s = J_{nvc} (2\mu_{pn})^{-1/2} (\varepsilon_b - \eta_m)^{-1/2}$ . The overall variation in  $\beta_s$  as a function of  $J_n$  is shown in fig-3.5(a).

Similarly as shown in fig-3.5(b), the negative ion speed  $V_{ns}$  at the sheath edge remains essentially constant for  $J_n < J_{nmax}$  as  $V_{ns} = (2\mu_{pn})^{1/2} (\varepsilon_b - \eta_c)^{1/2}$ ; but it increases for the case  $J_n > J_{nmax}$  to commensurate with the increase in depth of the potential well  $\eta_k$ .

### 3.2.5 Potential distribution due to virtual cathode

The virtual cathode separates the entire sheath into two regions; (a) the region between the sheath edge and minima of virtual cathode and (b) region between the virtual cathode to the electrode. Hence to get the entire spatial potential distribution between the emitting electrode and the sheath edge, the potential distribution obtained independently in these regions are stitched together.

**(a) Potential distribution between sheath-edge and the potential minima of virtual cathode (i.e.  $0 < \eta(X) < \eta_m$ )**

This is the region between a permeable hypothetical electrode situated at the



potential minima of virtual cathode and the sheath edge. The potential of the hypothetical electrode can be assigned as  $\eta_m = \eta_c + \eta_k$ , in which  $\eta_k$  is already determined in figure-3.5(b). Considering  $J_{nvc}$  as the negative ion flux crossing the virtual cathode with average energy  $\varepsilon_b$ , then Poisson's equation-(3-20) is iteratively solved to obtain the spatial potential distribution inside the sheath, with the new boundary condition  $\eta(0) = 0$  and  $\eta(X_v) = \eta_m$ ; where  $X_v$  is the position of virtual cathode with respect to sheath edge. The position  $X_v$  is uniquely determined by inspecting the electric field at the potential minima  $\eta'(X_v) = 0$ .

**(b) Potential distribution between virtual cathode and electrode (i.e.  $\eta_m < \eta(X) < \eta_c$ )**

The electrons and volume negative ions enters the region-B and see an accelerating potential ( $\eta_c - \eta_m$ ) towards the electrode. Therefore the speed of the electrons will vary according to,

$$v_e^2 = \langle v_e \rangle^2 - \frac{2e(\phi_m - \phi)}{m_e} \quad (3.31)$$

Where,  $\langle v_e \rangle = \sqrt{\frac{8K_B T_e}{\pi m_e}}$  is average thermal speeds of electrons. At the potential minima, thermal flux of electrons is given by;

$$j_e = \frac{1}{4} e n_{es} \exp\left(\frac{\phi_m}{T_e}\right) \langle v_e \rangle \quad (3.32)$$

Since the electron flux  $j_e$  is continuous throughout the sheath, therefore from (3-31) and (3-32), the electron density  $n_e(x)$  in this region is obtained on dividing  $j_e$  by  $e v_e(x)$ ;

$$n_e(x) = \frac{j_e}{e v_e(x)} \quad (3.33)$$

In the dimensionless form, it is given by;

$$N_e(X) = \frac{1}{4} \left[ 1 - \frac{\pi}{4} (\eta_m - \eta) \right]^{-1/2} \exp(\eta_m) \quad \text{for} \quad \eta_m < \eta(X) < \eta_c \quad (3.34)$$

A similar consideration also applies to volume negative ions, which is expressed in normalized form as follows;

$$N_v(X) = \frac{1}{4} \frac{\alpha_s}{\sqrt{\gamma_v}} \left[ 1 - \frac{\pi}{4} \gamma_v (\eta_m - \eta) \right]^{-1/2} \exp(\gamma_v \eta_m) \quad \text{for } \eta_m < \eta(X) < \eta_c \quad (3.35)$$

The negative ion density in the region  $\phi_m < \phi(X) < \phi_c$  is obtained from flux conservation as;

$$n_n(x) = \frac{j_n \exp\left(\frac{\phi - \phi_c}{T_e}\right)}{e (2E_b/m_n)^{1/2}} \quad (3.36)$$

In the dimensionless form, it is given by;

$$N_n(X) = \frac{J_n \exp(\eta - \eta_c)}{\varepsilon_b^{1/2} (2\mu_{pn})^{1/2}} \quad (3.37)$$

In contrast to above, positive ions experience a repelling potential  $(\eta_c - \eta_m)$ . Therefore from the ion flux conservation, positive ion density can also be expressed in the normalized form as follows:

$$N_p(X) = \frac{N_{ps} U_B}{(U_B^2 - 2\eta)^{1/2}} \quad (3.38)$$

In (3-38)  $N_{ps}$  and  $U_B$  are expressed according to the equation (3-21) and (3-27) respectively, in which  $\eta_c$  has been replaced by  $\eta_m$  and  $J_n$  by  $J_{nvc}$ , i.e.

$$N_{ps} = 1 + \alpha_s + \frac{J_{nvc}}{\sqrt{2\mu_{pn}}} (\varepsilon_b - \eta_m)^{-1/2} \quad (3.39)$$

$$U_B = \sqrt{\frac{1 + \alpha_s + \frac{J_{nvc}}{\sqrt{2\mu_{pn}}} (\varepsilon_b - \eta_m)^{-1/2}}{1 + \alpha_s \gamma_v - \frac{J_{nvc}}{2\sqrt{2\mu_{pn}}} (\varepsilon_b - \eta_m)^{-3/2}}} \quad (3.40)$$

Equation (3-39) and (3-40) gives the normalized values of density and speed for positive ions at the sheath edge when virtual cathode has formed. Hence the potential distribution in the region  $\eta_m < \eta(X) < \eta_c$  is found by solving the Poisson's

equation (3-20) iteratively with the boundary condition  $\eta(X_v) = \eta_m$  and  $\eta(X_s) = \eta_c$ . It gives an unique value of  $X_s$  such that  $\eta'(X_v) = 0$  is simultaneously satisfied.

Fig-3.6 shows a typical plot of potential distribution inside the sheath for three

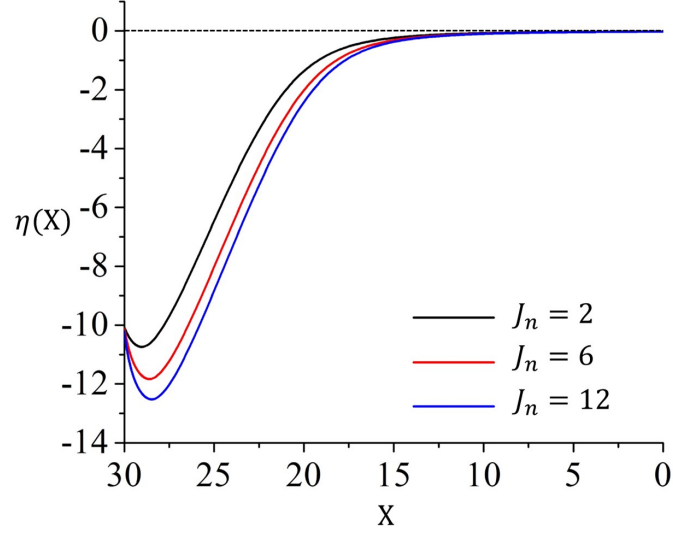


Figure 3.6: The plot of potential distribution inside the sheath for  $J_n = 2, 6$  and  $12$ . The parameter used here are  $\eta_c = -10$ ,  $\varepsilon_b = 0.2$  and  $\alpha_s = 0$ . The electrode position is defined at  $X = 30$ .

distinct values of  $J_n = 2, 6$  and  $12$ . The electrode potential is kept fixed at  $\eta_c = -10$ . As can be seen from the figure, the depth of the potential minima  $\eta_k$  increases with  $J_n$  in order to accommodate more negative ions inside the sheath. It is also seen that the position of potential minima shifts away from the emitting electrode on increasing  $J_n$ , as it requires a greater distance to accommodate a higher negative ion flux inside the sheath.

### 3.3 Bohm speed during Negative Ion Emission from the electrode

Equation (3-27) & (3-40) respectively provides the Bohm speed  $U_B$  for the case  $J_n < J_{nmax}$  (below the space charge limit) &  $J_n > J_{nmax}$  (above the space charge limit). A similar result was also obtained by Palacio et al [159] and Amemiya et

al [149] for the case of an electron emitting electrode. However their results were restricted below space charge limiting current.

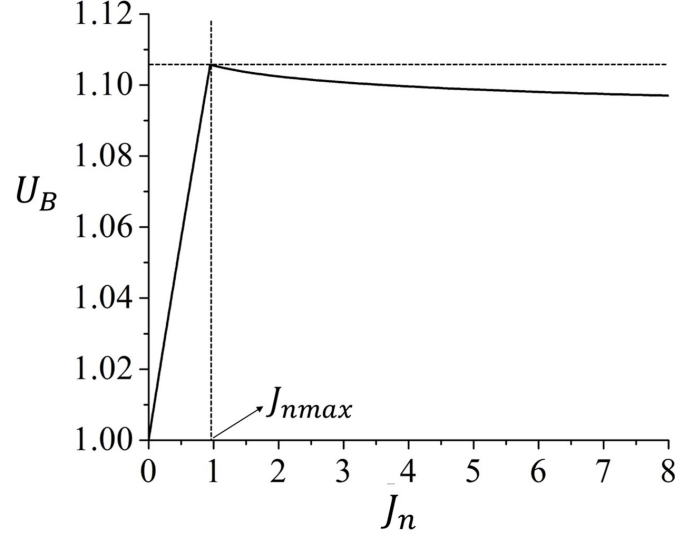


Figure 3.7: The variation of Bohm speed  $U_B$  of positive ions as a function of emitted flux  $J_n$ . The typical parameters are  $\varepsilon_b = 0.2$  and  $\alpha_s = 0$ . The electrode is at constant potential  $\eta_c = -10$

Figure-3.7 plots the Bohm speed  $U_B$  as a function of negative ion flux  $J_n$ . It is seen that  $U_B$  increases linearly with  $J_n$  below the space charge limit i.e.  $J_n < J_{nmax}$ . Above this limit  $U_B$  decreases slightly and then it attains a constant value as  $J_n$  increases.

The reason for observing a linear rise in  $U_B$  in the limit  $J_n < J_{nmax}$  can be explained on the basis of quasi-neutrality requirement at the sheath boundary. As observed from fig-3.5(a), since the parameter  $\beta_s$  at the sheath edge increases linearly with  $J_n$ ; therefore the normalized positive ion density  $N_{ps}$  at the sheath edge should also increase according to quasi-neutral equilibrium;  $N_{ps} \equiv n_{ps}/n_{es} = 1 + \alpha_s + \beta_s$ . If contribution of volume negative ions at the sheath edge is neglected temporarily, i.e.  $\alpha_s = 0$ , then the normalized positive ion density ratio  $N_{ps} = n_{ps}/n_{es}$  at the sheath edge would also vary linearly, as the negative ion emission flux  $J_n$  increases. Hence to maintain a constant positive ion density at the sheath edge, it requires that the

electron density should proportionately decrease at the sheath edge,

$$n_{ps}(constant) = n_{es}(\downarrow) + n_{ns}(\uparrow) \quad (3.41)$$

The electron density and potential at the sheath edge is related by the Boltzmann distribution i.e.  $n_{es} \sim \exp(\eta)$ . Thus a fall in electron density at the sheath edge will be associated with a corresponding increase in the magnitude of  $\eta$  (in a small boundary layer close to the sheath edge).

Whereas, in the limit when  $J_n > J_{nmax}$ ,  $\beta_s$  at the sheath edge decreases [see fig-3.5(a)]. Therefore according to (3-41), electron density should correspondingly increase. The increase in electron density at the sheath edge requires a lower potential drop within an infinitesimally small region close to the sheath. This potential could alter the positive ion speed at the sheath entrance.

The above observations suggest that the variation in positive ion Bohm speed due to negative ion emission depends on the electron density at the sheath edge, which is actually associated with the potential drop across quasi-neutral pre-sheath region. In Chapter-4, a more detail description of the positive ion speed at the sheath boundary is provided, which analyze the pre-sheath region that is responsible for the acceleration of positive ions towards the sheath boundary.

Fig-3.8(a) & (b) shows the effect of electrode potential  $\eta_c$  on density  $\beta_s$  and speed  $V_{ns}$  of negative ions at the sheath edge for a constant flux  $J_n$ . The corresponding variation in Bohm speed has been plotted in fig-3.8(c). It is seen that the speed  $V_{ns}$  increases monotonically with  $\eta_c$ . According to the flux conservation  $J_{nvc} = \beta_s V_{ns}$ , it is then expected that the negative ion density  $\beta_s$  should fall at the sheath edge which is observed in fig-3.8(a). As a result, the corresponding value of  $N_{ps} = 1 + \beta_s$  will also reduce.

The above condition can be satisfied only if electron density  $n_{es}$  increases at the

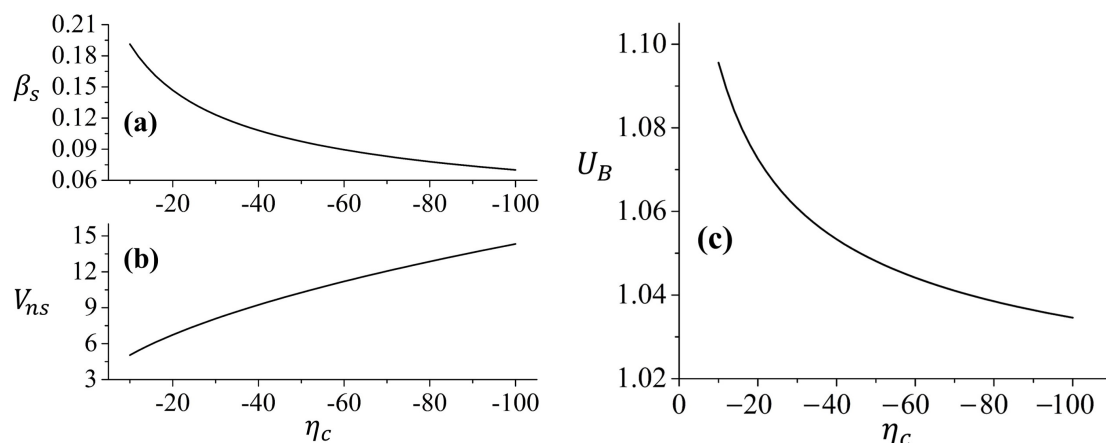


Figure 3.8: The variation of (a) the negative ion density  $\beta_s$  (b) the speed  $V_{ns}$  and (c)  $U_B$  as a function of electrode potential  $\eta_c$  for constant initial energy  $\varepsilon_b = 0.2$  and flux  $J_n = 12$ .

sheath edge, which demands for a smaller potential drop within the small region close to the sheath edge. Consequently positive ions at the sheath edge  $U_B$  should also reduce as seen fig-3.8(c).

### 3.4 Sheath width characteristics

The 1-dimension model of sheath presented in section-3.2 can be applied to estimate the sheath width  $X_s$  in front of the negative ion emitting electrode. Here  $X_s$  is the normalized distance from the sheath edge up to the point where the potential approaches  $\eta_c$ . When the negative ion emission is above the space charge limit, the sheath width is found by summing the spatial distance of potential minima  $\eta_m$  from the sheath edge and the distance between the electrode and the potential minima.

In Fig-3.9(a), the sheath width  $X_s$  for a negative ion emitting electrode has been plotted (the solid line) as a function of the electrode potential  $\eta_c$ . It is found that the sheath width increases monotonically with negative potential  $\eta_c$  on the electrode. To compare the trend, the sheath width for a non-emitting electrode is also plotted which are calculated using approximate Child-Langmuir (CL) solution ( $U_B = 0$ )

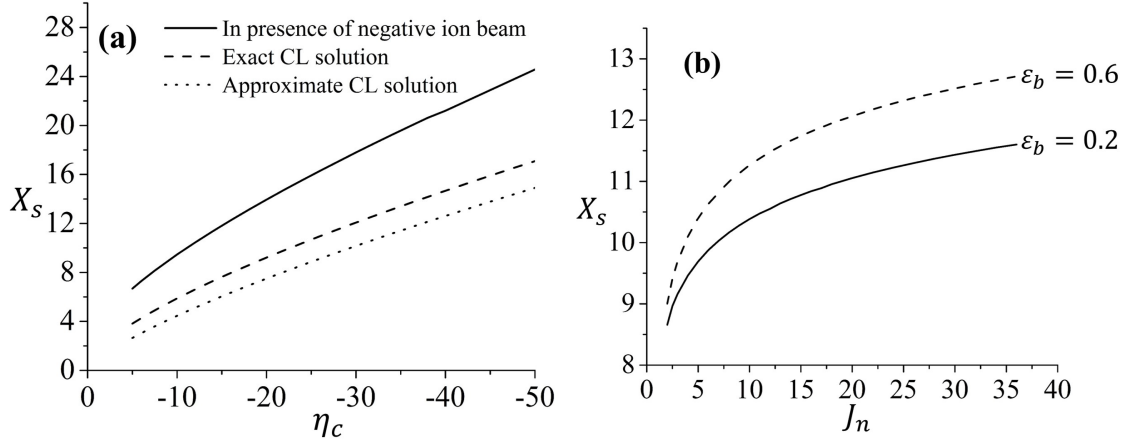


Figure 3.9: Variation of sheath thickness with respect to (a) electrode potential  $\eta_c$  for constant  $J_n = 4$  and  $\varepsilon_b = 0.2$  and (b) emitted negative ion flux  $J_n$  for a constant electrode bias  $\eta_c = -10$ . A comparison with Child-Langmuir (CL) sheath-width is shown; the dotted and the dashed curve correspond to the approximate CL solution ( $U_B = 0$ ) and exact CL solution ( $U_B \neq 0$ ) respectively. The typical parameters  $\alpha_s = 0$  is assumed.

and exact CL solution ( $U_B \neq 0$ ) respectively [11].

The dashed curve corresponds to the case  $J_n = 0$ , which is obtained by substituting the parameters  $A = 2$ ,  $B = 0$ ,  $N_{ps} = 1$  and  $U_B = 1$  in (3-22). This reduces the equation to  $d\eta/dX = \sqrt{2[(1 - 2\eta)^{1/2} - 1]}$ . On integrating with boundary condition  $\eta(0) = 0$  and  $\eta(X_s) = \eta_c$ , an analytical solution for the sheath width can be found as follows;

$$X_s = \sqrt{2}/3(2 + \sqrt{1 + 2\eta_c})\sqrt{-1 + \sqrt{1 + 2\eta_c}} \quad (3.42)$$

In the second case (dotted curve), positive ion speed at the sheath edge is neglected i.e.  $U_B = 0$ . This approximation reduces the above expression of  $X_s$  to the conventional Child-Langmuir law as,  $X_s^2 = (4\sqrt{2}/9)\eta_c^{3/2}$  [116]. The trend in  $X_s$  in case of emitting electrode resembles the conventional Child-Langmuir sheath width; however its magnitude is found to be consistently higher compared to non-emitting electrode [fig-3.9(a)]. The reason for observing a consistently higher sheath width for a negative ion emitting electrode can be qualitatively discussed as follows:

The emission of negative ions from an electrode can be considered as an equivalent positive ion current entering the sheath. As the analytical model suggests that the negative ion density at the sheath edge has a decreasing trend with increase in the electrode potential [fig-3.8(a)]. Hence the number density of positive ions at the sheath edge will also decrease in order to conserve the quasi-neutral equilibrium. However to shield the negative potential on the electrode effectively, the sheath must expand to bring in more positive ions inside the sheath region. As a result a higher sheath width is possible for a negative ion emitting electrode.

A similar argument can be also given for observing higher sheath width in fig-3.9(b) due to increase in initial average energy of negative ions. In this case, more number of negative ions can overcome the potential barrier of the virtual cathode to reach the sheath edge. As a result the negative ion contribution at the sheath edge increases, while the supply of positive charges to the electrode decreases. This results in the sheath expansion for shielding the potential at the electrode surface.

## 3.5 Discussion

The planar 1-D analytical model of a negative ion emitting electrode provides a simple link between flux and energy of the injected negative ion and the spatial potential distribution adjacent to the emitting electrode. This problem has relevance to plasma & ion extraction grids of a negative ion source.

G. I. Dimov et al [162] investigated the effect of negative ion emission in a penning type negative ion source, in which an independently biased emitter, as shown in figure-3.10(a), was considered. When the emitter surface was very close to the plasma ( $\delta = 0.1$  mm), it was reported that the transported flux of  $H^-$  ions from the emitter surface increases with the emitter bias and tends to saturate as the bias was further enhanced. A similar qualitative behavior has also been observed using



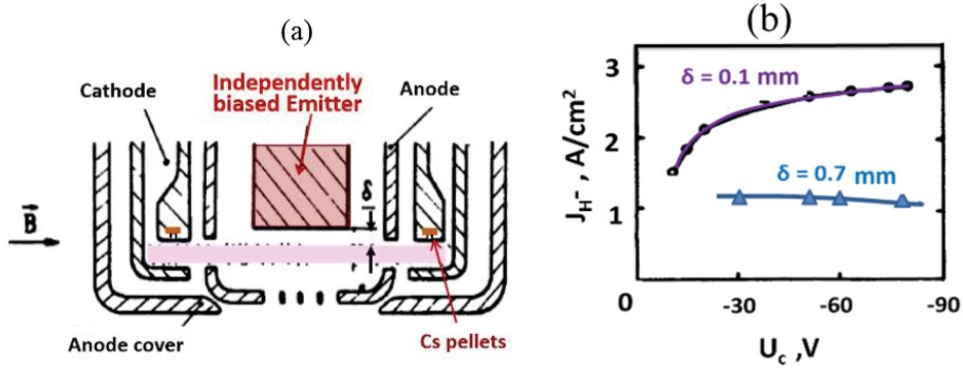


Figure 3.10: (a) The cross sectional view of a penning type negative ions source with an independent biased emitter placed at a variable spacing  $\delta$  from the plasma edge. (b) The extracted  $H^-$  current as a function of emitter bias  $U_c$  for two different spacing  $\delta = 0.1$  mm and 0.7 mm from the plasma column edge. *Courtesy: Belchenko, Y. I. et al (2018)*

our present 1-dimensional model shown in fig-3.11.

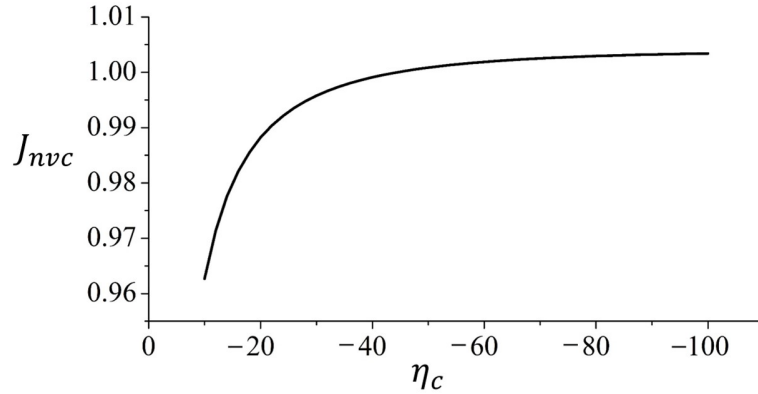


Figure 3.11: The variation of transported flux  $J_{nvc}$  of negative ions at the sheath edge as a function of electrode potential  $\eta_c$ . The injected flux  $J_n = 12$ ,  $\alpha_s = 0$  and initial kinetic energy  $\varepsilon_b = 0.2$  are assumed as parameter.

From the analytical model [c.f. 3-30], it can be seen that for a very large value of  $\eta_c$ , the transported negative ion flux  $J_{nvc}$  across the sheath tends to a value  $J_{nvc} \rightarrow (\sqrt{\mu_{pn}}) (1 + \alpha_s) \sqrt{(1 + \alpha_s) / (1 + \alpha_s \gamma_v)} = (\sqrt{\mu_{pn}}) \times (N_{ps} U_B)$ . This is found to be proportional to  $\sqrt{m_p/m_n}$  times the positive ion flux entering the sheath edge. Therefore, the analytical result predicts that the extraction of surface produced negative ions across the sheath is not only limited due to formation of virtual cathode

but it also greatly depends on the positive ion flux that is available at the sheath edge. Hence, merely by increasing negative ion emission from the electrode will not improve the extraction of negative ions across the sheath due to the virtual cathode formation. On the other hand, the transported flux of negative ions can be increased by applying a higher negative biasing to the electrode. However the maximum transported flux is limited by the amount of positive ion flux determined at the sheath edge. This implies that the negative ion emission will be more in the case of a denser plasma having higher population of positive ions presence in the bulk. This behavior has also been qualitatively addressed in another simulation work [21].

From application point of view, the present analytical model can be suitably used to compare the PIC (particle-in-cell) simulation results of a self-consistent  $H^-$  ion production from a biased plasma grid (planar electrode) due to impinging neutrals  $H$  and  $H_2$  and their transport across the extraction region of a hybrid negative ion source [21]. In this negative ion source, both volume and surface production of negative ions were considered. The schematic of the simulation setup and the related details are given in fig-1 of ref-[21].

In the PIC simulation, the spatial domain extends from a fixed point inside the bulk plasma  $x = 0$  up to the plasma grid position  $x_s = 1\text{cm}$ , similar to situation described in fig-3.1. The plasma grid is biased at 20 V with respect to the plasma potential  $\phi_s \sim 22\text{V}$ . Thus the relative potential of the plasma grid is  $\phi_c = -2\text{V}$ .

The neutral density of  $H$  and  $H_2$  that were considered in the simulation are  $n_H = 1 \times 10^{19} \text{ m}^{-3}$  and  $n_{H_2} = 3 \times 10^{19} \text{ m}^{-3}$  with corresponding temperatures  $T_H = 0.6 \text{ eV}$  and  $T_{H_2} = 0.15 \text{ eV}$ . In addition, plasma parameters assumed in the above simulation at  $x = 0$  are  $n_{es} = 9 \times 10^{16} \text{ m}^{-3}$ ,  $n_{vs} = 2.5 \times 10^{16} \text{ m}^{-3}$ ,  $T_{e,v} \sim 1\text{eV}$  and  $E_b \sim 0.6\text{eV}$ .

With the help of above parameters, the emitted current density of negative ions

from the plasma grid can be calculated using the formula  $j_n = eY_0(\Gamma_H + \Gamma_{H_2}) \approx 498Am^{-2}$ ; in which  $\Gamma_{H,H_2} = \frac{1}{4}n_{H,H_2}\sqrt{\frac{8eT_{H,H_2}}{\pi m_{H,H_2}}}$  are the thermal flux of neutrals  $H$  and  $H_2$  impinging the plasma grid respectively,  $Y_0 \sim 0.15$  [12] is conversion efficiency of both neutral species to form  $H^-$  ions.

For comparing with the simulation results, we apply the following dimensionless quantities:  $\eta_c = -2$ ,  $J_n = 6.86$ ,  $\alpha_s = 0.27$ ,  $\gamma_v = 1$  and  $\varepsilon_b = 0.6$  as input parameter in to our model.

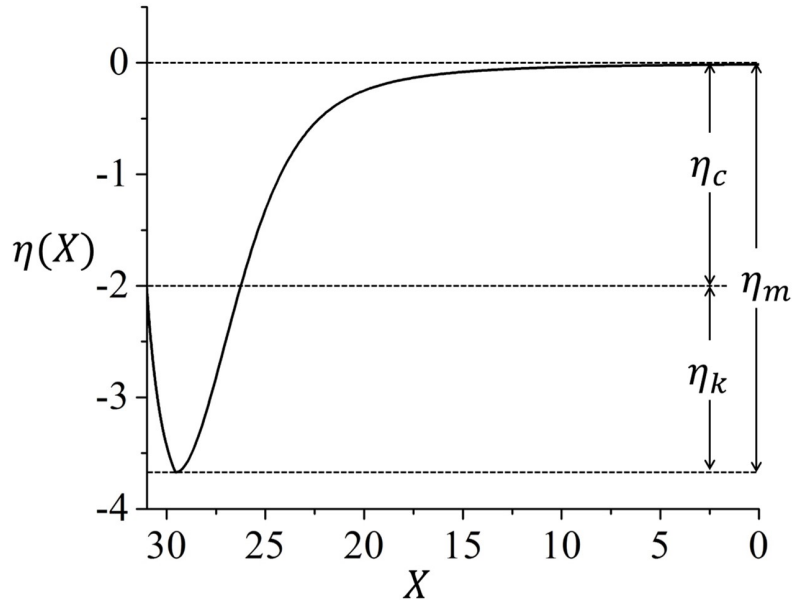


Figure 3.12: The plot of potential distribution inside the sheath for  $J_n = 6.86$ . The parameter used here are  $\eta_c = -2, \varepsilon_b = 0.6$ ,  $\alpha_s = 0.27$  and  $\gamma_v = 1$ . The electrode position is defined at  $X = 31$ .

Figure-3-12 shows the plot of spatial potential distribution. From the figure, the depth of potential minima with respect to the grid is found to be  $\eta_k \approx -1.67$ . Furthermore, the flux of negative ions crossing the sheath, has been calculated using (3-29) i.e.  $J_{nvc} = J_n e^{\eta_k} \approx 1.29$ . Therefore the percentage fraction of transported negative ion flux across the sheath amount to  $\left(\frac{J_{nvc}}{J_n} \times 100\right) \sim 19\%$ ; which implies that the remaining  $\sim 81\%$  of the flux will get reflected towards the plasma grid due to the formation of virtual cathode near the electrode surface.

In the PIC simulation, the reflected flux was found to be as high as ( $\sim 90\%$ ), whereas the position of the potential minima was found to be  $\sim 0.1\text{mm}$  from the plasma grid. It is interesting to observe that our analytical model predicts the potential minima at  $\sim 0.07\text{mm}$  (corresponding to dimensionless value  $\sim 2.4$ ); which is found to be reasonably in good agreement with PIC simulation reported in Ref-[21]. The small difference can be because our model considered only single positive ion  $H^+$  in contrast to PIC which considered all the species  $H^+, H_2^+$  and  $H_3^+$ . The above examples shows that a simple 1-dimension analytical model of a planar electrode can very well explain the behavior of negative ion emitting electrode in both experiments as well as in simulation.

### 3.6 Summary & Conclusion

In this chapter, a simple analytical model for a negative ion emitting electrode has been revisited and the modelling results have been validated by comparing with the experimental and PIC simulation results published by different authors. The negative ion emission from an electrode is similar to an electron emitting sheath originally developed by Amemiya [149] and later extended for the negative ions by McAdam et al [18]. The findings in those works mainly focused on the analytical derivation of spatial potential distribution inside the sheath leading to virtual cathode due to negative ion emission from the electrode surface.

In this work, an analytical formula for positive ion Bohm speed has been obtained. It is found that the Bohm speed becomes a function of the applied potential on the electrode surface and emission flux of negative ions. An important observation finds that the negative ion flux crossing the sheath cannot exceed the positive ion flux entering into the sheath, irrespective of applied potential on the electrode. The Bohm speed is found to increase linearly with the negative ion emission flux below

the space charge limit. However, it slightly decreases above space charge limit and attains a constant value as emission is further increased.

Another important result from this study shows that the sheath width is enhanced due to emission of negative ions from the electrode surface. The sheath width is an important parameter to optimize the appropriate grid size during 2D/3D PIC-MCC (particle-in-cell with Monte-Carlo collision) simulation techniques [99]. Its significance can also be realized by the fact that the information of sheath width can be critical to optimize the geometry of the ion extracting grids for a negative ion beam source. Presence of negative space charge adjacent to the plasma grid can adversely affect negative ion extraction from the plasma [163]. The present model can also be applied in a typical experiments where set of electrical grids are biased to extract beams of positive/negative ions [23]. Thus negative ion emission from an electrode and its consequence on the plasma sheath region has been demonstrated in view of applications associated with negative ion sources.



## Chapter 4

# The Pre-Sheath region of a negative ion emitting electrode

Pre-sheath is a weak electric field region that connects the quasi-neutral plasma to the non-neutral sheath region near the electrode. Its significance arise because it provides a directed flow to the positive ions towards the sheath boundary. The characteristics of pre-sheath region has been widely reported for the case of electro-negative plasmas using analytical models [6, 102, 164–166]; however the pre-sheath due to a negative ion emitting electrode has not been adequately addressed. In chapter-3, we found that during negative ion emission from the electrode surface, the positive ion speed was found to increase at the sheath boundary. Therefore the pre-sheath potential structure due to negative ions injected from the plasma sheath boundary towards the bulk plasma needs to be examined.

In this Chapter, the pre-sheath region has been explicitly solved, in which a constant flux of negative ions with initial energy corresponding to the potential on the electrode are injected from the sheath edge towards the bulk plasma. The negative ions are further accelerated as they traverse across the pre-sheath. The analytical model is then applied to investigate the spatial density and potential

distribution inside the pre-sheath region.

In section-4.1 a brief outline on the pre-sheath involving negative ions and its application to a negative ion emitting electrode is provided. The 1-D fluid model is presented in section-4.2. The analytical results with discussion are provided in section-4.3 & 4.4. Finally, the work is summarized in section-4.5.

## 4.1 Pre-sheath in negative ion plasma

The behavior of pre-sheath in negative ion containing plasma has been widely reported [6, 102, 103, 116]. The bulk negative ions have lower mobility than electrons, as a result they mostly remain confined within the bulk plasma. Therefore an increase in negative ion population will have a diminishing effect on pre-sheath potential. This will further reduce the positive ion speed at the sheath edge. There are several factors which can influence the pre-sheath length and the magnitude of potential drop across it. Ion-neutral and electron-neutral collision inside the pre-sheath region is one of the important factor, which can increase the potential fall in the pre-sheath region [167]; besides, presence of a transverse magnetic field can also affect the pre-sheath[168].

In the present perspective, the negative ions which are emitted from the surface will gain acceleration in the sheath and they will be further accelerated on entering the pre-sheath region. This additional negative ions in the pre-sheath is expected to change the quasi-neutral equilibrium throughout the pre-sheath region. The pre-sheath will govern, how much negative ions can enter the pre-sheath region and get accommodated inside the bulk plasma. Analytical study by Orson Sutherland et al [169] found that the variation of extracted current of negative ions have functional dependence on both sheath as well as the pre-sheath region. Though ion-ion interaction inside the sheath may be ignored, however ion-ion/ion-neutral collision mean



free path may be comparable with pre-sheath length[116]. In another study, time resolved measurement of density and potential with the help of Langmuir probe conducted in NIFS-R&D negative ion source[170] had shown that the pre-sheath in front of the caesiated plasma grid is deeply penetrated into the bulk plasma as a result of increasing the negative ion emission from the plasma grid. This gives a clear indication of pre-sheath elongation due to negative ion emission from an electrode surface. It was also found that increase in  $H^-$  concentration due to negative ion emission resulted in a decrease of electron density inside the pre-sheath. The overall quasi-neutrality is then maintained by  $H^+$  and  $H^-$ . The elongation of pre-sheath has been also observed in electro-negative discharges, where the shielding length of pre-sheath ambipolar field is longer than in the usual electron-ion pre-sheath [116].

The implication from the above observation suggests that the pre-sheath region is strongly affected by the presence of negative  $H^-$  ions emitted from low work function surfaces in negative ion sources. A suitable analytical model of pre-sheath will therefore be essentially helpful to independently study the impact of negative ion emission flux on the pre-sheath potential drop. The analytical model formulated in this chapter considers a negative ion flux injected from the sheath edge inside a quasi-neutral pre-sheath consisting of positive ions, electrons and bulk negative ions. Using this model, the potential distribution, the pre-sheath length and the characteristic positive ion speed at the pre-sheath boundary have been investigated.

## 4.2 1-D model of pre-sheath

In fig-4.1, schematic of a planar 1-dimensional pre-sheath region is shown; on the left  $x = 0$  marks the center of the bulk plasma and on the right is the plasma sheath boundary (PSB)  $x = x_l$ . Both potential  $\phi(0)$  and electric field  $\phi'(0)$  at the boundary  $x = 0$  are assumed to be zero. The pre-sheath length  $x_l$  is the distance where the

electric field  $\phi'(x_l) \rightarrow \infty$  (infinity) [171]. The sheath region is assumed to start at  $x > x_l$ .

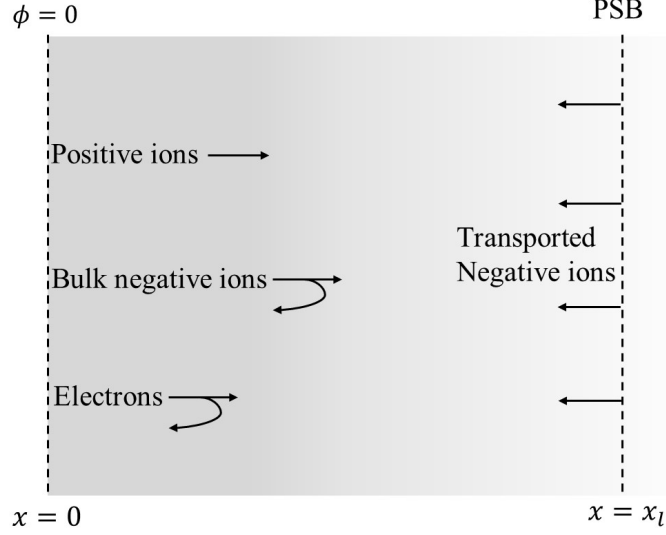


Figure 4.1: A schematic showing the charged particle transport inside the pre-sheath region, represented by arrow. A finite flux of negative ion beam is assumed to enter at the plasma-sheath boundary ( $x = x_l$ ). The center of the bulk plasma is represented at  $x = 0$ ; where the electric field and potential are assumed to be zero.

The electrons and volume negative ions inside pre-sheath are described by Boltzmann distribution [11].

$$n_e = n_{e0} \exp\left(\frac{\phi}{T_e}\right) \quad (4.1)$$

$$n_v = n_{v0} \exp\left(\frac{\phi}{T_v}\right) \quad (4.2)$$

Here  $n_{e0}$  and  $n_{v0}$  are density of electrons and bulk negative ions defined at  $x = 0$ . A constant flux  $j_n$  of negative ions enters the pre-sheath from the PSB at  $x = x_l$  and flows towards the bulk plasma. On the other hand, the positive ions flowing towards the sheath edge undergo columbic/momentum loss collisions with background charge species (electron, volume negative ions and neutrals) respectively. Unlike the sheath region, these collisions cannot be neglected inside the pre-sheath, as the mean free path of these collisions can be comparable with the characteristic pre-sheath length. With above assumptions, the flux and energy conservation equations for the cold

positive ions inside the pre-sheath can be written as follows [172]:

$$\frac{d}{dx} (n_p v_p) = Z n_e \quad (4.3)$$

$$m_p v_p \frac{dv_p}{dx} + e \frac{d\phi}{dx} + m_p v_p \left( \nu_p + Z \frac{n_e}{n_p} \right) = 0 \quad (4.4)$$

In (4-3) the ionization frequency  $Z$  is assumed to be constant [171, 172]. Since at low pressures, the collision frequency  $\nu_p$  due to positive ion-neutral interactions is smaller than the ionization frequency ( $\nu_p \ll Z$ ) Hence the last term in (4-4) can be approximated as  $m_p v_p Z (n_e/n_p)$ [172].

The negative ion flux  $j_n$  is assumed to be constant throughout the pre-sheath. However, the momentum loss of these ions as a result of ‘frictional drag’ during collision with Maxwellian electrons and volume negative ions can take place. The rate of momentum loss for such collisions due to electrons and volume negative ions are given respectively as [Ch-14 in [161]]:

$$\frac{d \langle v_n \rangle_e}{dt} = - \frac{2^{1/2} e^4 m_e^{1/2} Z_n^2 \ln \Lambda}{12 \pi^{3/2} \varepsilon_0^2 m_n (K_B T_e)^{3/2}} (n_e v_n) \quad (4.5)$$

$$\frac{d \langle v_n \rangle_v}{dt} = - \frac{Z_v^2 Z_n^2 e^4 \ln(\Lambda)}{4 \pi \varepsilon_0^2 m_v m_n} \left( \frac{n_v}{v_n^2} \right) \quad (4.6)$$

In the above equations,  $\ln \Lambda$  is coulomb logarithm,  $m_e$  and  $m_{v,n}$  are the respective masses of electron, volume negative ion and injected negative ions respectively. Here  $Z_{n,p,v}$  for similar charged state ions has been assumed to be one ( $Z_{n,p,v} = 1$ ).

The columbic interaction between the cold positive ions ( $T_p \ll T_e$ ) and injected negative ions is vanishingly small; as it varies inversely to the cube of their relative speed [161]. Since the speed of negative ions injected at the PSB is sufficiently high as compared to counter-streaming positive inside the pre-sheath [ $v_n \approx 5c_s$  i.e.  $V_{ns} \approx 5$ , see fig-3.5(b)], therefore the momentum loss of these negative ion during collision with positive ions can be neglected.

Thus, the continuity and the momentum equations for injected negative ions are given as follows:

$$j_n = j_{ns} = en_n v_n = j_{n0} \quad (4.7)$$

$$m_n v_n \frac{dv_n}{dx} - e \frac{d\phi}{dx} + A_e (n_e v_n) + A_i \frac{n_v}{v_n^2} + \nu_n m_n v_n = 0 \quad (4.8)$$

Here  $\nu_n$  is negative ion-neutral collision frequency;  $A_e$  and  $A_i$  are constants given by;

$$A_e = \frac{2^{1/2} e^4 m_e^{1/2} Z_n^2 \ln \Lambda}{12\pi^{3/2} \varepsilon_0^2 (K_B T_e)^{3/2}} \quad \& \quad A_i = \frac{Z_v^2 Z_n^2 e^4 \ln \Lambda}{4\pi \varepsilon_0^2 m_v} \quad (4.9)$$

Furthermore, quasi-neutrality condition is considered to be valid inside the entire pre-sheath, hence:

$$n_p = n_e + n_v + n_n \quad (4.10)$$

Finally, the above equations can be written in dimensionless form as follows;

$$N_e = \exp(\eta) \quad (4.11)$$

$$N_v = \alpha_0 \exp(\gamma_v \eta) \quad (4.12)$$

$$\frac{d}{dX} (N_p V_p) = N_e \quad (4.13)$$

$$V_p \frac{dV_p}{dX} + \frac{d\eta}{dX} + V_p \left( \delta_p + \frac{N_e}{N_p} \right) = 0 \quad (4.14)$$

$$N_n V_n = J_n \quad (4.15)$$

$$- \frac{d\eta}{dX} - \mu_{np} \frac{J_n^2}{N_n^3} \frac{dN_n}{dX} + A'_e J_n \left( \frac{N_e}{N_n} \right) + (A'_i / J_n^2) (N_v N_n^2) + \mu_{np} \delta_n \left( \frac{J_n}{N_n} \right) = 0 \quad (4.16)$$

$$N_p = N_e + N_v + N_n \quad (4.17)$$

Here the normalization rules follow as;

$$\begin{aligned}
X &= Zx/c_s, V_{p,n} = v_{p,n}/c_s, \eta = e\phi/K_B T_e, N_{p,v,n,e} = n_{p,v,n,e}/n_{e0}, \gamma_v = T_e/T_v, \\
\alpha_0 &= n_{v0}/n_{e0}, \beta_0 = n_{n0}/n_{e0}, J_n = j_n/(en_{e0}c_s), \mu_{np} = m_n/m_p, \\
A'_e &= A_e(n_{e0}/m_p Z), A'_i = A_i(n_{e0}/m_p Z c_s^3), \delta_{p,n} = \nu_{p,n}/Z \quad (4.18)
\end{aligned}$$

Note that the position coordinate  $x$  is normalized by the ionization length ( $c_s/Z$ ) [6]. The characteristic length of the pre-sheath is determined by the ion mean free path rather than the Debye length. Therefore the Poisson's equation inside the pre-sheath is given by;

$$q^2 \left( \frac{d^2 \eta}{dX^2} \right) = (N_e + N_v + N_n - N_p) \quad (4.19)$$

In (4.19),  $q = (\lambda_{D0}Z)/c_s$  is defined as non-neutrality parameter [6]. Generally  $q \ll 1$  since the ionization length ( $c_s/Z$ ) is much larger than the Debye length  $\lambda_{D0}$ . Equation-(4-17) is a direct consequence of the above Poisson's equation with  $q = 0$ .

## 4.3 Results and discussion

### 4.3.1 Pre-sheath dependence on volume negative ions

If the injected negative ions in to the pre-sheath is temporarily neglected, then it can be seen that the above set of equations (4-11 to 4-14 & 4-19 with  $N_n = 0$ ) reduce to the case of a typical electro-negative discharge comprising of electrons, cold positive ions and volume negative ions. In this case, the potential distribution inside the pre-sheath region can be analytically solved as an initial value problem rather than boundary value problem as adopted in chapter-3 for solving the sheath region. That is, for a given set of initial values at the center of the discharge

( $X = 0$ ), the integration of equations (4-11 to 4-19) is carried towards the sheath edge. Since positive ion flow is outward, therefore its solution is obtained by the upstream boundary conditions; which can be defined as  $\eta(0) = 0$ ,  $V_p(0) = 0$  and  $N_p(0) = 1 + \alpha_0$ .

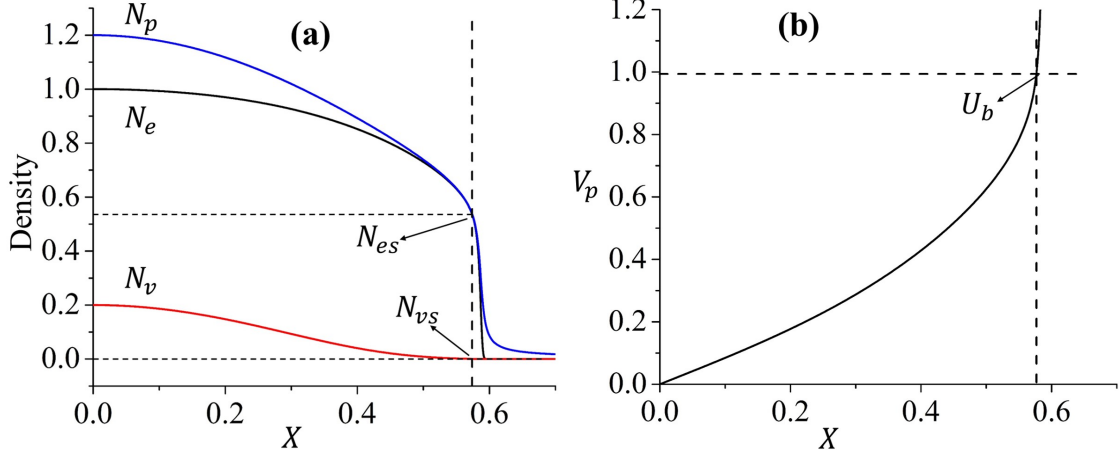


Figure 4.2: Plots showing spatial profile of (a) the charge particle density of individual species and (b) the positive ion speed. The vertical dashed line shows the pre-sheath end. The parameter considered at  $X = 0$  are  $\alpha_0 = 0.2$  and  $\gamma_v = 10$ .

Fig-4.2(a) & (b) shows the density distribution of individual species and spatial distribution of positive ion speed respectively for an arbitrarily chosen non-neutrality parameter  $q = 10^{-3}$ . If however, the ionization length ( $c_s/Z$ ) is much larger than  $\lambda_{D0}$  so that  $q \approx 0$  [116], then the equation (4-17) preserves the exact quasi-neutrality inside the pre-sheath. Hence pre-sheath region is sharply truncated at a position where the electric field  $E_s \rightarrow \infty$  (infinity) [116]. The position where this abrupt transition takes place can be recognized as the pre-sheath edge or the plasma-sheath boundary, as indicated by the vertical dashed line in fig-4.2(a) & (b).

The location of the pre-sheath edge can be further verified by inspecting the positive ion speed, which should acquire the characteristic Bohm speed at this boundary. For a bulk electronegativity parameter  $\alpha_0 = 0.2$  &  $\gamma_v = 10$  as input, the relative negative ion concentration at the plasma-sheath boundary is found to be  $\alpha_s \equiv (N_{vs}/N_{es}) = 6.4 \times 10^{-6}$  from (4-12) [see fig-4.2(a)]. The normal-

ized value of Bohm speed corresponding to this value is found from formula to be  $U_B \equiv \sqrt{(1 + \alpha_s) / (1 + \gamma_v \alpha_s)} \approx 0.99$ , which is in agreement with the positive ion speed at the pre-sheath boundary, as shown by a vertical dashed line in fig-4.2(b).

In fig-4.3, the pre-sheath potential profile for different values of  $\alpha_0 = 0, 1.5, 2$  is solved assuming the exact quasi-neutrality relation (4-17). The pre-sheath is truncated at the point where the positive ion reach the Bohm speed and denoted by the symbol '×'.

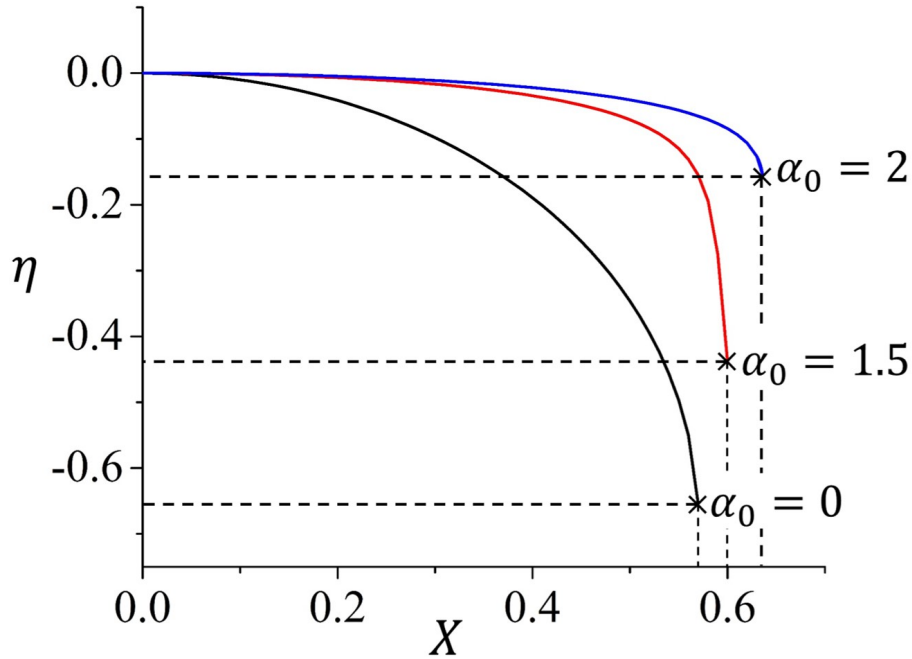


Figure 4.3: Plots showing spatial variation of pre-sheath potential  $\eta$  for  $J_n = 0$  and different values of bulk electro-negativity parameter  $\alpha_0 = 0, 1.5, 2$  &  $\gamma_v = 10$ . The origin inside the bulk plasma is defined at  $X = 0$  where potential and electric field is zero. Symbols '×' denotes the end of the pre-sheath regio.

From the above figure, it can be seen that the pre-sheath potential drop reduces as the concentration of volume negative ions in the bulk increases. This observation is consistent with earlier reported works, which suggest that the rate with which the positive ion accelerate inside the pre-sheath is reduced [6, 165, 167]. Therefore, the positive ions traverse a longer distance in the bulk plasma to attain its characteristic Bohm speed. Consequently, the characteristic pre-sheath length is elongated as

observed in fig-4.3. Moreover, due to fall in the positive ion Bohm flux at the sheath edge, the ambipolar loss of electrons towards the sheath boundary is also reduced.

### 4.3.2 Pre-sheath dependence on injected negative ions

If a finite flux  $J_n$  of negative ions is injected from the sheath boundary at  $X = X_l$ , and assuming that the flux  $J_n$  remain conserved; therefore the flux  $J_{n0}$  at  $X = 0$  would be equal to  $J_n$ .

Furthermore, the potential drop across the pre-sheath region is equivalent to the energy gained by positive ions while it moves from  $X = 0$  to  $X = X_l$ . Therefore from energy conservation, the normalized density  $\beta_0$  which corresponds to injected negative ions at  $X = 0$  is related to  $J_n$  by;

$$\beta_0 = J_n (V_{ns}^2 + \mu_{pn} U_B^2)^{-1/2} \quad (4.20)$$

Thus for a given flux  $J_n$  of negative ions emitted from the electrode, the speed of negative ions  $V_{ns}$  and positive ion speed  $U_B$  from fig-3.5(b) & fig-3.7 of chapter-3 respectively are substituted in (4-20) to find the density  $\beta_0$  at  $X = 0$ .

Similarly the electro-negativity parameter  $\alpha_0$  at  $X = 0$  can be related to  $\alpha_s$  by relation;

$$\alpha_0 = \alpha_s \exp \left[ \left( \frac{\gamma_v - 1}{2} \right) U_B^2 \right] \quad (4.21)$$

Once the boundary value of densities  $\alpha_0$  and  $\beta_0$  at  $X = 0$  are found, the potential distribution inside the pre-sheath can be solved by using the set of equation (4-11) to (4-17) using the initial boundary conditions  $\eta'(0) = 0$ , the potential  $\eta(0) = 0$ , the initial positive ion speed  $V_p(0) = 0$  and the quasi-neutrality condition  $N_p(0) = 1 + \alpha_0 + \beta_0$ .



The pre-sheath equations are solved using the exact quasi-neutrality condition [c.f. (4-17)] up to the point where the electric field ‘blows up’ i.e.  $E_s(\eta_s, X_l) \equiv \eta'(X_l) \rightarrow \infty$ ; here  $X_l$  is dimensionless pre-sheath length and  $\eta_s$  is potential at the sheath edge.

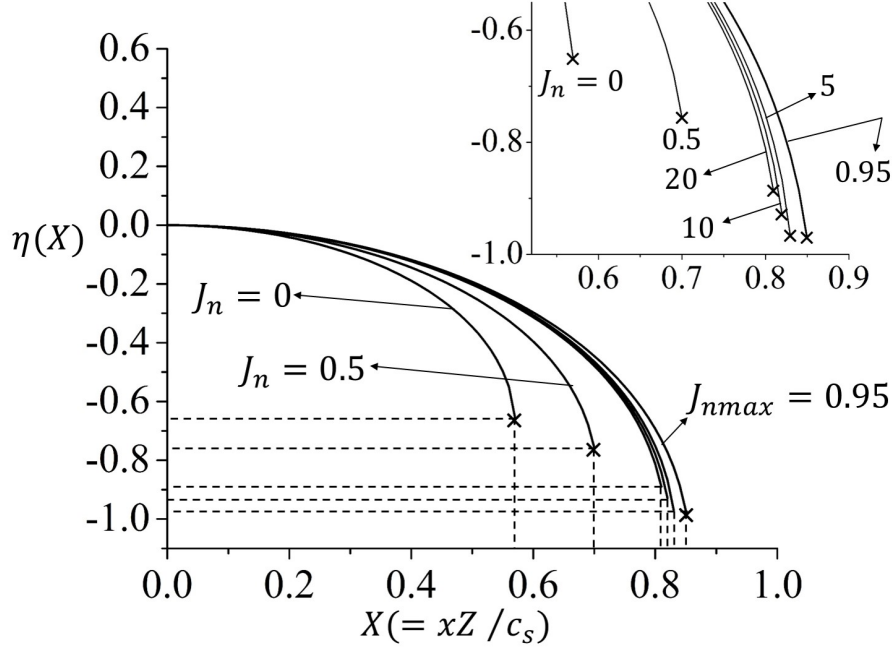


Figure 4.4: The spatial distribution of pre-sheath potential  $\eta(X)$  for a range of injected flux  $J_n = 0$  to 20. The position  $X = 0$  is the center of discharge and the symbol ‘x’ denotes the end of the pre-sheath at  $X = X_l$ . The typical parameters are  $\alpha_0 = 0$ ,  $A'_e = 0.1$ ,  $A'_i = 0$ ,  $\mu_{np} = 1$ ,  $\delta_{n,p} \approx 0$ .

In Fig-4.4, potential distribution in the pre-sheath are shown for a range of negative ion flux for corresponding  $J_n$  values used to obtain the plots in fig-3.4(a). The figure clearly shows that as  $J_n$  increases, the potential drop increases steadily across the pre-sheath. The maximum potential drop across pre-sheath corresponds to the critical flux at space charge limited value  $J_{nmax} \sim 0.95$ . Therefore the presence of negative ion flux injected in pre-sheath gives rise to a greater potential drop due to which the positive ions are accelerated from the bulk plasma towards the sheath boundary at a relatively higher speed than in the absence of  $J_n$ . Thus the above result is in qualitative agreement with fig-3.7 of chapter-3, which showed a marked

increase in  $U_B$  as  $J_n$  was increased from zero to  $J_{nmax} = 0.95$ . The pre-sheath length is also found to increase during presence of  $J_n$ , which is discussed below.

### 4.3.3 Characteristic Pre-sheath Length

In a low pressure electro-positive discharge, the electrons can be described by Boltzmann distribution[171]. The potential distribution inside the pre-sheath is determined from the ambipolar electric field  $E \approx -\frac{K_B T_e}{en_e} \frac{dn_e}{dx}$  [11]. On the other hand, the positive ion speed  $v_p = \mu_p E$  is obtained in terms of the ion-neutral collision mean free path  $\lambda_{in} = v_p/\nu_{in}$ ; which can be written as  $v_p^2 = \lambda_{in} \left( \frac{K_B T_e}{m_p} \right) \frac{1}{n_e} \frac{dn_e}{dx}$ . Here  $\mu_p$  is mobility of positive ions. Approximating the density gradient term  $\frac{1}{n_e} \frac{dn_e}{dx}$  across the pre-sheath length by  $\sim 1/R$  for  $n_{es} \ll n_{e0}$ , the positive ion speed at the plasma-sheath boundary is found to scale as  $v_p \approx \sqrt{\frac{K_B T_e}{m_p}} \left( \frac{\lambda_{in}}{R} \right)^{1/2}$ . This implies that the positive ions acquire the acoustic speed at a distance of the order of ion-neutral collision mean free path ( $R \sim \lambda_{in}$ ).

In the scenario when ion-neutral collision is ignored, however the electron-impact ionization can be considered as a momentum loss process for the ions inside the pre-sheath. Therefore under the steady-state, an electron-ion pair created is balanced by the ambipolar loss of positive ions at the characteristic ion acoustic speed. This approximation leads to a characteristic scale length of the pre-sheath for this case.

Fig-4.5 presents the dimensionless pre-sheath length as a function of the injected flux  $J_n$ . From the figure, it can be seen that the pre-sheath length increases up to the space charge limited flux  $J_n = J_{nmax}$  and then decreases slowly as the negative ion flux is increased above  $J_{nmax}$  value. The observed trend in  $X_l$  varies in similar manner as the transported flux of negative ions which gets saturated for  $J_n > J_{nmax}$  after the virtual cathode is formed [c.f. fig-3.4(a)].

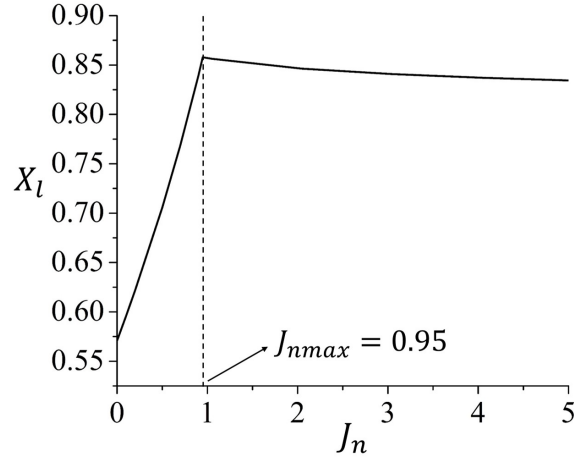


Figure 4.5: Plot for pre-sheath length with respect to emission flux  $J_n$ , where  $J_{nmax} \approx 0.95$ . The parameters are same as considered in fig-4.4

The normalized pre-sheath length  $X_l$  from (4-18) is expressed as  $X_l = l/(c_s/Z)$  where  $Z$  is the ionization frequency,  $c_s$  is the ion acoustic speed and  $l =$  geometric pre-sheath length. The term  $(c_s/Z)$  is known as the ionization length[6]. In the case of pure electron-ion plasma, the characteristic length  $l = 0.57(c_s/Z)$ [116] indicates the fact that the geometric length is less than the ionization length. However due to presence of negative ion beam, this factor is found to be  $0.85(c_s/Z)$  as seen from fig-4.5 which is approximately close to one ionization length.

## 4.4 Interpretation of Bohm speed

In chapter-3, the Bohm speed of positive ions was found to increase when a constant flux  $J_n$  of negative ions were introduced from the electrode surface. The emission flux  $J_n$  was varied from 0 to 8 and the impact on the Bohm speed was investigated. It was found that for  $J_n < 0.95$ , i.e. below the space charge limited emission, the Bohm speed increased linearly. However for  $J_n > 0.95$ , the emission gets space charge limited and the Bohm speed attains nearly a constant value. This observation can be closely related to the potential drop inside the pre-sheath as plotted in fig-4.4. It can be observed that the pre-sheath potential drop increases as

the negative ion flux increases inside the pre-sheath. Therefore, a higher potential drop across the pre-sheath will eventually result in providing a greater acceleration to the positive ions as they enter the plasma-sheath boundary. This is in agreement with the increase in the Bohm speed observed in fig-3.7 of chapter-3.

The Bohm speed obtained in chapter-3 considered the electric field at the plasma-sheath boundary to be zero; whereas in the case of pre-sheath, the plasma-sheath boundary is determined at the point where the electric field tends to become infinite. Therefore for smoothly joining the sheath region to the adjacent quasi-neutral pre-sheath, the Bohm condition given by (3-27) is not satisfied for  $E_s \rightarrow 0$  but for  $E_s(X_l) \rightarrow \infty$  while locating the sheath edge by solving pre-sheath. This can be verified by finding the various quantities and their derivative at the pre-sheath edge.

First, eliminating  $\frac{dV_p}{dX}|_{X_l}$  from (4-13) and (4-14), the derivative  $\frac{dN_p}{dX}|_{X_l}$  is given by;

$$U_B \left( \frac{dN_p}{dX} \right) |_{X_l} + \frac{N_{ps}}{U_B} \left( E_s - U_B \frac{e^{\eta_s}}{N_{ps}} \right) = 0 \quad (4.22)$$

Whereas, the derivative  $\left( \frac{dN_n}{dX} \right)$  is found from (4-16) as;

$$E_s - \mu_{np} \left( \frac{J_n^2}{N_{ns}^3} \right) \left( \frac{dN_n}{dX} \right) |_{X_l} + A'_e J_n [\eta_s / N_{ns}] + (A'_i \alpha_0 / J_n^2) [N_{ns}^2 e^{\gamma_v \eta_s}] = 0 \quad (4.23)$$

The density derivative  $\left( \frac{dN_p}{dX} \right)$  and  $\left( \frac{dN_n}{dX} \right)$  are related with the following equation obtained from (4-17);

$$\left( \frac{dN_p}{dX} \right) |_{X_l} = - (e^{\eta_s} + \gamma_v e^{\gamma_v \eta_s}) E_s + \frac{dN_n}{dX} |_{X_l} \quad (4.24)$$

Substituting  $\left( \frac{dN_n}{dX} \right)$  and  $\left( \frac{dN_p}{dX} \right)$  from (4-22) and (4-23) respectively in equation (4-24) and again using the quasi-neutrality condition  $N_{ps} = e^{\eta_s} + \alpha_0 e^{\gamma_v \eta_s} + N_{ns}$ , we get;

$$E_s = \frac{\left[ \frac{N_{ps}}{U_B^2} + \mu_{np} \left( \frac{J_n^2}{N_{ns}^3} \right) - (\eta_s + \alpha_0 \gamma_v e^{\gamma_v \eta_s}) \right]}{\left[ \frac{\eta_s}{U_B} - A'_e J_n (\eta_s / N_{ns}) - (A'_i \alpha_0 / J_n^2) (N_{ns}^2 e^{\gamma_v \eta_s}) \right]} \quad (4.25)$$

We observe that as  $E_s \rightarrow \infty$ ,  $U_B$  from (4-25) can be evaluated in terms of bulk parameter as;

$$U_B^2 = \frac{e^{\eta_s} + \alpha_0 e^{\gamma_v \eta_s} + N_{ns}}{e^{\eta_s} + \alpha_0 \gamma_v e^{\gamma_v \eta_s} - \mu_{np} \left( \frac{J_n^2}{N_{ns}^3} \right)} \quad (4.26)$$

For  $N_{ns} = 0$ , i.e. in absence of emission, (4-26) represents the usual Bohm speed in terms of bulk parameter in an electronegative plasma[164].

## 4.5 Summary & conclusion

In summary, the pre-sheath region next to the negative ion emitting sheath has been studied with the help of 1-D fluid equations. From the study, it is observed that the potential drop across the pre-sheath increases as a constant flux of injected negative ions stream towards the center of the discharge. Consequently, the Bohm speed of positive ions also gets enhanced. This result is consistent with the Bohm speed derived by solving the sheath equations in chapter-3.

The present chapter highlights some of the most fundamental difference between the behavior of negative ions created in the bulk plasma and that born at low work function surfaces inside the plasma. It is well known that the bulk negative ions reduces the Bohm speed at the sheath edge as compared to electron-ion plasma. A decrease in positive ion speed leaving the sheath boundary also reduces the ambipolar loss of positive ions towards the sheath. Accordingly, the electrons are also confined inside the pre-sheath. On the other hand, an opposing effect is seen if a constant flux of negative ions is introduced from the plasma-sheath-boundary;

---

it results in an increase in pre-sheath potential drop. Thus the ambipolar loss of positive ion towards the sheath edge is expected to increase, also reducing the confinement of electrons inside the bulk. *One similarity between the above cases is that the pre-sheath length increases due to both volume negative ions and surface produced negative ions [see fig-4.3 & 4.4]. This is to provide the perfect shielding of the ambipolar field inside the pre-sheath.* As can be seen from fig-4.3 & 4.4, the rate  $d\eta/dX$  with which the positive ions drift from bulk plasma towards the sheath edge is reduced for increasing concentration of negative ions. This results in an increase of the pre-sheath length, allowing positive ions to travel a longer distance to gain the Bohm speed.

In the above study, we have considered that the streaming flux of negative ions against the background positive ions and electrons is constant throughout the pre-sheath. This is necessary in negative ion source to avoid collisional loss of negative ions extracted from the sheath & pre-sheath region of the plasma grid inside the expansion region. The magnetic filter is one of the means to reduce the electron temperature, which increase the survival rate of negative ions inside the plasma. However, for other applications, such as in magnetron sputtering discharges, the oxygen negative ions created at the target can undergo inelastic collisions with the neutrals and other charged particles present inside the sheath & pre-sheath and therefore the damaging the thin film at the substrate can be reduced. In this scenario, such losses are useful. It will be interesting to study the impact of such collisional losses on to the plasma behavior in the future.

## Chapter 5

# Floating Potential and its application in negative ion plasma

Floating potential of an isolated probe is perhaps the simplest measurements that can be performed inside a plasma. At this potential, the net current drawn by the probe due to both negative and positive charges is reduced to zero. The floating potential at any two spatially distinct position in a plasma can provide an estimate about the local electric field [173, 174]; while it is also possible to measure the electron temperature from the floating potential of a cold and a hot emissive probe for the case of a Maxwellian plasma [52].

The floating condition of an isolated electrode can be explicitly derived by equating the sum of individual fluxes due to all charged species to zero. The flux of charge species arriving at the probe surface is governed by the intrinsic properties of the plasma. Therefore, there is an underlying connection between the plasma parameters and the potential acquired by an isolated probe. There are several factors that can affect the floating potential such as non-thermal electrons in the discharge [175] and the presence of negative ions inside the bulk plasma [176–179]. The negative ions in the bulk can affect the flux of positive ions at the probe surface [6]. On the

other hand, the emission of negative ions can also affect the floating potential of isolated grids in a typical negative ions source[15, 22, 151, 180, 181].

In this chapter, two main applications related to floating potential of an electrode has been addressed in context to negative ion emitting surfaces in a negative ion source and non-emissive probes used for the diagnostics of negative ions.

Section-5.1 presents an analytical model of a floating electrode emitting negative ions and discusses the space charge limited emission from the surface. The effect of bulk negative ions on the floating sheath characteristics of a non-emitting electrode is presented in section-5.2 and its application in the estimation of negative ion density and temperature experimentally has been described in the section 5.3. Subsequently, the chapter concludes by outlining the important results in section 5.4.

## 5.1 Floating potential of a negative ion emitting electrode

In electron emitting probes, the floating potential tends to shift towards the plasma potential with increase in emission [52]. Likewise negative ion emission from a floating electrode can also change the potential structure inside the sheath of the emitting surface, like in ion extraction grids which are typical of ion sources.

Negative ion emitting surfaces can be metal or an insulator [182]. In metals, negative ions are formed at surfaces coated with low work-function element like cesium and barium [90]. There are insulators, like polycrystalline diamond surfaces, can also facilitate negative ion emission of hydrogen and oxygen with a high yield [15]. Wide band gap insulator LiF(100) surface gives rise to oxygen negative ions with conversion yield as much as 70% of the total impinging flux of positive ions and neutrals [180]. Y Fujiwara et al, reported the thermionic emission of  $O^-$  from



a solid oxide surface of Yttria-stabilized zirconia (YSZ) [151].

The effect of negative ion emission from a floating plasma grid was initially addressed in a simulation study by Wunderlich et al using a 1d3v (1-dimensional and 3 velocity component) PIC code [22]. The simulation enabled to study the impact of neutral atomic density of hydrogen and deuterium on the surface production of  $H^-$  and  $D^-$  negative ions and their transport across the sheath. Although the virtual cathode formation around a floating electron emitting probe is a common phenomenon [52, 154, 183]. However due to heavier mass, the effect of negative ion emission from an electrode is expected to have a greater influence on the virtual cathode inside the sheath than an electron emitting electrode.

In the following section, an analytical model of a planar, negative ion emitting electrode has been derived for the case of a floating electrode to obtain the potential and density distribution inside the sheath.

### 5.1.1 Analytical Model

Referring to the case of a planar, negative ion emitting electrode in fig-3.2 of Chapter-3, we can fairly extend the underlying model to the floating case. Since the electrode in this case is floating, hence the floating potential can be obtained by equating the net current at the electrode surface to zero, i.e.

$$j_{pw} + j_{nw} = j_{vw} + j_{ew} \quad (5.1)$$

In the above equation,  $j$ 's denotes the current densities of individual species which are assumed to have similar charged state. The first letter of subscript for different  $j$ 's denote the respective charge species and the subscript ' $w$ ' denotes a floating wall / electrode surface.

The individual current densities of electrons and volume negative ions at the electrode surface is given by [8, 87]:

$$j_{ew} = \frac{1}{4}en_{es}\langle v_e \rangle \exp\left(\frac{e\phi_f}{K_B T_e}\right) \quad (5.2)$$

$$j_{vw} = \frac{1}{4}en_{vs}\langle v_v \rangle \exp\left(\frac{e\phi_f}{K_B T_v}\right) \quad (5.3)$$

In the above equations,  $\phi_f$  is floating potential; whereas other symbols have their usual meaning.

We assume the two floating potential cases; (a) below the space charge limit, and (b) above space charge limit.

**(a) *Floating potential below space charge limit***

As described in chapter-3, the negative ions are emitted with an average energy  $E_b$  from the electrode surface and gain energy due to potential drop across the sheath. Applying flux conservation to both positive ions and negative ions inside the collision-less sheath, we get;

$$j_{nw} = en_{ns}v_{ns} \quad (5.4)$$

$$j_{pw} = en_{ps}v_{ps} \quad (5.5)$$

Where  $n_{ps}$  and  $n_{ns}$  represent the respective densities of positive and negative ions at the sheath edge. The densities of various species in equation (5-2) to (5-5) are related by quasi-neutrality condition at the sheath edge as follows;

$$n_{ps} = n_{es} + n_{vs} + n_{ns} \quad (5.6)$$

The energy conservation equation can be used to write the expression for the negative ion speed  $v_{ns}$  at the sheath edge;

$$v_{ns} = \sqrt{\frac{2(E_b - e\phi_f)}{m_n}} \quad (5.7)$$

Therefore the current balance equation (5-1) can be written in terms of floating potential as;

$$n_{ps}v_{ps} + n_{ns}v_{ns} = \frac{1}{4}n_{es}\langle v_e \rangle \exp\left(\frac{e\phi_f}{K_B T_e}\right) + \frac{1}{4}n_{vs}\langle v_v \rangle \exp\left(\frac{e\phi_f}{K_B T_v}\right) \quad (5.8)$$

Defining the following normalization rule;  $\alpha_s = \frac{n_{vs}}{n_{es}}, \beta_s = \frac{n_{ns}}{n_{es}}, \gamma_v = \frac{T_e}{T_v}, c_s = \sqrt{\frac{K_B T_e}{m_p}}, U_B = \frac{v_{ps}}{c_s}, V_{ns} = \frac{v_{ns}}{c_s}, \eta_f = \frac{e\phi_f}{K_B T_e}, N_{ps} = \frac{n_{ps}}{n_{es}}, J_n = \frac{j_{nw}}{en_{es}c_s}, \varepsilon_b = \frac{E_b}{K_B T_e}$ ; with the symbols having their usual meanings.

Equation (5-8) is then reduced to an expression of normalized floating potential  $\eta_f$  as:

$$\sqrt{2\pi}(\beta_s V_{ns} + N_{ps} U_B) = \sqrt{\mu_{pe}} \exp(\eta_f) + \frac{\alpha_s}{\sqrt{\gamma_v}} \sqrt{\mu_{pv}} \exp(\gamma_v \eta_f) \quad (5.9)$$

The normalized density  $\beta_s$  and the flux  $J_n$  of negative ion is related by the flux and energy conservation equations (5-4) and (5-7) respectively as;

$$J_n = \beta_s (2\mu_{pn})^{1/2} (\varepsilon_b - \eta_f)^{1/2} \quad (5.10)$$

On the other hand, from normalized quasi-neutrality condition  $N_{ps} = 1 + \alpha_s + \beta_s$  [c.f. (5-6)] defined at the sheath edge, the positive ion density  $N_{ps}$  can be expressed in terms of  $J_n$  using (5-10) as follows;

$$N_{ps} = 1 + \alpha_s + \frac{J_n}{\sqrt{2\mu_{pn}}} (\varepsilon_b - \eta_f)^{-1/2} \quad (5.11)$$

In chapter-3, the positive ion speed  $U_B$  at the sheath boundary for a biased electrode with  $\eta_c$  was found [c.f. (3-27)]. The same expression is also applicable for the case of floating electrode, in which the electrode potential  $\eta_c$  is now replaced with the floating potential  $\eta_f$ , as given below;

$$U_B = \sqrt{\frac{1 + \alpha_s + \frac{J_n}{\sqrt{2\mu_{pn}}} (\varepsilon_b - \eta_f)^{-1/2}}{1 + \alpha_s \gamma_v - \frac{J_n}{2\sqrt{2\mu_{pn}}} (\varepsilon_b - \eta_f)^{-3/2}}} \quad (5.12)$$

Finally on substituting  $J_n$ ,  $N_{ps}$  and  $U_B$  from (5-10, 11, 12) into (5-9), the normalized floating potential  $\eta_f$  can be expressed in terms of  $J_n$  as follows;

$$\left[ 1 + \alpha_s + \frac{J_n}{\sqrt{2\mu_{pn}}} (\varepsilon_b - \eta_f)^{-1/2} \right]^{3/2} \left[ 1 + \alpha_s \gamma_v - \frac{J_n}{2\sqrt{2\mu_{pn}}} (\varepsilon_b - \eta_f)^{-3/2} \right]^{-1/2} + J_n = \sqrt{\frac{\mu_{pv}}{2\pi}} \frac{\alpha_s}{\sqrt{\gamma_v}} \exp(\gamma_v \eta_f) + \sqrt{\frac{\mu_{pe}}{2\pi}} \exp(\eta_f) \quad (5.13)$$

Equation-(5-13) gives  $\eta_f$  for the case when  $J_n < J_{nmax}$ , i.e. when the emission flux  $J_n$  is below the space charge limited flux  $J_{nmax}$ .

**(b) Floating potential above space charge limited emission**

When  $J_n > J_{nmax}$ , a virtual cathode of depth  $\eta_k$  is developed with respect to the floating electrode. To obtain the floating potential  $\eta_f$ , the current balance equation (5-1) due to various charges appearing at the electrode surface needs to be determined, considering the presence of virtual cathode. Following the steps provided for the case  $J_n > J_{nmax}$  in section-3.2.5(b) of chapter-3, the individual fluxes of electrons and volume negative ions are given by;

$$J_{ew} = \sqrt{\frac{\mu_{pe}}{2\pi}} \exp(\eta_m) \quad (5.14)$$

$$J_{vw} = \frac{\alpha_s}{\sqrt{\gamma_v}} \sqrt{\frac{\mu_{pv}}{2\pi}} \exp(\gamma_v \eta_m) \quad (5.15)$$

In (5-14) and (5-15),  $\eta_m$  is potential at the virtual cathode with respect to the sheath edge and expressed as  $\eta_m = \eta_f + \eta_k$ .

In contrast to the volume negative ions and electrons, the negative ions emitted from the electrode experience a retarding potential due to  $\eta_k$ . Therefore the flux  $J_{nvc}$  of negative ions reaching at the potential minima is related to the injected flux  $J_n$  by;

$$J_{nvc} = J_n \exp(\eta_k) \quad (5.16)$$

Where  $J_{nvc}$  for the case of floating emitting electrode is given by [c.f. 3-30];

$$J_{nvc} = \frac{N_{ps} U_B^2 \left[ \left(1 - \frac{2\eta_m}{U_B^2}\right)^{1/2} - 1 \right] + (e^{\eta_m} - 1) + \left(\frac{\alpha_s}{\gamma_v}\right) (e^{\gamma_v \eta_m} - 1)}{2 (2\mu_{pn})^{-1/2} (\varepsilon_b - \eta_m)^{1/2} \left[ 1 - \left(1 + \frac{\eta_m}{(\varepsilon_b - \eta_m)}\right)^{1/2} \right]} \quad (5.17)$$

The negative ion flux  $J_{nvc}$  which overcomes the potential minima will be further accelerated towards the sheath edge. Whereas the remaining flux  $J_n [1 - \exp(\eta_k)]$  will be reflected back towards the electrode.

On the other hand, the positive ion flux  $N_{ps} U_B$  after entering the sheath edge will follow the flux conservation throughout the sheath, therefore;

$$J_{pw} = N_{ps} U_B \quad (5.18)$$

In (5-18), the positive ion density  $N_{ps}$  at the sheath edge and Bohm speed  $U_B$  in presence of virtual cathode are given by;

$$N_{ps} = 1 + \alpha_s + \frac{J_{nvc}}{\sqrt{2\mu_{pn}}} (\varepsilon_b - \eta_m)^{-1/2} \quad (5.19)$$

$$U_B = \sqrt{\frac{1 + \alpha_s + \frac{J_{nvc}}{\sqrt{2\mu_{pn}}} (\varepsilon_b - \eta_m)^{-1/2}}{1 + \alpha_s \gamma_v - \frac{J_{nvc}}{2\sqrt{2\mu_{pn}}} (\varepsilon_b - \eta_m)^{-3/2}}} \quad (5.20)$$

The floating potential condition gives;

$$J_{ew} + J_{vw} = J_n \exp(\eta_k) + N_{ps} U_B \quad (5.21)$$

Finally, on substituting the various fluxes in (5-21), the floating potential above the space charge limited value can be expressed as;

$$\left[ 1 + \alpha_s + \frac{J_{nvc}}{\sqrt{2\mu_{pn}}} (\varepsilon_b - \eta_m)^{-1/2} \right]^{3/2} \left[ 1 + \alpha_s \gamma_v - \frac{J_{nvc}}{2\sqrt{2\mu_{pn}}} (\varepsilon_b - \eta_m)^{-3/2} \right]^{-1/2} + J_n \exp(\eta_k) = \sqrt{\frac{\mu_{pv}}{2\pi}} \frac{\alpha_s}{\sqrt{\gamma_v}} \exp(\gamma_v \eta_m) + \sqrt{\frac{\mu_{pe}}{2\pi}} \exp(\eta_m) \quad (5.22)$$

Equation-(5-13) and (5-22) gives the solution for floating potential  $\eta_f$  when the emission is below and above the space charge limit respectively.

Once the potential  $\eta_f$  on the floating electrode is calculated from (5-13) and (5-22), the potential distribution inside the sheath is obtained by solving the Poisson's equation-3-20, following the same steps as in the case of biased electrode discussed in Chapter-3. Only the basic difference is that the potential on the electrode is calculated by applying the floating condition using equations (5-13) and (5-22) respectively.

### 5.1.2 Analytical results and Comparison with PIC simulation

Figure-5.1(a) & (b) shows the potential distribution inside the sheath for a range of emission flux from  $J_n = 0$  to  $J_n = 1.6$ . As seen in the above figures, the onset of space charge limited emission of negative ions appears by observing a change in the monotonic potential fall inside the sheath to a potential well created near the negative ion emitting electrode. The critical flux  $J_{nmax}$  above which the virtual cathode forms, is observed at  $J_{nmax} = 0.69$ . The depth  $\eta_k$  of the potential well and its position from the electrode surface seems to increase with  $J_n$ . Just like the case

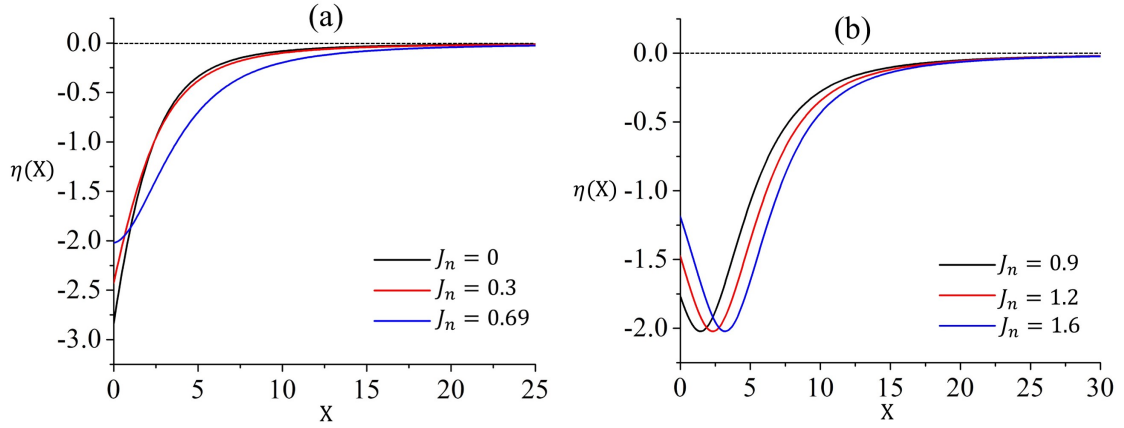


Figure 5.1: The spatial distribution of potential inside the floating sheath in H-plasma for the cases when (a) the emitted flux  $J_n < J_{nmax}$  and (b)  $J_n > J_{nmax}$ . Here  $J_{nmax} = 0.69$  is space charge limited value of emission. The parameters are  $\alpha_s = 0$  and  $\varepsilon_b = 0.35$ .

of a biased electrode, the virtual cathode near the floating electrode allows a fraction  $J_{nvc}/J_n$  of negative ions to cross the potential minima and reach at the sheath edge; here  $J_{nvc}$  is the transported negative ion flux at the sheath edge, given by (5-17).

When compared with a biased electrode [see fig-3.6 of Chapter-3], a contrasting behavior can be noticed in fig-5.1(b); that the overall depth in potential minima  $\eta_m$  with respect to the sheath edge remains unchanged even when the negative ion flux  $J_n$  increases. In contrast, the potential minima  $\eta_m$  actually get more deepened with respect to the sheath edge for the case of a biased electrodes. This is because the floating potential is governed by the current balance at the electrode surface; hence it adjusts itself to regulate the negative ions transport above the space charge limited flux  $J_{nmax}$ .

In Figure-5.2, the transported flux of negative ions is shown. Since the potential minima  $\eta_m$  is independent on  $J_n$ , therefore from (5-17), the transported flux  $J_{nvc}$  remains constant and it equals the space charge limited value  $J_{nmax}$  as can be evinced in fig-5.2. In conclusion, it is observed that when  $J_n < J_{nmax}$ , all the flux  $J_n$  emitted from the electrode gets totally transported across the sheath; whereas for

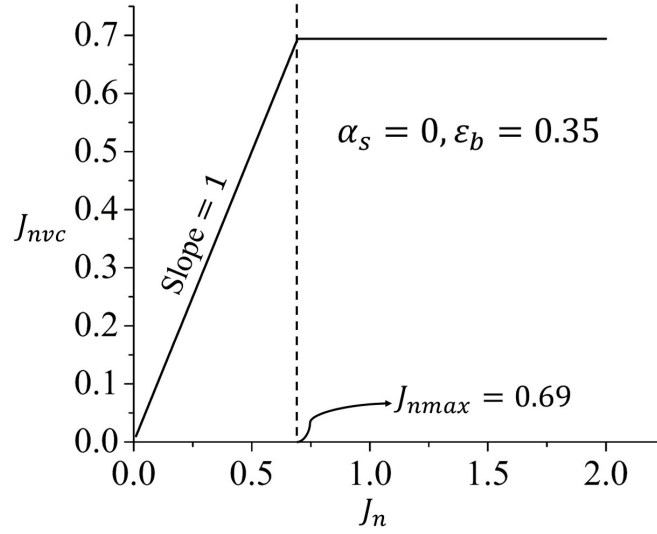


Figure 5.2: The plot for transported flux  $J_{nvc}$  at the sheath edge as a function of injected flux  $J_n$  of  $H^-$  ion from the electrode. Here  $J_{nmax} = 0.69$  is space charge limited value corresponding to the parameters  $\alpha_s = 0$  and  $\epsilon_b = 0.35$ . The slope=1 signifies the fact that the emitted flux  $J_n$  gets totally transported at the sheath edge for  $J_n < J_{nmax}$ .

$J_n > J_{nmax}$ , the transported flux  $J_{nvc}$  remains equal to the space charge limited value  $J_{nmax}$ .

In Fig-5.3, the magnitude of the floating potential and positive ion Bohm speed are plotted as a function of flux  $J_n$ . The overall graph has been divided in to two regions. Region-I of the plot corresponds to the case when the emission flux  $J_n$  is below the space charge limiting current and the solution for  $\eta_f$  is given by (5-13). Region-II corresponds to the case when  $J_n$  is greater than the space charge limit. The solution of  $\eta_f$  in this case is given by (5-22). It is found that the magnitude of  $\eta_f$  decreases monotonically with  $J_n$  in both the region-I & II. Whereas the positive ion speed linearly increases in region-I and attains a constant value in region-II.

The monotonic fall in the absolute value of floating potential with  $J_n$  is similar to the case of an electron emitting electrode. However under similar condition, the space charge limited flux is found to be at much higher value  $J_{nmax} \approx 10.55$  for an equivalent electron emitting electrode, owing to lower electron mass than the negative ions.



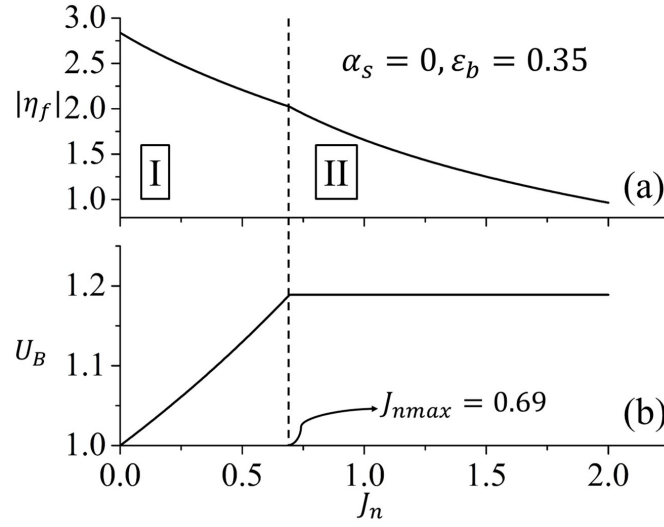


Figure 5.3: (a) The variation in magnitude of floating potential  $\eta_f$  and (b) positive ion Bohm speed  $U_B$  as a function of injected flux  $J_n$  for H-plasma ( $\mu_{pn} = 1$ ). The region-I & II corresponding to  $J_n < J_{nmax}$  and  $J_n > J_{nmax}$  denotes the emission below and above the space charge limited value  $J_{nmax}$  respectively.

In the figure, the fall in  $\eta_f$  is associated with an increase in positive ion Bohm speed  $U_B$ , as the injected negative ion flux  $J_n$  is increased up to  $J_{nmax}$ . This can be explained as follows;

Assuming  $\alpha_s \sim 0$ , equation-(5-9) will reduce to;

$$\exp(\eta_f) \cong N_{ps}U_B + J_n \quad (5.23)$$

The electron flux on the left hand side of (5-23) is balanced by the sum of positive ions and negative ion flux from the electrode. Below the space charge limit,  $U_B$  increases linearly with  $J_n$ . This results in a corresponding increase in the positive ion flux  $N_{ps}U_B$  at the sheath edge. Therefore in order to maintain the floating condition, the electron term  $\exp(\eta_f)$  on the right hand side of (5-23) should also increase at the sheath edge. In order to enhance the contribution of electrons at the sheath edge, the sheath potential  $\eta_f$  tends to fall, as observed in fig-5.3(a).

The relevance of the above analytical model can be seen while dealing with the sheath region close to a floating plasma grid of a high power/density  $H^-$  ion source.

D Wunderlich et. al. investigated this problem using 1d3v (1-dimensional 3 velocity component) PIC simulation [22]. In their simulation, surface production of  $H^-$  ion due to atomic H neutral bombardment on a floating plasma grid was considered to be the dominant mechanism whereas the volume production was assumed to be absent i.e.  $\alpha_s = 0$ . In addition to  $H^+$ ,  $H^-$  and electrons, the  $Cs^+$  ion was also incorporated in their simulation. However, from their simulation result, it was concluded that the impact of cesium ion on the plasma sheath was very small.

In the above simulation study, the emission of  $H^-$  ions from the plasma grid was varied by changing the background neutral density in range of  $10^{18}$  to  $10^{19} m^{-3}$ . The emitted flux of  $H^-$  ions in their case can be calculated from the formula  $j_n = eY(T_H)\Gamma_H$ ; where  $\Gamma_H = \frac{1}{4}n(H)\sqrt{\frac{8eT_H}{m_H\pi}}$  is the flux of neutral H-atom impinging on the electrode surface and  $Y(T_H)$  is negative ion yield for a Maxwellian distribution of H atom with temperature  $T_H$  [12]. The yield  $Y(T_H) \approx 0.12$  for  $T_H = 0.8$  eV was found from the study conducted by Lee and Seidl [12].

For a typical neutral density  $n(H) = 10^{19} m^{-3}$ , the emitted flux of  $H^-$  ions can be estimated to be  $j_n \sim 670 A/m^2$ . Hence for a given average energy  $E_b = 0.7eV$  of  $H^-$  ions emitted from the plasma grid, the dimensionless flux  $J_n$  and average energy  $\varepsilon_b$  are  $J_n = 0.77$  and  $\varepsilon_b = 0.35$  respectively. The other plasma parameters which were used as input in their simulation are  $n_{ps} \sim 3.9 \times 10^{17} m^{-3}$ ,  $n_{es} \sim 3.5 \times 10^{17} m^{-3}$ ,  $T_e = 2eV$ ,  $T_p = 0.8eV$ ,  $T_H = 0.8eV$  and  $j_n \sim 670A/m^2$ . The above parameters are used in our model to find the analytical solution of the potential distribution and the density profile inside the sheath.

The spatial potential distribution considering  $J_n = 0.77$  and  $\varepsilon_b = 0.35$  is plotted in fig-5.4(a), where the formation of virtual cathode can be clearly seen. Fig-5.4(b) presents the density profile of electron ( $N_e$ ),  $H^+$  ( $N_p$ ) and surface produced  $H^-$  ( $N_n$ ) for the same  $J_n$  and  $\varepsilon_b$  of negative ions. Whereas fig-5.5 shows the density and potential plot from the Wunderlich's simulation work [22].

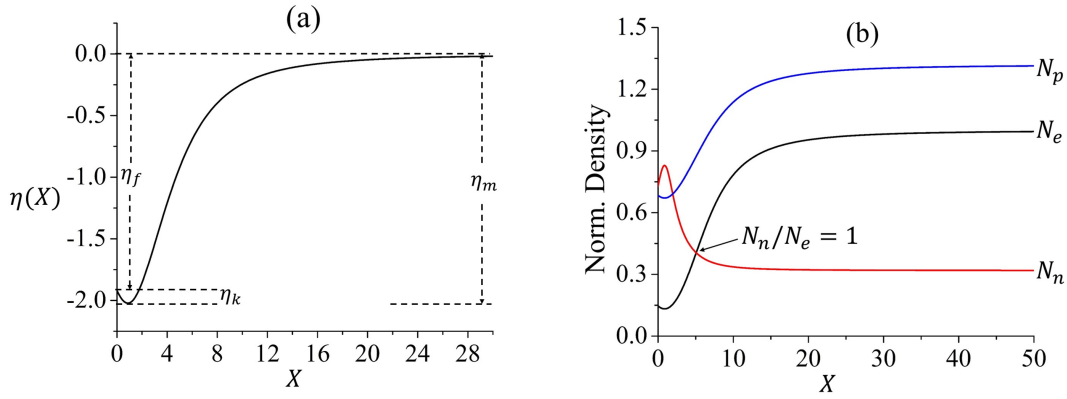


Figure 5.4: The spatial distribution of (a) potential and (b) charged particle density inside the floating sheath for  $J_n = 0.77$ . The floating potential at the electrode is found to be  $\eta_f = -1.91$ ; whereas the virtual cathode depth is  $\eta_k = -0.10$ . The density ratio  $N_n/N_e = 1$  is found at normalized distance  $X \approx 5.0$  from the floating electrode ( $X = 0$ ). The parameters  $\alpha_s = 0$  and  $\varepsilon_b = 0.35$  are used.

It can be seen from the figure that the negative ions have a strong influence on the physics of sheath region. The density ratio  $N_n/N_e = 1$  is observed at the normalized distance  $X \approx 5.0$  from the electrode  $X = 0$ . This distance corresponds to  $x \sim 0.8 \times 10^{-4}m$  for the typical plasma parameter considered above and is in close agreement with the simulation result where  $x \sim 0.75 \times 10^{-4}m$  is observed [c.f. fig-5.5]. Moreover, the ratio  $N_n/N_e$  acquires a saturation value  $\sim 0.33$  at  $x > 10^{-4}m$  far from the electrode. This is also in accordance with the measured density ratio in ref-[184].

The table-5.1 provides a comparison of parameters obtained from the present fluid model with the simulation result by D Wunderlich.

1d3v PIC Simulation	Fluid Model
$\phi_f = -4.21V$	$\phi_f = -3.84V$
$\phi_k = -0.25V$	$\phi_k = -0.20V$
$N_n/N_e = 1$ at $x \sim 0.75 \times 10^{-4}$ m	$N_n/N_e = 1$ at $x \sim 0.8 \times 10^{-4}$ m

Table 5.1: Comparison of un-normalized floating potential  $\phi_f$  and virtual cathode depth  $\phi_k$  obtained from fluid model with the PIC simulation using the same plasma parameters.

From the above table it is seen that the floating potential and virtual cathode

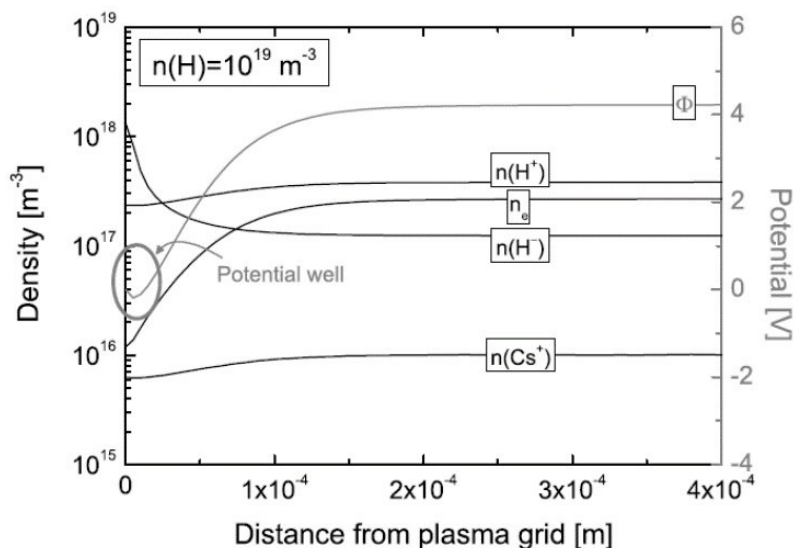


Figure 5.5: The density distribution (left y-axis) and potential distribution (right y-axis) inside the sheath of a floating negative ion emitting electrode placed at origin  $X = 0$ . *Courtesy: D. Wunderlich, Plasma Sources Science and Technology, 18.4 (2009): 045031.*

depth obtained from the fluid model are slightly less as compared to the reported PIC simulation. This marginal difference might be due to exclusion of  $Cs^+$  in the fluid model which is actually responsible for developing more shielding field on the floating electrode and therefore would demand higher magnitude of floating potential on the electrode.

## 5.2 Sheath potential of a floating non-emitting electrode

For a non-emitting electrode i.e.  $J_n = 0$ , the floating potential given by (5-13) reduces to;

$$\sqrt{\mu_{pe}} \exp(\eta_f) + \frac{\alpha_s}{\sqrt{\gamma_v}} \sqrt{\mu_{pv}} \exp(\gamma_v \eta_f) = \sqrt{2\pi} (1 + \alpha_s) \sqrt{\frac{(1 + \alpha_s)}{(1 + \alpha_s \gamma_v)}} \quad (5.24)$$

Hence, equation (5-24) gives an explicit dependence of bulk negative ions parameter

$\alpha_s$  on the floating potential  $\eta_f$  for the case of a planar non-emitting electrode immersed in an electro-negative plasma. This is a transcendental equation and needs to be solved numerically.

### 5.2.1 Floating potential dependence over bulk plasma parameters

Consider the case of a hydrogen discharge found in wide range of practical applications, in which  $H^+$  and  $H^-$  are the most dominant ionic species [81]. Therefore substituting  $m_p = m_v = 1$  amu in (5-24), the mass ratio  $\mu_{pv}$  and  $\mu_{pe}$  can be calculated.

Figure 5.6 shows a plot of the floating potential  $|\eta_f|$  as function of  $\alpha_s$ , while keeping the negative ion temperature parameter fixed at  $\gamma_v = 1, 10$  &  $60$ . The characteristics show certain interesting trends. It is seen that the magnitude of  $\eta_f$  increases initially and attains a maximum value  $\eta_{fc}$  corresponding to a critical value  $\alpha_{sc}$ . For further increase in  $\alpha_s > \alpha_{sc}$ , a monotonic fall in magnitude of  $\eta_f$  is observed. Also, higher  $\gamma_v$  value results in a higher magnitude of floating potential. The critical value  $\alpha_{sc}$  above which the floating potential magnitude monotonically falls can be obtained from (5-24) by equating the slope  $d|\eta_f|/d\alpha_s = 0$ , which is related with  $|\eta_f|$  as;

$$|\eta_f| = -\frac{1}{\gamma_v} \ln \left[ \sqrt{\frac{2\pi\gamma_v/\mu_{pv}\sqrt{1+\alpha_{sc}}}{2(1+\alpha_{sc}\gamma_v)^{3/2}}} \frac{3 + \gamma_v(-1 + 2\alpha_{sc})}{2(1 + \alpha_{sc}\gamma_v)^{3/2}} \right] \quad (5.25)$$

In Fig-5-7,  $|\eta_{fc}|$  and the corresponding  $\alpha_{sc}$  are plotted as a function of  $\gamma_v$ . It is found that  $|\eta_{fc}|$  increases monotonically as  $\gamma_v$  values are increased from 1 to 60. On the other hand,  $\alpha_{sc}$  tends to a saturation value  $\sim 0.5$  for a very large values of  $\gamma_v$ .

For the case when  $\alpha_s < \alpha_{sc}$  (i.e.  $\alpha_s$  is below 50%), it can be seen from (5.2) & (5.3) that the electron flux on the electrode is larger by a factor  $\sim \frac{43}{\alpha_s} \sqrt{\gamma_v}$  as compared to negative  $H^-$  ion flux. As a result, the negative ions have a weaker influence on the

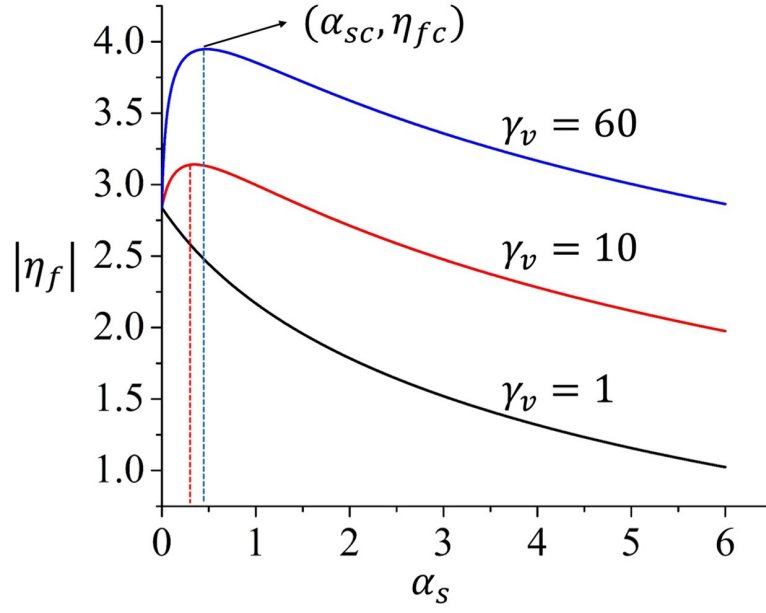


Figure 5.6: Plots of absolute value of normalized floating potential  $|\eta_f|$  as a function of  $\alpha_s$  for  $\gamma_v = 1, 10, 60$ .

floating potential as compared to the more energetic electrons. However, presence of  $H^-$  ions inside the bulk plasma reduces the positive ion speed (Bohm speed)  $U_B$  at the sheath edge substantially, as shown in fig-(5.8). As can be seen in the figure, the fall in  $U_B$  is about  $\sim 50\%$  for  $\gamma_v = 10$  and  $\sim 78\%$  for  $\gamma_v = 60$  corresponding to  $\alpha_s \approx 0.5$ . Moreover,  $U_B$  tends to a constant value as the negative ion population exceeds 50 % of total electron population (Fig 5-8).

The reason for observing an initial rise in  $|\eta_f|$  can be explained as follows:

As  $\alpha_s$  increases, the positive ion speed  $U_B$  reduces at the sheath edge (fig-5-8). This has an overwhelming impact on reducing the positive ion flux arriving at the electrode. As a result, the electrode will accumulate an excess of negative ion species initially and develops a higher negative potential to repel the electrons in order to match the reduction in positive ion flux at the electrode surface [see fig-5.6 for  $\alpha_s < \alpha_{sc}$ ].

In contrast to the above, when  $\alpha_s > \alpha_{sc}$  (i.e. above 50%), then the contribution of negative ions begins to dominate over the electrons. The Bohm speed is also seen

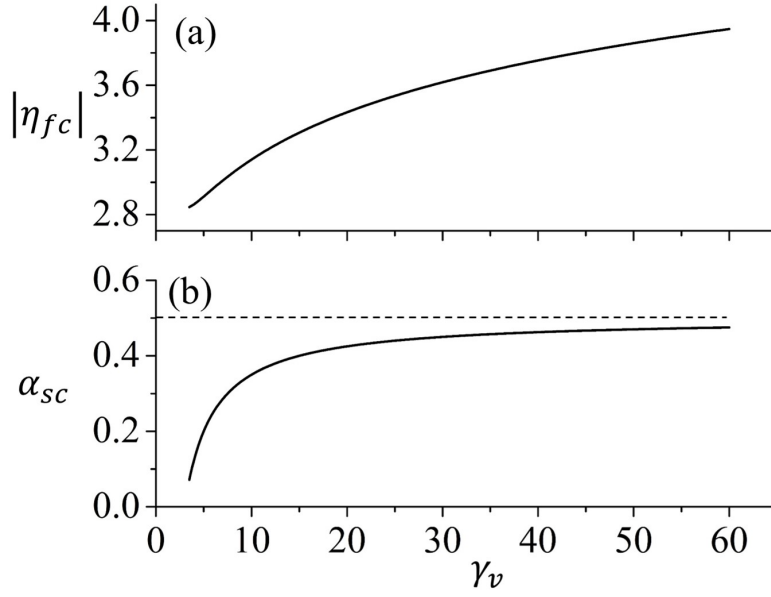


Figure 5.7: Plot of (a)  $\alpha_{sc}$  and (b)  $|\eta_{fc}|$  as a function of  $\gamma_v$ .

to become independent of  $\alpha_s$  (fig-5.8). Due to this, the positive ion flux arriving at the electrode remain independent of  $\alpha_s$ . Hence the magnitude of  $|\eta_f|$  will tend to fall as a significant fraction of electrons arriving at the electrode surface is now replaced by the negative ions [see fig-5.6 for  $\alpha_s > \alpha_{sc}$ ]

Here it is important to discuss the two limiting cases, (a)  $\alpha_s \rightarrow 0$  and (b)  $\alpha_s \rightarrow \infty$ . For  $\alpha_s \rightarrow 0$ , equation (5-24) gives the magnitude of floating potential  $|\eta_f| \rightarrow \ln \sqrt{m_p/2\pi m_e}$ ; which corresponds to the case of a purely electro-positive plasma [11]. On the other hand as  $\alpha_s \rightarrow \infty$ , i.e in ion-ion plasma[185], the floating potential magnitude  $|\eta_f| \rightarrow (1/\gamma_v) \ln \sqrt{m_p/2\pi m_v}$ . This simply implies that even for  $m_p \approx m_v$  in ion-ion plasma, the magnitude of floating sheath potential has a finite value  $|\eta_f| \neq 0$ , instead of vanishing completely. This difference is caused due to the underlying assumption that the positive ions are cold. In fact when  $e\phi_f \approx K_B T_p$  ( $T_p$  is positive ion temperature), i.e. when the ion thermal energy becomes comparable to the potential drop across the floating sheath, then the ion motion is no longer described by the drift equation and their temperatures should be taken in to account.

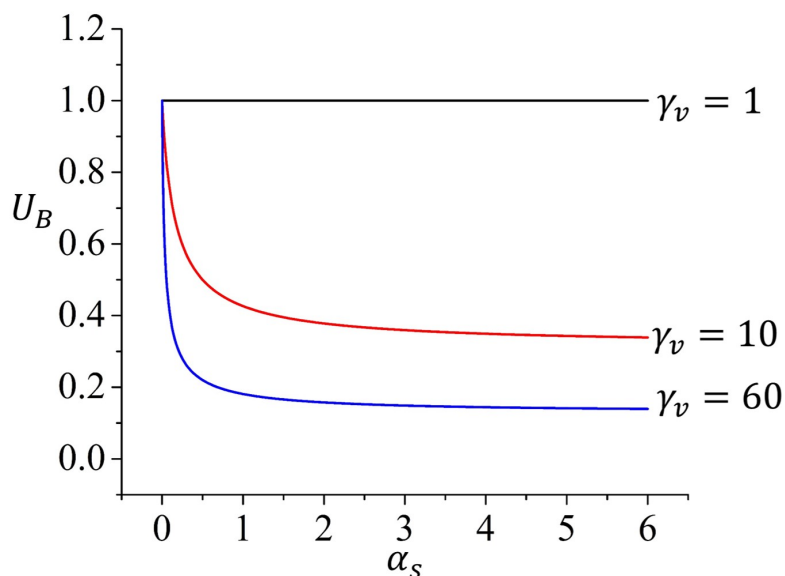


Figure 5.8: Variation of normalized Bohm velocity  $U_B \equiv V_{ps} = v_{ps}/c_s$  with electronegativity parameter  $\alpha_s$  for  $\gamma_v = 1, 10$  &  $60$ .

### 5.3 Application of cold probe floating potential for determining negative ion parameters

In section-5.2, it has been shown that the floating potential of a cold, non-emitting electrode is strongly dependent on the sheath edge density and the temperature of negative ions. This relation can be extrapolated to estimate the negative ion parameters affecting the floating potential of a probe immersed in non-equilibrium, electro-negative plasma.

The following section presents the basic methodology for determining the negative ion parameters from  $I(V_B)$  characteristics of a Langmuir probe.

#### 5.3.1 Finding the electronegativity parameter $\alpha$ and $\gamma_v$

In a typical  $I(V_B)$  characteristics of a cylindrical Langmuir probe, the ratio  $R(V_f)$  of positive ion current  $I_p(V_f)$  to the sum of current  $I_e(V_f)$  &  $I_v(V_f)$  due to electrons



& negative ions respectively at floating potential  $V_f$  is unity. Therefore;

$$R(V_f) \equiv \frac{I_e(V_f) + I_v(V_f)}{I_p(V_f)} = 1 \quad (5.26)$$

Assuming Boltzmann distribution for electrons and volume negative ions, which is usually a valid assumption for low pressure plasma, the currents  $I_e(V_f)$  and  $I_v(V_f)$  collected by the cylindrical probe of radius  $a$  and length  $l$  can be expressed as;

$$I_e(V_f) = \frac{1}{4}e(2\pi al)n_{e0}\langle v_e \rangle \exp\left[-\frac{(V_p - V_f)}{T_e}\right] \quad (5.27)$$

$$I_v(V_f) = \frac{1}{4}e(2\pi al)n_{v0}\langle v_v \rangle \exp\left[-\gamma_v\frac{(V_p - V_f)}{T_e}\right] \quad (5.28)$$

Here  $n_{e0}$  and  $n_{v0}$  are density of electrons and volume negative ions in the bulk respectively;  $\langle v_{e,v} \rangle = \sqrt{\frac{8K_B T_{e,v}}{\pi m_{e,v}}}$  are average thermal speeds of electrons and negative ions respectively;  $m_{e,v}$  and  $T_{e,v}$  are respective masses and temperature of electron and bulk negative ions;  $V_p$  and  $V_f$  are the plasma potential and the floating potential respectively;  $\gamma_v = T_e/T_v$  is temperature ratio of electron to the volume negative ions. The positive ion current  $I_p(V_f)$  is given as;

$$I_p(V_f) = h e n_{p0} (2\pi b l) u_B \quad (5.29)$$

Here  $b$  is the sheath radius corresponding to the floating potential  $V_f$ . If the sheath thickness  $(b - a) \ll a$  at floating potential, then the effective probe area  $[2\pi b l]$  at the floating potential can be approximated to the actual probe area  $(2\pi a l)$ .

Furthermore,  $h = n_{ps}/n_{p0}$  is a correction factor introduced due to the presence of pre-sheath, which basically relates the positive ion density  $n_{p0}$  in the bulk plasma to the corresponding value  $n_{ps}$  at the sheath edge;  $n_{ps}$  and  $n_{p0}$  individually satisfy the quasi-neutrality condition as  $n_{ps} = n_{es}(1 + \alpha_s)$  and  $n_{p0} = n_{e0}(1 + \alpha_0)$ ; where  $\alpha_0 = n_{v0}/n_{e0}$  and  $\alpha_s = n_{vs}/n_{es}$  are the electro-negativity parameter in the bulk and

at the sheath edge respectively.

The positive ion speed at the sheath edge  $u_B$  is given by [11];

$$u_B = \sqrt{eT_e/m_p} \sqrt{(1 + \alpha_s) / (1 + \alpha_s \gamma_v)} \quad (5.30)$$

The density of electrons and volume negative ions at the sheath edge is related to their respective density in the bulk plasma by  $n_{es} = n_{e0} \exp\left(-\frac{1}{2} \frac{1 + \alpha_s}{1 + \alpha_s \gamma_v}\right)$  and  $n_{vs} = n_{v0} \exp\left(-\frac{\gamma_v}{2} \frac{1 + \alpha_s}{1 + \alpha_s \gamma_v}\right)$ . Hence, the electro-negativity parameter at the sheath edge  $\alpha_s$  is related to the value  $\alpha_0$  in the bulk plasma by;

$$\alpha_s = \alpha_0 \exp\left[-\frac{(\gamma_v - 1)}{2} \frac{1 + \alpha_s}{1 + \alpha_s \gamma_v}\right] \quad (5.31)$$

Therefore the correction factor  $h$  can be expressed in terms of  $\alpha_s$  as follows;

$$h = \frac{n_{ps}}{n_{p0}} = \frac{1 + \alpha_s}{\exp\left[\frac{1}{2} \frac{1 + \alpha_s}{1 + \alpha_s \gamma_v}\right] \left(1 + \alpha_s \exp\left[\frac{(\gamma_v - 1)}{2} \frac{1 + \alpha_s}{1 + \alpha_s \gamma_v}\right]\right)} \quad (5.32)$$

Substituting (5-27) to (5-29) in (5-26), the floating condition of the probe gives;

$$\begin{aligned} \sqrt{\mu_{pe}} \exp\left[-\frac{(V_p - V_f)}{T_e}\right] + \sqrt{\mu_{pv}} \frac{\alpha_s}{\sqrt{\gamma_v}} \exp\left[\frac{(\gamma_v - 1)}{2} \frac{1 + \alpha_s}{1 + \alpha_s \gamma_v}\right] \exp\left[-\gamma_v \frac{(V_p - V_f)}{T_e}\right] \\ = \sqrt{2\pi} \exp\left[-\frac{1}{2} \frac{1 + \alpha_s}{1 + \alpha_s \gamma_v}\right] \sqrt{\frac{1 + \alpha_s}{1 + \alpha_s \gamma_v}} \end{aligned} \quad (5.33)$$

Furthermore, at the plasma potential, the net saturation current ratio  $R(V_p) = \frac{I_e(V_p) + I_v(V_p)}{I_p(V_p)}$  is expressed as;

$$R = \frac{\sqrt{\mu_{pe}} + \sqrt{\mu_{pv}} \frac{\alpha_s}{\sqrt{\gamma_v}} \exp\left[\frac{(\gamma_v - 1)}{2} \frac{1 + \alpha_s}{1 + \alpha_s \gamma_v}\right]}{\sqrt{2\pi} (1 + \alpha_s) \exp\left[-\frac{1}{2} \frac{1 + \alpha_s}{1 + \alpha_s \gamma_v}\right] \sqrt{\frac{1 + \alpha_s}{1 + \alpha_s \gamma_v}}} \quad (5.34)$$

In equations (5-33) and (5-34), there are a total of 6 unknown parameters ( $V_p$ ,  $V_f$ ,  $\alpha_s$ ,  $\gamma_v$ ,  $R$  and  $T_e$ ). Out of which, the parameters  $V_p$ ,  $V_f$ ,  $T_e$  and the saturation

current ratio  $R$  can be experimentally determined from the  $I(V_B)$  characteristic of a cylindrical Langmuir probe. Hence, the remaining parameters,  $\alpha_s$  and  $\gamma_v$  can be found by simultaneously solving (5-33) & (5-34). Once  $\alpha_s$  is obtained, the bulk electronegativity  $\alpha_0$  can be readily found using (5-31).

### 5.3.2 Experimental Results and discussion

For applying the above model, an experiment has been conducted in oxygen discharge using the experimental setup-1 described in Chapter-2. In the experiment, the parameters namely the saturation current ratio, the electron temperature, plasma potential, the floating potential and electron temperature are determined by the cylindrical Langmuir probe positioned in axis of the experimental chamber. For comparing the saturation current ratios, the probe has been initially calibrated with argon plasma.

#### (a) Langmuir Probe Characteristics

A typical plot for  $I(V_B)$  characteristic of the Langmuir probe in oxygen plasma is shown in Fig-5.9(a). The floating potential  $V_f$  is determined by inspecting the probe bias  $V_B$  at which the net current  $I$  collected by the probe is zero. The region below  $V_f$  has been enlarged in the same graph [inset graph (b)] to clearly visualize the positive ion saturation region. The ion saturation current  $I_{ps}$  has been determined by extrapolating the straight line up to the floating potential  $V_B = V_f$ . By doing this, the dependency of  $I_{ps}$  on the sheath thickness can be minimized. The value of  $V_p$  is determined by identifying the maxima in the first derivative of probe current as shown in Fig-5.9(c). The current corresponding to  $V_p$  gives the net saturation current ( $I_{es} + I_{vs}$ ) contributed from electrons and negative ions.

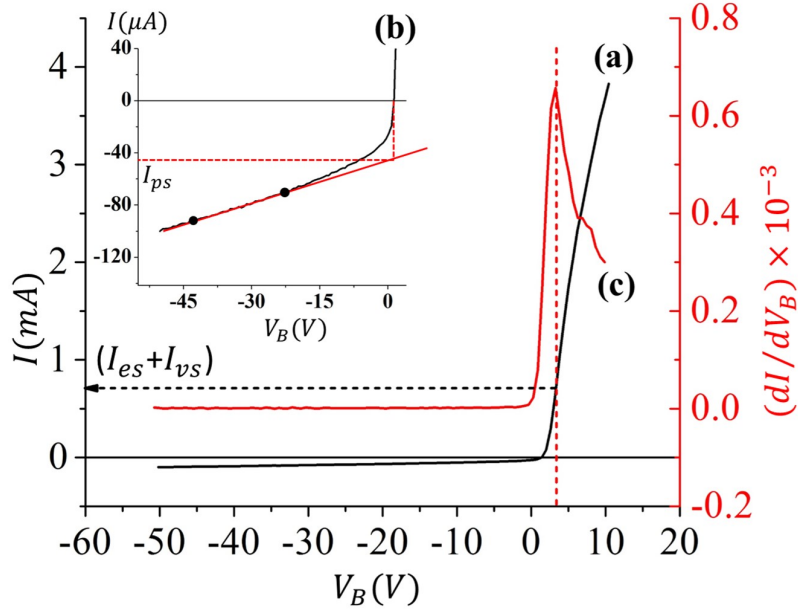


Figure 5.9: Plot of (a) a typical  $I(V_B)$  characteristics in an oxygen discharge, (b) ion saturation current  $I_{ps} = 45 \mu\text{A}$  obtained by extrapolating up to floating potential  $V_f = 1.3$  V and (c) the first derivative  $(dI/dV_B)$  curve giving the plasma potential  $V_p = 3.8$  V. The current corresponding to  $V_p$  gives the net saturation current  $(I_{es} + I_{vs}) = 0.7$  mA. The discharge power is  $P_w = 143$  watts & operating pressure is  $P = 4$  Pa.

A detail analyses of the above plot to obtain the electron temperature  $T_e$  shows two distinct slopes in the semi-log plot of  $I_e$  verses  $V_B$  as shown in fig-5.10. This corresponds to bi-Maxwellian electron distribution with temperatures  $T_{eb} = 0.6$  eV and  $T_{eh} = 4.6$  eV corresponding to bulk and hot population respectively.

Considering the bulk electron temperature  $T_{eb} = 0.6$  eV and floating potential  $V_f = 1.3$  V, the approximate value of the plasma potential can be estimated as  $V_p \approx V_f + 4.7 T_{eb} \approx 4.1$ . Here, we have considered  $O_2^+$  (mass 32 amu) as the most dominant positive ions species in oxygen [89]. This is consistent with the one estimated from the first derivative of the probe current ( $V_p = 3.8$  V) [c.f. fig-5.9(c)]. Another important fact which is evident from the fig-5.10 is that the slope of  $\ln(I_e)$  vs  $V_B$  curve corresponding to the hot electrons is found to appear below the floating

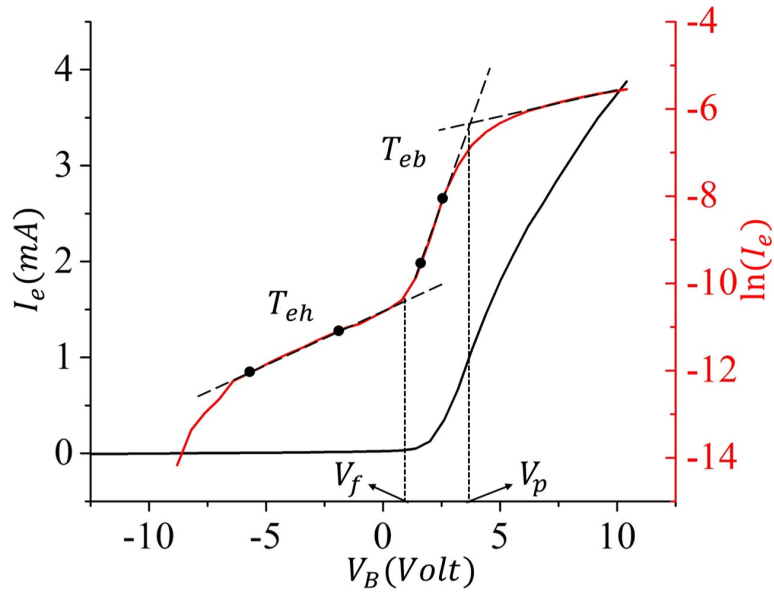


Figure 5.10: The plot for electron current  $I_e$  (left y-axis) and natural log of  $I_e$  (right y-axis) with respect to the probe bias  $V_B$ . Two slopes in  $\ln(I_e)$  plot corresponds to the two electron temperature  $T_{eb} = 0.6eV$  and  $T_{eh} = 4.6eV$ . The discharge power is  $P_w = 143$  watts & operating pressure is  $P = 4$  Pa.

potential. Therefore, in the overall characteristics, the hot electrons are apparently masked by the dominant contribution of positive ion flux to the probe surface. This can be verified by fitting a straight line in  $\ln(I_e)$  vs  $V_B$  curve corresponding to hot population, which makes an intercept with the line  $V_p = 3.8V$ . This gives an approximate estimate of current due to hot population of electron ( $\sim 70\mu A$ ) which is found to have only  $\sim 10\%$  contribution in total current ( $\sim 0.7mA$ ).

Figure-5-11 shows the plot of bulk and hot electron temperatures for a wide range of operating powers and gas pressures in oxygen discharge. It can be seen that the electron temperatures  $T_{eb}$  and  $T_{eh}$  remains almost constant with increase in the discharge power. However a slight decrement in  $T_{eb}$  is observed as the pressure is increased in the discharge chamber [186].

### (b) Saturation current ratio

Before obtaining the net saturation current ratio contributed due to electrons and negative ions in oxygen plasma, the Langmuir probe is first calibrated with argon

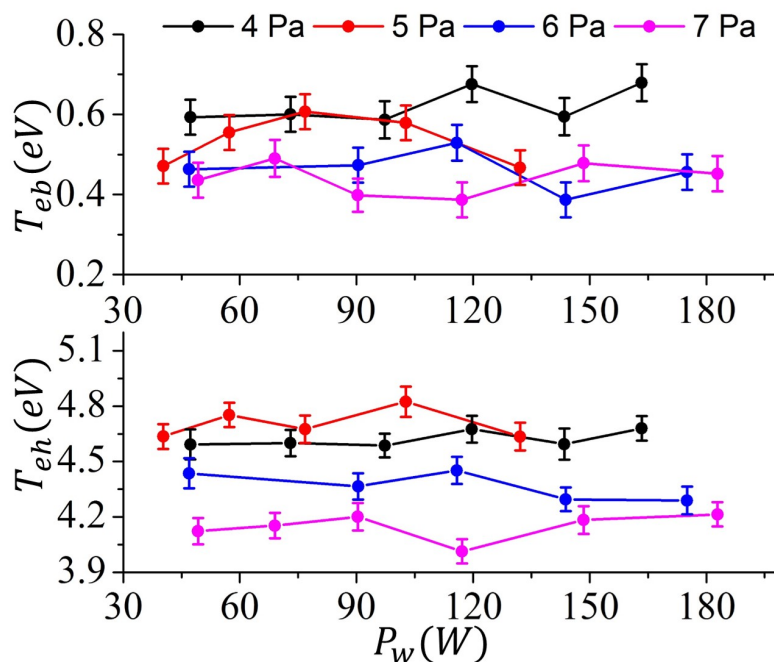


Figure 5.11: The plot for electron temperature  $T_{eb}$  and  $T_{eh}$  with respect to discharge power in oxygen plasma for pressure range  $P = 4$  Pa to 7 Pa.

plasma, which is purely composed of electrons and positive ions. Hence putting  $\alpha_s = 0$  in (5-34), the ratio  $R$  of the electrons to positive ion current is reduced to a constant factor  $R = \exp(1/2)\sqrt{m_p/2\pi m_e}$  ( $\approx 180$  for argon) [29]. This solely depends on the respective mass ratio. However in the case of electro-negative plasma, the relative ratio changes due to the contribution of negative ions as the probe bias approaches the plasma potential. In fig-(5.12) the saturation current ratio are plotted for both argon and oxygen discharge. As seen in the figure, the saturation current ratio remains almost constant for argon discharge, whereas it increases in the case for oxygen [186].

However, we observe an underestimated value of  $R$  by a constant value  $\sim 4.6$  even for the case of argon. The reason for observing this has been discussed in chapter-2. Therefore, in order to get the corrected values of saturation current ratio in oxygen, this constant value has been used as a correction factor for oxygen discharge. The similar calibration technique has also been adopted by several authors [25–28, 107, 108]. In fig-5.13, the calibrated ratio  $R$  for the oxygen discharge has been shown for

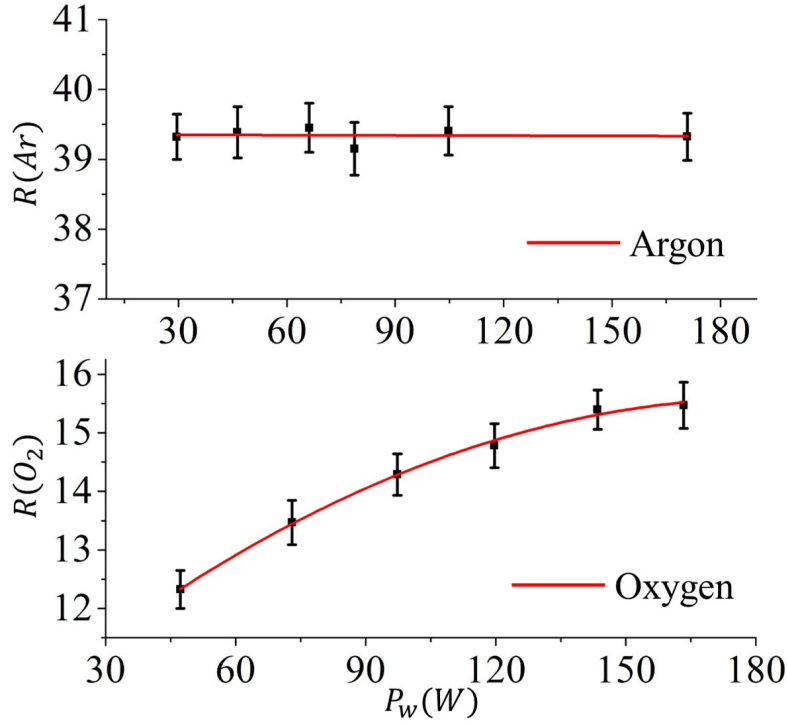


Figure 5.12: The plot for saturation current ratio with respect to discharge power in argon and oxygen discharge. The operating pressure is kept fixed at  $P = 4$  Pa.

a range of discharge power and operating pressure.

Furthermore, by using the measured values of  $V_p$  and  $V_f$  from  $I(V_B)$  characteristic and considering the bulk electron temperature  $T_e$ , the normalized values of floating potential  $(V_p - V_f)/T_e$  can be obtained. These are plotted in fig-5.14 with respect to the discharge power for a range of operating pressure.

Finally, incorporating the calibrated ratio  $R$  from fig-5.13 and the normalized potential  $\eta_f = (V_p - V_f)/T_e$  from fig-5.14, equation (5-33) and (5-34) are simultaneously solved to find the electronegativity parameter  $\alpha_s$  and the temperature ratio  $\gamma_v$ . Once  $\alpha_s$  is obtained, the corresponding value  $\alpha_0$  in the bulk can be found from (5-31).

Fig-5.15(a) & (b) shows the plot of  $\alpha_0$  and  $\gamma_v$  as a function of the discharge power for a range of pressures. It is seen that the electro-negativity parameter  $\alpha_0$  consistently decreases with the discharge power, but it increases with rise in background gas pressure [89, 187]. On the other hand, the corresponding values of  $\gamma_v$  remains almost constant with the discharge power but varies in the range  $\sim 8$  to  $\sim 12$

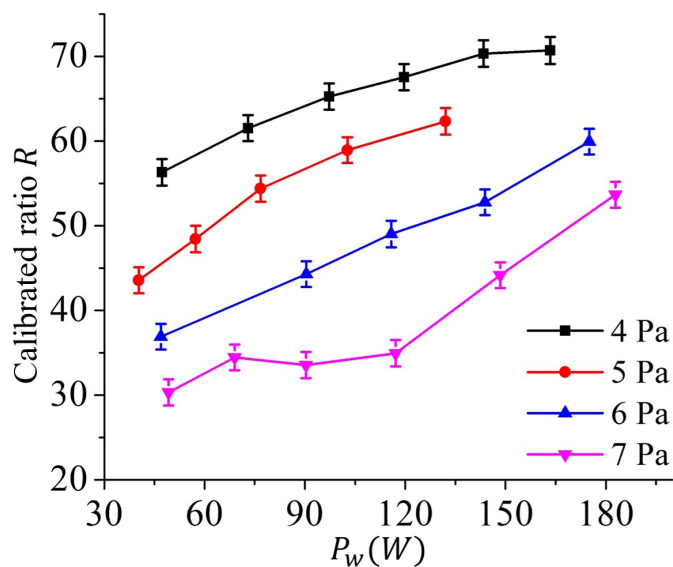


Figure 5.13: The plot for saturation current ratio with respect to discharge power and for various pressure in oxygen discharge.

with the pressure. Knowing  $\gamma_v$  values from fig-5.15(b) and bulk electron temperature from fig-5.11, the negative ion temperature can be estimated from the relation  $\gamma_v = T_e/T_v$ ; which is found to be in range  $\sim 0.05$  eV to  $\sim 0.07$  eV.

The observed trend in  $\alpha_0$  with discharge power and pressure can be explained as follows:

In an electro-negative discharge, the negative ions are continuously created and lost via series of reaction process. Oxygen negative ions inside the discharge is mainly produced by dissociative-attachment (DA) of ground state and metastable state neutrals. Whereas they are lost via; (1) electron impact detachment, (2) recombination of negative with positive ions and (3) excited neutrals impact detachment. However the loss due to ion-ion recombination is less probable than the detachment losses particularly for moderate to high pressures range [8].

With the increases in discharge power, the electron number density inside the discharge also increases. As a result, the negative ion density gets reduced due to electron impact detachment. On the other hand, with increase in the neutral gas density, the production rate of ground and metastable state atoms/molecules



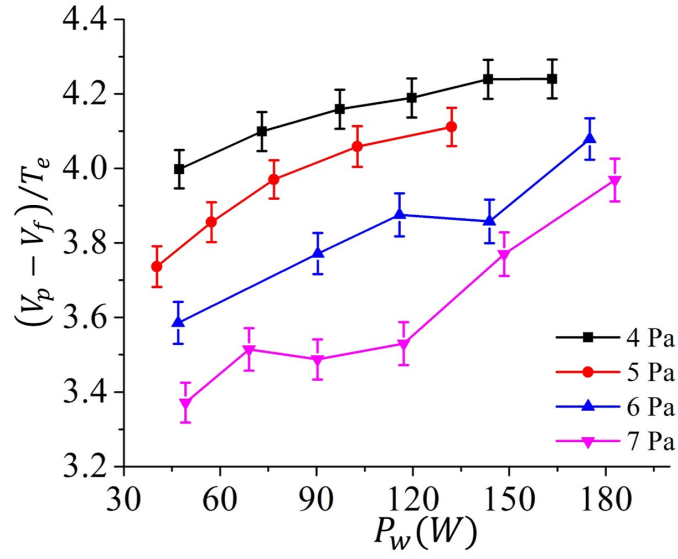


Figure 5.14: The plot for normalized value of floating potential  $(V_p - V_f)/T_e$  with respect to discharge power and for various pressure in oxygen discharge.

responsible for negative ion production through DA is comparatively larger than the loss rate of negative ions due to electron impact detachment [7, 87]. Hence as the fig-5.15(a) suggests, the electro-negativity parameter increases with a rise in gas pressure.

The rate of negative ion production also depend critically on electron temperature [11]. The hot electrons colliding with the oxygen molecules dissociate them into ground and metastable atoms/molecules, while the bulk or cold population of electrons attach themselves to these ground and metastable atoms/molecules to produce oxygen negative ions as the final product [81]. Therefore, the continuous increase in production rate of negative ions with the rise in gas pressure is associated with the loss in average kinetic energy of both hot and bulk population of electrons and hence their temperature is slightly reduced as observed in fig-5.11.

From fig-5.15(b), it can be seen that the electron temperature is about  $\sim 10$  times higher than the negative ion temperature i.e.  $\gamma_v \approx 10$ . In low pressure plasmas, the positive ions are generally in thermal equilibrium at room temperature ( $\sim 0.025$  eV) with the background neutrals [188]. Therefore, the negative ion temperature is

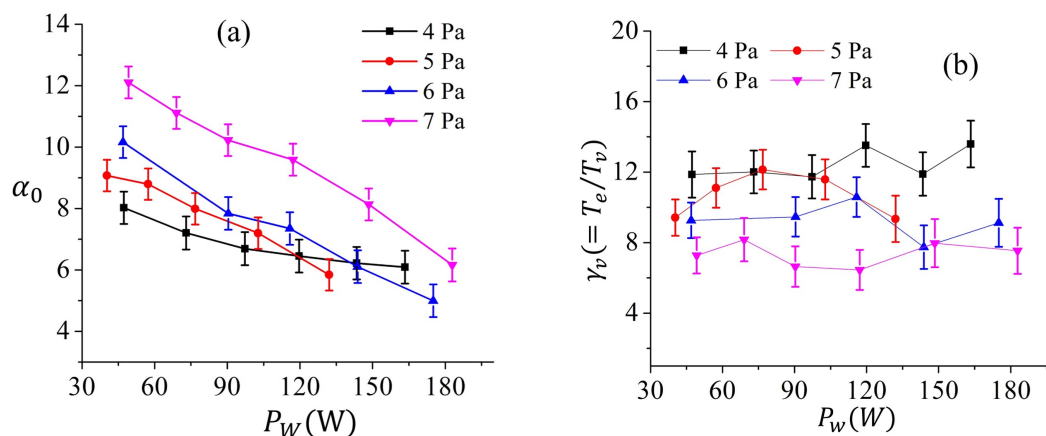


Figure 5.15: The plot for (a) the electro-negativity parameter  $\alpha_0$  and (b) the temperature ratio  $\gamma_v$  with respect to discharge power and for various pressure in oxygen discharge.

slightly higher than the positive ion temperature but less than the electron temperature, i.e.  $T_p < T_v < T_e$ . The reason for this is explained below:

In an electronegative discharge, the negative ions are continuously created and lost throughout the discharge. Those created in or near the boundary of the discharge i.e. near the sheath region, are accelerated towards the main body of plasma due to electron confining field and therefore gaining a large amount of kinetic energy. These negative ions impart their energy during collision with the heavy particles (positive ions and neutrals) due to their comparable mass and therefore cool down effectively and equilibrate to the gas temperature soon after they are formed. However, the probability of such elastic collisions for negative ions can be relatively low at low pressures and reduced further when the gas pressure is decreased. In such a highly destructive surrounding, these ions are often destroyed before they get significantly cooled. This results in elevating the mean negative ion temperature considerably higher compared to background positive ions.

### (c) Discussion

The trend of  $\alpha_0$  with discharge power and gas pressure is found to be in agreement with the reported work on global modeling of oxygen plasma by Gudmundsson

et al [89] and also in [189]. The variation in relative fraction of negative ions to the electrons obtained from Gudmundsson's work is shown in fig-5.16 for various discharge and gas pressure.

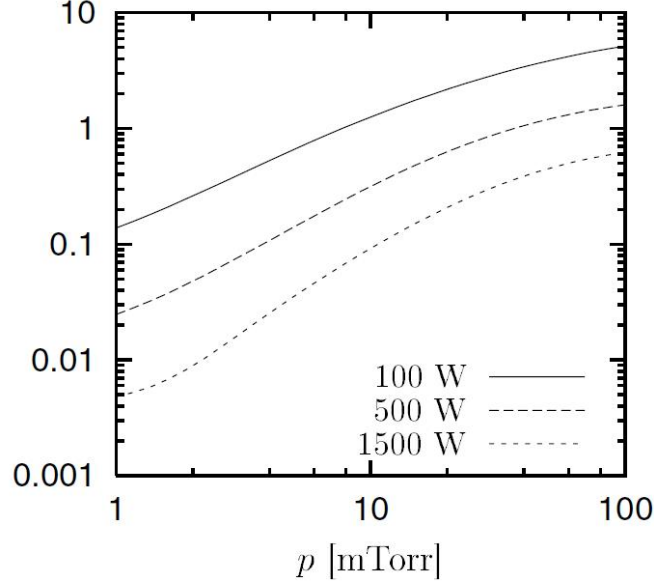


Figure 5.16: The electro-negativity parameter  $\alpha_0 = n_-/n_e$  with respect to pressure for three distinct discharge power 100, 500 and 1500 W. Courtesy: *J. T. Gudmundsson et al, J. Phys. D: Phys. 34, 1100–1109 (2001)*.

The above results was based on volume averaged model of an oxygen discharge obtained for a cylindrical geometry in the pressure range 1-100 mTorr. The electrons were assumed Maxwellian with temperature in range 1-7eV. In our case the operating pressure is in the range 30-50 mTorr and the electron temperature is in the range of  $\sim 0.5\text{eV}$  to  $1\text{eV}$ . As seen from the figure-5.16, the electro-negativity parameter decreases with discharge power but found to increase with the background gas pressure. This result is consistent with the observed trends obtained using the unique floating potential technique as demonstrated in fig-5.15(a). However, the magnitude of electro-negativity parameter is found to be  $\sim 1.5$  times higher in our case. This could be due to experimental error in the measurements of different parameters associated with the Langmuir probe technique.

The accuracy of the floating potential method to determine negative ion param-

eters will largely depend on precise estimation of the saturation current ratio. To estimate the underlying error, the saturation current ratio  $R$  from (5-34) can be expressed in the form;

$$R = A + B \quad (5.35)$$

Where;

$$A = \sqrt{\frac{\mu_{pe}}{2\pi}} \frac{(1 + \alpha_s)^{-3/2}}{(1 + \alpha_s \gamma_v)^{-1/2}} \exp\left(\frac{1}{2} \frac{1 + \alpha_s}{1 + \alpha_s \gamma_v}\right) \& \quad B = \sqrt{\frac{\mu_{pv}}{2\pi}} \frac{\alpha_s}{\sqrt{\gamma_v}} \frac{(1 + \alpha_s)^{-3/2}}{(1 + \alpha_s \gamma_v)^{-1/2}} \exp\left(\frac{\gamma_v}{2} \frac{1 + \alpha_s}{1 + \alpha_s \gamma_v}\right) \quad (5.36)$$

Using (5-35), the percentage error in  $R$  after few steps of algebraic manipulation is obtained as;

$$\frac{\delta R}{R} = f_1(\alpha_s, \gamma_v) \frac{\delta \alpha_s}{\alpha_s} \pm f_2(\alpha_s, \gamma_v) \frac{\delta \gamma_v}{\gamma_v} \quad (5.37)$$

Similarly, the floating potential equation (5-33) can be expressed as;

$$L = M + N \quad (5.38)$$

Where;

$$L = \sqrt{\mu_{pe}} \exp(\eta_f), M = \sqrt{\mu_{pv}} \frac{\alpha_s}{\sqrt{\gamma_v}} \exp\left[\frac{\gamma_v - 1}{2} \frac{1 + \alpha_s}{1 + \alpha_s \gamma_v}\right] \exp[\gamma_v \eta_f] \text{ and} \quad N = \sqrt{2\pi} \exp\left[-\frac{1}{2} \frac{1 + \alpha_s}{1 + \alpha_s \gamma_v}\right] \sqrt{\frac{1 + \alpha_s}{1 + \alpha_s \gamma_v}} \quad (5.39)$$

Using (5-38), the percentage error in  $\alpha_s$  and  $\gamma_v$  are related as;

$$f_3(\alpha_s, \gamma_v) \frac{\delta \alpha_s}{\alpha_s} \pm f_4(\alpha_s, \gamma_v) \frac{\delta \gamma_s}{\gamma_s} = 0 \quad (5.40)$$

The function  $f_1$ ,  $f_2$ ,  $f_3$  and  $f_4$  are given by;

$$\begin{aligned}
 f_1(\alpha_s, \gamma_v) &= \left( \frac{1 - \alpha_s}{1 + \alpha_s} \right) \left[ 1 - \frac{\alpha_s (\gamma_v - 1)^2}{2(1 + \alpha_s \gamma_v)^2} \right], f_2(\alpha_s, \gamma_v) = \frac{\alpha_s \gamma_v (\gamma_v - 1) (1 - \alpha_s)}{2(1 + \alpha_s \gamma_v)} \\
 f_3(\alpha_s, \gamma_v) &= \left[ 1 - \frac{\alpha_s (\gamma_v - 1)^2}{2(1 + \alpha_s \gamma_v)^2} \right] M - \frac{\alpha_s^2 (\gamma_v - 1)^2}{2(1 + \alpha_s) (1 + \alpha_s \gamma_v)^2} N \\
 \&f_4(\alpha_s, \gamma_v) &= \left[ \frac{(\gamma_v - 1) (1 + \alpha_s^2 \gamma_v) - 2\gamma_v \eta_f (1 + \alpha_s \gamma_v)^2}{(1 + \alpha_s \gamma_v)^2} \right] M - \frac{\alpha_s^2 \gamma_v (\gamma_v - 1)}{2(1 + \alpha_s \gamma_v)^2} N
 \end{aligned} \tag{5.41}$$

Finally from (5-31), the error  $\delta\alpha_0/\alpha_0$  in  $\alpha_0$  can be found as;

$$\frac{\delta\alpha_0}{\alpha_0} = \left[ 1 - \frac{\alpha_s (\gamma_v - 1)^2}{2(1 + \alpha_s \gamma_v)^2} \right] \frac{\delta\alpha_s}{\alpha_s} \pm \left[ \frac{\alpha_s \gamma_v (\gamma_v - 1) (1 - \alpha_s)}{2(1 + \alpha_s \gamma_v)^2} \right] \frac{\delta\gamma_v}{\gamma_v} \tag{5.42}$$

Equation (5-37), (5-40) and (5-42) can be simultaneously solved to find the error  $\delta\alpha_0/\alpha_0$  and  $\delta\gamma_v/\gamma_v$  in  $\alpha_0$  and  $\gamma_v$  respectively for experimentally measured error  $\delta R/R$  in  $R$ . The above analyses suggests that a small deviation of  $\sim 3\%$  in the measurement of  $R$  can lead to an uncertainty of  $\sim 6\%$  in the estimated values of  $\alpha_0$ ; and around  $\sim 12\%$  in  $\gamma_v$ . This has been illustrated by the error bars in figure 5-15(a) & (b) for variation in  $\alpha_0$  and  $\gamma_v$ .

Another method to experimentally determine negative ion temperature using the floating potential method was described in our previous paper [186]. In that work, the floating potential variation with electro-negativity parameter was obtained theoretically using equation-5.24, while keeping  $\gamma_v$  as a parameter. It was shown that for a particular value of  $\gamma_v$ , the theoretically obtained trend of floating potential verses electro-negativity parameter closely resembles with the trend obtained in the experiment using Langmuir probe. Hence, by finding the best fit between theoretical and experimental trend of  $\eta_f$  vs  $\alpha_s$ , the parameter  $\gamma_v$  can be approximately determined for a particular experiment. This is illustrated through the plots shown in figure-5.17. However, in that model the electronegativity parameter  $\alpha_s$  was estimated at

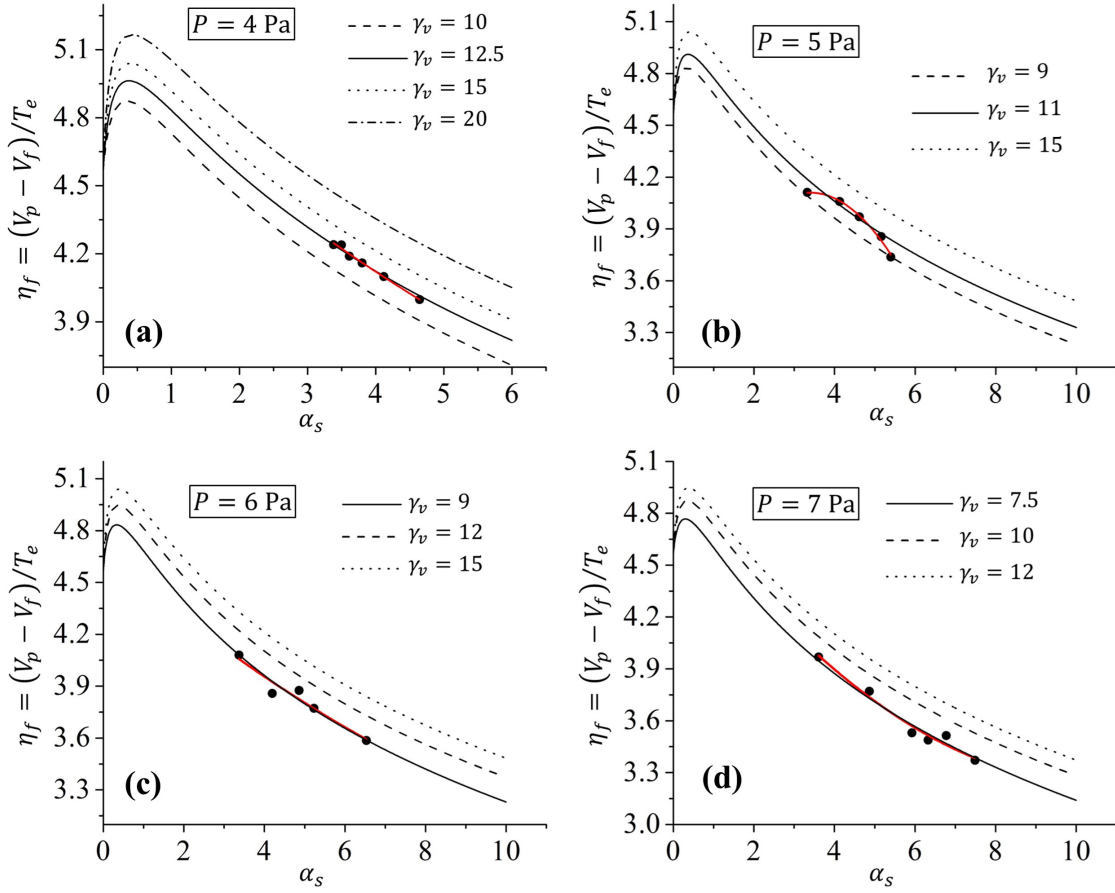


Figure 5.17: The theoretical plots of normalized value of floating potential  $\eta_f$  a function of  $\alpha_s$  for different  $\gamma_v$ . The scattered data points are obtained in the experiment for which the polynomial fit of  $2^{nd}$  order is observed to be the best fit coinciding with the theoretical curves for (a)  $\gamma_v \approx 12.5$  at pressure  $P = 4$  Pa, (b)  $\gamma_v \approx 11$  at pressure  $P = 5$  Pa (c)  $\gamma_v \approx 9$  at  $P = 6$  Pa and (d)  $\gamma_v \approx 7.5$  at  $P = 7$  Pa.

the sheath edge and not in the bulk plasma. This could result in certain amount of error in the estimation of absolute value of  $\gamma_v$ . Nevertheless, the qualitative trend of  $\alpha_s$  and floating potential with change in gas pressure and discharge power will remain the same.

## 5.4 Summary & Conclusion

In this chapter, the floating sheath characteristics for the case of a negative ion emitting and a non-emitting electrode immersed in an electro-negative plasma have

been separately investigated. Although the surface emission and bulk production of negative ions are completely two different production mechanism for negative ions in a discharge, however the magnitude of the floating potential on the electrode is found to decrease due to rise in both bulk electro-negativity and also as negative ion emission flux increases from the electrode. The positive ion Bohm speed, on the other hand, increases linearly with the emission flux of negative ions from the electrode, which is contrary to the effect of negative ions created in bulk for which the Bohm speed is found to decrease substantially. Thus the negative ions in the bulk plasma not only influence the sheath properties, but their production inside the sheath can also implicitly affect the bulk plasma characteristics.

Although the emission of negative ions from a floating substrate is equivalent to electron emitting surfaces as found in thermionic/secondary electron emission, however its impact on the sheath is much more pronounced as compared to electron emission due to larger mass of negative ions than electron. The negative ion emission from a floating substrate has important implication towards understanding the behavior of a floating sheath involving non-conducting emitters such as diamond, graphite and polycrystalline surfaces applied for efficient production of negative ions in negative ion sources. These emitters have advantage over the conventional Cs or Ba coated metallic emitters due to their long time operation in negative ion sources.

The role of magnetic field in surface emission based negative ion sources is important to filter out the co-existing electron flux during negative ion extraction. The present model can be further extended to study the impact of magnetic field on the transported flux of negative ions across the negative ion emitting sheath.

As an application to the floating potential characteristic of a non-emitting electrode, a cylindrical Langmuir probe has been used to estimate negative the ion temperature in an oxygen discharge by measuring the saturation current ratio  $R$  and the absolute value of floating potential  $\eta_f$  on the cylindrical probe surface. Since

both the measured quantity  $R(\alpha_0, \gamma_v)$  and  $\eta_f(\alpha_0, \gamma_v)$  are functionally dependent on the electronegativity parameter  $\alpha_0$  and the temperature ratio  $\gamma_v$ , therefore based on a phenomenological model, the value of  $\alpha_0$  as well as negative ion temperature  $T_v$  in terms of the temperature ratio  $\gamma_v = T_e/T_v$  can be experimentally determined. The present experiment suggests that the range of  $\gamma_v$  varies from  $\sim 8$  to  $\sim 12$ .

Although determining  $\alpha_0$  and  $\gamma_v$  from  $I(V_B)$  characteristic of the Langmuir probe is straightforward and simple, however their estimation is critically depends on the accuracy of determining the saturation current ratio. The presence of magnetic field can also affect the saturation current ratio due to finite larmor radius around the cylindrical probe. As a future scope, the above method could be applied in magnetized plasma environment to estimate negative ion parameter.

An important limitation in the above method is that the sheath thickness at the floating potential of the probe is neglected. Therefore the present method is applicable in the plasma where the thin sheath approximation is valid for  $I(V_B)$  characteristic analysis of Langmuir probe.



# Chapter 6

## Cylindrical DC sheath and its application to hairpin probe

### 6.1 Introduction

The DC sheath around a cylindrical wire is quite unique and it has a major significance in cylindrical probes that are widely used in the diagnostics of low temperature plasmas [190–192]. The sheath width around the cylindrical wire continues to increase with the applied probe bias; as a result, the positive ion saturation current at the probe surface increases due to an increase in the effective current collection area of the probe [193, 194]. In case of a hairpin probe, if the sheath radius becomes comparable with the inter-spacing between the probe pins, then it leads to a significant underestimation in electron density [30]. Therefore DC sheath width is an important parameter in cylindrical probes.

There are elegant theories available on cylindrical probes, which accounts for sheath width around a cylindrical wire [61, 131, 195, 196]; however due to its minuscule size, there is no straightforward method to measure it accurately. The sheath width is not only a function of applied voltage on the probe, but also depends on

---

electron/ion number density, electron temperature as well as negative ion parameters in case of an electro-negative plasmas [165].

The hairpin probe gives a possibility to estimate the sheath width around the hairpin probe experimentally based on a capacitance model developed by Peijak et al [30]. The capacitance model involves sheath width as a parameter, which was derived using a step-front sheath model [Ch-1 fig-1.3(c)]. Later N. Sirse et al applied the Child Langmuir law instead of step front sheath model to determine the sheath width [140]. However the electron temperature was separately measured with the help of an auxiliary Langmuir probe. In a recent work, David J Peterson [197] determined the electron-neutral collisional frequency in a high pressure discharge; however, the electron temperature required as an input to determine the collision rate was found from simulation.

In this work, the technique of applying a DC biased hairpin to obtain plasma parameter is introduced and negative ion fraction has been determined in the case of electronegative oxygen discharge. In section-6.2, the radial flow model of a cylindrical wire probe in a plasma containing electrons, negative ions and positive ions is presented to determine the sheath width. Section 6.3 discusses the basic methodology to find the sheath width, electron temperature and negative ion fraction in an argon/oxygen discharge. The diagnostic technique for investigating the effect of DC bias on the probe's resonance frequency is described in section-6.4. This is followed by experimental results and discussion in section-6.5. Finally, the main highlights of the Chapter is given in Section-6.6.

## 6.2 The radial flow model for cylindrical sheath

Radial flow model is a widely applied probe theory to describe ion motion inside the cylindrical sheath and associated current collection to the probe surface [61].

The model considers a pair of coaxial cylinders, with a central conducting electrode acting as the probe having a length  $l$  and radius  $r = a$ . The radius  $r = b$  of outer cylinder is defined as the sheath boundary as shown in the figure-6.1. The probe is biased at a negative potential  $\phi(a) \equiv \phi_a$  with respect to the potential at sheath boundary  $\phi(b) = 0$ . The length  $l$  is assumed to be much greater than the radius  $a$  so that the end effect of the probe is negligible [198]. Due to negative potential  $\phi_a < 0$ , a positive ion rich sheath is developed inside the region between  $r = a$  to  $r = b$ . Therefore the sheath thickness is given by  $s = b - a$ . Inside the sheath, the positive ions are radially accelerated towards the central electrode or probe.

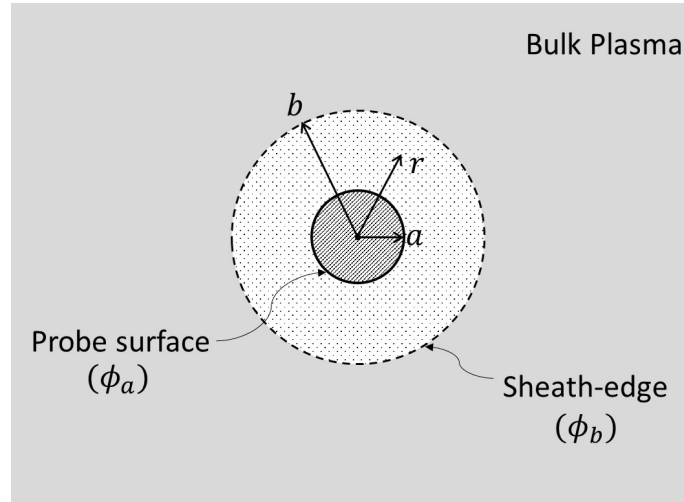


Figure 6.1: Schematic of sheath formation around the cross-section of a cylindrical probe with radius  $a$ . The sheath radius is  $b$ . The potential on the probe and at the sheath edge are respectively  $\phi_a$  and  $\phi_b$ .

The basic assumptions in this model are as follows: For collision-less, non-equilibrium plasmas, the negative charge species (electrons and negative ions) are assumed to have Boltzmann distribution [155],

$$n_{e,v}(r) = n_{e,vs} \exp\left(\frac{\phi(r)}{T_{e,v}}\right) \quad (6.1)$$

Here  $n_{e,vs}$  represent the density of electrons and negative ions at the sheath edge respectively; whereas  $T_{e,v}$  are their respective temperatures. The positive ions enters radially from the sheath edge with a finite Bohm velocity  $u_B$  [44]. For a low pressure

case, the ion-neutral mean free paths inside the sheath can be considered to be greater than the sheath dimension [116]. Therefore, positive ions are radially accelerated inside the sheath with zero angular momentum. Let  $\phi \equiv \phi(r)$  defines the potential anywhere inside the sheath. The assumption that  $s \ll l$  allows to approximate one dimensional model. Hence in cylindrical coordinates, the flux continuity and momentum equation for positive ions can be written as [165].

$$\frac{d}{dr} (rn_p v_p) = 0 \quad (6.2)$$

$$m_p \frac{d}{dr} (rn_p v_p^2) = -en_p r \frac{d\phi}{dr} \quad (6.3)$$

Whereas the Poisson equation is given by;

$$r \frac{d^2\phi}{dr^2} + \frac{d\phi}{dr} = -er \frac{(n_p - n_e - n_v)}{\varepsilon_0} \quad (6.4)$$

Using boundary conditions  $\phi(b) = 0$ ,  $n_p(b) = n_{ps}$  and  $v_p(b) = u_B$ , equation (6.2) & (6.3) can be simultaneously solved to obtain:

$$rn_p = bn_{ps} \left( 1 - \frac{2e\phi(r)}{m_p u_B^2} \right)^{-1/2} \quad (6.5)$$

Here  $n_{ps}$  is positive ion density, satisfying the quasi-neutrality condition  $n_{ps} = n_{vs} + n_{es}$  at the sheath edge. Introducing dimensionless parameter  $\alpha_s = n_{vs}/n_{es}$  in (6.5) and further substituting in (6.4) gives;

$$\begin{aligned} & r \frac{d^2\phi(r)}{dr^2} + \frac{d\phi}{dr} \\ &= -\frac{en_{es}}{\varepsilon_0} \left[ b(1 + \alpha_s) \left( 1 - \frac{2e\phi(r)}{m_p u_B^2} \right)^{-1/2} - r \exp\left(\frac{\phi(r)}{T_e}\right) - \alpha_s r \exp\left(\gamma_v \frac{\phi(r)}{T_e}\right) \right] \end{aligned} \quad (6.6)$$

Here  $\alpha_s$  is electro-negativity parameter defined at the sheath edge.

Whereas,  $u_B = \sqrt{\frac{eT_e}{m_p}} \sqrt{\frac{1+\alpha_s}{1+\gamma_v\alpha_s}}$  is positive ion Bohm speed and  $\gamma_v = \frac{T_e}{T_v}$  is temperature ratio of electron to negative ions.

Equation (6.6) can be re-written in terms of Debye length  $\lambda_{Ds} = \sqrt{\frac{\varepsilon_0 T_e}{en_{es}}}$  at the sheath edge, electron temperature  $T_e$  and sheath thickness  $b$  as follows;

$$-\frac{\lambda_{Ds}^2}{T_e} r \frac{d^2\phi(r)}{dr^2} - \frac{\lambda_{Ds}^2}{T_e} \frac{d\phi}{dr} = b(1+\alpha_s) \left(1 - \frac{2\phi(r)}{U_B^2 T_e}\right)^{-1/2} - r \exp\left(\frac{\phi(r)}{T_e}\right) - \alpha_s r \exp\left(\gamma_v \frac{\phi(r)}{T_e}\right) \quad (6.7)$$

In (6.7),  $U_B = \sqrt{\frac{1+\alpha_s}{1+\gamma_v\alpha_s}}$  is dimensionless Bohm speed of positive ions.

It can be shown that on substituting  $\alpha_s = 0$ , equation (6.7) reduces to Bohm speed for a electro-positive plasma, consisting of electrons and singly charged positive ions; i.e.

$$-\frac{\lambda_{Ds}^2}{T_e} \left(r \frac{d^2\phi(r)}{dr^2}\right) - \frac{\lambda_{Ds}^2}{T_e} \frac{d\phi}{dr} = b \left(1 - \frac{2\phi(r)}{T_e}\right)^{-1/2} - r \exp\left(\frac{\phi(r)}{T_e}\right) \quad (6.8)$$

In deriving (6.7) & (6.8), potential on the probe surface was defined with respect to the sheath edge. However in actual experiments, the DC bias  $V_B$  applied to the probe and the plasma potential  $V_p$  both are measured with respect to the grounded vacuum vessel. Furthermore, there exists a finite potential drop across the pre-sheath  $\Phi_p$ . Therefore, in order to apply (6.7) & (6.8) in an experiment, the probe potential should be considered as  $\phi_a = V_B - (V_p + \Phi_p)$ .

Moreover, the electron density  $n_{e0}$  in the bulk plasma is related to its corresponding density  $n_{es}$  at the sheath edge by  $n_{es} = n_{e0} \exp\left(-\frac{\Phi_p}{T_e}\right)$ . With this relation, the Debye length  $\lambda_{Ds} = \sqrt{\frac{\varepsilon_0 T_e}{en_{es}}}$  at the sheath edge can be found with regard to the electron density  $n_{e0}$  measured in the bulk plasma.

For electro-negative plasma, the pre-sheath potential  $\Phi_p$  is given by;

$$\frac{\Phi_p}{T_e} = \frac{1}{2} \frac{1 + \alpha_s}{1 + \gamma_v \alpha_s} \quad (6.9)$$

Whereas, it reduced to  $\frac{\Phi_p}{T_e} = \frac{1}{2}$  for pure electro-positive argon plasma.

Once  $\lambda_{Ds}$  and  $T_e$  are experimentally determined, equation-(6.7) & (6.8) can be iteratively solved by providing the boundary condition  $\phi_a = V_B - (V_p + \Phi_p)$  and  $\phi_b = 0$  to find a unique value of  $b$  for which the boundary condition  $\phi'(b) = \frac{K_B T_e}{e \lambda_{Ds}}$  [171] is simultaneously satisfied. Once  $b$  is obtained for a given  $V_B$ ,  $s \equiv b - a$  gives the sheath width around the cylindrical wire at  $V_B$ .

### 6.3 DC biased hairpin probe: Underlying concept

In chapter-2, the basic principle of a hairpin probe was introduced for an ideal case in which the sheath around the resonator pins had been ignored. However, if a constant negative dc potential is applied to the hairpin probe, a sheath develops around the probe pins as shown in figure-6.2.

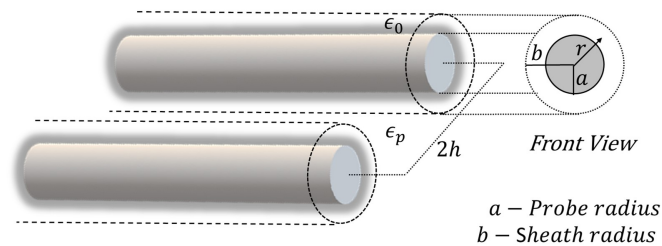


Figure 6.2: The schematic of the sheath formed around the hairpin tips. The sheath radius is  $b$ , and probe radius is  $a$  (front view). The separation between the hairpin is  $2h$ .

Due to formation of sheath, a substantial region between the pins become devoid of electrons. The sheath region can be treated as a free-space having vacuum dielectric constant  $\epsilon_0$ . As a result, the HP sees an effective dielectric constant  $\epsilon_{eff}$  due

to the contribution of both plasma dielectric  $\epsilon_p$  and the sheath dielectric  $\epsilon_0$  around the probe pins [fig-6.2]. Since  $\epsilon_0 > \epsilon_p$ , therefore  $\epsilon_{eff}$  will be higher, as a result the probe's resonance frequency will shift towards a lower value. Hence the electron density is underestimated according to the formula described in equation-(2-12) of Chapter-2.

For compensating the effect due to sheath width on probe's resonance frequency, Sands et al. [199] introduced a sheath correction factor  $\xi_s$ , which is a function of sheath radius  $b$ . This was derived by equating the equivalent capacitance formed by the conjugate dielectric between the pins with the series combinations of individual capacitances due to sheath and plasma between the probe pins. Hence, equation (2.12) can be modified to express the plasma frequency as follows;

$$f_p^2 = \frac{f_r^2 - f_0^2}{\xi_s} \quad (6.10)$$

with  $\xi_s$  as the correction factor given by;

$$\xi_s = 1 - \frac{f_0^2 \ln\left(\frac{2h}{a} - 1\right) - \ln\left(\frac{2h}{b} - 1\right)}{f_r^2 \ln\left(\frac{2h}{a} - 1\right)} \quad (6.11)$$

Combining equations (6.10) and (6.11), it allows to relate the sheath radius  $b$  with probes resonance frequency  $f_r$  that can be obtained experimentally; provided electron plasma frequency  $f_p$  is known. Since  $f_p$  should not change by biasing the probe, hence it can be determined accurately if the sheath around the hairpin is vanishingly small. This situation can be achieved by biasing the probe up to the plasma potential  $V_p$ . Hence,

$$f_r^2(V_p) - f_0^2 = \frac{f_r^2(V_B) - f_0^2}{\xi_s(V_B)} \quad (6.12)$$

Where  $f_r(V_p)$  &  $f_r(V_B)$  corresponds to resonance frequency when the probe is biased at  $V_p$  &  $V_B$  respectively. The overall concept has two important benefits:

(1) It allows to determine the sheath radius experimentally as a function of probe bias  $V_B$ ; without relying on electron temperature from other diagnostic.

(2) The sheath width corresponding to floating potential  $V_f$  can be used to estimate the electron temperature by equating the total current collected by the probe to zero.

In addition, positive ion saturation current to the hairpin for a sufficiently large negative bias can be used to determine negative ion parameters  $\alpha_0$ . This is described below.

Applying net current at floating potential to zero, we get;

$$I_e(V_f) + I_v(V_f) = I_p(V_f) \quad (6.13)$$

with subscripts  $e$ ,  $v$  and  $p$  corresponds to electron, volume negative ion and positive ions. The individual currents due to electrons and negative ions can be expressed:

$$I_{e,v}(V_f) = [2\pi eal]n_{e,v0}\sqrt{\frac{eT_{e,v}}{2\pi m_{e,v}}}\exp\left(-\frac{V_p - V_f}{T_{e,v}}\right) \quad (6.14)$$

Whereas for the positive ions;

$$I_p(V_f) = h[2\pi eb(V_f)l]n_{p0}\sqrt{\frac{eT_e}{m_p}}\sqrt{\frac{1 + \alpha_s}{1 + \gamma_v\alpha_s}} \quad (6.15)$$

In (6.15),  $h = n_{ps}/n_{p0}$  is correction factor which relates the positive ion density inside the bulk ( $n_{p0}$ ) to its corresponding sheath edge density ( $n_{ps}$ ) [c.f. (5-32) Chapter-5]. Quasi-neutrality condition is satisfied at the sheath edge, i.e.  $n_{ps} = n_{es} + n_{vs}$  and also inside the bulk plasma  $n_{p0} = n_{e0} + n_{v0}$ . The sheath radius  $b(V_f)$  corresponds at the floating potential  $V_f$ ; which can be determined from equation (6.12) by replacing  $V_B$  with  $V_f$ .

As usual, the constant parameters  $m_{e,p,v}$  are the respective masses of electrons,



positive ions and negative ions,  $e$  is the electronic charge and  $T_{e,v}$  are the temperature of electrons and negative ions respectively;  $\alpha_s = n_{vs}/n_{es}$  is ratio of negative ion to electron concentration at the sheath edge and  $\gamma_v = T_e/T_v$  is temperature ratio of electron to negative ions.

In equations (6.14), the current collecting area for electrons and negative ions has been considered as the probe area, since these are the thermal currents reaching the probe surface. On the other hand for positive ions, the effective collection area of the probe corresponds to the sheath area. This is because the positive ion flux remain conserved inside the sheath [166].

Substituting  $I_{e,v}(V_f)$  and  $I_p(V_f)$  from (6.14) and (6.15) in (6.13), an expression can be obtained which relates the electro-negativity parameter  $\alpha_s$  and  $\gamma_v$  in terms of sheath-width  $b(V_f)$  and the normalized floating potential  $\frac{V_p - V_f}{T_e}$  as follows;

$$\begin{aligned} hb(V_f)(1 + \alpha_0) \sqrt{\frac{1 + \alpha_s}{1 + \gamma_v \alpha_s}} \\ = \frac{a}{\sqrt{2\pi}} \left[ \sqrt{\mu_{pe}} \exp\left(-\frac{V_p - V_f}{T_e}\right) + \sqrt{\mu_{pv}} \frac{\alpha_0}{\sqrt{\gamma_v}} \exp\left(-\gamma_v \frac{V_p - V_f}{T_e}\right) \right] \end{aligned} \quad (6.16)$$

Where,  $\mu_{pe,v} = m_p/m_{e,v}$  is the relative mass of positive ions to electrons /negative ions. The electronegativity parameters,  $\alpha_0$  and  $\alpha_s$  in equation (6.16) corresponds to bulk plasma and the sheath edge respectively. They are related as;

$$\alpha_0 = \alpha_s \exp\left[\left(\frac{\gamma_v - 1}{2}\right) \frac{1 + \alpha_s}{1 + \gamma_v \alpha_s}\right] \quad (6.17)$$

In (6.16), there are two unknown parameters  $\alpha_s$  and  $\gamma_v$ , which needs to be determined; hence another equation is required. This can be obtained by biasing the probe sufficiently to a negative potential to draw an ion saturation current  $I_p(V_B)$ ,

which is expressed as;

$$I_p(V_B) = h[2\pi eb(V_B)l](1 + \alpha_0) \sqrt{\frac{eT_e}{m_p}} \sqrt{\frac{1 + \alpha_s}{1 + \gamma_v \alpha_s}} \quad (6.18)$$

where  $b(V_B)$  is the sheath radius corresponds to the bias voltage  $V_B$ . Now (6.16), (6.17) and (6.18) can be simultaneously solved to determine the parameters  $\alpha_0$  and  $\gamma_v$ .

Furthermore, on substituting  $\alpha_0 = 0$  for a pure electro-positive plasma, equation (6.16) reduces to;

$$\frac{b(V_f)}{a} = \exp\left(-\frac{1}{2}\right) \sqrt{\frac{\mu_{pe}}{2\pi}} \exp\left[-\frac{V_p - V_f}{T_e}\right] \quad (6.19)$$

The above equation relates the sheath thickness at the floating potential  $b(V_f)$  to the electron temperature. Thus the above technique provides possibility to determine  $T_e$  in an electro-positive plasma

## 6.4 DC Biased hairpin Probe: The experimental process

To bias the hairpin, which is made of tungsten wire having diameter 0.15 mm, a 0.5 mm pure copper wire is twisted at the short-circuited end of the hairpin and pulling it tightly through the ceramic tube, as shown in fig-6.3. The electrical connection is tested to ensure good conductivity between the copper wire and the hairpin. The length of the hairpin probe as measured from the center of the short-circuited end is  $L + h = 26.0$  mm; the separation between the pins is  $2h = 3.0$  mm.

The biasing circuit of the hairpin is same as that applied to Langmuir probe setup

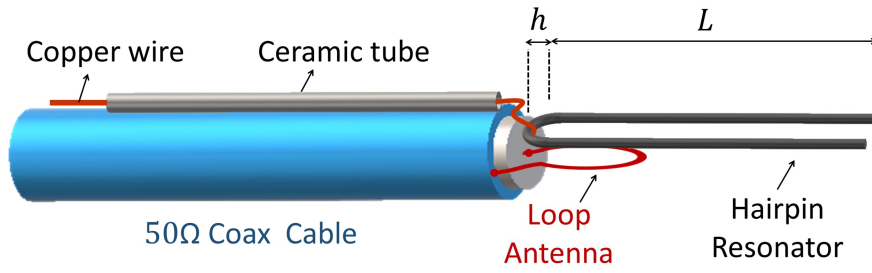


Figure 6.3: The schematic of DC biased hairpin probe. The total length of hairpin is  $L + h$ .

described in Chapter-2. The resonance detection circuit of the hairpin also remains the same as described in chapter-2 for the operation of a floating hairpin [see section-2.4]. When a constant negative DC voltage  $V_B$  is applied to the hairpin, a positive ion sheath is formed around the probe tip, whose thickness is expected to decrease as the probe is biased towards the plasma potential  $V_p$ . As a result, the resonance frequency  $f_r$  of the probe will continue to shift towards the higher frequency value, until the effective dielectric constant  $\epsilon_{eff} = \epsilon_p$ . The effect of biasing on the resonance signal is shown in figure-6.4.

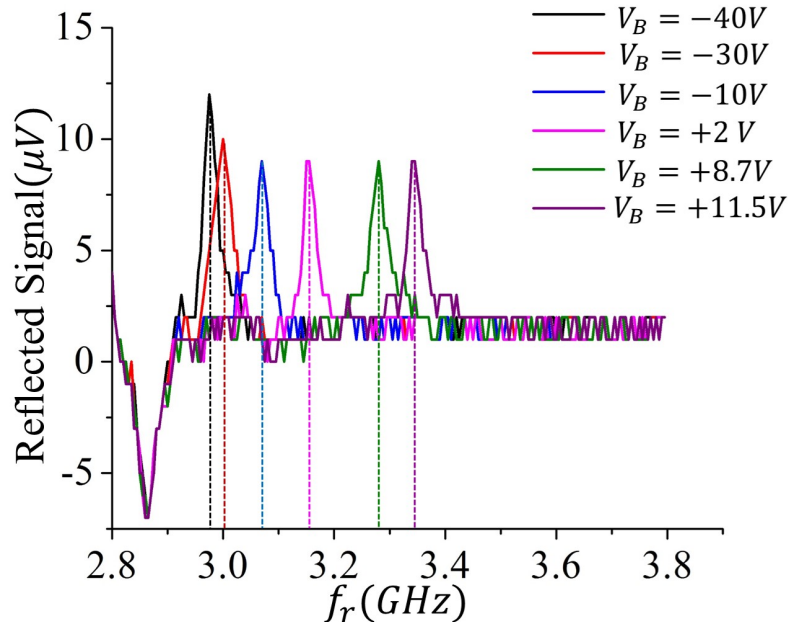


Figure 6.4: The reflected microwave signal (subtracted by the vacuum value) with respect to the frequency sweep  $f_r$  (GHz) for various bias applied to the probe. The operating pressure is  $P = 1.8$  Pa and discharge power is  $P_w = 49.5$  W.

In the above figure, the resonance signal at various DC bias has been subtracted from the signal acquired in the absence of plasma. Therefore the resonance signal corresponding to vacuum resonance frequency  $f_0 = 2.86$  GHz is identified by the minima in the above plot. The theoretical value of resonance frequency considering  $L = 26.0$  mm also gives a value 2.88 GHz, which is sufficiently close to the measured resonance signal. Furthermore, it is also observed that the quality of resonance signal is not deteriorating much with the probe bias. Thus the check ensures that the addition of external biasing circuit does not affect the performance of the probe due to unwanted capacitive loading. The subtraction method cancel the common background noise and improves the signal to noise ratio.

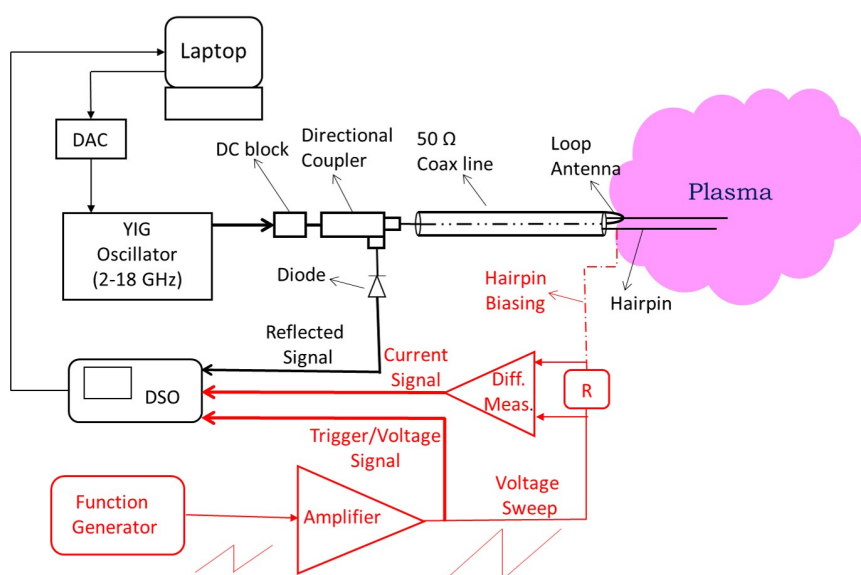


Figure 6.5: Schematic of the biased hairpin measurement circuit. The resonance detection circuit and the biasing circuit to the hairpin are individually shown in black and red color respectively.

For automating the system, the bias given on the probe was ramped from -60 V to +20 V at 100 Hz by using a combination of low amplitude saw-tooth signal from a function generator (Agilent Model No: 33522A) and a linear amplifier (Falco System-WMA-300). The corresponding current drawn by the hairpin probe was measured across a series resistor ( $R = 330\Omega$ ) using a differential probe (SIGLENT

Diff probe Model no: DPB 5150) and acquired in the digital oscilloscope (DSO Tektronix 3034C). Simultaneously, microwave frequency range from 2.0 GHz to 4.0 GHz was applied to the loop antenna of the hairpin in steps of 5 MHz and the corresponding reflected signal was acquired, digitized and stored in a PC. At each time during the ramping phase, the microwave frequency on the loop antenna was kept constant. Therefore the probe resonated at different times due to change in sheath width, which is a function of the biasing voltage applied on the hairpin. This technique is similar to time-resolved method applied in pulsed plasma [133]. The only difference is that the sheath width around hairpin is changing, while the background plasma remains in steady state.

A typical time-resolved resonance frequency verses applied voltage on the probe is plotted in fig-6.6(a). The current drawn by the biased hairpin probe and its first derivative are also shown in the same figure-6.6(b) & 6.6(c) respectively.

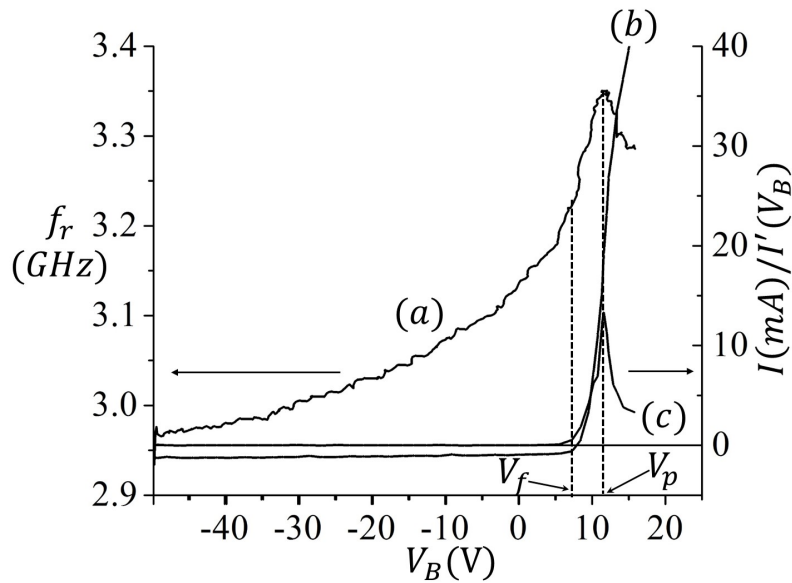


Figure 6.6: The variation in (a) resonance frequency  $f_r$  and (b) current collected by the hairpin with respect to the probe bias voltage  $V_B$  at a typical discharge power  $P_w = 49.5$  W and operating pressure  $P = 1.8$  Pa. The peaks observed in frequency curve and the (c) first derivative curve coincide at the same bias, providing the plasma potential  $V_p = 11.5$  V, whereas the floating potential  $V_f = 7.5$  V is obtained directly by measuring the potential on the floating probe inside the discharge.

In above figure, the maxima in resonance frequency  $f_r$  and the first derivative of

$I - V_B$  trace seems to coincide at the bias  $V_B = +11.5\text{V}$ , indicating that the bias  $V_B = V_p$  corresponds to plasma potential [31, 144]. At plasma potential, the sheath becomes vanishingly small around the resonator pins. Above plasma potential, i.e.  $V_B > V_p$ ,  $f_r$  seems to drop. This could be possible due to formation of an electron sheath around probe tips, as a result of which the electrons are rapidly lost to the probe. This leads to a fall in electron density around the hairpin and therefore the corresponding fall in resonance frequency as evinced from the figure.

In the entire experiment the maximum probe current drawn by the probe ( $< 15$  mA) is typically 8 % compared with the discharge current ( $\sim 160$  mA). However during the experiment, one should limit biasing the probe extensively above the plasma potential, otherwise it could contaminate the probe surface by sputtering or could damage the probe-electronics due to large return current.

## 6.5 Experimental results

### 6.5.1 Determining the Sheath Width

The sheath width  $s = b - a$ , is a function of sheath radius  $b$ , where  $a = 0.075$  mm is the wire radius. For obtaining the sheath radius, equations-(6.11) and (6.12) are simultaneously solved, in which the resonance frequency  $f_r(V_p)$  at the plasma potential is identified from the inflection point of  $f_r$  vs  $V_B$  curve. A typical plot of probe radius  $b$  as a function of probe bias  $V_B$  for three different discharge power in argon plasma is shown in figure-6.7. The plasma potential  $V_p$  corresponds to the bias voltage at which the sheath radius  $b = a$ ; this is shown in the inset graph.

The sheath radius decreases as the bias  $V_B$  on the probe approaches towards the plasma potential  $V_p$ . At  $V_p$ , the sheath radius becomes equal to probe radius. Furthermore, the sheath width is found to be higher when the discharge is operated

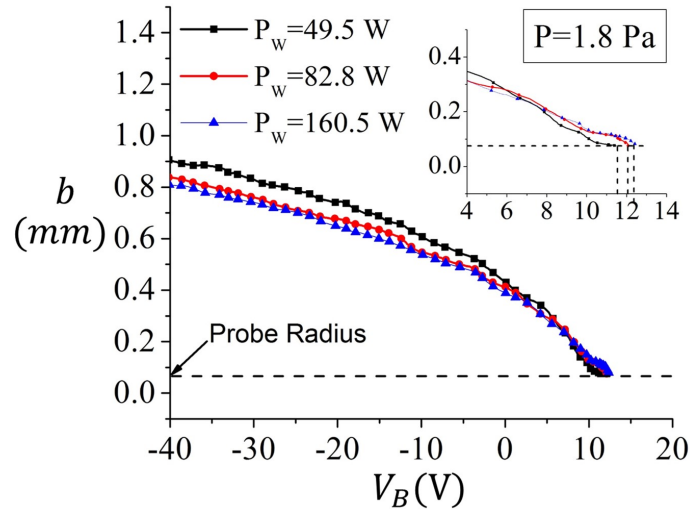


Figure 6.7: The variation in sheath thickness,  $s = (b - a)$  with probe bias  $V_B$  for a typical operating pressure 1.8 Pa is shown. The probe radius is  $a = 0.075$  mm; whereas the sheath radius  $b$  is calculated by solving (6.11) & (6.12).

at lower power, as the corresponding plasma density is low.

Similarly, the sheath width for electro-negative oxygen plasma can be found using same set of equations.

The constant parameters obtained from the experiments in argon and oxygen plasma are given in table-6.1 & 6.2 respectively:

Sr. No.	Discharge Power (Watts)	Plasma Potential $V_p$ (V)	Floating Potential $V_f$ (V)	$b(V_f)$ (mm)	$f_r(V_p)$ (GHz)	$f_r(V_f)$ (GHz)	$I_{ps}$ (mA) at $V_B = -40V$	$b(V_B)$ (mm) at $V_B = -40V$
1.	18.2	9.5	6.9	0.27	3.13	3.04	0.45	1.0
2.	49.5	11.5	8.5	0.17	3.35	3.27	1.05	0.92
3.	82.8	12.4	9.3	0.16	3.53	3.44	1.27	0.85
4.	160.5	12.5	9.4	0.15	3.60	3.49	1.32	0.82

Table 6.1: The various measured parameters from the experiment for 1.8 Pa pressure in argon plasma

### 6.5.2 Finding Electron temperature

The electron temperature can be found from equation (6.19) for the case of electro-positive argon plasma. For this, information of plasma potential  $V_p$  and

Sr. No.	Discharge Power (Watts)	Plasma Potential $V_p$ (V)	Floating Potential $V_f$ (V)	$b(V_f)$ (mm)	$f_r(V_p)$ (GHz)	$f_r(V_f)$ (GHz)	$I_{ps}$ ( $\times 10^{-4}$ ) (A) at $V_B = -40V$	$b(V_B)$ (mm) at $V_B = -40V$
1.	10.5	5.3	1.4	0.52	2.99	2.93	2.01	0.90
2.	23.7	7.8	4.2	0.46	3.08	2.99	3.77	0.89
3.	48.2	11.6	7.9	0.38	3.17	3.07	5.64	0.87
4.	82.1	13.8	10.5	0.29	3.26	3.14	7.71	0.88
5.	99.2	14.9	11.3	0.30	3.28	3.15	8.17	0.87

Table 6.2: The various measured parameters from the experiment for 1.8 Pa pressure in oxygen plasma.

sheath radius  $b(V_f)$  at the floating potential is required. These quantities can be easily obtained from the plot of  $f_r$  vs  $V_B$  curve. The values of  $b(V_f)$  for 1.8 Pa is given in table-6.1 for argon plasma.

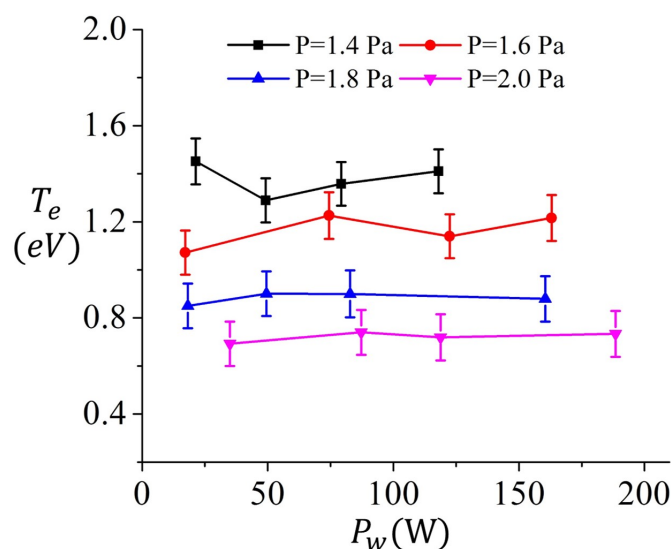


Figure 6.8: The variation in electron temperature,  $T_e$  with regards to the power & pressure in argon plasma.

It is seen from figure-6.8 that the electron temperature remains almost constant with the varying discharge power. This is in agreement with global power balance model [89]. On the other hand as the gas pressure increases, the electron temperature falls due to increase in electrons collisions with background neutrals, causing the average kinetic energy of the electrons to reduce.

In order to validate the electron temperature obtained using the above exper-



imental technique, we took advantage of the radial flow model [c.f. eqn-(6.8)] of cylindrical sheath described in section 6.2 to calculate the sheath width and compared it with the sheath width determined experimentally from the capacitance model.

In the analytical model [c.f. eqn-6.8],  $\lambda_{D_s}$  and  $T_e$  are the two independent parameters. The absolute electron density  $n_{e0}$  can be found by biasing the probe up to plasma potential. On the other hand,  $T_e$  is obtained from the above experimental technique. Therefore the Debye length  $\lambda_{D_s}$  can be calculated at the sheath edge by using  $n_{es} = 0.61n_{e0}$ . This has been supplied in equation-6.8 to calculate sheath width analytically. This is shown for typical discharge powers 49.5 W & 82.8W at a fixed pressure 1.8 Pa.

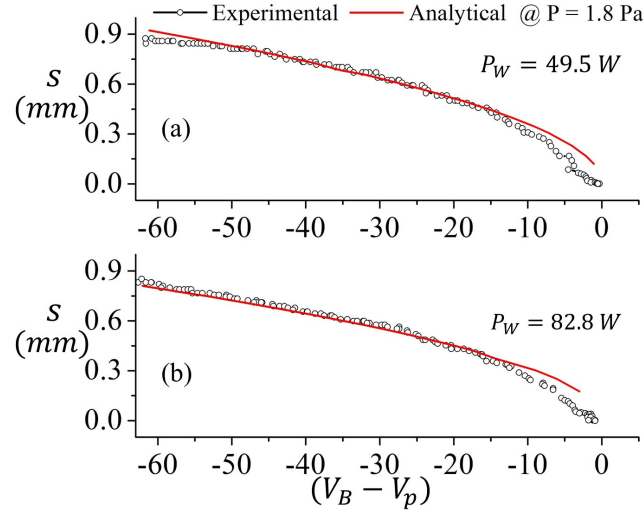


Figure 6.9:  $T_e$  obtained in fig-6.8 along with the  $n_{e0}$  found from measured resonance frequency at the  $V_p$  are used in equation-6.8 to obtain the sheath thickness with respect probe bias (solid curve). The typical discharge power considered are (a)  $P_w = 49.5$  W (b)  $P_w = 82.8$  W at pressure 1.8 Pa. The solid curve obtained from the analytical model shows a good match with the sheath thickness found from the experiment (bubbled curve).

From the above plots, a good agreement observed between the sheath width calculated theoretically and from the experimental technique, suggests that the biased hairpin probe can be a promising method to determine electron temperature in electro-positive plasma.

For the further verification of above technique, one can also determine electron temperature from the positive ion saturation current corresponding to a very large negative bias  $V_B = -40V$  relative to the plasma potential at which the contribution of electrons and negative ions can be neglected. This is given by;

$$I_{ps}(V_B) = 0.6[2\pi ebl]n_{e0}\sqrt{\frac{eT_e}{m_p}} \quad (6.20)$$

Equation-(6.20) gives the value of  $T_e$  as function of  $I_{ps}(V_B)$  and sheath radius  $b(V_B)$  corresponding to bias  $V_B$  applied on the hairpin as;

$$T_e = \frac{I_{ps}^2 m_p}{1.44e^{3/2} (\pi bl)^2 n_{e0}^2} \quad (6.21)$$

Figure-6.10 (a), (b) & (c) shows the respective plots for positive ion saturation cur-

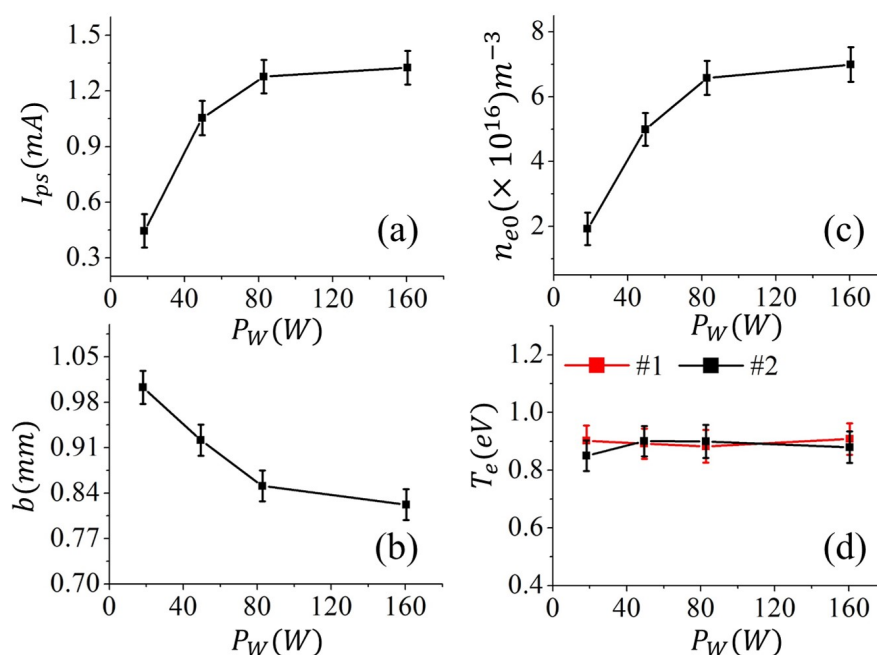


Figure 6.10: The variation in (a) ion saturation current  $I_{ps}$ , (b) the sheath radius  $b$  and (c) the absolute electron density  $n_{e0}$  as a function of discharge power in argon plasma. Figure-(d) compares  $T_e$  obtained from ion saturation current (#1) and floating potential condition (#2) respectively. The operating pressure is 1.8 Pa

rent  $I_{ps}$ , sheath radius  $b$  and electron density  $n_{e0}$  with respect to discharge power for

a fixed probe bias  $V_B = -40V$ . The operating pressure is  $P = 1.8$  Pa. Substituting the values of  $I_{ps}$ ,  $b(-40V)$  and  $n_{e0}$ , the electron temperature  $T_e$  can be calculated from (6.21). This is plotted in figure-6.10(d) along with the electron temperature obtained by the previous technique in fig-6.8.

Thus above techniques suggest that there are two possible ways to calculate electron temperature using a biased hairpin resonator probe. In the first method, the information of probe sheath radius is required at the floating potential; whereas in the second method; positive ion saturation as well as sheath radius at a sufficiently large negative bias are needed as a parameter to calculate  $T_e$ .

### 6.5.3 Finding $\alpha_0$ and $T_e$ in an electro-negative plasma

To find  $\alpha_0$  and  $T_e$  in an electro-negative oxygen discharge, we further use equation (6.16) and (6.18). The sheath radius  $b$  at the floating potential  $V_f$  and for a sufficiently large negative bias  $V_B = -40V$  on the probe, can be determined experimentally using the biased resonance probe technique as described in section 6.3. Furthermore, while  $\alpha_0$  is a strongly varying parameter in a discharge, whereas negative ion temperature generally remain constant in the range of  $0.025 - 0.1eV$  as reported in many papers [11, 155, 200]. Therefore by considering a realistic value of negative ion temperature  $T_v \approx 0.05eV$ , the unknown parameters in equation (6.16) and (6.18) reduces to  $\alpha_0$ ,  $\alpha_s$  and  $T_e$ .

Thus there are three unknown parameters  $\alpha_0$ ,  $\alpha_s$  and  $T_e$  and three equations namely (6.16), (6.17) and (6.18); hence  $\alpha_0$  and  $T_e$  can be determined by solving these equations simultaneously.

Figure-6.11 & 6.12 shows the plot of  $\alpha_0$  and  $T_e$  respectively for a particular discharge condition with parameters given in Table-6.2. In the above figure,  $\alpha_0$  decreases with increase in discharge power. This is because the mechanism behind

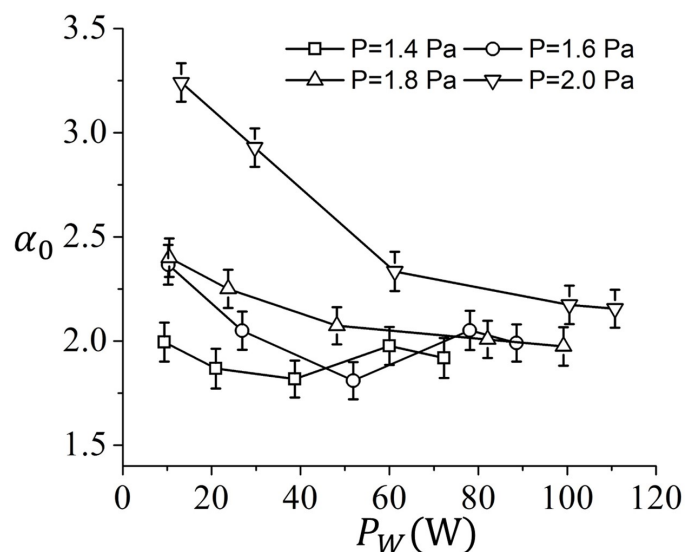


Figure 6.11: Plot of electro-negativity parameter  $\alpha_0$  as a function of discharge power & pressure in oxygen plasma;  $\alpha_0$  and  $T_e$  are found out by solving equation (6.16), (6.17) and (6.18) simultaneously, assuming the negative ion temperature to be  $T_v \approx 0.05$  eV.

negative ion production/loss is mainly governed by two competing and contrasting processes; namely the electron attachment and electron impact detachments [11]. Since the electron temperature does not vary significantly with increase of discharge power. As a result the dissociative attachment rate, which is a function of  $Te$  does not vary significantly. However an increase in number density of electrons with discharge power leads to higher probability of electron impact detachment. Hence bulk electro-negativity tends to fall with rise in discharge power.

It is also seen from fig-6.11 that on increasing the pressure from 1.4 Pa to 2.0 Pa, the electro-negativity increases almost by a factor of 3. The reason for observing an increase in  $\alpha_0$  with pressure is caused due to rapid fall in electron temperature, which results in reduction in electron-impact detachment rate. The typical values of  $\alpha_0$  obtained in figure-6.11 is also found to be consistent with global modeling of oxygen plasma by Gudmundsson et al [89].

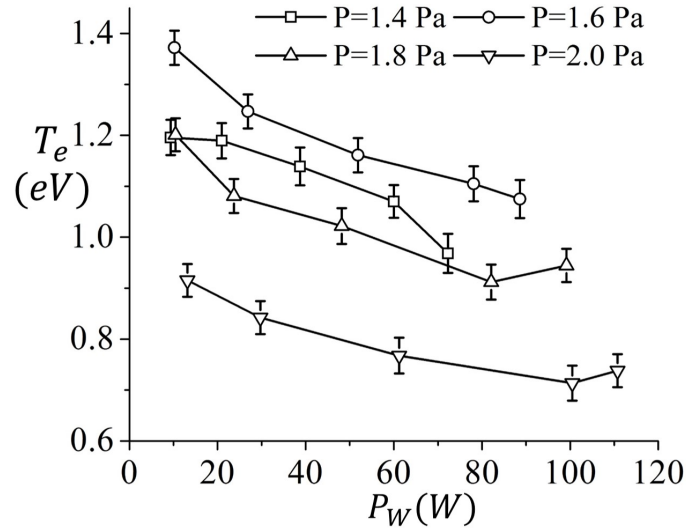


Figure 6.12: Variation in electron temperature  $T_e$  with discharge power & pressure in oxygen plasma.

## 6.6 Summary and Conclusion

In this chapter, a DC biased hairpin resonator probe has been presented. Using this technique, the plasma parameters viz., electron temperature, plasma potential and negative ion density has been determined experimentally. Besides, the biased hairpin probe is also capable to estimate the sheath width around the cylindrical wire, which has been compared with the radial flow model of a cylindrical sheath. A good agreement is found between the sheath width obtained experimentally using Peijak's capacitance model with the radial flow model. This not only validates the two independent approaches; but the DC biased hairpin probe can also be useful for correcting sheath effects in cylindrical Langmuir probes. This is left as a future scope for further investigation.

The second most important outcome regards to the wider application of hairpin probe in a low temperature plasmas. The conventional hairpin probe can only provide electron density. However with DC bias, other plasma parameters like electron temperature and negative ion parameters has been determined for the first time. The possible use of this technique to determine  $\alpha_0$  and  $T_e$  in an electro-negative discharge

is quite unique, since it could offer a simple and less-expensive tool as compared to sophisticated laser photo-detachment or cavity-ring-down spectroscopy techniques. The DC biased hairpin probe can scan the off-axis region outside the line of sight of laser beam inside a given plasma setup. The obtained trends of  $\alpha_0$  in oxygen plasma is found to be in agreement with the results reported by other authors.

As a future scope, the biased hairpin probe needs to be tested in magnetized plasma case in which the electron saturation current is quite limited. One would need to account for the correction factors due to the finite larmor radius around the cylindrical wire. Also one need to account for the perturbation arising from biasing the probe to draw electron saturation current. This may be limited by partially shielding the exposed cylindrical wire with a capillary tube. It would also be important to test the above technique in capacitive RF discharge. This could be challenging because of rapid changes in plasma potential relative to the probe bias. As a result the probe feed-through needs to be mechanically designed appropriately to introduce a resonant filter circuit for compensating the RF oscillation inside the plasma. Nevertheless the work reported here can be considered as an important milestone, based on which further developments will take place to make the resonance hairpin probe as a versatile tool for the diagnostics of low temperature plasmas, both in laboratories as well as in industrial plasma setups.

# Chapter 7

## Summary, Conclusions and Future scope of work

### 7.1 Summary & Conclusion

Summarizing the overall work, the thesis provide a fundamental study on sheaths and its applications in negative ion containing plasma. In particular, analytical model for a planar sheath has been formulated to study the behavior of sheath and pre-sheath during negative ion emission from an electrode surface. The results indicate a substantial increase in positive ion speed at the sheath boundary due to emission. This is found to be consistent with a greater potential drop inside the pre-sheath. For a critical value of emission flux, the emission becomes space charge limited and a virtual cathode is created in front emitting electrode. Due to this, the Bohm speed of positive ions and the transported flux of negative ions are observed to get saturated for further increase in emission. It is also found that the negative ion flux transported across the sheath towards the bulk plasma cannot be greater than the Bohm flux entering the sheath region from the bulk. Thus the transport properties of negative ions depend not only on the sheath characteristics,

but the flux/energy of positive ions entering the sheath is also influenced due to negative ion emission. The study also reveals that the space charge effect for a floating electrode emitting negative ions is more pronounced compared to an electron emitting electrode under identical conditions. The analytical results are found to be in good agreement with particle-in-cell simulations results reported elsewhere. The above study is fundamentally important for the development of negative ion sources, wherein low work function substrates are introduced for enhancing negative ion production inside the discharge.

A major part of the thesis work also devotes to the application of sheaths in electric probe diagnostics. The analytical model developed in this study along with the existing sheath capacitance model are used to determine the sheath width around cylindrical wire of hairpin resonator probe. The sheath width is an important parameter which is required for estimating the effective dielectric permittivity of the region between the probe's tip. The hairpin probe is popular among the electric probe diagnostics due to its accuracy and reproducibility in the measurement. It is highly sensitive to the change in dielectric medium surrounding the probe tips. Therefore an electrically biased hairpin resonator probe is developed in which the sheath width is externally controlled by applying negative DC potential on the hairpin tips. The negative biasing shifts the probe resonance frequency towards the vacuum resonance as the sheath width increase around the HP probe. The sheath width found by basic capacitance model is compared with the analytical model which shows a good agreement. Using this method, the hairpin probe provide not only the electron density, but it can also estimate other plasma parameters such as electron temperature, negative ion density as well as plasma potential inside the discharge; thereby broadening the scope of hairpin probe for application in low pressure plasma discharges. In addition to it, an analytical model is applied to a non-emitting Langmuir probe for determining negative ion temperature in an oxygen discharge



Some important results from the thesis are summarized as follows:

In Chapter-3, parametric study of space charge limited emission has been carried out which finds that there exists a critical value of negative ion flux  $J_{nvc}$  that can be transported across the sheaths. The upper limit of  $J_{nvc}$  is always found to remain lower than the positive ion flux entering at the sheath boundary. This chapter also discusses a revised formula of positive ion Bohm speed when the electrode is emitting negative ions. Among other important results, the sheath width determined analytically for the case of a negative ion emitting electrode is consistently higher than the sheath width calculated by using Child Langmuir Law for a non-emitting electrode. Chapter-4 mainly pertains to the pre-sheath in presence of a beam of negative ion flux streaming against background positive ions. It is found that the pre-sheath potential drop monotonically increases with increase in negative ions flux entering into pre-sheath. This observation also substantiate the result obtained in Chapter-3, which shows increase in positive ion speed at the sheath boundary during negative ion emission commensurate with increase in pre-sheath potential drop. In Chapter-5, floating case for both an emitting and non-emitting electrode immersed in an electronegative plasma is considered. It is found that floating potential magnitude decreases monotonically with increase in both bulk electro-negativity and negative ion emission from the electrode surface. However below a critical electro-negativity inside the bulk plasma, the floating potential magnitude shows an increasing trend for non-emitting electrode. The floating potential of non-emitting probe is applied in an experiment to determine negative ion temperature in an electronegative oxygen discharge. In Chapter-6, a DC biased hairpin resonance probe is introduced. So far, the resonance hairpin probe was traditionally applied for determining electron density in low temperature and low pressure plasmas. The sheath model developed in the previous chapter is used for determining the sheath capacitance from which a range of plasma parameters is determined using the hairpin probe. This technique also provides a tool for determining the sheath width experimentally, which

are otherwise difficult to measure as the sheath dimensions being extremely small. In conclusion, the thesis tries to address some unsolved issues having significance towards understanding of negative ion emission from an electrode and its impact on positive ion flow through the pre-sheath and sheath region. This study has significance in negative ion sources where cesiated surface are introduced inside the discharge for enhancing negative ion emission. The sheath width is also an important parameter which can impact the ion optics near a floating / electrically biased metallic grids. In plasma processing, negative ion emission from the sheath is quite common. In the literature, a very limited amount of work is found in context of negative ion emission from an electrode and its impact on sheath as well as bulk plasma behavior. The study also provide some innovative application of sheaths in plasma probing technique which enable to determine negative ion parameters inside the discharge. Another important application of the present simple 1-D model is to calculate the sheath width. Due to high plasma density and large volume, the modelling of a typical negative ion source with 2D/3D PIC-MCC (particle-in-cell with Monte-Carlo collision) simulation techniques is quite difficult for real plasma condition; since the size of the simulation grid and number of the simulating particles are dependent on the ratio of discharge dimension ( $\sim\text{cm}$ ) to the Debye length ( $\sim\mu\text{m}$ ). In order to overcome this issue, scaling of plasma parameters is performed to reduce grid size and number of simulation particles for efficient computing. The simulation result is then extrapolated to the real condition by using some scaling laws. Such scaling laws are highly dependent on sheath width information near the plasma grid for the simulation of negative ion sources. The information about the sheath width obtained from the present study can be helpful in such scenario.

## 7.2 Future Scope of the Work

The thesis work presented here is mainly focused on 1-Dimensional model of a

planar sheath, which addressed some of the gap area in the research about the sheath and pre-sheath region in presence of a negative ion emission from the electrode. The one dimensional model also considered a collision-less sheath, which is applicable in case of low pressure discharges. However in plasma processing applications, the discharges are operated at wide range of pressures using mixture of gases. For example-Capacitive Coupled RF discharges used in industrial plasma tool apply two or more frequencies coupled to the discharge electrodes, which result in ionization near the sheath and in the pre-sheath region. The ion energy distribution also gets modified on account of driving voltage waveform on the electrode. In addition to it, the time-dependent sheaths are also relevant in different types of plasma processing systems including reactive ion etching in pulse-dc / rf magnetron discharges. It will be interesting to see how the 1-dimensional model can be extended for the above scenarios.

Also in the analytical model, the ion-ion interaction in the pre-sheath has been ignored. However interaction of beam negative ions coming from an electrode with background gas could be relevant for high pressures. The present work may also be extended for collisional pre-sheath to include the global production/loss balance of emitted negative ions in the bulk plasma using the above fluid model. Another aspects which can be relevant in ion sources arise due to external magnetic field. Transverse magnetic field can alter the electron dynamic and emission of negative ion from the electrode. This is relevant for both plasma processing application such as pulse-dc magnetron and Hi-PIMS as well as negative ion sources where strong magnetic filter-field present transverse to the ion extraction grids can affect the space charge creation as well as emission characteristics of negative ions from the electrode surface. The above points can possibly lead to larger scope for future investigation.



# Bibliography

- [1] P Frazer Williams. *Plasma processing of semiconductors*. Vol. 336. Springer Science & Business Media, 2013.
- [2] Ludvik Martinu and Daniel Poitras. “Plasma deposition of optical films and coatings: A review”. In: *Journal of Vacuum Science & Technology A: Vacuum, Surfaces, and Films* 18.6 (2000), pp. 2619–2645.
- [3] Hiroyuki Kawano and Francis Michael Page. “Experimental methods and techniques for negative-ion production by surface ionization. Part I. Fundamental aspects of surface ionization”. In: *International Journal of Mass Spectrometry and Ion Physics* 50.1-2 (1983), pp. 1–33.
- [4] MADHAVAN M Menon. “Neutral beam heating applications and development”. In: *Proceedings of the IEEE* 69.8 (1981), pp. 1012–1029.
- [5] R Hemsworth et al. “Status of the ITER heating neutral beam system”. In: *Nuclear Fusion* 49.4 (2009), p. 045006.
- [6] TE Sheridan, P Chabert, and RW Boswell. “Positive ion flux from a low-pressure electronegative discharge”. In: *Plasma Sources Science and Technology* 8.3 (1999), p. 457.
- [7] AJ Lichtenberg et al. “Modeling electronegative plasma discharges”. In: *Journal of applied physics* 75.5 (1994), pp. 2339–2347.

- 
- [8] AJ Lichtenberg et al. “Transitions and scaling laws for electronegative discharge models”. In: *Plasma Sources Science and Technology* 9.1 (2000), p. 45.
- [9] IG Kouznetsov, AJ Lichtenberg, and MA Lieberman. “Internal sheaths in electronegative discharges”. In: *Journal of applied physics* 86.8 (1999), pp. 4142–4153.
- [10] David Bohm. “The characteristics of electrical discharges in magnetic fields”. In: *Qualitative Description of the Arc Plasma in a Magnetic Field* (1949).
- [11] MA Lieberman. “A.. Lichtenberg, “Principles of plasma discharges and materials processing.” ohn Wiley & Sons”. In: *INC., New York* (1994), p. 572.
- [12] Brian S Lee and M Seidl. “Surface production of H<sup>-</sup> ions by hyperthermal hydrogen atoms”. In: *Applied physics letters* 61.24 (1992), pp. 2857–2859.
- [13] FA Haas, LM Lea, and AJT Holmes. “A ‘hydrodynamic’ model of the negative-ion source”. In: *Journal of Physics D: Applied Physics* 24.9 (1991), p. 1541.
- [14] Jindrich Musil et al. “Pulsed dc magnetron discharge for high-rate sputtering of thin films”. In: *Journal of Vacuum Science & Technology A: Vacuum, Surfaces, and Films* 19.2 (2001), pp. 420–424.
- [15] P Wurz, R Schletti, and MR Aellig. “Hydrogen and oxygen negative ion production by surface ionization using diamond surfaces”. In: *Surface science* 373.1 (1997), pp. 56–66.
- [16] L Schiesko et al. “Caesium influence on plasma parameters and source performance during conditioning of the prototype ITER neutral beam injector negative ion source”. In: *Plasma Physics and Controlled Fusion* 53.8 (2011), p. 085029.
- [17] Tomaz Gyergyek and Milan Čerček. “Sheath in front of a negatively biased collector that emits electrons and is immersed in a two electron temperature plasma”. In: *Contributions to Plasma Physics* 45.8 (2005), pp. 568–581.

- [18] R McAdams et al. “Transport of negative ions across a double sheath with a virtual cathode”. In: *Plasma Sources Science and Technology* 20.3 (2011), p. 035023.
- [19] Sejal Shah and M Bandyopadhyay. “Effect of surface produced negative ions on near wall sheath”. In: *Plasma Physics and Controlled Fusion* 51.3 (2009), p. 035015.
- [20] AJT Holmes. “A one-dimensional model of a negative ion source”. In: *Plasma Sources Science and Technology* 5.3 (1996), p. 453.
- [21] F Taccogna et al. “Modeling of a negative ion source. III. Two-dimensional structure of the extraction region”. In: *Physics of plasmas* 17.6 (2010), p. 063502.
- [22] D Wunderlich, R Gutser, and U Fantz. “PIC code for the plasma sheath in large caesiated RF sources for negative hydrogen ions”. In: *Plasma Sources Science and Technology* 18.4 (2009), p. 045031.
- [23] Trevor Lafleur, D Rafalskyi, and Ane Aanesland. “Alternate extraction and acceleration of positive and negative ions from a gridded plasma source”. In: *Plasma Sources Science and Technology* 24.1 (2014), p. 015005.
- [24] Hiroshi Amemiya. “Probe diagnostics in negative ion containing plasma”. In: *Journal of the Physical Society of Japan* 57.3 (1988), pp. 887–902.
- [25] AG Nikitin, F El Balghiti, and M Bacal. “Comparison of negative ion density measurements by probes and by photodetachment”. In: *Plasma Sources Science and Technology* 5.1 (1996), p. 37.
- [26] Jerome Bredin, Pascal Chabert, and Ane Aanesland. “Langmuir probe analysis in electronegative plasmas”. In: *Physics of Plasmas* 21.12 (2014), p. 123502.
- [27] M Shindo et al. “Determination of negative-ion density in an electron cyclotron resonance c4f8 plasma”. In: *Surface and Coatings Technology* 116 (1999), pp. 1065–1069.

- 
- [28] P Chabert et al. “Electrostatic probe measurement of the negative ion fraction in an SF6 helicon discharge”. In: *Plasma Sources Science and Technology* 8.4 (1999), p. 561.
- [29] Robert L Merlino. “Understanding Langmuir probe current-voltage characteristics”. In: *American Journal of Physics* 75.12 (2007), pp. 1078–1085.
- [30] RB Piejak et al. “The hairpin resonator: A plasma density measuring technique revisited”. In: *Journal of applied physics* 95.7 (2004), pp. 3785–3791.
- [31] RB Piejak, J Al-Kuzee, and N St J Braithwaite. “Hairpin resonator probe measurements in RF plasmas”. In: *Plasma Sources Science and Technology* 14.4 (2005), p. 734.
- [32] Priscilla C Frisch, Seth Redfield, and Jonathan D Slavin. “The interstellar medium surrounding the Sun”. In: *Annual Review of Astronomy and Astrophysics* 49 (2011), pp. 237–279.
- [33] Daniel Verscharen, Kristopher G Klein, and Bennett A Maruca. “The multi-scale nature of the solar wind”. In: *Living reviews in solar physics* 16.1 (2019), pp. 1–136.
- [34] Leonard Searle. “Review of Publications-Gaseous Nebulae by LH Aller”. In: *Journal of the Royal Astronomical Society of Canada* 51 (1957), p. 170.
- [35] M Ji Buonsanto. “Ionospheric storms—A review”. In: *Space Science Reviews* 88.3 (1999), pp. 563–601.
- [36] Ronald Stephen Hemsworth and Takashi Inoue. “Positive and negative ion sources for magnetic fusion”. In: *IEEE Transactions on Plasma Science* 33.6 (2005), pp. 1799–1813.
- [37] GA Bazilevskaya et al. “Cosmic ray induced ion production in the atmosphere”. In: *Space Science Reviews* 137.1 (2008), pp. 149–173.



- [38] J. Reece Roth. *Industrial plasma engineering*. Vol. 1. IOP Publishing Ltd 1995, 1995. Chap. 9.
- [39] Francis F Chen. “Helicon discharges and sources: a review”. In: *Plasma Sources Science and Technology* 24.1 (2015), p. 014001.
- [40] Zhaoyuan Ning and Zhaoxing Ren. “Electron cyclotron resonance (ECR) plasma investigation and application”. In: *Progress in physics* 12.3 (1992), pp. 38–61.
- [41] Cornelis P Dullemond and Carsten Dominik. “Dust coagulation in protoplanetary disks: A rapid depletion of small grains”. In: *Astronomy & Astrophysics* 434.3 (2005), pp. 971–986.
- [42] C Dominik and AGGM Tielens. “The physics of dust coagulation and the structure of dust aggregates in space”. In: *The Astrophysical Journal* 480.2 (1997), p. 647.
- [43] Henry Berry Garrett. “The charging of spacecraft surfaces”. In: *Reviews of Geophysics* 19.4 (1981), pp. 577–616.
- [44] K-U Riemann. “The Bohm criterion and sheath formation”. In: *Journal of Physics D: Applied Physics* 24.4 (1991), p. 493.
- [45] K-U Riemann. “Plasma-sheath transition in the kinetic Tonks-Langmuir model”. In: *Physics of plasmas* 13.6 (2006), p. 063508.
- [46] RN Franklin. “The plasma–sheath boundary region”. In: *Journal of Physics D: Applied Physics* 36.22 (2003), R309.
- [47] JH Ingold. “Two-Fluid Theory of the Positive Column of a Gas Discharge”. In: *The Physics of Fluids* 15.1 (1972), pp. 75–85.
- [48] Sidney A Self. “Exact Solution of the Collisionless Plasma-Sheath Equation”. In: *The Physics of Fluids* 6.12 (1963), pp. 1762–1768.

- 
- [49] Karl-Birger Persson. “Inertia-Controlled Ambipolar Diffusion”. In: *The Physics of Fluids* 5.12 (1962), pp. 1625–1632.
- [50] RM Clements. “Plasma diagnostics with electric probes”. In: *Journal of Vacuum Science and Technology* 15.2 (1978), pp. 193–198.
- [51] Kenzo Yamamoto and Takayoshi Okuda. “On the floating probe method for the measurement of ionized gas”. In: *Journal of the Physical Society of Japan* 11.1 (1956), pp. 57–68.
- [52] JP Sheehan and N Hershkowitz. “Emissive probes”. In: *Plasma Sources Science and Technology* 20.6 (2011), p. 063001.
- [53] S Binwal et al. “Parametric study of a pin-plane probe in moderately magnetized plasma”. In: *Measurement Science and Technology* 26.12 (2015), p. 125015.
- [54] Martin Hudis and LM Lidsky. “Directional langmuir probe”. In: *Journal of Applied Physics* 41.12 (1970), pp. 5011–5017.
- [55] Harold M Mott-Smith and Irving Langmuir. “The theory of collectors in gaseous discharges”. In: *Physical review* 28.4 (1926), p. 727.
- [56] JE Allen. “Probe theory-the orbital motion approach”. In: *Physica Scripta* 45.5 (1992), p. 497.
- [57] R.H. Huddlestone and S.L. Leonard. *Electric Probes in "Plasma Diagnostic Techniques", ch 4 by F F Chen*. Academic Press, New York, 1965.
- [58] Francis F Chen. “Langmuir probe analysis for high density plasmas”. In: *Physics of Plasmas* 8.6 (2001), pp. 3029–3041.
- [59] Isaac D Sudit and R Claude Woods. “A study of the accuracy of various Langmuir probe theories”. In: *Journal of applied physics* 76.8 (1994), pp. 4488–4498.

- [60] JE Allen, RLF Boyd, and P Reynolds. “The collection of positive ions by a probe immersed in a plasma”. In: *Proceedings of the Physical Society. Section B* 70.3 (1957), p. 297.
- [61] Francis F Chen. “Numerical computations for ion probe characteristics in a collisionless plasma”. In: *Journal of Nuclear Energy. Part C, Plasma Physics, Accelerators, Thermonuclear Research* 7.1 (1965), p. 47.
- [62] Ira B Bernstein and Irving N Rabinowitz. “Theory of electrostatic probes in a low-density plasma”. In: *The Physics of Fluids* 2.2 (1959), pp. 112–121.
- [63] James G Laframboise. *Theory of spherical and cylindrical Langmuir probes in a collisionless, Maxwellian plasma at rest*. Tech. rep. TORONTO UNIV DOWNSVIEW (ONTARIO) INST FOR AEROSPACE STUDIES, 1966.
- [64] Ain A Sonin. “Free-molecule Langmuir probe and its use in flow-field studies.” In: *AIAA Journal* 4.9 (1966), pp. 1588–1596.
- [65] KA Graf and JH De Leeuw. “Comparison of Langmuir probe and microwave diagnostic techniques”. In: *Journal of Applied Physics* 38.11 (1967), pp. 4466–4472.
- [66] ROGER E KIEL. “Electrostatic probe theory for free molecular cylinders.” In: *AIAA Journal* 6.4 (1968), pp. 708–712.
- [67] EW Peterson and L Talbot. “Collisionless electrostatic single-probe and double-probe measurements”. In: *AIAA Journal* 8.12 (1970), pp. 2215–2219.
- [68] Christoph Steinbruchel. “A new method for analyzing Langmuir probe data and the determination of ion densities and etch yields in an etching plasma”. In: *Journal of Vacuum Science & Technology A: Vacuum, Surfaces, and Films* 8.3 (1990), pp. 1663–1667.

- 
- [69] G Narasimhan and Ch Steinbruchel. “Analysis of Langmuir probe data: Analytical parametrization, and the importance of the end effect”. In: *Journal of Vacuum Science & Technology A: Vacuum, Surfaces, and Films* 19.1 (2001), pp. 376–378.
- [70] George J Schulz and Sanborn C Brown. “Microwave study of positive ion collection by probes”. In: *Physical Review* 98.6 (1955), p. 1642.
- [71] Z Zakrzewski and T Kopiczynski. “Effect of collisions on positive ion collection by a cylindrical Langmuir probe”. In: *Plasma Physics* 16.12 (1974), p. 1195.
- [72] Francesco Taccogna, Savino Longo, and Mario Capitelli. “Ion orbits in a cylindrical Langmuir probe”. In: *Physics of plasmas* 13.4 (2006), p. 043501.
- [73] YS Chou, L Talbot, and DR Willis. “Kinetic theory of a spherical electrostatic probe in a stationary plasma”. In: *The Physics of Fluids* 9.11 (1966), pp. 2150–2167.
- [74] L Talbot and YS Chou. “Langmuir probe response in the transition regime”. In: *Rarefied Gas Dynamics* 2.Suppl 5 (1969), pp. 1723–1737.
- [75] Antoine Rousseau, E Teboul, and Stephane Beechu. “Comparison between Langmuir probe and microwave autointerferometry measurements at intermediate pressure in an argon surface wave discharge”. In: *Journal of applied physics* 98.8 (2005), p. 083306.
- [76] M Tichý et al. “A collisional model of the positive ion collection by a cylindrical Langmuir probe”. In: *Contributions to Plasma Physics* 34.1 (1994), pp. 59–68.
- [77] Felipe Iza and Jae Koo Lee. “Particle-in-cell simulations of planar and cylindrical Langmuir probes: Floating potential and ion saturation current”. In: *Journal of Vacuum Science and Technology A: Vacuum, Surfaces, and Films* 24.4 (2006), pp. 1366–1372.

- [78] O Chudáček et al. “Langmuir probe determination of charged particle number density in a flowing afterglow plasma”. In: *Contributions to Plasma Physics* 35.6 (1995), pp. 503–516.
- [79] PM Bryant. “Theory of cylindrical Langmuir probes in weakly ionized, non-thermal, stationary and moderately collisional plasmas”. In: *Plasma Sources Science and Technology* 18.1 (2008), p. 014013.
- [80] A Sherman. “Plasma-assisted chemical vapor deposition processes and their semiconductor applications”. In: *Thin Solid Films* 113.2 (1984), pp. 135–149.
- [81] M Bacal. “Volume production of hydrogen negative ions”. In: *Nuclear Instruments and Methods in Physics Research Section B: Beam Interactions with Materials and Atoms* 37 (1989), pp. 28–32.
- [82] Norbert Kaiser. “Review of the fundamentals of thin-film growth”. In: *Applied optics* 41.16 (2002), pp. 3053–3060.
- [83] E Stoffels, WW Stoffels, and GMW Kroesen. “Plasma chemistry and surface processes of negative ions”. In: *Plasma Sources Science and Technology* 10.2 (2001), p. 311.
- [84] JN Bardsley and JM Wadehra. “Dissociative attachment and vibrational excitation in low-energy collisions of electrons with H<sub>2</sub> and D<sub>2</sub>”. In: *Physical Review A* 20.4 (1979), p. 1398.
- [85] C Lee and MA Lieberman. “Global model of Ar, O<sub>2</sub>, Cl<sub>2</sub>, and Ar/O<sub>2</sub> high-density plasma discharges”. In: *Journal of Vacuum Science & Technology A: Vacuum, Surfaces, and Films* 13.2 (1995), pp. 368–380.
- [86] JI Fernández Palop et al. “Transient processes in an Ar<sup>+</sup> I<sub>2</sub> dc discharge”. In: *J. Appl. Phys* 80.8 (1996).
- [87] AJ Lichtenberg et al. “Modelling plasma discharges at high electronegativity”. In: *Plasma Sources Science and Technology* 6.3 (1997), p. 437.

- 
- [88] H Amemiya. “Diagnostics of negative ions using probe and laser in plasmas (oxygen discharge)”. In: *Vacuum* 58.2-3 (2000), pp. 100–116.
- [89] JT Gudmundsson et al. “Electronegativity of low-pressure high-density oxygen discharges”. In: *Journal of Physics D: Applied Physics* 34.7 (2001), p. 1100.
- [90] Marthe Bacal and M Wada. “Negative ion production by plasma-surface interaction in caesiated negative ion sources”. In: *AIP Conference Proceedings*. Vol. 1515. 1. American Institute of Physics. 2013, pp. 41–48.
- [91] Ursel Fantz, P Franzen, and D Wunderlich. “Development of negative hydrogen ion sources for fusion: Experiments and modelling”. In: *Chemical Physics* 398 (2012), pp. 7–16.
- [92] JR Hiskes, A Karo, and M Gardner. “Mechanism for negative-ion production in the surface-plasma negative-hydrogen-ion source”. In: *Journal of Applied Physics* 47.9 (1976), pp. 3888–3896.
- [93] M Seidl and A Pargellis. “Production of negative hydrogen ions by sputtering adsorbed hydrogen from a cesiated molybdenum surface”. In: *Physical Review B* 26.1 (1982), p. 1.
- [94] M Seidl et al. “Negative surface ionization of hydrogen atoms and molecules”. In: *Journal of applied physics* 79.6 (1996), pp. 2896–2901.
- [95] H Verbeek, W Eckstein, and RS Bhattacharya. “Negative hydrogen ion formation by backscattering from solid surfaces”. In: *Surface Science* 95.2-3 (1980), pp. 380–390.
- [96] Vadim Dudnikov. “Thirty years of surface plasma sources for efficient negative ion production”. In: *Review of scientific instruments* 73.2 (2002), pp. 992–994.
- [97] André Anders. “Tutorial: Reactive high power impulse magnetron sputtering (R-HiPIMS)”. In: *Journal of applied physics* 121.17 (2017), p. 171101.

- [98] Nikolay Britun et al. “Plasma diagnostics for understanding the plasma–surface interaction in HiPIMS discharges: a review”. In: *Journal of Physics D: Applied Physics* 47.22 (2014), p. 224001.
- [99] Gwenaël Fubiani et al. “Modeling of plasma transport and negative ion extraction in a magnetized radio-frequency plasma source”. In: *New Journal of Physics* 19.1 (2017), p. 015002.
- [100] EA Bogdanov and AA Kudryavtsev. “The conditions for realization of the Boltzmann distribution of negative ions in a plasma”. In: *Technical Physics Letters* 27.11 (2001), pp. 905–907.
- [101] RN Franklin and J Snell. “The low-pressure positive column in electronegative gases including space charge-matching plasma and sheath”. In: *Journal of Physics D: Applied Physics* 31.19 (1998), p. 2532.
- [102] RN Franklin. “The fluid model of the positive column of a discharge with negative ions at low pressure joining plasma and sheath”. In: *Journal of Physics D: Applied Physics* 32.16 (1999), p. L71.
- [103] JI Fernández Palop et al. “Sheath structure in a plane probe immersed in an electronegative plasma”. In: *Journal of applied physics* 77.7 (1995), pp. 2937–2944.
- [104] James W Bradley et al. “Resonance hairpin and Langmuir probe-assisted laser photodetachment measurements of the negative ion density in a pulsed dc magnetron discharge”. In: *Journal of Vacuum Science & Technology A: Vacuum, Surfaces, and Films* 29.3 (2011), p. 031305.
- [105] Jim Conway et al. “Using the resonance hairpin probe and pulsed photodetachment technique as a diagnostic for negative ions in oxygen plasma”. In: *Plasma Sources Science and Technology* 19.6 (2010), p. 065002.

- 
- [106] N Sirse et al. “Resonance Hair Pin Probe and Laser Photo Detachment Technique for Measuring Time Resolved Negative Ion Density in Pulsed DC Magnetron Discharge”. In: *Bulletin of the American Physical Society* 55 (2010).
- [107] M Bowes and JW Bradley. “The behaviour of negative oxygen ions in the afterglow of a reactive HiPIMS discharge”. In: *Journal of Physics D: Applied Physics* 47.26 (2014), p. 265202.
- [108] SD You et al. “A study of the plasma electronegativity in an argon–oxygen pulsed-dc sputter magnetron”. In: *Journal of Physics D: Applied Physics* 43.50 (2010), p. 505205.
- [109] N Sirse, SK Karkari, and MM Turner. “Probing negative ion density and temperature using a resonance hairpin probe”. In: *Plasma Sources Science and Technology* 24.2 (2015), p. 022001.
- [110] RN Franklin. “Electronegative plasmas—Why are they so different?” In: *Plasma Sources Science and Technology* 11.3A (2002), A31.
- [111] Noah Hershkowitz. “Role of plasma-aided manufacturing in semiconductor fabrication”. In: *IEEE transactions on plasma science* 26.6 (1998), pp. 1610–1620.
- [112] Delphine Merche, Nicolas Vandencastele, and François Reniers. “Atmospheric plasmas for thin film deposition: A critical review”. In: *Thin Solid Films* 520.13 (2012), pp. 4219–4236.
- [113] J Roland Jacobsson. “Review of the optical properties of inhomogeneous thin films”. In: *Inhomogeneous and Quasi-Inhomogeneous Optical Coatings*. Vol. 2046. International Society for Optics and Photonics. 1993, pp. 2–8.
- [114] Chang Heon Yi et al. “Oxide surface cleaning by an atmospheric pressure plasma”. In: *Surface and Coatings Technology* 177 (2004), pp. 711–715.
- [115] A Belkind and S Gershman. “Plasma cleaning of surfaces”. In: *Vacuum Coating and Technology November* (2008), pp. 46–57.



- [116] Raoul N Franklin. “Plasma phenomena in gas discharges”. In: *oxny* (1976).
- [117] SG Walton, RL Champion, and Yicheng Wang. “Negative ion emission from a stainless steel surface due to positive ion collisions”. In: *Journal of applied physics* 84.3 (1998), pp. 1706–1707.
- [118] Petrus Wilhelmus van Amersfoort. “Formation of negative ions on a metal surface”. In: (1987).
- [119] Yasuhiko Takeiri. “Negative ion source development for fusion application”. In: *Review of Scientific Instruments* 81.2 (2010), 02B114.
- [120] J Andreu et al. “Filament discharge plasma of argon with electrostatic confinement”. In: *Journal of Physics D: Applied Physics* 18.7 (1985), p. 1339.
- [121] M Hanada et al. “Development of negative ion sources for the ITER neutral beam injector”. In: *Fusion engineering and design* 56 (2001), pp. 505–509.
- [122] J Vlcek, AD Pajdarova, and J Musil. “Pulsed dc magnetron discharges and their utilization in plasma surface engineering”. In: *Contributions to Plasma Physics* 44.5-6 (2004), pp. 426–436.
- [123] Samuel D Ekpe et al. “Effect of magnetic field strength on deposition rate and energy flux in a dc magnetron sputtering system”. In: *Journal of Vacuum Science & Technology A: Vacuum, Surfaces, and Films* 27.6 (2009), pp. 1275–1280.
- [124] K Toki et al. “Small helicon plasma source for electric propulsion”. In: *Thin Solid Films* 506 (2006), pp. 597–600.
- [125] Geraldo Roberson et al. “Global model simulations of low-pressure oxygen discharges”. In: *Brazilian journal of physics* 37.2A (2007), pp. 457–465.
- [126] Gérard Gousset et al. “Experimental study of a dc oxygen glow discharge by VUV absorption spectroscopy”. In: *Plasma chemistry and plasma processing* 7.4 (1987), pp. 409–427.

- 
- [127] Norihiro Ito et al. “Effects of energetic ion bombardment on structural and electrical properties of Al-doped ZnO films deposited by RF-superimposed DC magnetron sputtering”. In: *Japanese Journal of Applied Physics* 49.7R (2010), p. 071103.
- [128] Sankar Moni Borah. “Direct current magnetron glow discharge plasma characteristics study for controlled deposition of titanium nitride thin film”. In: *Journal of Materials* 2013 (2013).
- [129] Mubarak A Mujawar. “Studies on constricted hollow anode plasma source for negative ion production”. PhD thesis. Dublin City University, 2013.
- [130] Samah I Radwan, H El-Khabeary, and AG Helal. “Study of the secondary electron emission coefficient using disc and conical electrodes”. In: *Canadian Journal of Physics* 94.12 (2016), pp. 1275–1281.
- [131] Francis F Chen, John D Evans, and Donald Arnush. “A floating potential method for measuring ion density”. In: *Physics of Plasmas* 9.4 (2002), pp. 1449–1455.
- [132] Jongdae Kim et al. “Temporal measurement of plasma density variations above a semiconductor bridge (SCB)”. In: *IEEE transactions on instrumentation and measurement* 44.4 (1995), pp. 843–846.
- [133] SK Karkari et al. “A floating hairpin resonance probe technique for measuring time-resolved electron density in pulse discharge”. In: *Measurement Science and Technology* 18.8 (2007), p. 2649.
- [134] SK Karkari et al. “Performance of a floating hairpin probe in strongly magnetized plasma”. In: *Contributions to Plasma Physics* 50.9 (2010), pp. 903–908.
- [135] SK Karkari et al. “Measurement of electron density in a laser produced plasma using a hairpin resonance probe”. In: *PLASMA SOURCES SCIENCE & TECHNOLOGY* 17.3 (2008).

- [136] Shantanu K Karkari, C Gaman, and Albert R Ellingboe. “Observation of Electron Density Oscillations in Confined Plasma with Two Radio-Frequency Capacitive Sheath”. In: *2007 IEEE 34th International Conference on Plasma Science (ICOPS)*. IEEE. 2007, pp. 224–224.
- [137] SK Karkari, AR Ellingboe, and C Gaman. “Direct measurement of spatial electron density oscillations in a dual frequency capacitive plasma”. In: *Applied Physics Letters* 93.7 (2008), p. 071501.
- [138] SK Karkari and AR Ellingboe. “Effect of radio-frequency power levels on electron density in a confined two-frequency capacitively-coupled plasma processing tool”. In: *Applied physics letters* 88.10 (2006), p. 101501.
- [139] GA Curley et al. “Surface loss rates of H and Cl radicals in an inductively coupled plasma etcher derived from time-resolved electron density and optical emission measurements”. In: *Journal of Vacuum Science & Technology A: Vacuum, Surfaces, and Films* 28.2 (2010), pp. 360–372.
- [140] Nishant Sirse. “Resonance hairpin probe for electronegative plasma diagnostics”. PhD thesis. Dublin City University, 2013.
- [141] GS Gogna and SK Karkari. “Microwave resonances of a hairpin probe in a magnetized plasma”. In: *Applied Physics Letters* 96.15 (2010), p. 151503.
- [142] GS Gogna et al. “Dielectric covered hairpin probe for its application in reactive plasmas”. In: *Applied Physics Letters* 101.4 (2012), p. 042105.
- [143] GS Gogna, SK Karkari, and MM Turner. “Interpreting the behavior of a quarter-wave transmission line resonator in a magnetized plasma”. In: *Physics of Plasmas* 21.12 (2014), p. 123510.
- [144] FA Haas, J Al-Kuzee, and N St J Braithwaite. “Electron and ion sheath effects on a microwave “hairpin” probe”. In: *Applied Physics Letters* 87.20 (2005), p. 201503.

- 
- [145] Stijn Mahieu et al. “Modeling the flux of high energy negative ions during reactive magnetron sputtering”. In: *Journal of Applied Physics* 106.9 (2009), p. 093302.
- [146] Vasily Gushenets, Alexey Bugaev, and Efim Oks. “Boron vacuum-arc ion source with LaB6 cathode”. In: *Review of Scientific Instruments* 90.11 (2019), p. 113309.
- [147] Yu I Belchenko, GI Kuznetsov, and EA Grigoryev. “Hydrogen negative ion source with LaB 6 inserts”. In: *Review of Scientific Instruments* 71.2 (2000), pp. 1079–1081.
- [148] GD Hobbs and JA Wesson. “Heat flow through a Langmuir sheath in the presence of electron emission”. In: *Plasma Physics* 9.1 (1967), p. 85.
- [149] H Amemiya, BM Annaratone, and JE Allen. “The double sheath associated with electron emission into a plasma containing negative ions”. In: *Journal of plasma physics* 60.1 (1998), pp. 81–93.
- [150] Jon M Andersson et al. “Energy distributions of positive and negative ions during magnetron sputtering of an Al target in Ar/ O 2 mixtures”. In: *Journal of applied physics* 100.3 (2006), p. 033305.
- [151] Yukio Fujiwara et al. “An oxygen negative ion source of a new concept using solid oxide electrolytes”. In: *Journal of The Electrochemical Society* 150.2 (2003), E117.
- [152] Motoi Wada. “Plasma-surface interaction in negative hydrogen ion sources”. In: *Review of Scientific Instruments* 89.5 (2018), p. 052103.
- [153] G Serianni et al. “Neutralisation and transport of negative ion beams: physics and diagnostics”. In: *New Journal of Physics* 19.4 (2017), p. 045003.
- [154] MY Ye and S Takamura. “Effect of space-charge limited emission on measurements of plasma potential using emissive probes”. In: *Physics of Plasmas* 7.8 (2000), pp. 3457–3463.

- [155] RN Franklin and J Snell. “The Boltzmann relation in electronegative plasmas: When is it permissible to use it?” In: *Journal of Plasma Physics* 64.2 (2000), pp. 131–153.
- [156] ST Melnychuk et al. “Reflection of hydrogen atoms from metal and semiconductor targets”. In: *Journal of Vacuum Science & Technology A: Vacuum, Surfaces, and Films* 7.3 (1989), pp. 2127–2131.
- [157] S Mochalskyy, AF Lifschitz, and T Minea. “Extracted current saturation in negative ion sources”. In: *Journal of Applied Physics* 111.11 (2012), p. 113303.
- [158] Osamu Fukumasa, Masayuki Hosoda, and Hiroshi Naitou. “Relationship between extraction of H<sup>-</sup> ions optimized by plasma grid potential and plasma parameters in a bucket source”. In: *Review of scientific instruments* 63.4 (1992), pp. 2696–2698.
- [159] JH Palacio Mizrahi and Ya E Krasik. “Bohm velocity in the presence of a hot cathode”. In: *Physics of Plasmas* 20.8 (2013), p. 083510.
- [160] RJ Umstattd et al. “Space charge-limited emission above the 1-D Child-Langmuir limit”. In: *Third IEEE International Vacuum Electronics Conference (IEEE Cat. No. 02EX524)*. IEEE. 2002, pp. 131–132.
- [161] Robert J Goldston and Paul Harding Rutherford. *Introduction to plasma physics*. CRC Press, 1995.
- [162] Yu I Belchenko et al. “Development of surface-plasma negative ions sources at the Budker Institute of nuclear physics”. In: *AIP Conference Proceedings*. Vol. 2052. 1. AIP Publishing LLC. 2018, p. 030006.
- [163] Francesco Taccogna et al. “Negative-ion-source modeling: From expansion to extraction region”. In: *IEEE transactions on plasma science* 36.4 (2008), pp. 1589–1599.
- [164] N St J Braithwaite and John E Allen. “Boundaries and probes in electronegative plasmas”. In: *Journal of Physics D: Applied Physics* 21.12 (1988), p. 1733.

- 
- [165] H Amemiya, BM Annaratone, and JE Allen. “The collection of positive ions by spherical and cylindrical probes in an electronegative plasma”. In: *Plasma Sources Science and Technology* 8.1 (1999), p. 179.
- [166] JI Fernández Palop et al. “Transition of the sheath structure in an electrostatic probe from electropositive to electronegative plasma”. In: *Journal of applied physics* 91.5 (2002), pp. 2587–2593.
- [167] JI Fernández Palop et al. “Effect of collisions in the stratified presheath in electronegative plasmas”. In: *Applied physics letters* 88.26 (2006), p. 261502.
- [168] Kiomars Yasserian, Morteza Aslaninejad, and Mahmood Ghoranneviss. “Structure of presheath-sheath in magnetized electronegative plasma”. In: *Physics of Plasmas* 16.2 (2009), p. 023504.
- [169] Orson Sutherland et al. “Comparison between experiment and two simulation strategies for the extraction of focused ion beams”. In: *Review of scientific instruments* 75.7 (2004), pp. 2379–2386.
- [170] K Tsumori et al. “Spatial distribution of the charged particles and potentials during beam extraction in a negative-ion source”. In: *Review of Scientific Instruments* 83.2 (2012), 02B116.
- [171] Valery A Godyak and Natalia Sternberg. “Smooth plasma-sheath transition in a hydrodynamic model”. In: *IEEE transactions on plasma science* 18.1 (1990), pp. 159–168.
- [172] JI Fernández Palop et al. “Sheath structure in electronegative plasmas”. In: *Plasma Sources Science and Technology* 16.1 (2007), S76.
- [173] B Liebig and JW Bradley. “Space charge, plasma potential and electric field distributions in HiPIMS discharges of varying configuration”. In: *Plasma Sources Science and Technology* 22.4 (2013), p. 045020.

- [174] Robert F Kemp and JMs Sellen Jr. “Plasma potential measurements by electron emissive probes”. In: *Review of Scientific Instruments* 37.4 (1966), pp. 455–461.
- [175] Mark J Kushner. “Floating sheath potentials in non-Maxwellian plasmas”. In: *IEEE transactions on plasma science* 13.1 (1985), pp. 6–9.
- [176] R Morales Crespo et al. “Floating potential and sheath thickness for cylindrical and spherical probes in electronegative plasmas”. In: *Journal of applied physics* 99.5 (2006), p. 053303.
- [177] Guillermo Fernando Regodon et al. “Floating potential in electronegative plasmas for non-zero ion temperatures”. In: *Plasma Sources Science and Technology* 27.2 (2018), p. 025014.
- [178] Paul Bryant. “Floating potential of spherical probes and dust grains in collisional plasmas”. In: *Journal of Physics D: Applied Physics* 36.22 (2003), p. 2859.
- [179] Haruo Shindo and Yasuhiro Horiike. “Floating potential in negative-ion-containing plasma”. In: *Japanese journal of applied physics* 30.1R (1991), p. 161.
- [180] C Auth, AG Borisov, and H Winter. “High fractions of negative ions in grazing scattering of fast oxygen atoms from a LiF (100) surface”. In: *Physical review letters* 75.12 (1995), p. 2292.
- [181] L Schiesko et al. “H<sup>-</sup> production on a graphite surface in a hydrogen plasma”. In: *Plasma Sources Science and Technology* 17.3 (2008), p. 035023.
- [182] Gilles Cartry et al. “Alternative solutions to caesium in negative-ion sources: a study of negative-ion surface production on diamond in H<sub>2</sub>/D<sub>2</sub> plasmas”. In: *New Journal of Physics* 19.2 (2017), p. 025010.

- 
- [183] Alif Din. “Numerical solutions of sheath structures in front of an electron-emitting electrode immersed in a low-density plasma”. In: *Physics of Plasmas* 20.9 (2013), p. 093505.
- [184] S Christ-Koch et al. “Laser photodetachment on a high power, low pressure rf-driven negative hydrogen ion source”. In: *Plasma Sources Science and Technology* 18.2 (2009), p. 025003.
- [185] Wataru Oohara and Rikizo Hatakeyama. “Pair-ion plasma generation using fullerenes”. In: *Physical review letters* 91.20 (2003), p. 205005.
- [186] AK Pandey and SK Karkari. “Characteristics of floating potential of a probe in electronegative plasma”. In: *Physics of Plasmas* 24.1 (2017), p. 013507.
- [187] Hiroshi Amemiya. “Production of electron-free plasma by using a magnetic filter in radio frequency discharge”. In: *Japanese journal of applied physics* 30.10R (1991), p. 2601.
- [188] Derek Monahan. “Modelling The Electronegative Discharge”. PhD thesis. Dublin City University, 2007.
- [189] Hiroshi Amemiya. “Production of electron-free plasma by using a magnetic filter in radio frequency discharge”. In: *Japanese journal of applied physics* 30.10R (1991), p. 2601.
- [190] H Hutchinson. “Principles of Plasma Diagnostics, Chapter-3: Cambridge Univ”. In: *iversity Press* 37 (1987), pp. 25–38.
- [191] P Kudrna and E Passoth. “Langmuir Probe Diagnostics of a Low Temperature Non-Isothermal Plasma in a Weak Magnetic Field”. In: *Contributions to Plasma Physics* 37.5 (1997), pp. 417–429.
- [192] Francis F Chen. “Langmuir probe diagnostics”. In: *Mini-Course on Plasma Diagnostics, IEEEICOPS meeting, Jeju, Korea. 2003.*



- [193] Juan Manuel Diaz-Cabrera et al. “Accurate measurement of the ion saturation current collected by a cylindrical Langmuir probe in cold plasmas”. In: *Plasma Processes and Polymers* 17.11 (2020), p. 2000073.
- [194] J Ballesteros et al. “Influence of the positive ion temperature in cold plasma diagnosis”. In: *Applied physics letters* 89.10 (2006), p. 101501.
- [195] JI Fernandez Palop et al. “Theoretical ion current to cylindrical Langmuir probes for finite ion temperature values”. In: *Journal of Physics D: Applied Physics* 29.11 (1996), p. 2832.
- [196] J Basu and C Sen. “Sheath thickness for a cylindrical or spherical probe placed in a plasma”. In: *Japanese Journal of Applied Physics* 12.7 (1973), p. 1081.
- [197] David J Peterson et al. “Electron neutral collision frequency measurement with the hairpin resonator probe”. In: *Plasma Sources Science and Technology* 26.9 (2017), p. 095002.
- [198] Sigvald Marholm and Richard Marchand. “Finite-length effects on cylindrical Langmuir probes”. In: *Physical Review Research* 2.2 (2020), p. 023016.
- [199] Brian L Sands, Nicholas S Siefert, and Biswa N Ganguly. “Design and measurement considerations of hairpin resonator probes for determining electron number density in collisional plasmas”. In: *Plasma Sources Science and Technology* 16.4 (2007), p. 716.
- [200] JW Bradley et al. “Space and time resolved Langmuir probe measurements in a 100 kHz pulsed rectangular magnetron system”. In: *Surface and Coatings Technology* 142 (2001), pp. 337–341.